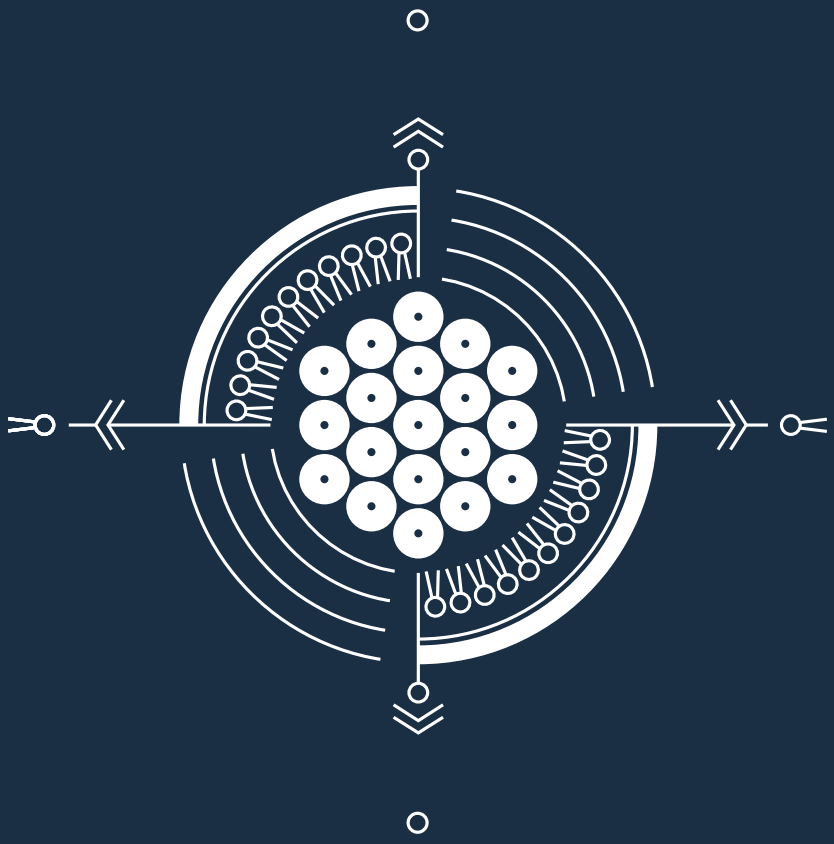

MONODISPERSE BUBBLES AND DROPLETS

for medical applications

Tim Segers

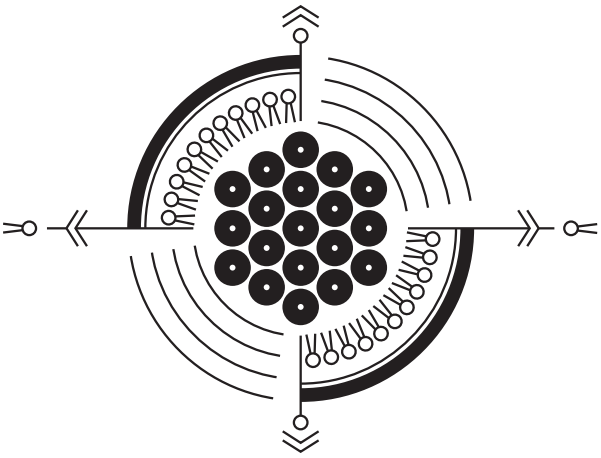

MONODISPERSE BUBBLES AND DROPLETS

for medical applications

Samenstelling promotiecommissie:

Prof. dr. ir. J. W. M. Hilgenkamp (voorzitter, secretaris)	Universiteit Twente, TNW
Prof. dr. A.M. Versluis (promotor)	Universiteit Twente, TNW
Prof. dr. ir. N. de Jong (promotor)	Erasmus MC Medical Center
Prof. dr. ir. A. van den Berg	Universiteit Twente, EWI
Prof. dr. J. Engbersen	Universiteit Twente, TNW
Prof. dr. ir. M. Kreutzer	TU Delft
Prof. dr. A. P. Lee	University of California at Irvine
dr. ir. P. J. A. Frinking	Bracco Suisse SA

The research described in this thesis is part of the research program NanoNextNL, a micro and nanotechnology consortium of the Government of the Netherlands and 130 partners. This thesis was carried out at the Physics of Fluids group of the Faculty of Science and Technology of the University of Twente.

Cover design:
Compass to guide the reader through the world of monodisperse bubbles that self-assemble in a hexagonal lattice. The bubbles are coated with phospholipids that can shed during radial oscillations. Radially oscillating bubbles produce sound waves. Lex en Tim Segers.

Nederlandse titel:
Mondisperse bellen en druppels voor medische toepassingen

Publisher:
Tim Segers, Physics of Fluids, University of Twente,
P.O. Box 217, 7500 AE Enschede, The Netherlands
http://pof.tnw.utwente.nl
t.j.segers@alumnus.utwente.nl

© Tim Segers, Enschede, The Netherlands 2015.
No part of this work may be reproduced by print, photocopy or any other means without the permission in writing from the publisher.
ISBN 978-90-365-3899-2

MONODISPERSE BUBBLES AND DROPLETS FOR MEDICAL APPLICATIONS

PROEFSCHRIFT

ter verkrijging van
de graad van doctor aan de Universiteit Twente,
op gezag van de rector magnificus,
prof. dr. H. Brinksma,
volgens besluit van het College voor Promoties
in het openbaar te verdedigen
op woensdag 29 mei 2015 om 16.45 uur

door

Tim Joseph Segers

geboren op 14 April 1987

te Almelo

Dit proefschrift is goedgekeurd door de promotoren:
Prof. dr. A.M. Versluis
Prof. dr. ir. N. de Jong

Contents

CONTENTS

1 Introduction[1]

Ultrasound is the most widely used medical imaging modality. It offers low-risk and portable imaging, it produces real time images, which can be taken at bed-side, and it is inexpensive as compared to computed tomography (CT) and magnetic resonance imaging (MRI). The working principle is based on the scattering and reflection of transmitted ultrasound waves at interfaces and tissue inhomogeneities with different acoustic impedances. An ultrasound image can be constructed from the time of flight and the intensity of the received echos. Typical ultrasound frequencies used are in the range of 1 to 50 MHz, where the highest frequencies result in the highest spatial resolution due to its shorter wavelength. For higher frequencies, however, the penetration depth is reduced as a result of attenuation, which increases linearly with frequency. Therefore the optimum imaging frequency is always a trade-off between resolution and imaging depth.

Tissues in the body contain acoustical inhomogeneities which scatter ultrasound and light up in an ultrasound images. On the other hand, blood is a poor ultrasound scatterer and the visibility of the blood pool can be enhanced by the use of stabilized microbubbles as an ultrasound contrast agent (UCA). Ultrasound contrast agents consist of a suspension of stabilized microbubbles with a size between 0.5 and 10 μm in diameter, so they can safely pass even the smallest vascular beds. Bubbles are highly echogenic due to the acoustic impedance mismatch with their liquid surrounding and due to the resonance behavior of the bubble vibrations. The interaction of bubbles and ultrasound and the influence of the stabilizing shell is subject of extensive study, summarized in this chapter, and our improved insight into the underlying physical mechanisms gives rise to increased performance of ultrasound contrast agents and their use in medical imaging and therapy.

This chapter will give an overview of the applications and design considerations of microbubbles for medical applications. First, the use of microbub-

[1]Published as: T. Segers, N. de Jong, D. Lohse, M. Versluis, *Microfluidics for medical applications*, Microbubbles for medical applications, ISBN: 978-1-84973-637-4, DOI:10.1039/9781849737593, RSC Nanoscience & Nanotechnology (2014)

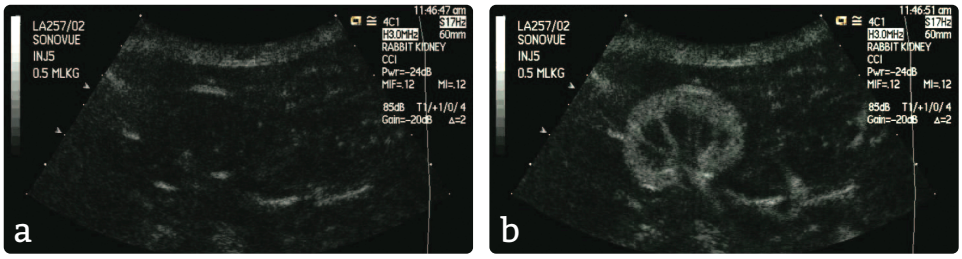

Figure 1.1: Ultrasound contrast microbubble imaging of the kidney. Ultrasound echo image of a rabbit kidney. a) Before arrival of the ultrasound contrast agent and b) contrast enhancement due to presence of the ultrasound contrast agent[2].

bles for imaging and therapeutic purposes is introduced. The physical characteristics of microbubbles in a sound field are then described in order to understand the processes by which microbubbles enhance ultrasound imaging contrast. The third section explains that microbubbles may quickly dissolve in the surrounding liquid and that they need to be stabilized by a coating. The standard contrast agent production methods are given in the fourth section as well as more recent methods to produce monodisperse bubble suspensions using lab-on-a-chip devices. Finally, the dynamics of coated bubbles is discussed and methods to characterize the dynamics are presented.

1.1 Microbubbles for imaging

The mechanism by which the microbubbles enhance the contrast is twofold. First, acoustic waves are scattered by the bubbles due to the large difference in acoustic impedance between the gas and the surrounding liquid. Second, the large compressibility of the gas bubbles results in radial oscillations of the bubbles in response to the ultrasound pressure waves. The radial oscillations are highly non-linear and produce non-linear sound waves which are exploited in contrast-enhanced ultrasound imaging. The strong scattering of the microbubbles allows for the visualization and quantification of blood perfusion in organs, e.g. heart, liver or kidney[1]. Figure 1.1 shows an ultrasound image of a rabbit kidney before (A) and after (B) arrival of a bolus injection of an ultrasound contrast agent.

The sensitivity of the bubble detection, down to a single bubble *in-vivo*, facilitates targeted molecular imaging applications for the diagnosis of diseases at the molecular level. Targeting ligands that bind specifically to selective biomarkers on the blood vessel wall can be labeled to the micro-

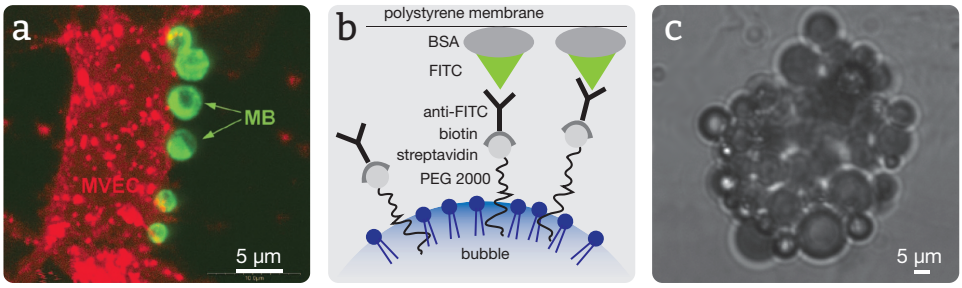

Figure 1.2: a) Fluorescent microscopy image of microbubbles (MB) targeted to a microvascular endothelial cell (MVEC)[1]. b) Microbubbles can be targeted to a membrane in an experimental setting by labeling the bubbles with a PEG2000 spacer connected to streptavidin. A strong biotin-streptavidin bond between the bubble and the membrane is utilized when the membrane is labeled with BSA connected to FITC, anti-FITC and biotin[5]. c) A complex of microbubbles targeted to a stem cell[6]. These complexes are echogenic and they can therefore be directed using acoustic radiation forces towards diseased tissue to upregulate the therapeutic targeting efficiency.

bubble shell[3], see Fig. 1.2. The approach here is to inject targeted bubbles intravenously, then to wait 5 to 10 minutes for the freely flowing bubbles to be washed out by the lungs and the liver and then to image the adherent bubbles using ultrasound. One other approach is to discriminate acoustically between freely flowing and adherent bubbles through spectral differences through a resonance shift of the adherent bubbles due to the interaction between the bubble and the vessel wall[4,5]. This approach would require that all bubbles have the same response to the ultrasound driving signal which is up to now not possible because of the large size distribution of the commercial agents. Recently microbubbles were targeted to stem cells[6] to produce echogenic complexes which can be directed towards diseased tissue using acoustic radiation forces to upregulate the therapeutic targeting efficiency (Fig. 1.2c).

1.2 Microbubbles for therapy

Contrast agent microbubbles can themselves serve as therapeutic agents. Several configurations are possible here. First, a drug can be co-administered with the bubbles while ultrasound-induced bubble oscillations close to cells promote local drug uptake through mechanical stress to the adjacent cell membranes, a process called sonoporation. Second, UCAs can be loaded

with drugs, e.g. for the local delivery of chemotherapeutic drugs[1,3] with a narrow therapeutic index, or for the delivery of genes, such as siRNAs[7–9]. The payload can be directly incorporated in the bubble coating[10], or in the core of the bubble[11,12], or in liposomes attached to the bubble shell[13]. Drug-loaded microbubbles can be imaged at low acoustic pressures aiding the guidance and realtime monitoring of the therapy, then at higher acoustic pressures rupture of the bubble shell triggers drug release. Ideally, the release of such a payload follows a step response after passing an insonation pressure threshold for the controlled release of the payload in a confined and highly localized region determined by the position of the acoustic focus and the position of the bubbles. The prime focus of such a local delivery is to reduce the systemic exposure to toxic drugs and to increase the delivery efficacy by preventing early capture of the drugs or genes by the systemic system. Various therapeutic bubble systems are displayed in Fig. 1.3.

The mechanical stress exerted by the oscillating microbubbles leading to sonoporation, i.e. the transient increase in cell membrane permeability, can be caused by several mechanisms. Oscillating bubbles in close vicinity to cells will cause palpation or normal stresses on the cell membranes through the attractive secondary radiation forces between the bubbles and the cells[16,17]. Furthermore, asymmetric bubble oscillation and oscillatory translations may lead to the build up of acoustic streaming around the bubble[18], which will induce a shear stress on the cell membrane. Moreover, acoustic streaming will enhance the influx of fresh therapeutic agent through local mixing. Driving the bubbles at higher acoustic pressures can lead to asymmetric collapse of the bubble and the formation of a liquid jet, a violent process called inertial cavitation[19–21]. The liquid jet can reach a speed ranging from 10-100 m/s[22,23], resulting in pore formation in the cell membrane. Typically, short ultrasound pulses are used to avoid irreversible membrane poration, leading to cell death. The interaction between oscillating bubbles and the blood-brain barrier (BBB) has shown the ability to transiently disrupt the tight junctional complexes, which normally prevent the entry of therapeutic drugs into the brain[24–26].

1.3 Microbubbles for cleaning

High-intensity focused ultrasound, or HIFU, utilizes long pulse ultrasound to create thermal ablation for deep tissue surgery and is promoted by the use of microbubbles[27–29]. In extracorporeal shockwave lithotripsy, cavitating clouds of microbubbles created in the focus of a shockwave lead to mechanical ablation to break kidney stones[30,31]. Each year many people suffer from

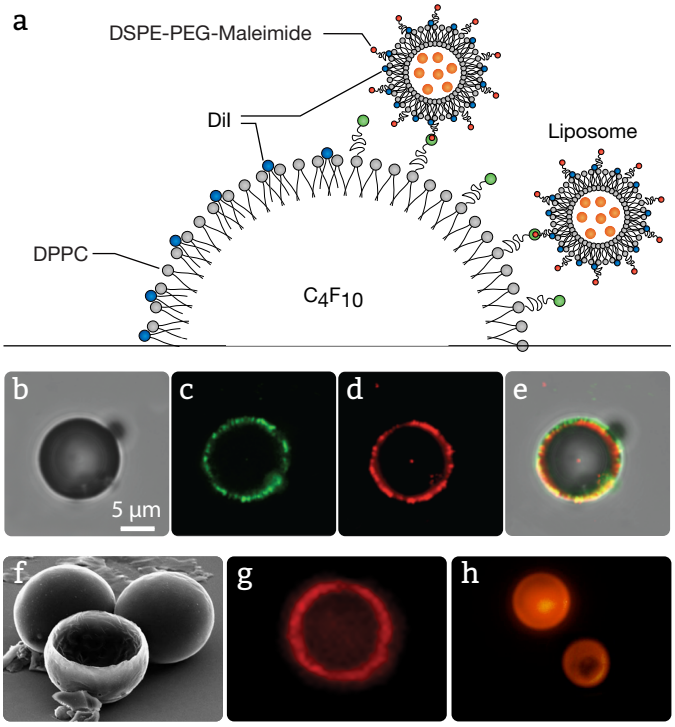

Figure 1.3: a) Schematic representation of a typical drug-loaded fluorescently labeled phospholipid coated microbubble[14]. The drug is loaded in liposomes attached to the bubble shell. b) A brightfield image of such a drug loaded microbubble[14] and fluorescent images of c) bodipy-labeled liposomes and d) of the DiI-labeled phospholipid shell. e) An overlay of the images shows that the loaded liposomes are situated outside the bubble shell. f) A SEM image of a hard-shelled microcapsules[15]. g) These capsules can be filled with air or h) they can be filled with an oil containing hydrophobic drugs.

a stroke. Ischemic stroke results from an occlusion of a major blood vessel in the brain by a blood clot, which decreases or suppresses blood supply downstream which may lead to long term disability or death. Contrast agent microbubbles can be used in combination with ultrasound to lyse thrombi in the blood vessel, restoring blood flow, a process termed sonothrombolysis[32]. The microbubbles can be injected next to the blood clot while being insonified with ultrasound or, alternatively and in a more controlled manner, IV-injected microbubbles targeted to the blood clot bind to the target and are subsequently insonified with ultrasound. The microbubble oscillations may lead to microstreaming and cavitation (microjetting) and the

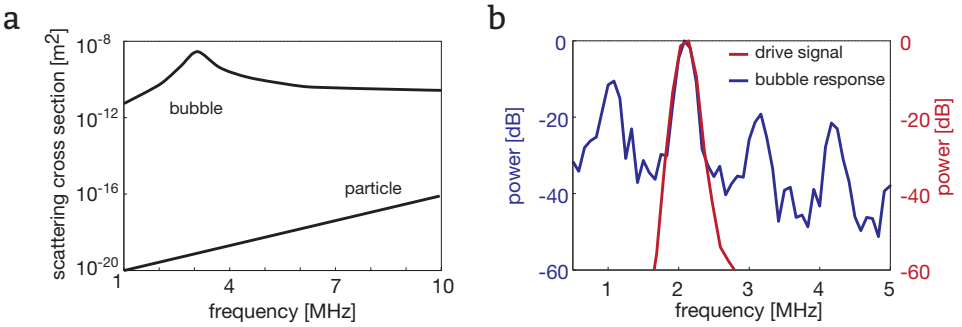

Figure 1.4: a) The scattering cross section of a bubble can be 1 billion times larger than that of a solid particle of the same size[33]. In addition, the scattering cross section of a bubble gains another two orders of magnitude if it is driven at its resonance frequency. b) The bubble oscillations are highly non-linear, generating harmonics of the fundamental driving frequency exploited to discriminate between linear tissue echoes and harmonic bubble echoes[34].

combined action of mechanical stress exerted, mixing of an anti-coagulant such as rTPA, and flow may lead to a controlled disintegration of the blood clot in such a high-risk area.

1.4 Microbubble basics

Contrast microbubbles produce a very strong echo, which can be 1 billion times stronger than the echo of solid particles of the same size[33], owing to the large compressibility of the gas core of the bubbles, see Fig. 1.4. In addition, the bubbles resonate to the driving ultrasound field, adding another two order of magnitude to its scattering cross section. Finally, the bubbles oscillate non-linearly, generating harmonics of the fundamental driving frequency, which allows efficient discrimination of the linear tissue echoes from the harmonic bubble echoes, boosting its contrast ability, which is expressed in the contrast-to-tissue ratio (CTR).

1.4.1 Microbubble dynamics

The bubble dynamics is governed by the equation of motion for a spherical bubble, known as the Rayleigh-Plesset (RP) equation[35]. The RP-equation follows directly from Bernoulli's principle (Newton's 2nd law) and the continuity equation:

$$\rho R\ddot{R} + \frac{3}{2}\rho\dot{R}^2 = p_i - p_e \tag{1.1}$$

where ρ is the liquid density and R, $\dot{R}$, and $\ddot{R}$ represent the radius of the bubble, the velocity of the bubble wall, and the acceleration of the bubble wall, respectively. p_i is the bubble's internal pressure and it depends on the properties of the gas. p_e is the external pressure and it includes the pressure contributions of the ambient pressure, the interfacial pressure and the driving pressure $p_A(t)$. Equation (1.1) is an ordinary differential equation and its solution, given any driving pressure pulse $p_A(t)$, is the radius of the bubble as a function of time, $R(t)$. The nonlinear features of the bubble response, or echo, originate directly from the nonlinearities in the above equation. Once the radial dynamics is known, the pressure emitted by the bubble, $p_s(t)$ (in medical ultrasound literature termed the scattered pressure), can be calculated from the conservation of mass and momentum[36]:

$$p_s = \frac{\rho R}{r}(2\dot{R}^2 + R\ddot{R}) \tag{1.2}$$

where r is the distance to the bubble. Thus, for any given driving pressure pulse $p_A(t)$ the nonlinear echo $p_s(t)$ can be calculated for an oscillating spherical bubble.

To understand the resonance behavior of microbubbles it is insightful to linearize the bubble dynamics equation. Assuming a sinusoidal pressure pulse in addition to the ambient pressure, $p_e = p_0 + p_A sin\omega t$, with angular frequency $\omega = 2\pi f$ with f the ultrasound frequency, and assuming small amplitude oscillations $R = R_0(1+x)$, where R_0 is the ambient bubble radius and $x \ll R_0$. Neglecting higher-order terms in x, Eq. (1.1) then reduces to the classical differential equation of a simple driven harmonic oscillator[37]:

$$\ddot{x} + \omega_0^2 x = \frac{p_A}{\rho R_0} sin\omega t \tag{1.3}$$

with a characteristic bubble oscillation eigenfrequency

$$\omega_0 = \sqrt{\frac{3\kappa p_0}{\rho R_0^2}}, \tag{1.4}$$

with κ the polytropic exponent of the gas. The analogy to a mass-spring system is that the liquid surrounding the bubble acts as a mass, while the gas acts as a spring. Thus, the bubble resonates to the driving pressure field, and it has a resonance frequency f_R where a maximum amplitude is observed, see the resonance curve displayed in Fig. 1.10. Figure 1.10 will be discussed in more detail later in this chapter. The system experiences damping, which can be appreciated from the width of the resonance curve. The energy loss mechanisms associated with damping can be attributed to

acoustic reradiation and following a more detailed analysis also from viscous damping through the liquid viscosity and thermal damping due to the build-up of a thermal boundary layer around the bubble[38]. The total dimensionless damping constant, i.e. the sum of all the damping contributions, for microbubbles of a typical size of 5 μm is 0.1, therefore the resonance frequency is very close to the eigenfrequency of the bubble[37], $f_R \approx f_0$. Note that the eigenfrequency is inversely proportional to the radius of the bubble, through Eq. (1.4). For an air bubble in water the relation $f_0 \cdot R_0 \approx 3$ μmMHz applies, as was derived earlier by Minnaert[39]. Thus, a 3 μm diameter bubble will have an eigenfrequency near 2 MHz, which is right at the heart of clinical medical ultrasound imaging.

The way the bubbles are driven by ultrasound leading to an echo is depicted in Figure 1.5. A typical transmit pulse consists of a number of cycles of ultrasound at a single frequency and propagates in the direction of the focal region where the bubble is contained. The bubble is driven into oscillation by the successive wave of high and low pressure. The radial response of the bubble and the subsequent movement of the liquid surrounding the bubble leads to a sound emission which is propagating spherically in all directions[36]. The transducer will pick up the echo emitted within the receiving cone angle of the transducer. Given the nonlinear response of the radial bubble dynamics the echo will also contain this particular nonlinear signature and the fundamental frequency and its harmonics (second and third harmonic and subharmonic) will be picked up by the receiving unit within the available bandwidth of the transducer.

Harmonic imaging techniques make use of the non-linear bubble echo to cancel the linear echoes originating from tissue[42]. The pulse inversion technique[43] makes use of two ultrasound pulses with a 180° phase shift and adds the two echoes to cancel out the linear tissue response. Power modulation imaging[44] is a pulse-echo scheme in which two pulses with different acoustic pressure are emitted. The echoes acquired in receive mode are then scaled to the transmit pressure and subtracted to cancel out the linear signal leaving the non-linear signal originating from the bubbles. Finally, subharmonics of the bubble echo[45] are of interest to build up a contrast image, even though it has a lower resolution due to its lower frequency. The reason is that the transmitted ultrasound pulse may deform through nonlinear propagation, forming higher harmonics, and tissue signal leaks into the harmonic bubble signal through linear scattering. On the other hand this exact feature is exploited in tissue harmonic imaging, without the use of contrast bubbles.

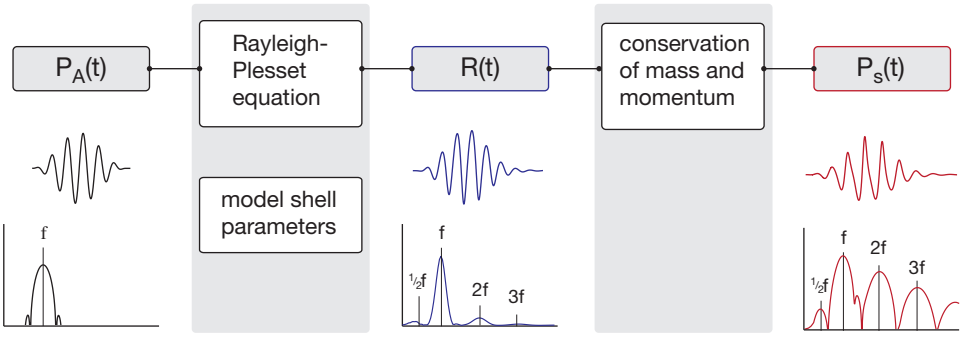

Figure 1.5: Microbubble modeling after Sijl *et al.*[40]. An ultrasound pulse $P_A(t)$ of several cycles at a single frequency f drives radial bubble oscillations, R(t). These can be modeled with a Rayleigh-Plesset-type model with the inclusion of shell pressure terms resulting from the shell viscosity and shell elasticity parameters[41]. The power spectrum of the radial bubble oscillations shows harmonics of the fundamental driving frequency. The bubble oscillations lead to a sound wave in the far field containing harmonics of the driving ultrasound frequency.

1.5 Microbubble stability

Microbubbles are inherently unstable as a result of the capillary force and the resulting diffusion. The internal pressure of a bubble P_i is given by the ambient pressure P_0 plus the interfacial pressure contribution $2\sigma/R$, with σ the surface tension and R the radius of the bubble. For a 2 µm air bubble in water the interfacial pressure amounts to 1 bar. Hence the gas is rapidly squeezed out of the bubble and the bubble dissolves. The rate at which dissolution occurs comes from a diffusive balance[46]:

$$\dot{R} = \frac{D(c_i - c_s)R_gT}{M(P_0 + \frac{4\sigma}{3R})}\left(\frac{1}{R} + \frac{1}{\sqrt{\pi Dt}}\right) \tag{1.5}$$

where R is the bubble radius, $\dot{R}$ the time derivative of the bubble radius, D is the diffusivity constant for the interface at a given temperature and pressure, c_i the initial dissolved gas concentration in the liquid, c_s is the gas concentration at the bubble surface, R_g is the universal gas constant, T the absolute temperature, σ the interfacial surface tension, R_0 the initial bubble radius, P_0 the ambient pressure, M the molecular weight of the gas and t is time. Figure 1.6 shows the fate of microbubbles. In this example it takes a 5 µm diameter bubble approximately 90 ms to dissolve. Microbubbles of a size of 3 µm and 1 µm in diameter take a considerably shorter time to dissolve, 25 ms and 2 ms, respectively. Note that the bubbles follow the

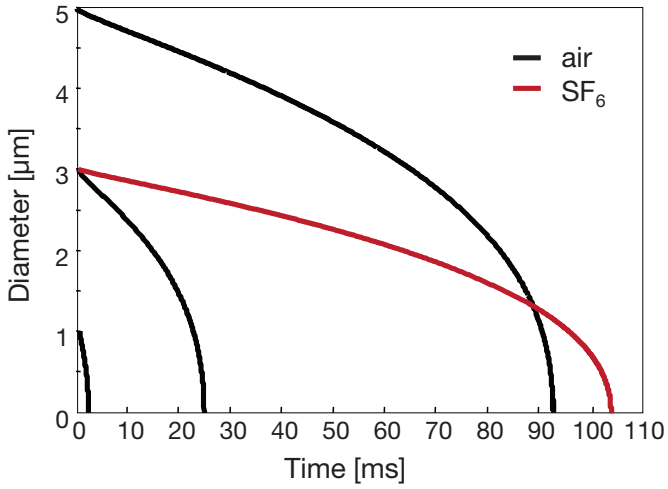

Figure 1.6: Microbubble dissolution curves[46]. A 5 μm air bubble in water dissolves in approximately 90 ms. A 3 μm and a 1 μm air bubble dissolve in 25 ms and 2 ms, respectively. Exchanging the gas core of the 3 μm bubble by a high-molecular weight gas (SF_6) shows a fourfold increase of its lifetime.

exact same dissolution curve once they reach the same size. In practice, the dissolution rate is strongly dependent on the local gas fraction of the surrounding liquid, c_i, which may change in the medium surrounding the bubble once the bubble dissolves and in the presence of flow, other bubbles and solid and free interfaces. Thus, for the use of microbubbles for the aforementioned medical applications, dissolution of the microbubble must be prevented.

There are two ways to approach the dissolution problem: to add a coating to the interface of the bubble and to change the gas in the core of the bubble. The first approach has two main effects. First, the addition of a surfactant coating leads to a reduction of the surface tension, which will decrease directly the dissolution rate. Second, the presence of a surfactant layer at the interface will hinder dissolution through that interface. By changing the gas in the core to an inert high-molecular weight gas with low solubility, e.g. sulfur hexafluoride, SF_6, or perfluorocarbons, e.g. octafluoropropane C_3F_8 or perfluorobutane C_4F_{10}, the lifetime of the bubble can be extended. Figure 1.6 shows the fourfold increase of the lifetime of the 3 µm bubble by exchanging the gas core of the bubble. With the above approaches combined and implemented the total lifetime of the bubble can be extended to 5–10 minutes following intravenous injection. It should also

be noted that typically long-chain poly-ethylene glycol (PEG) spacers are added to the bubble surface to improve circulation lifetime *in-vivo*. Perfluorocarbon gas-filled microbubbles can be stable for several days when kept in a vial under protective gas cover and freeze-dried bubbles can be stored for several years.

The very first class of stabilized microbubbles were coated by denaturated human serum albumin. Agents in this category include air-filled Quantison (Upperton Limited, Nottingham, UK) (Fig. 1.7A)[47] and octafluoropropane-filled Optison (GE Healthcare)[48]. The albumin coating results in a relatively stiff shell[49] and the stiffness of the shell can be tuned by the use of coatings of different thickness. While the oscillation amplitude of hard-shelled microbubbles is dramatically reduced, the mechanism of contrast echo generation lies more in the bursting of the shell, leading to the release of a free gas bubble, with limited lifetime, but long enough to generate an echo above the noise level[50].

Microbubbles can also be stabilized by the use of surfactants containing a hydrophobic tail and a hydrophilic head, which desorb and arrange at the free interface of the microbubble. Soap detergent surfactants, such as Tween and Dreft, are popular microbubble stabilizers for *in-vitro* use. Clinically approved microbubble contrast agents use purified phospholipids such as DPPC, also well-known pulmonary surfactants found in the alveoli, to cover and stabilize the interface. Unlike biological membranes and liposomes, where these lipids form a lipid bilayer, these long-chain lipids form a monolayer, which may change the bubble dynamics upon insonation through its viscoelastic properties. The flexible nature of the monolayer however retains much of its ability to oscillate. Interestingly, the nonlinear effects introduced by the viscoelastic monolayer promotes the nonlinear echo and therefore boosts the contrast-to-tissue ratio. Commercial agents in this category include Sonovue (Bracco Suisse S.A.) (Fig. 1.7B)[53], Definity (Lantheus Medical Imaging)[54] and Sonazoid (GE Healthcare)[48].

For several reasons the use of serum albumin has been less desirable and the coatings of the newer class of agents have now been replaced by biocompatible polymers, ranging from polyvinyl alcohol (PVA), polylactic acid (PLA) (see Fig. 1.7C) and polylactic-co-glycolic acid (PLGA). This type of polymeric microbubble is also popular as a drug delivery vehicle in the form of acoustically triggerable capsules. The *in-vitro* use of thermoplastic-coated microbubbles, e.g. with a PVC-AN shell[55], remains popular for scientific purposes. Agents of this type include nitrogen-filled Cardiosphere (Point Biomedical) and perfluorobutane-filled Imagify (Acusphere)[56].

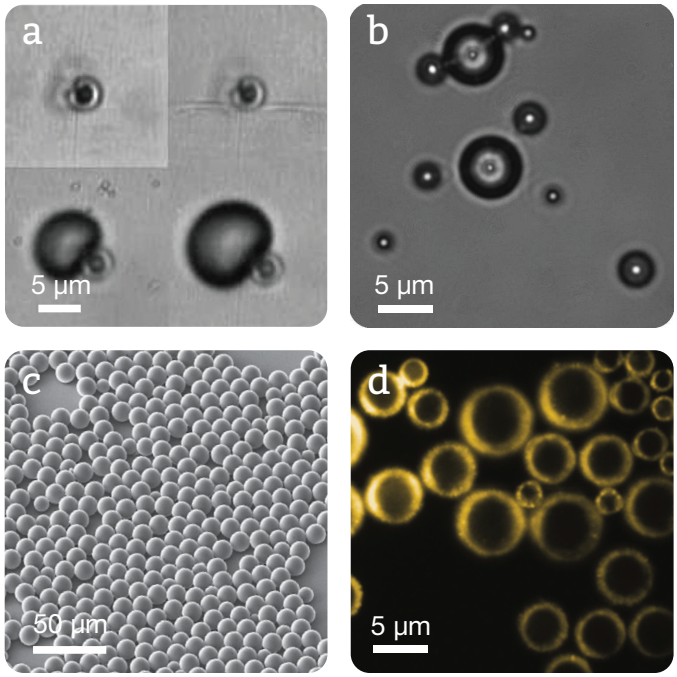

Figure 1.7: Various types of encapsulated agents for imaging and drug-delivery applications. a) Albumin-coated bubbles (Quantison) showing release of a free gas bubble upon rupture of the shell[47]. b) Soft-shelled lipid-coated microbubbles (BR-14 Bracco Research S.A.). c) monodisperse polymeric microbubbles[51] (Image by courtesy of Philips Research Laboratories Europe). d) DiI fluorescently labeled lipid bubbles[52].

1.6 Microbubble formation

Ultrasound contrast agents for medical use are widely available. Most of them come in a vial and have to be resuspended to form a bubble suspension. Typically one to ten billion bubbles in a volume of 1-2 mL are injected in a human perfusion study. The traditional contrast agent production methods are sonication and shaking of a solution of water-soluble surfactants or polymers. Agitation of the fluid results in the inclusion of small air bubbles in the fluid and subsequent diffusion of the coating material to the gas-water interface results in stable microbubbles by a self-assembly of the coating material[13]. The conventional processing techniques offer high yield and low production cost but poor control over microbubble size and uniformity.

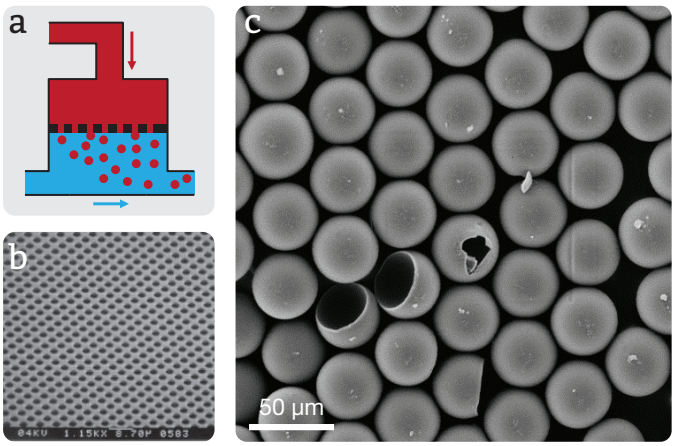

Figure 1.8: Membrane emulsification technology to make monodisperse polymeric microbubbles[59]. a) A polymer dissolved in a solvent is emulsified by a Nanosieve membrane (b) with mono-sized pores to make monodisperse polymeric emulsion microdroplets. c) SEM image of microcapsules formed after freeze drying the emulsion droplets. Images by courtesy of Nanomi monosphere technology, The Netherlands.

Emulsification processes were also shown to lead to high-yield bubble production methods. A polymer is dissolved in a solvent and mixed with water by high shear emulsification[57] resulting in micrometer droplets of dissolved polymer in water. Hard-shelled water-filled microspheres are formed when the solvent is evaporated. The capsules are then washed to remove excess solvent, then freeze-dried to produce gas-filled capsules[58]. A narrow size distribution can be obtained by membrane emulsification of a premix of polymer, polymer solvent and water through a mono-sized porous membrane, see Fig. 1.8. The capsules can also be partly, or fully filled with oil by these emulsification techniques to produce acoustically active hydrophobic drug carriers[15].

For therapeutic applications of microbubbles it becomes increasingly important to be able to predict the acoustic response of the microbubble or of loaded microbubble suspensions which resulted in the development of new production methods for even narrower size distributions. Inkjet printing has been employed to improve microbubble uniformity[51]. Monodisperse droplets of a polymer solution are printed in water from an ink-jet printhead. Polymer-shelled microbubbles are then produced by evaporation of the solvent in a similar way as the membrane emulsification method. While lower in production rate, the ink-jet printing technique has the advantage of

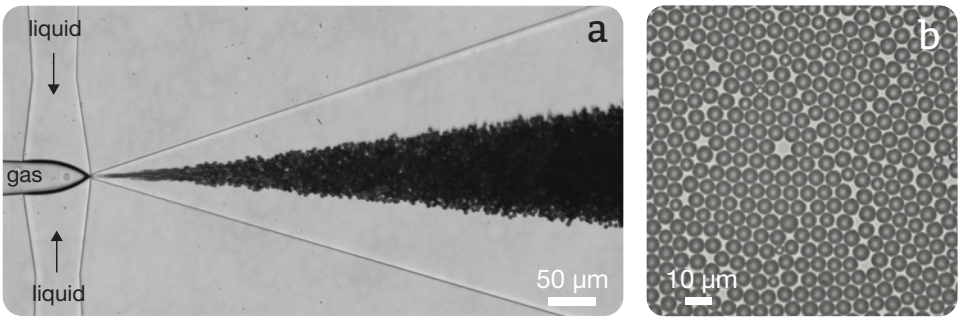

Figure 1.9: a) Flow-focusing geometry for monodisperse microbubble formation by focusing a gas thread between two liquid co-flows through a narrow orifice[69] at a production rate of 300.000 bubbles per second. b) Harvested stable monodisperse bubbles produced in a flow focusing device[70].

being able to change the droplet size rather easily by changing the droplet formation parameters online in the printhead.

Highly monodisperse droplets and bubbles can be produced using flow focusing techniques[60–63]. Figure 1.9 shows how a central gas or a liquid thread is focused in between two external liquid flows through an orifice, where the thread is pinched off to form monodisperse bubbles or droplets. This microfluidic technique offer advantages over methods such as piezo ink-jet printing in that bubbles can be formed in a single step without the need for further processing steps, e.g. to remove solvents. Flow focusing techniques have also shown to be able to produce concentric bubbles with an outer oil layer facilitating drug loading[64]. A challenging aspect of this approach is to understand how the monodisperse bubbles can be encapsulated with a biocompatible coating to stabilize them[65–67], to investigate how to maintain the monodispersity of bubbles produced at high production rates over time[64], and to investigate the dynamics of different coating materials for *in-vivo* and clinical use[68].

1.7 Microbubble modeling and characterization

The coating of the microbubble changes the bubble dynamics[71–74]. The addition of a surfactant layer and resulting pressure contributions from the viscoelastic shell must be incorporated into the RP-equation, Eq. 1.1. The elasticity of the shell increases the stiffness of the system, hence an increase of the resonance frequency is expected. Similarly the viscosity of the shell leads to energy loss and increased damping. The dynamical behaviour can

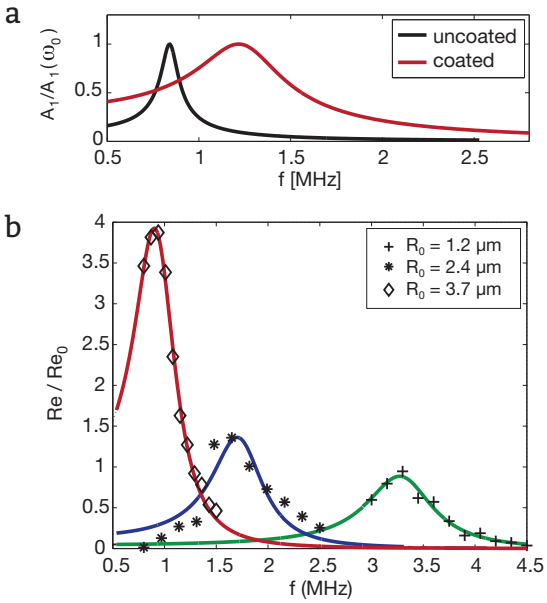

Figure 1.10: Resonance curves. a) Resonance curve of an uncoated 3.8 μm bubble and of a bubble of the same size with a phospholipid coating. The coating increases the stiffness of the system resulting in an increased resonance frequency. The viscosity of the coating leads to an increased energy dissipation, or damping, resulting in a broadened resonance curve. b) A scan of the relative amplitudes of oscillation, of 3 bubbles of different size, as a function of the insonation frequency. A Rayleigh-Plesset type model accounting for the bubble shell can be fitted to the measured resonance curves (solid lines) to extract information on the bubble shell viscoelastic parameters.

be modeled as was shown before in figure 1.5 by including the shell parameters in the Rayleigh Plesset model. Literature reports a shell viscous damping contribution of 75% of the total damping, so governing the resulting oscillation amplitudes and scattered pressures. Figure 1.10A shows the normalized resonance curve of a coated bubble. The effect of the viscoelastic shell is evident with an increase of the resonance frequency of nearly 40% and broadening of the resonance curve as a result of increased damping.

Recently it was discovered that nonlinear properties of the bubble shell are important at small oscillation amplitudes[41]. A high concentration of lipids for example may lead to buckling of the lipid shell upon compression, while the bubble may rupture upon expansion, forming lipid islands on the otherwise free interface, thereby exposing the gas directly to the liquid. In

addition gas loss through diffusion leads to a higher concentration of lipids at the bubble surface, which may lead to folding or budding of the lipid layer. This may eventually result in expulsion of the excess lipids, which in turn leads to a higher surface tension, promoting gas loss, etcetera. In addition, the interfacial rheology is important to fully describe the origin and the details of the nonlinear echo, and details can be found in refs.[67,75]. One important conclusion of the recent work on nonlinear properties of the shell is that the frequency of maximum response is invariably pressure-dependent[75], and a breakaway from the classical Minnaert theory.

1.7.1 Optical characterization

Microbubble dynamics models are validated through single bubble optical characterization. The optical visualization of a sample of microbubbles under the microscope is relatively straightforward, but the real-time visualization of the bubble dynamics upon insonation with a 2-MHz ultrasound pulse is quite challenging and it requires high-speed imaging at a frame rate near 10-20 million frames per second. Several camera systems[76–78] are capable or reaching such high frame rates and in addition acquire a high number of frames of 100 or more. A higher number of frames allows for the measurements of the bubble response at various acoustic parameters, such as pressure[79] and frequency[80], or both[75]. A scan of the bubble response with varying frequency leads to the recording of the resonance curve[80], see Fig. 1.10B, and provides valuable information on the shell viscoelastic properties. Recent advances in ultra high-speed fluorescence microscopy, some performed at frame rates exceeding 20 million frames per second[77,78], have revealed new insight in lipid shedding, drug release[14] and drug uptake mechanisms[52,81] and valuable information for bubble-mediated medical applications.

1.7.2 Sorting techniques

Commercial off-the-shelf ultrasound contrast agents typically have a wide size distribution. With the transducers at a rather narrow frequency range, this means that only a small selection of microbubbles participates in the generation of the non-linear echo, i.e. only those microbubbles that are resonant to the driving ultrasound frequency. Thus, the scattering efficiency and resulting sensitivity can be improved by narrowing down the size distribution and to make the agent more monodisperse. This is particularly useful for techniques now being developed in molecular imaging with ultrasound. As mentioned before, excellent monodispersity can be achieved

in flow-focusing devices and the size of the microbubbles can be tuned by tuning the gas and liquid flow rates of the device. One promising approach is to sort the bubbles. Figure 1.11 summarizes various sorting techniques, e.g. by filtering[79] or by decantation[82]. A selection of bubbles can also be extracted by means of centrifugation[83] or by using a microfluidic sorting strategy, e.g. using pinched flow fractionation[84]. All these approaches lead to a sorting of bubbles by size and as indicated before in section 1.4, from the nonlinear effect of the coating, it could also be advantageous to sort microbubbles based on their acoustical properties, rather than size, as was demonstrated recently[85].

1.7.3 Acoustical characterization

From the examples above while discussing damping and energy loss mechanisms it is evident that a high concentration of bubbles at resonance not only delivers a strong (nonlinear) echo, but also extracts pulse energy from the driving pulse and the total echo may be attenuated by absorption. Hence it is important to measure the scattering to attenuation ratio[87,89] (STAR) of the microbubble suspension, the suspension being a native commercial agent, freshly produced bubbles in a flow-focusing device or sorted bubbles extracted from a polydisperse bubble collection. Such a STAR measurement is displayed in Fig. 1.12 and can be performed in a small water tank with a central container holding the microbubble suspension under continuous stirring. A transmit pulse is sent through the sample and the pulse is received by a transducer at the opposite end of the water tank and as such it will represent the attenuation. At the same time a transducer placed at a 90° angle to the transmit pulse focused at the sample region of interest measures the scattered signal. To fully characterize the contrast bubble suspension, these measurements must be performed for the full parameter space of acoustic pressures and frequencies, in addition to the concentration of the agent.

1.7.4 Conclusions

Microbubbles are globally used in a clinical setting to perform contrast-enhanced ultrasound imaging. The use of microbubbles for molecular imaging has recently entered the clinical phase were the first targeted bubbles were used for the early detection and localization of prostate cancer[90]. Microbubbles have also been clinically used to successfully induce middle cerebral artery recanalization in combination with rTPA. Ultrasound imaging in combination with microbubbles has therefore shown to have a great poten-

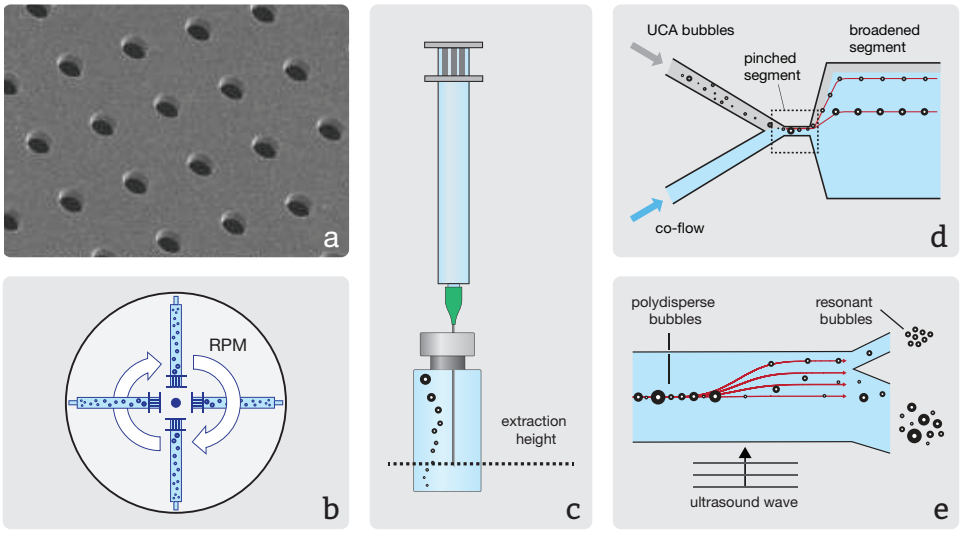

Figure 1.11: Sorting strategies for ultrasound contrast agent enrichment. a) Pore filters can be used to filter bubbles to size[79,86]. Two filters of different size are needed to band-pass filter a bubble suspension. b) Bubbles can be sorted using the difference in gravitational force acting on bubbles of different size. Centrifugation of the bubble suspension can be applied to increase the efficiency of this sorting technique[83]. c) The buoyancy force can also be used through decantation[82,87], the larger bubbles rise faster in a fluid than the smaller bubbles. d) Pinched flow fractionation[84] is a microfluidic sorting technique which can be utilized to sort microbubbles[88] by pinning them to a wall by a co-flow in the pinched segment. Size-selective sorting is achieved through expansion into the broadened segment by microfluidic amplification. e) Acoustic bubble sorting[85] sorts bubbles to their acoustic property rather than to their size. Bubbles are displaced from the center line in a microfluidic channel, where they are injected, by a traveling acoustic wave through the primary radiation force. The displacement is strongly coupled to the resonance behavior of the microbubbles.

tial for molecular imaging, for therapy and for drug delivery applications.

Microbubbles for *in-vivo* use can be coated with several biocompatible coatings, ranging from hard-shelled polymer agents to soft-shelled, more acoustically active, phospholipid agents. Both coating materials can be used to devise targeted drug-loaded bubbles. Soft-shelled bubbles can transport drugs incorporated in their shell, in liposomes attached to their shell or in an oil layer inside the bubble. Hard-shelled agents are more robust and can carry a variety of drug loads in liquid form. The dynamical behaviour of both hard-shelled and soft-shelled bubbles is studied extensively and is well-

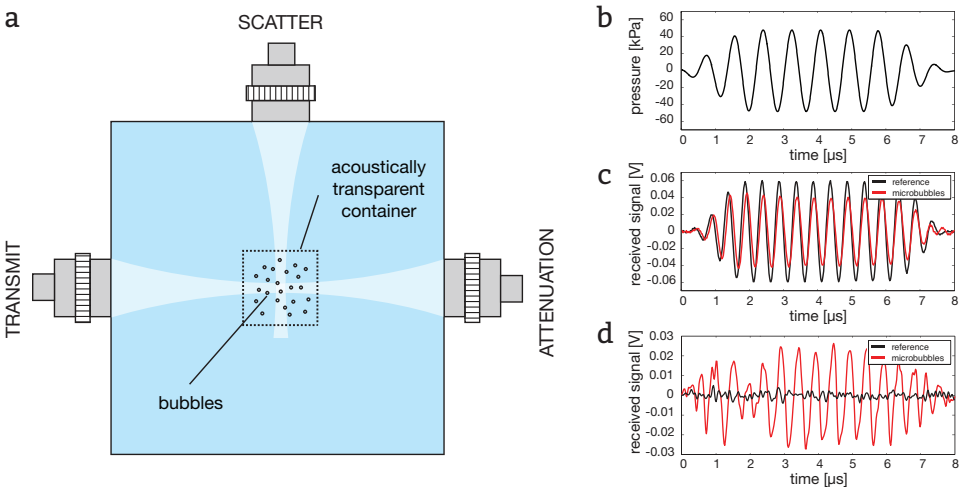

Figure 1.12: Bubble suspensions can be characterized by measuring the scattering and attenuation of acoustic waves by the bubbles. A transmit transducer sends an ultrasound pulse of several acoustic cycles (b) through the bubble sample and it is received by a transducer at the opposite side of the water tank. c) The received signals of a water-filled container and a container filled with a bubble suspension can be divided to find the frequency-dependent, pressure-dependent and concentration-dependent attenuation of the bubble cloud. At the same time a transducer placed at a 90° angle to the transmit transducer measures the scattered acoustic signal (d). The measured frequency dependent scattering and attenuation characteristics are divided to find the scattering to attenuation (STAR) ratio as a function of the acoustic parameters (frequency and pressure) and bubble concentration.

understood. Rayleigh-Plesset-type models have been modified to account for the non-linear behaviour of the viscoelastic shell and are able to describe the dynamical bubble behaviour in detail.

Bubble detection pulse-echo schemes, microbubble-based molecular imaging with ultrasound and targeted drug delivery would benefit to a great extent from a well-controlled bubble response. Therefore techniques are now being developed to produce bubble suspensions with a narrow size distribution. Examples are membrane emulsification for the production of hard-shelled agents and flow-focusing techniques for lipid-shelled bubbles. Nevertheless, coating the bubbles in a stable way while maintaining the monodispersity over time is difficult and a few hurdles need to be overcome before we see the commercial introduction of monodisperse contrast agents.

Acknowledgments

This work is supported by the Foundation for Fundamental Research on Matter FOM, the Technology Foundation STW and NanoNextNL, a micro and nanotechnology consortium of the Government of the Netherlands and 130 partners.

2

Acoustic bubble sorting for ultrasound contrast agent enrichment[1]

An ultrasound contrast agent (UCA) suspension contains encapsulated microbubbles with a wide size distribution, with radii ranging from 1 to 10 μm. Medical transducers typically operate at a single frequency, therefore only a small selection of bubbles will resonate to the driving ultrasound pulse. Thus, the sensitivity can be improved by narrowing down the size distribution. Here, we present a simple lab-on-a-chip method to sort the population of microbubbles on-chip using a traveling ultrasound wave. First, we explore the physical parameter space of acoustic bubble sorting using well-defined bubble sizes formed in a flow-focusing device, then we demonstrate successful acoustic sorting of a commercial UCA. This novel sorting strategy may lead to an overall improvement of the sensitivity of contrast ultrasound by more than 10 dB.

[1]Published as: T. Segers, M. Versluis, *Acoustic bubble sorting for ultrasound contrast agent enrichment*, Lab Chip, **14**(10), 1705-1714 (2014)

2.1 Introduction

Ultrasound is the most widely used medical imaging modality. It is based on the scattering of acoustic waves from inhomogeneities in tissue. Blood, however, is a poor ultrasound scatterer and the visibility of the blood pool can be enhanced using stabilized microbubbles as an ultrasound contrast agent (UCA). The bubbles produce a strong resonant echo, which can be 1 billion times stronger than the echo of solid particles of the same size[33], owing to the large compressibility of the gas core of the bubbles. The contrast enhancement makes it possible to visualize the blood pool and to quantify organ perfusion[1]. The sensitivity of bubble detection down to single bubbles *in-vivo* facilitates targeted molecular imaging applications using ultrasound with targeting ligands attached to the bubble shell[3]. UCAs can also be loaded with drugs, e.g. for the local delivery of chemotherapeutic drugs with a narrow therapeutic index[91,92], or genes, such as siRNAs[7,8].

The oscillation of the bubbles in the driving ultrasound field is governed by a strong coupling between the microbubble size and the ultrasound driving frequency through the Minnaert eigenfrequency of the bubbles[39]. UCAs are commercially available as a suspension of encapsulated microbubbles with a relatively wide manufacturer-dependent size distribution with radii ranging from 1 to 10 μm. Clinical ultrasound systems operate at a narrow bandwidth optimized for the type of ultrasound transducer and clinical application, consequently only a small fraction of the bubbles resonates to the driving ultrasound field. Thus, the sensitivity of contrast-enhanced ultrasound perfusion imaging can be improved by narrowing down the size distribution. Moreover, a fully resonant bubble population of drug-loaded agents will be much more efficient in the local delivery to target cells, in addition to saving a substantial portion of its expensive or toxic payload. For preclinical testing in small animal models, the injected contrast agent volume is much lower than the volume that can be injected into humans, so also here one could benefit from enriched, more resonant, contrast bubbles. Finally, for the use of targeted molecular imaging with ultrasound it would be highly beneficial to discriminate adherent bubbles from freely floating ones, which can be achieved through spectral differences through a resonance shift of the adherent bubbles of a single size[4,5]. Moreover, only a small percentage of the total injected dose is typically retained at the target site and it is therefore important to have all of the targeted bubbles in the size range optimized for detection. For all these reasons it is of great interest to devise a method to inject only the resonant bubbles.

A resonant bubble suspension can be realized in three different ways:

monodisperse bubbles can be formed directly in a flow-focusing device, or commercially available UCA can be filtered or they can be sorted. Flow-focusing techniques have proven to be a versatile tool for highly controlled formation of monodisperse droplets and bubbles[60,61]. In a flow-focusing geometry a gas thread is focused in between two external liquid flows through a constriction, where the gas is pinched off to form monodisperse bubbles[62,63]. One challenging aspect of this approach is to investigate how the monodisperse bubbles could be encapsulated with a biocompatible coating to stabilize them[65–67], to investigate how to maintain the monodispersity of bubbles produced at high production rates over time[64], and to investigate the dynamics of different coating materials for in-vivo and clinical use[68]. Enriching commercially available UCAs can be done by means of mechanical filtration[79]. Bubbles can be filtered by a pore filter, however, this may easily result in bubble fragmentation due to elevated pressures and to filter clogging. Moreover, bubbles not passing the filter are lost and can not be re-used.

Size-selective sorting methods are based on the forcing of bubbles. Bubbles with a different size experience a body force of different magnitude. The force can be a result of gravity, fluidic forces, or radiation forces, both optical and acoustical. One sorting method is reported by Goertz *et al.*[82] who isolated smaller bubbles through decantation. The basis of this procedure is that gravitational forces are balanced by viscous drag forces; larger bubbles rise faster in the fluid due to a larger buoyant force although in practice this is not a well-controlled process. Similarly, Feshitan *et al.*[83] isolate size fractions from a polydisperse UCA by centrifuging the suspension. A cylinder with the agent is rotated at high speed after which the bubbles were extracted from the cylinder at certain heights.

On-line continuous sorting methods for bubbles are not reported to the best of our knowledge. However, numerous publications on microfluidic continuous sorting methods for particles and cells are presented. Nieuwstadt *et al.*[93] use lift forces to sort particles in a straight microfluidic channel. Another method to sort particles in a flow field is called pinched flow fractionation, first reported by Yamada *et al.*[84]. Sorting particles in acoustic fields is extensively reported[94–97]. In general, an ultrasound standing wave (USW) is set up between two reflecting channel walls in a $\lambda/2$ microfluidic resonator chip resulting in a pressure node in the center of the channel. Particles are injected into the channel from where they will be dispersed over the width of the channel by the primary radiation force. While solid particles are mainly driven by the primary radiation force of the ultrasound, bubbles will also be susceptible to radiation pressure generated by neighbouring bubbles, termed

secondary radiation force[16,17]. Moreover, the reflecting walls present the bubbles with a virtual image bubble which through the secondary radiation force leads to mutual attraction, illustratively named the Narcissus effect[98]. Primary and secondary radiation forces for bubbles are of the same order of magnitude making an USW sorting strategy unfeasible through bubble clustering and drift towards the channel walls.

The use of a *traveling* acoustic wave has the advantage that the channel dimensions are decoupled from the wavelength of the ultrasound. Therefore the frequency can be tuned for optimal performance in the required size range of the sorting chip. Here, we present a new and simple acoustic bubble sorting method contained in a lab-on-a-chip device. We make use of travelling waves of low acoustic pressure. The use of continuous wave ultrasound allows for a finite net displacement of the bubbles during multiple cycles, whereas the ultrasound frequency allows for size-selectivity through resonance. First we describe the design of the microfluidic device in which the bubbles can be sorted. We test its working principle for bubbles of well-defined size formed in a flow-focusing device and show that sorting bubbles with a size similar to those contained in UCAs is feasible. Finally, we show that a suspension of UCA bubbles can be efficiently sorted using this novel sorting strategy.

2.2 Acoustic bubble sorting theory

A traveling ultrasound wave propagates in positive y-direction (the vertical in Fig. 2.1):

$$P(y,t) = P_A \sin(2\pi f t - ky), \tag{2.1}$$

where $k = 2\pi f/c$ is the wavenumber of the wave with frequency f and speed of sound c and with P_A the acoustic pressure amplitude. A bubble will experience a radiation force

$$F_R = -V \cdot \nabla P, \tag{2.2}$$

where both the pressure gradient ∇P and the volume V of the bubble are time-dependent with different phase contributions. This leads to an unsteady force that changes periodically both in direction and in magnitude[37].

The time dependent volume of the bubble in the traveling wave can be obtained from a Rayleigh-Plesset-type equation[37]:

$$\rho\left(\ddot{R}R + \frac{3}{2}\dot{R}^2\right) = \left(P_0 + \frac{2\sigma}{R_0}\right)\left(\frac{R_0}{R}\right)^{3\kappa}\left(1 - \frac{3\kappa\dot{R}}{c}\right) - P_0 - P_A - \frac{2\sigma}{R} - \frac{4\nu\dot{R}}{R}, \tag{2.3}$$

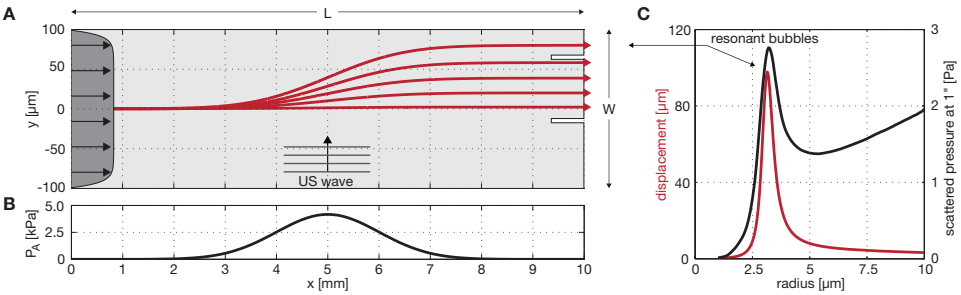

Figure 2.1: The acoustic bubble sorting principle. (A) Bubble trajectories in a high aspect ratio microfluidic channel (L = 1 cm, W = 200 µm, $W/H = 10$). Size-selectivity is accomplished through the resonant behavior of the microbubbles by the radiation force of a traveling acoustic wave with a maximum pressure amplitude of 4.5 kPa (B). Figure C shows the displacement (red solid line) from the center of the channel (y = 0) as a function of the bubble radius. The black solid line in C shows the scattered pressure calculated at a distance of 1 in. as a function of the bubble size. The resonant bubbles are displaced over the largest distance into the upper outlet and are therefore separated from the polydisperse bubble population. The pressure scattered from the resonant bubbles is the largest as can be seen from the black line in figure C.

where ρ is the liquid density, c the speed of sound in the liquid, κ the polytropic exponent of the gas inside the bubble, with P_0 the local hydrodynamic pressure within the channel and P_A the acoustic pressure, as before. R_0 is the initial bubble radius, R the time-dependent radius of the bubble and the overdots denote its time derivatives. The solution to Eq. 2.3 gives the radius of the bubble as a function of time, $R(t)$.

The translational motion of a bubble in the y-direction propelled by the primary radiation force F_R is counteracted by a viscous drag force F_D and due to acceleration of the bubble by an added mass force F_A[99–101]. UCA bubbles are coated with phospholipids that fully immobilize the gas-air interface and they can therefore be modeled using a point-particle approach as rigid spheres with a time dependent radius. We set up the force balance for this system:

$$0 = F_R + F_A + F_D = \frac{4}{3}\pi R^3 \dot{u}_l \rho - \frac{1}{2}\rho_l \frac{d}{dt}\left(\frac{4}{3}\pi R^3(\dot{y}_b - u_l)\right) \\ -6\pi\mu R(\dot{y}_b - u_l), \qquad (2.4)$$

where $\dot{y}_b$ is the transverse velocity of the bubble, u_l is the fluid velocity and d/dt represents differentiation with respect to time. Inertia of the bubble is neglected because of the small gas density as compared to water.

The radiation force F_R on a bubble due to the pressure wave is calculated from the pressure gradient $\partial P/\partial x = -\rho Du/Dt$. Convective effects are negligible here and it reduces to $\partial P/\partial x = -\rho_l \partial u_l/\partial t$ [102]. The added mass force F_A gives the force that must be exerted in order to accelerate a rigid sphere in its surrounding fluid, and for spherical objects it is well-known [103]. It is independent of the boundary condition and of the Reynolds number, however since R and u_l are time-dependent, the expression for the added mass force is more extended: $F_A = 2/3\pi\rho R^3(\dot{u}_l - \ddot{y}_b) + 2\pi\rho R^2\dot{R}(u_l - \dot{y}_b)$. The quasi-steady drag F_D describes the Stokes drag acting on the bubbles as they are translated. Simple Stokes drag was taken because the bubbles are insonified at low acoustic pressures ($P_A \approx 10$ kPa) resulting in relatively small translational velocities $\dot{y}_b$ and bubble Reynolds numbers ($Re_b = 2\rho R\dot{y}_b/\mu$) smaller than 1. The laminar flow field u in a microchannel with a rectangular cross-section at a given lateral position y and a height level z can be calculated by solving the Hagen-Poiseuille equation, see e.g. Bruus [104]:

$$u(y,z) = \frac{4H^2\Delta P}{\pi^3\mu L}\sum_{n,odd}^{\infty}\frac{1}{n^3}\left[1 - \frac{cosh(n\pi\frac{y}{H})}{cosh(n\pi\frac{W}{2H})}\right]\sin(n\pi\frac{z}{H}), \tag{2.5}$$

with L the length of the channel, W its width and H its height, μ the kinematic viscosity of the liquid and ΔP the pressure drop across the channel. For a channel with an aspect ratio W/H of 10 the flow profile is shown entering from the left in Fig. 2.1A. Thus, lift forces, which may counteract the translation induced by the ultrasound, are negligible because of the absence of a flow gradient (hence zero vorticity) over almost the entire channel width W.

The translation of bubbles in a size range of 1 to 10 μm transported by flow with a maximum downstream velocity of 0.1 m/s through a microfluidic channel is modeled by solving the coupled radial dynamics, Eq. 2.3 and translation, Eq. 2.4. As a first approximation, we assume that the microfluidic channel is acoustically transparent. This implies that the bubbles do not interact with the channel walls. Furthermore, it is assumed that the bubbles are initially positioned at the center of the channel (both in width and in height, $y = 0; z = 0$) and that they are transported downstream with the flow velocity. The bubbles are injected at position $x = 0$. The ultrasound frequency is 1 MHz and the acoustic pressure amplitude P_A was set to have a Gaussian shape with a maximum amplitude of 4.5 kPa in the center of the channel (Fig. 2.1B). A microfluidic channel length L of 1 cm was chosen. The aspect ratio W/H was chosen to be 10 with a channel width W of 200 μm resulting in a pressure drop ΔP of 20 kPa. The surface tension and density of water are used, $\sigma = 0.072$ N/m and $\rho_l = 1000$ kg/m^3,

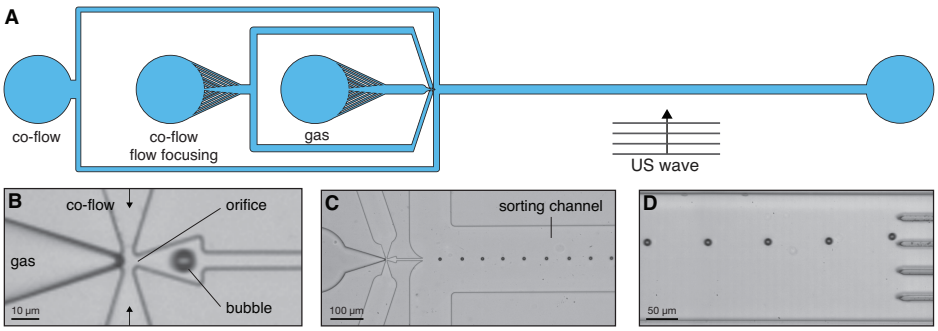

Figure 2.2: Acoustic bubble sorter. (A) shows the design of the experiments performed with the bubbles produced in a flow focusing device (B). Microbubbles are formed in a narrow orifice and directed into the sorting channel where an extra liquid co-flow is added to compensate for the bigger cross section (C). A traveling acoustic wave generated by an embedded piezo transducer displaces the bubbles over the channel width (D). Note: the channel lengths are not drawn to scale.

respectively. The polytropic gas constant was set to unity, $\gamma = 1$, as we use low driving pressure and isothermal behavior can be assumed in the gas core of the bubbles. The coupled equations are solved numerically in MATLAB by an ordinary differential equation solver `ode45`. The corresponding boundary conditions were $\dot{y}_b = 0$ and $\ddot{y}_b = 0$ at $t = 0$.

Figure 2.1C shows the modeled displacement in the y-direction. We also plot the scattered pressure[36] of single microbubbles as a function of the bubble radius. The plot shows that the most resonant bubble sizes are displaced over the largest distance and that they can be separated from the other bubbles using the outlets of the sorting chip, see Fig. 2.1A. The output bubble size distribution can be controled by tuning the ultrasound frequency of the traveling wave. Shifting it towards higher frequencies will provide smaller bubble sizes in the output of the sorter and vice versa, lower ultrasound frequencies lead to an enriched suspension containing larger bubbles. The width of the size distribution at the outlet can be tuned by controling the amplitude of the ultrasound wave. A higher pressure amplitude results in a larger overall displacement for all bubbles, providing a wider size distribution and more bubbles at the outlet. Narrowing the output size distribution can be achieved by lowering the pressure amplitude resulting in an enriched suspension of highly resonant bubbles.

2.3 Acoustic bubble sorting: chip design

The chip designs are displayed in Figs. 2.2A and 2.3A. We use a chip bulk material with an acoustic impedance similar to that of water to prevent reflections at the channel walls, which results in bubbles being attracted to the walls. Moreover, the use of an acoustically homogeneous material prevents the build-up of standing waves. A PDMS-water interface has an acoustic reflection coefficient of only 20%[105], whereas for a glass-water or silicon-water interface nearly all the acoustic energy is reflected. We therefore build all sorting channels in PDMS.

The sorting channels (Fig. 2.2C) are straight large-aspect ratio channels with a piezo transducer embedded in the PDMS. The transducer generates a traveling acoustic wave perpendicular to the flow direction to push the bubbles to the top half of the channel. Outlet collection channels and chambers were not incorporated in the present design to avoid flow disturbances due to hydrodynamic pressure differences across the various outlets. Nevertheless, channel spacers were added to the sorting channel to mimic such outlets (Fig. 2.2D).

The molds for the PDMS chips were fabricated using standard soft lithography techniques[106]: a layer of SU-8 was spin-coated on top of a silicon wafer, UV-exposed through a mask containing the channel features, and developed to be ready for replica molding. PDMS was mixed in the standard 1 : 10 ratio, degassed, poured over the mold and cured at 65°C for one hour, then cut to size. Prior to bonding, the fluidic ports were punched through the PDMS. The PDMS containing the channel features was plasma-bonded to a flat backing slab of PDMS for acoustic homogeneity. Teflon tubing (PEEK, Upchurch) was connected to the inlet channels through which gas, liquid, and ultrasound contrast agent were supplied. The outlets were connected to large diameter tubing to ensure atmospheric pressure at the outlet. The channels were filled with water immediately after bonding to maintain hydrophilicity.

The piezoelectric transducers are positioned such that they oscillate perpendicular to the sorting channel, in a slit cut though both PDMS layers parallel to the sorting channel at a distance of approximately 4.5 mm. They were glued using PDMS which was locally cured with a hot air gun. Three sizes of piezoelectric ceramics were used (surface area 5×2 mm^2, thickness 11 mm, 5×5 mm^2, thickness 2 mm, and 4×4 mm^2, thickness 1 mm) with center frequencies of 180 kHz, 1 MHz and 2 MHz, respectively. All transducers were driven at their thickness mode by an arbitrary waveform generator (Tabor Electronics, WW1072) operating in continuous mode. A

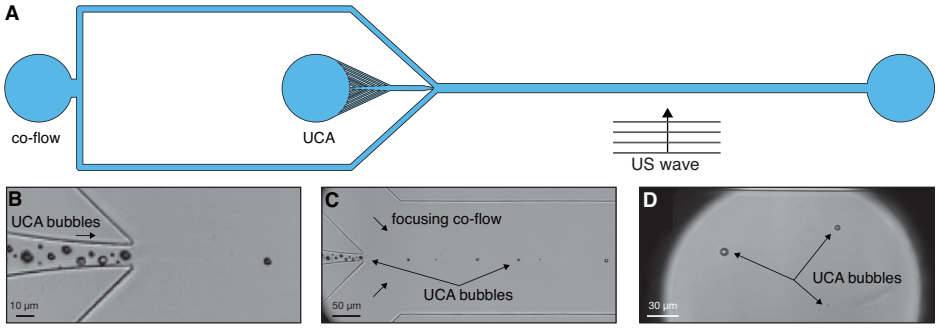

Figure 2.3: Acoustic bubble sorter for the sorting of UCAs. (A) shows the design. A microbubble suspension is hydrodynamically focused in between two liquid co-flows (B) forming a bubble train (C). A traveling acoustic wave pushes the bubbles in vertical direction downstream of the channel (D). Note: the channel lengths are not drawn to scale.

sinusoidal waveform was applied with amplitudes of 2.4, 2.7, and 2.1 V, respectively. A quantitative measurement of the acoustic pressure on-chip using non-intrusive methods can be done through indirect radiation pressure measurements[107] or using Schlieren imaging[108]. However, these techniques are not applicable with the low acoustic pressure amplitudes used here. We subdivide the chip in two pieces, cut along the sorting channel, and we construct a watertight container around the part containing the piezo by positioning it between two glass slides and sealing it with PDMS, see Fig. 2.4. A calibrated hydrophone (Onda HNR-050) connected to an x-y-z translation stage was put in the water-filled container and moved along the sorting channel at a stand-off distance of approximately 0.2 mm. The piezo transducer was driven at the experimental conditions to estimate the applied pressure and the pressure distribution inside the sorting channel. It was verified that the water level above the channel did not influence the pressure measurements. Also the hydrophone did not suffer from electromagnetic interference and crosstalk from the piezo transducer.

The sorting strategy was first tested by connecting a flow focusing geometry[69] to the sorting channel (Fig. 2.2B). In the flow focusing geometry a gas thread is focused between two co-flows through a narrow orifice. Bubbles are produced sequentially to form a train of equally sized and equally spaced bubbles. The spacing between the bubbles is important to minimize the attractive forces between the bubbles which leads to bubble clustering. Two or more bubbles attached to each other have a completely different reso-

nance behavior[37], which would render the proposed acoustic bubble sorting strategy impracticable. One can calculate that it is necessary to space the bubbles by a distance $d > 10R$[17].

Two flow focusing geometries were used to cover the gas and liquid flow rates to produce bubbles in the size range of interest, 1–25 μm. Bubbles with radii between 10 and 25 μm were produced in a flow focusing geometry with an orifice size of 20 μm, the smaller bubbles were produced with an orifice of 3 μm in size. Optically, the larger microbubbles are easier to measure and to size. The motivation for the smaller bubbles was to study the response of bubbles with a size similar to those of UCA microbubbles. The sizing of these bubbles suffers from the effects of Mie scattering, in addition to that of optical diffraction.

The bubble size was varied by varying the gas pressure. Nitrogen gas flow is controled by a pressure regulator (Omega, PRG101-25) connected to a pressure sensor (Omega, DPG1000B-30G). Both liquid co-flows contain a surfactant to stabilize the bubbles and are comprised of a 5% w-w solution of dish washing liquid (Dreft, Procter and Gamble) in de-ionized water. The flow rate is controled by a high-precision syringe pump (Harvard Apparatus, PHD 2000, Holliston, MA, USA).

The outlets of the flow focusing geometries enter at the half width of the sorting channel for symmetry, a co-flow is added here to compensate for the bigger cross section. The sorting channels had a cross section of

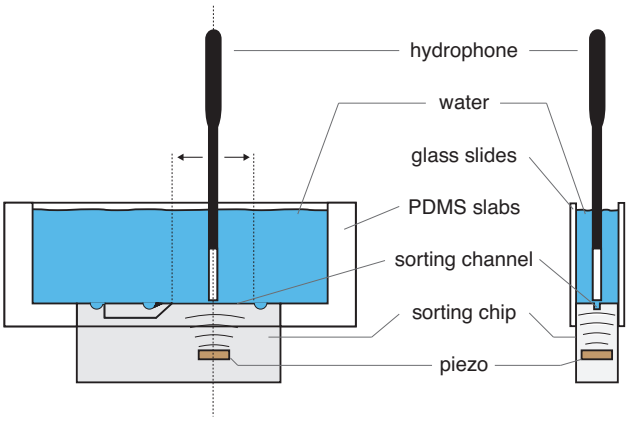

Figure 2.4: Pressure calibration setup. The sorting chip was cut in two halves along the sorting channel. A watertight container was constructed around the chip using two glass slides and a set of PDMS slabs. A calibrated hydrophone was moved along the channel axis to measure the acoustic pressure.

113 × 500 μm^2 and 14 × 200 μm^2 for the larger and smaller flow focusing geometry, respectively. Both sorting channels had a total length of 1 cm. The height of the channels was the same throughout, flow focusing part and sorting channels alike. The flow rates for the flow focusing experiments with the larger bubbles were 35 μL/min for the flow-focusing and 1 mL/min for the confluent flow. For the smaller bubbles, the flow rates were 1 μL/min and 10 μL/min, respectively. All liquid and gas flows were filtered by an in-line syringe filter to prevent channel clogging by dust particles.

A perfluorobutane-based ultrasound contrast agent (Bracco BR-14, Bracco Research Geneva) was supplied in a 5 mL vial. The bubbles form a suspension once water is injected into the vial and the stabilizing shell is formed by a mixture of DSPC/DPPC phospholipids surrounded by a PEG emulsifier. The bubble suspension was focused between two co-flows (Fig. 2.3B) to form a train of bubbles with sufficiently large interbubble spacing and then injected into the sorting channel, as before (Fig. 2.3C). The cross section of the sorting channel was 14 × 200 μm^2. The syringe pump controlling the UCA flow was positioned vertically with the needle tip pointing upward at a level several tens of cms lower than the sorting chip. With the bubbles being buoyant, the aid of gravity helped inject the bubble suspension into the sorting chip. The contrast bubbles were infused at a rate of 4 μL/min and the liquid co-flow had a total flow rate of 24 μL/min.

The translation of the bubbles in the sorting channel was imaged using a high-speed camera (Photron SA1.1) connected to a microscope (Olympus BX-FM modular system) equipped with a water-immersion objective (Olympus, LUMPlanFL). A 20× magnification objective was used for the flow focusing experiment with the largest microbubbles, a 40× objective during the flow focusing experiment with the smaller bubbles and a 60× objective during the UCA sorting experiments. The obtained resolution was 1 μm, 0.5 μm, and 0.3 μm per pixel, respectively. The system was illuminated in transmitted light mode using fiber illumination (Olympus ILP-1) connected to a collimation objective (10× Olympus Plan Achromat 0.25 NA) positioned below the fluidic chip to maximize the light intensity at the imaging position. All high-speed recordings were captured at 5000 frames per second giving a temporal resolution of 0.2 ms and the shutter time was set to 16 μs to minimize motion blur.

The high-speed movies were processed frame by frame in MATLAB. First a background graylevel was subtracted from each frame, second the frame was converted to a binary image using a thresholding algorithm. From the binary image the center of the bubble was determined and it was used to transform the cartesian image (x, y) into polar coordinates (r, θ). The

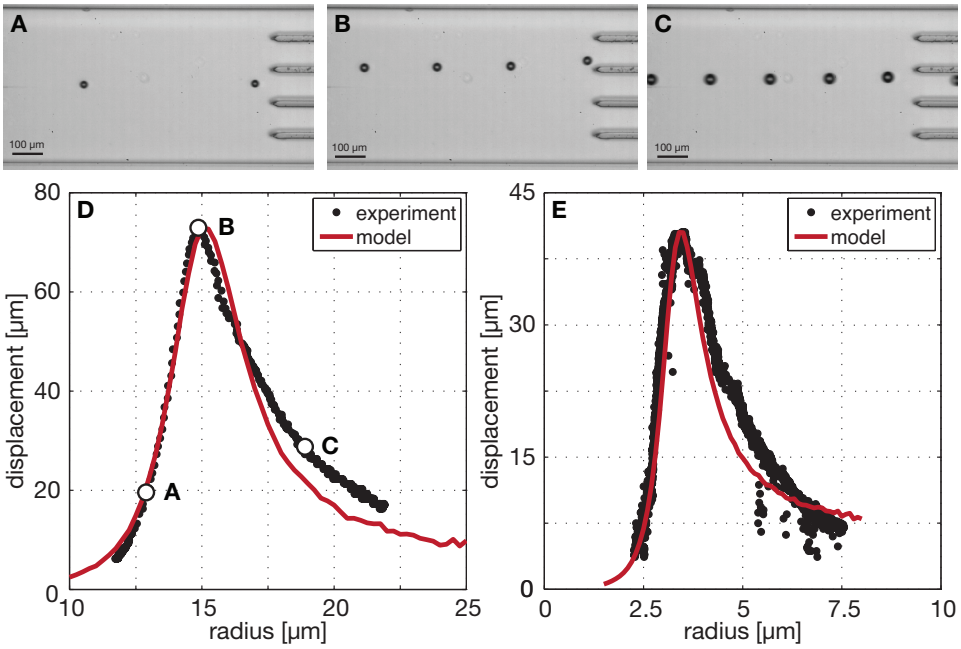

Figure 2.5: The acoustic bubble sorter in operation for bubbles produced in the flow focusing geometries. Bubbles with a resonance frequency higher (A) and bubbles with a resonance frequency lower (C) than the ultrasound frequency are displaced less than bubbles driven at resonance (B). Figure D shows the measured displacement as a function of the bubble radius (dots) for bubbles displaced in a 185 kHz wave. The solid red line shows the modeled displacement. Figure E shows the measured displacement as a function of bubble radius (dots) for bubbles displaced by a 1 MHz wave.

intensity values of the original image were averaged over all θ angles to suppress noise in the intensity profile of the image of the bubble and to achieve a sub-pixel precision. The inflection point on the intensity profile was then taken as the radius of the bubble.

2.4 Results

Figure 2.5 shows the acoustic bubble sorter in operation. Figure 2.5A–C were taken from the high-speed recordings and show the displacement of the bubbles in the y-direction (R = 13.2 µm, 15.0 µm, and 19.8 µm). The displacement of 566 bubbles normal to the direction of the channel flow is shown in Fig. 2.5D. The bubbles had a size range from 12 µm to 22 µm.

The open dots indicate the displacement of the bubbles from the top figures.

The displacement curve shows the resonant behaviour of the bubbles. The solid red line in Fig. 2.5D represents the modeled displacement. Input to the model were the ultrasound frequency $f = 185$ kHz, the speed of sound in water $c = 1490$ m/s, the density of water $\rho = 1000$ kg/m^3, and the measured pressure P_A. The pressure drop over the sorting channel $\Delta P = 5$ kPa was calculated from the applied flow rate and was used in equation 2.5 as input to the local hydrodynamic pressure P_0, being the atmospheric pressure plus the channel pressure which decreases linearly with increasing x. The bubbles produced here were coated with a surfactant and in the model we set the surface tension to $\sigma = 0.03$ N/m[63], and the surface tension of the gas-liquid interface was assumed not to vary with the bubble radius. The bubbles were also assumed to oscillate isothermally, therefore the polytropic gas constant was set to $\kappa = 1$.

Figure 2.5E shows the displacement of 1876 bubbles as a function of the bubble radius for the smaller flow focusing device. Here the bubbles range in size between 2.5 and 7.5 μm. The solid red line shows the modeled displacement using the measured acoustic pressure amplitude, as before. The pressure drop over the sorting channel was calculated to be $\Delta P = 100$ kPa. The input parameters to the model are the ultrasound frequency $f = 1$ MHz, the other input parameters, i.e. the speed of sound in water, the density of water and the surface tension of the surfactant interface, were taken as before.

Figure 2.6 shows the scatter plot of the displacement of 481 BR-14 UCA microbubbles by a 2 MHz traveling ultrasound wave. The displacement was measured 7 mm downstream of the entrance of the sorting channel. The size range is between 0.5 μm and 10 μm, and corresponds to the typical size distribution of BR-14. The typical acoustic pressure used here was 15 kPa. Extensive research on the dynamical behavior of ultrasound contrast agents has been performed in the past[71–73]. More recently it came to the attention that the nonlinear harmonic response of UCA is governed, not only by the classical Rayleigh-Plesset-type nonlinear bubble dynamics, but to a great extent also by the nonlinear properties of the bubble shell[41,74]. It was also shown that the shell surfactant concentration had a major impact on the generation of the harmonic response, i.e. even for bubbles of the same size a very different acoustic response can be observed[40,109]. The bubbles can oscillate in an elastic regime with a low concentration of phospholipids and finite surface tension, or they can oscillate in a buckled regime owing to the high concentration of phospholipids with virtually no surface tension[41]. The viscoelastic properties of the phospholipid shell of BR-14 contrast bubbles

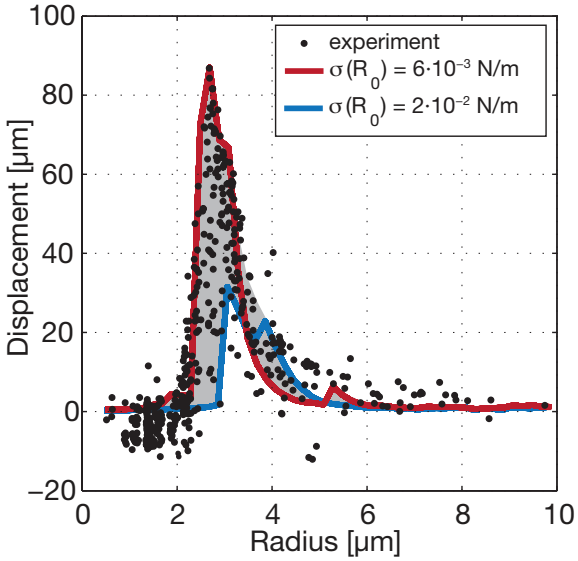

Figure 2.6: Experimentally obtained displacement of UCA bubbles as a function of the bubble size (dots). The red line shows the modeled displacement of coated bubbles with an initial surface tension of 6×10^{-3} N/m and the blue line shows the modeled displacement for a initial surface tension of 2×10^{-3} N/m. Varying the initial surface tension between these two values (gray area) show excellent agreement with the measured displacement.

can be incorporated into the bubble dynamics equation, Eq. 2.3, by adding pressure contributions for an effective shell elasticity and rate-dependent shell viscosity. The varying shell surfactant concentration is captured in a parameter termed the initial surface tension $\sigma(R_0)$ [109]. To induce the flow the pressure drop over the sorting channel was approximately 100 kPa. Such a large overpressure may compress the contrast bubbles, which results in bubbles ending up in their buckled state, or at least close to buckling, with an initial surface tension close to zero.

Numerical simulations of the displacement were performed using the measured acoustic pressure amplitude and the data for BR-14 bubbles from Overvelde *et al.* [75]. They showed that BR-14 bubbles are characterized by a shell elasticity of 2.5 N/m together with a shell viscosity of 6.0×10^{-9} kg/s. The initial surface tension $\sigma(R_0)$ of contrast microbubbles in their suspension varied between zero and 0.035 N/m. A polytropic gas constant of $\kappa = 1.07$ for perfluorobutane (C_4F_{10}) gas was used and all properties of the surrounding liquid were kept as before. Figure 2.6 shows the modeled dis-

placement of bubbles with an initial surface tension between 6×10^{-3} N/m (in red) and 2×10^{-2} N/m (in blue). The gray area fills all possible displacement curves between the two extremes and we find very good agreement with the measured results.

2.5 Discussion

Typically one to ten billion bubbles are injected in a human perfusion study. Injecting an enriched bubble suspension with a narrow size distribution may dramatically decrease the number of bubbles that is needed during such an imaging procedure, a decrease of 20-40 times is expected in favorable conditions. Still, with the single sorting channel, operated under the conditions as described here, it would take several hours to fill a vial with millions of resonant bubbles. Massive parallelization of the sorting method may be achieved by stacking microfluidic channel layers in close proximity to each other[110], which will then reduce the sorting time to under one minute.

Flow focusing techniques are capable of producing up to 10^6 bubbles per second from a single orifice[65]. While flow focusing techniques have an excellent track record in producing highly monodisperse bubble suspensions, also for coated bubbles, with a polydispersity index down to 0.2%, there is very little knowledge on the details of the coating characteristics and on the dynamic process of coating during formation. Thus, it can be very helpful, even for monodisperse bubble production facilities, to sort the suspension of bubbles in a subsequent step based on their acoustic property, not necessarily on size.

In preclinical small animal models, only a small amount of bubbles can be safely injected. For these protocols it is therefore of great importance to inject only those bubbles that are acoustically most responsive. Hence it would be beneficial to use sorted bubbles with high echogenicity instead of a polydisperse suspension containing a large fraction of smaller and larger non-resonant bubbles. This feature becomes even more important when using the contrast bubbles in harmonic imaging as all nonlinear harmonic behavior is concentrated near resonance. Thus, the injection of non-responsive larger bubbles will primarily contribute to a substantial scattering echo at the fundamental frequency and to attenuation of the transmit signal, thereby limiting the scattering to attenuation ratio (STAR) of the nonlinear echo. Acoustic bubble sorting is also beneficial for targeted bubbles for molecular imaging and to sort drug and gene loaded bubbles. The bubbles passing the bubble sorter at the waste outlet may be reinjected in another chip to be sorted at a different frequency for use in another treatment. Finally, the

expensive drug load and/or targeting ligands may also be recycled from the waste collection channel.

A few words on the modeling efforts are in order. We have added a linear damping term to the Rayleigh-Plesset model to account for the energy dissipation of the radial oscillations. These arise first of all from the presence of a surfactant layer to stabilize the bubbles produced in the flow focusing geometry and secondly from the interaction of the bubbles with the PDMS walls. Finally, we know from Devin[111] that thermal damping of bubbles with a size near 15 μm are dominant over the other damping contributions, such as acoustic reradiation and viscous dissipation. To cover all these (unknown) damping contributions we introduced a single damping factor δ_{add} as a pressure contribution in the form $-\delta_{\text{add}}\rho_l\omega R\dot{R}$ as in Eatock *et al.*[112]. The width of the modeled displacement curves in Fig. 2.5 were fitted to the measured displacement curves by varying δ_{add}. We find a total damping of 0.24 and 0.40 for the 15 μm and 3 μm bubbles, respectively. The total damping and the maximum displacement are highly coupled. Moreover, the modeled displacement strongly depends on the input acoustic pressure amplitude which was measured using an intrusive technique with a potential bias in both its amplitude and position. The combination of all these factors led us to scale the modeled displacement in Figs. 2.5D and E to the experimental data with a scaling factor of 1.7 and 1.4, respectively, while keeping good agreement in the overall shape of the displacement curve. For the contrast agent microbubbles we incorporate the visco-elastic shell parameters (shell elasticity, shell viscosity and surfactant concentration) directly from experimental microbubble characterization studies[75] and we find good agreement for the displacement curves and its sorting capabilities.

The microbubbles in our sorting channels are always close to the PDMS walls of the chip. There is a large inconsistency between the available theoretical models that describe the dynamics of microbubbles close to a compliant wall. Doikinov *et al.*[113] model the dynamics of contrast agent microbubbles near a polystyrene Opticell® membrane and their model predicts an increase of the resonance frequency for a bubble close to the wall. Hay *et al.*[114] find a decrease of the resonance frequency for a bubble between two viscoelastic layers. Recent experiments by Helfield *et al.*[115] show very different acoustical behavior for bubbles close to an agar wall (with a small difference in acoustic impedance, hence little change in the bubble dynamics) as compared to an Opticell membrane with considerably larger changes. The acoustic transparency of PDMS suggests a minor influence of the bubble-wall interaction with limited change to the dynamics of the bubbles. Experiments of single microbubbles with a given stand-off distance

to a PDMS wall or between two PDMS walls, e.g. using optical tweezers[116], should clarify the details of bubble-wall interactions relevant for our sorting chip.

2.6 Conclusions

We have demonstrated a simple lab-on-a-chip device to sort coated microbubbles on-line in a travelling acoustic wave. The bubbles are sorted to their acoustic property rather than to their size, which makes the proposed sorting strategy highly efficient for injection of a smaller dose, yet highly resonant, enriched bubble suspension for preclinical small animal imaging, for targeted molecular imaging using ultrasound, and for drug and gene delivery applications.

Acknowledgments

We acknowledge the help of Stefan Schlautmann in producing the soft-lithography molds and for assistance and training in the clean room facilities of MESA$^+$. We also thank David Fernandez-Rivas for sharing his insightful experimental experience in microfluidic fabrication technology. We thank Wim van Hoeve, Peter Frinking, Nico de Jong, and Detlef Lohse for stimulating discussions. We also want to thank Gert-Wim Bruggert, Martin Bos, and Bas Benschop for their skilful technical assistance. We thank Bracco Research Geneva for the supply of BR-14 ultrasound contrast agents. This work is supported by NanoNextNL, a micro and nanotechnology consortium of the Government of the Netherlands and 130 partners.

3

Bubble sorting in pinched microchannels for ultrasound contrast agent enrichment[1]

Ultrasound contrast agent (UCA) suspensions contain encapsulated microbubbles with a wide size distribution, with radii between 1 and 10 μm. Medical transducers generally operate at a narrow frequency bandwidth, severely limiting the fraction of bubbles that resonates to the driving ultrasound. Thus, the sensitivity of contrast enhanced ultrasound imaging, molecular imaging with targeted bubbles, and drug delivery with microbubbles can be improved by narrowing down the size distribution of the bubble suspension. Here, we use a low-cost lab-on-a-chip method for the sorting of microbubbles by their size without external actuation, based on a microfluidic separation technique known as pinched flow fractionation (PFF). We show by numerical investigation that the inclusion of particle rotation in the pinched segment is essential for an accurate description of the sorting behavior of particles with sizes close to the pinched segment width. Successful enrichment of a polydisperse contrast agent into a bubble suspension with a narrow size distribution (1.55 ± 0.42 μm) was achieved with a PFF-based microdevice. This sorting technique can be readily parallelized, and thus lead to an easy-to-use and robust device capable of at least a 10 dB improvement in the sensitivity of contrast ultrasound imaging.

[1]Submitted as: M.P. Kok, T. Segers, M. Versluis, *Bubble sorting in pinched microchannels for ultrasound contrast agent enrichment*, Lab Chip, (under review, 2015)

3.1 Introduction

Ultrasound imaging is the most widely used medical imaging modality. It is based on the scattering of sound waves from inhomogeneities in tissue. Contrary to tissue, blood and other liquids in the body scatter ultrasound poorly. Ultrasound contrast agents (UCA) can be added to the blood pool. They consist of stabilized microbubbles, which are excellent ultrasound scatterers, due to the large compressibility of their gas core. The echo produced by a microbubble can be up to a billion times stronger than that of a solid particle of equal size[71]. This strong response allows for the visualization of the blood pool, and can be used to quantify blood perfusion in organs[1]. To facilitate targeted molecular imaging with ultrasound, with a sensitivity up to a single bubble, the shell of the microbubbles allows for the attachment of targeting ligands[3]. The microbubbles can also be loaded with drugs, for use in highly localized delivery of drugs with a low therapeutic index such as chemotherapeutic drugs[91,92], or genes, such as siRNA or mRNA[7,8,117]. Commercially available UCAs generally consist of encapsulated microbubbles in suspension, with a relatively wide size distribution, with sizes ranging from 1 to 10 μm. Since clinical ultrasound systems operate at a narrow frequency bandwidth, and since the resonant frequency of microbubbles is strongly dependent on the size of the bubbles[71], a significant fraction of the microbubbles will not resonate to the driving ultrasound, while still attenuating the ultrasound. Thus, the sensitivity of contrast-enhanced ultrasound imaging can be improved by narrowing down the size distribution. Furthermore, a highly resonant bubble population also increases the efficiency of drug-loaded agents in releasing their payload. Finally, the use of targeted molecular imaging with ultrasound will highly benefit from the ability to discriminate between bubbles that adhere to a wall and those that freely float, which can be measured by a resonance shift of the adherent monodisperse bubbles[4,5]. Thus, for these reasons it is important to develop a method of obtaining monodisperse ultrasound contrast agents.

There are three main methods to obtain a monodisperse bubble suspension: direct production of monodisperse microbubbles, filtering of polydisperse UCA, or sorting thereof. Recent advances into the production of monodisperse UCA are promising, such as the use of flow-focusing devices to produce highly monodisperse bubble populations as reported by Hettiarachchi *et al*[65]. These methods are capable of producing highly monodisperse bubble populations at significant rates[64], however, challenges remain in maintaining the monodispersity for extended periods of time[66,118]. Mechanical filtration is a widely used technique, where the microbubble sus-

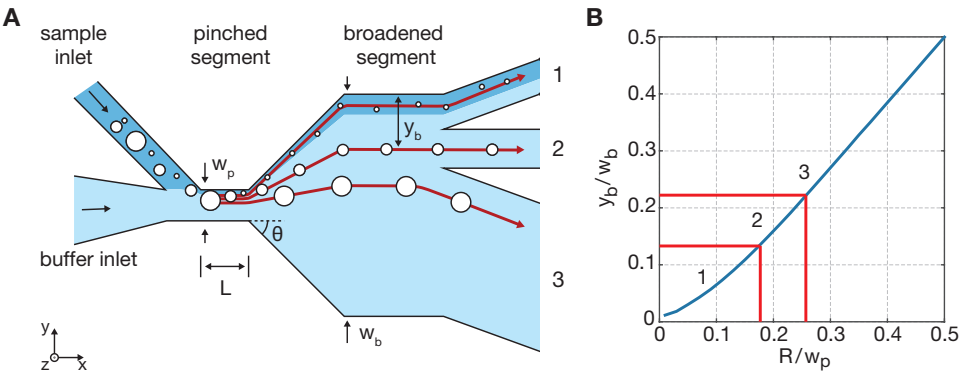

Figure 3.1: A) Top view of the microchannel geometry used in pinched flow fractionation. The microbubbles enter the pinched segment and are pinned against the wall by a co-flow. The microbubbles then separate due to the expansion of the channel, to be sorted into exit channels positioned in the broadened segment. The color indicates the inlet of origin for the fluid. B) The expected distance of bubbles from the wall in the broadened segment as a function of bubble radius, based on eq. 3.1 combined with an undisturbed velocity profile obtained from 2D COMSOL simulations. Using this result we can design a microdevice geometry to extract microbubbles within a specific size range.

pension is forced through a filter[87], acting as a low-pass filter. However, due to the deformability of the bubbles, bubbles larger than the pore size can also pass the filter. Depending on the amount of pressure used, bubbles are also likely to be fragmented due to being forced through the filter. Furthermore, the filters can become clogged.

Sorting of microbubbles is performed by employing a range of size-dependent forces acting on the microbubbles. Examples of forces used to sort particles in general are the buoyancy force (decantation[82] or centrifugation[83]), optical radiation force[119] and electrical potentials (for charged particles)[120]. Of special interest for the sorting of microbubbles is the acoustic radiation force, which allows for sorting by resonance[85]. Most of these techniques require an actuation force to act on the particles, which can be a complicating factor in the design of practical sorting devices, or requiring optical and acoustical transparency for example.

A novel lab-on-a-chip size-sorting technique for particles, known as pinched flow fractionation (PFF), uses only the properties of laminar flow in microfluidic devices[84]. The method has been successfully applied to the separation by size of solid spheres[84], emulsion droplets[121] and red blood cells[122]. Here we apply the method to the sorting of microbubbles.

The operating principle of PFF is illustrated in Fig. 3.1A. The microbubbles are introduced into a narrow channel, called the pinched segment, where the bubbles are pinned to the wall by a co-flow from a buffer inlet channel. The co-flow to sample flow rate ratio is typically in the order of 50:1. As the pinched segment expands into a broader segment, the distance from the center of the microbubbles to the wall is extended through microfluidic amplification. Because the centers of the large bubbles are located further from the wall, they end up closer to the center of the broadened segment. Creating exit channels at different positions thus allows for the sorting of the bubbles into several narrow size distributions.
For infinitesimally small, neutrally buoyant particles (that do not disturb the flow and follow the streamlines), the position in the broadened segment can be found as a function of the position in the pinched segment by tracking the streamlines using mass conservation, which leads to the following equation[123]:

$$\frac{\int_0^H dz \int_{w_b/2-y_b}^{w_b/2} dy\ u_{x,b}(y,z)}{\int_0^H dz \int_{-w_b/2}^{w_b/2} dy\ u_{x,b}(y,z)} = \frac{\int_0^H dz \int_{w_p/2-R}^{w_p/2} dy\ u_{x,p}(y,z)}{\int_0^H dz \int_{-w_p/2}^{w_p/2} dy\ u_{x,p}(y,z)}, \tag{3.1}$$

with H the height of the microchannel, w_b and w_p the width of the broadened and pinched segments, $u_{x,b/p}(y,z)$ the flow profile inside said segments, R the size of the particle and y_b the distance from the wall within the broadened segment.
Vig and Kristensen[124] found good agreement between this model and experimental data for particles up to ($R/w_p = 0.25$), using a velocity profile obtained from 2D simulations, neglecting the presence of the particles. Figure 3.1B shows the calculated separation by size. Based on these results, devices can be designed to obtain microbubbles of a specific size range.

3.2 Experimental methods

3.2.1 Microfluidic device design

The chip design is displayed in Fig. 3.2. The design comprises two inlet channels, and three outlet channels, positioned such that only a fraction of bubbles exits through each of the outlets. The two inlet channels merge into the pinched segment, with a width $w_p = 12$ µm and length $L = 40$ µm. The width is based on the size of the largest bubbles present in the suspension.

The pinched segment broadens into the broadened segment with a broadening angle $\theta = 60°$. The broadened segment has a width $w_b = 300$ μm. The broadened segment splits into three outlet channels 600 μm downstream of the pinched segment, with the center outlet located with its center at 20 μm from the side wall, with a width of 10 μm. These positions are designed for the selection for particles with a radius of 1.8 μm. The three outlet channels maintained their width ratios until the outlet ports, to ensure equal outlet hydrodynamic resistance. All the microchannels are 14 μm in height.

3.2.2 Materials and methods

The microfluidic device is fabricated using polydimethylsiloxane (PDMS). PDMS provides a simple and fast prototyping method and is ideal for optical imaging due to its transparency. The molds for the PDMS chips were fabricated using standard soft-lithography techniques[106]: a layer of SU-8 was spin-coated on top of a silicon wafer, UV-exposed through a mask containing the channel features, and developed to be ready for replica molding. The PDMS was mixed in the standard 1 : 10 ratio, degassed, poured over the mold and cured at 65°C for 90 minutes, then cut to size. Prior to bonding, the fluidic ports were punched through the PDMS. The PDMS slab containing the channel features was plasma-bonded to a flat backing slab of PDMS. The backing contains the center outlet port, in order to maintain a constantly rising path for the bubbles, which prevents them from piling up inside the tubing due to buoyancy. The outlets were connected to large diameter tubing to ensure atmospheric pressure at the outlet. The channels were filled with water within ten minutes after bonding to maintain hydrophilicity, while ensuring a strong bond. Teflon tubing was connected to the inlet channels through which the UCA sample and buffer liquid were supplied.

A research-grade contrast agent (Bracco BR-14, Bracco Research Geneva) was used for the characterization of the device. BR-14 microbubbles consist of a perfluorobutane gas core with a stabilizing shell coating of phospholipids. The syringe pump controlling the UCA flow was positioned vertically with the needle tip pointing upward at a level several tens of centimeters lower than the sorting chip. With the bubbles being buoyant, the aid of gravity helped to inject the bubble suspension into the sorting chip. The contrast bubbles were infused at a rate of 0.2 μL/min and the liquid co-flow had a flow rate of 10 μL/min. These flow rates result in an average flow speed in the pinched segment of approximately 1 m/s. The ratio (1:50) was chosen such that bubbles down to a size of 1 μm are successfully separated. To confirm that the microbubbles act similarly to solid particles (and as

such neglect buoyancy and deformability effects), solid particles of different sizes (1.0 and 3.5 μm mean radius, ThermoScientific, Fluoro-Max 35-2 and R0200, Waltham, MA, USA) were also sorted. Furthermore, the sorting device is placed such, that any movement due to buoyancy is perpendicular to the geometry as shown in Fig. 3.1.
The setup used to analyze the sorting performance has been described previously[85]. In short, the sorting process was imaged using a high-speed camera (Photron, FASTCAM SA-X) connected to a microscope (Olympus, BXFM). The microscope is fitted with one of several objectives: a 60× water-immersion objective (Olympus, LUMPlanFL) was used to measure the $y_b(R)$ curves, a 100× water-immersion objective (Olympus, LUMPlanFL) was used to measure the velocity of microbubbles flowing through the pinched segment, and a 50× long working distance objective (Olympus, SLMPlan) was used to measure the size distributions during sorting. The system was illuminated in bright-field mode using fiber illumination (Olympus ILP-1) connected to a collimation objective (10× Olympus Plan Achromat, 0.25 NA) positioned below the microfluidic chip to maximize the light intensity at the imaging position. The frame rate used was 10,000 frames per second when recording at the outflow positions and 140,000 frames per second when measuring the flow inside the pinched segment. These high frame rates ensured a sufficient time resolution for particle tracking. To minimize motion blur, the exposure time was set to 8 μs during recordings taken at 10,000 frames per second.

3.3 Results

3.3.1 Pinched flow fractionation for microbubbles

Figure 3.3A shows the broadened segment during operation. Separation of the microbubbles by size is clearly observed. The measurement location is positioned 300 μm from the end of the pinched segment. Figure 3.3B shows the measured positions of 50,000 bubbles as a function of the bubble radius. Some scatter is observed for smaller bubbles, which is due to the following. First, when multiple bubbles travel through the pinched segment in close proximity, bubble-bubble interactions can cause smaller bubbles to be positioned further away from the wall. Second, the finite flow rate ratio sets a lower limit on the size of particles that can be sorted successfully. In Fig.3.1, the darker blue region indicates the fluid layer consisting of liquid from the sample inlet. Bubbles smaller than the width of this fluid layer in the pinched segment are not pinned to the wall and as a result they are not sorted[84].

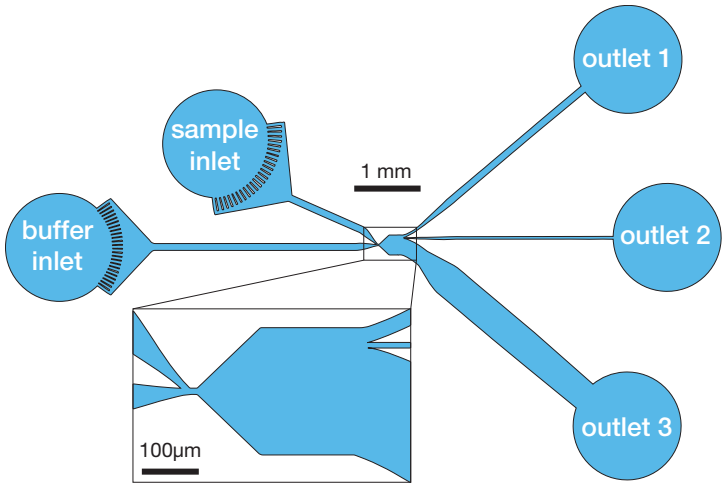

Figure 3.2: The pinched flow fractionation microdevice design. Two separate inlets, for both buffer and sample fluids lead into the pinched segment. The three outlets sort the particles toward multiple outlets for further extraction. All microfluidic channels have a height of 14 µm.

3.3.2 UCA enrichment using pinched flow fractionation

Based on the results as shown in Fig. 3.3, bubbles with sizes between 1 and 2 µm are expected to enter the center outlet channel. Figure 3.4 shows the probability of microbubbles entering the center outlet channel as a function of their radius. The data is based on measurements of approximately 4,500 microbubbles, measured during 10 seconds of sorting. The results show successful sorting of the UCA microbubbles, creating a bubble population with a mean size of 1.55 µm, and a standard deviation of 0.42 µm. Clear bandpass filtering behavior is observed, both bubbles smaller than the target size, and bubbles larger than the target size are excluded from the center outlet.

3.3.3 Sorting quantification

A quantitative comparison of the results as shown in Fig. 3.3B with the results of the model, Fig. 3.1B, shows that the distance from the wall in the broadened segment of large bubbles is significantly overestimated by the model, suggesting that the point particle approximation may fail for larger particles. The finite size of the particles influences the flow both by relative translation and by rotation, caused by the velocity gradient.

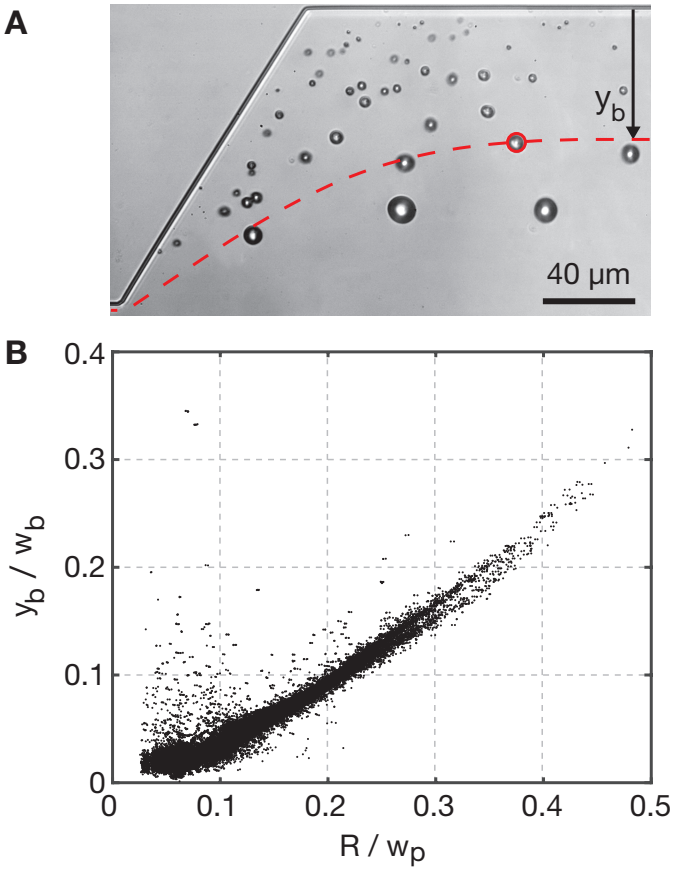

Figure 3.3: A) Image obtained from the measurements during the sorting of microbubbles at high concentration (A). To reduce the influence of bubble-bubble interactions, concentrations were kept low during measurements. B) The distance from the wall in the broadened segment y_b as a function of bubble radius R. Successful separation can clearly be observed.

To investigate this behavior, we determine the flow profile within the pinched segment, with a rotating and translating particle present, from 3D simulations using the COMSOL Multiphysics package[125]. This flow profile is then direct input to Eq. 3.1 to determine the position in the broadened segment $y_b(R)$. The simulation used for the model including the rotation is implemented as a stationary simulation of the flow in a square microchannel. The presence of the bubble is simulated by inserting a spheroid in the channel. The translational velocity and rotation rate combined provide the boundary conditions on this spherical surface. The translational velocity of the bub-

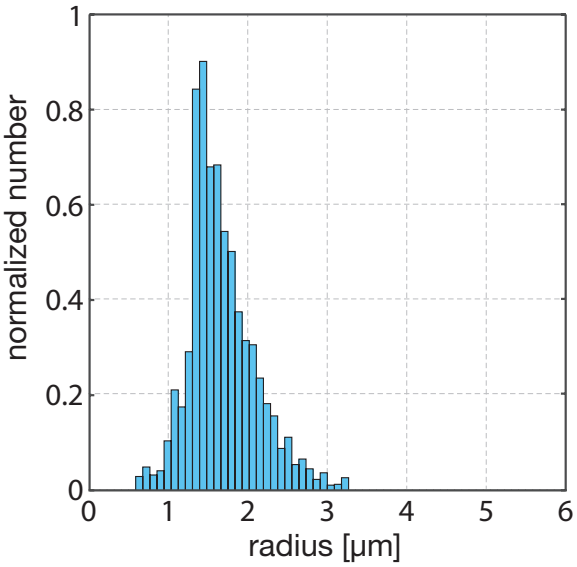

Figure 3.4: The fraction of the bubbles entering into the center outlet as a function of the bubble radius. The results show very high selectivity for bubbles of the desired dimensions.

bles, which is size-dependent, is determined from high speed measurements of bubbles as they flow through the pinched segment. The rotation rate of the particle is treated as a free parameter, since it cannot be obtained directly from the measurements.

Figure 3.5A shows the measured velocities, v_p, of the bubbles as they travel through the pinched segment, normalized by the average flow velocity, $\overline{u}$. A series of velocities was found, with the velocity increasing with size. Based on the measurements of the bubble velocities, maximum and minimum values were obtained for use in the simulations, indicated by the red and blue lines. Figure 3.5B shows the flow profiles obtained from the simulations for a number of cases, with and without particles, translating and rotating. The resulting position as a function of size and dimensionless rotation rate is then shown in Fig. 3.5C.

The results show that the rotation of the particle significantly modifies the flow profile in the pinched segment, causing the effluent position of the particle to lie closer to the wall in the broadened segment. Merely adding a translating, non-rotating, particle to the simulation does not change the outcome significantly. The results obtained for $\widetilde{\Omega} = 0.75$ show good agreement with the measured data. This value of the dimensionless rotation rate is

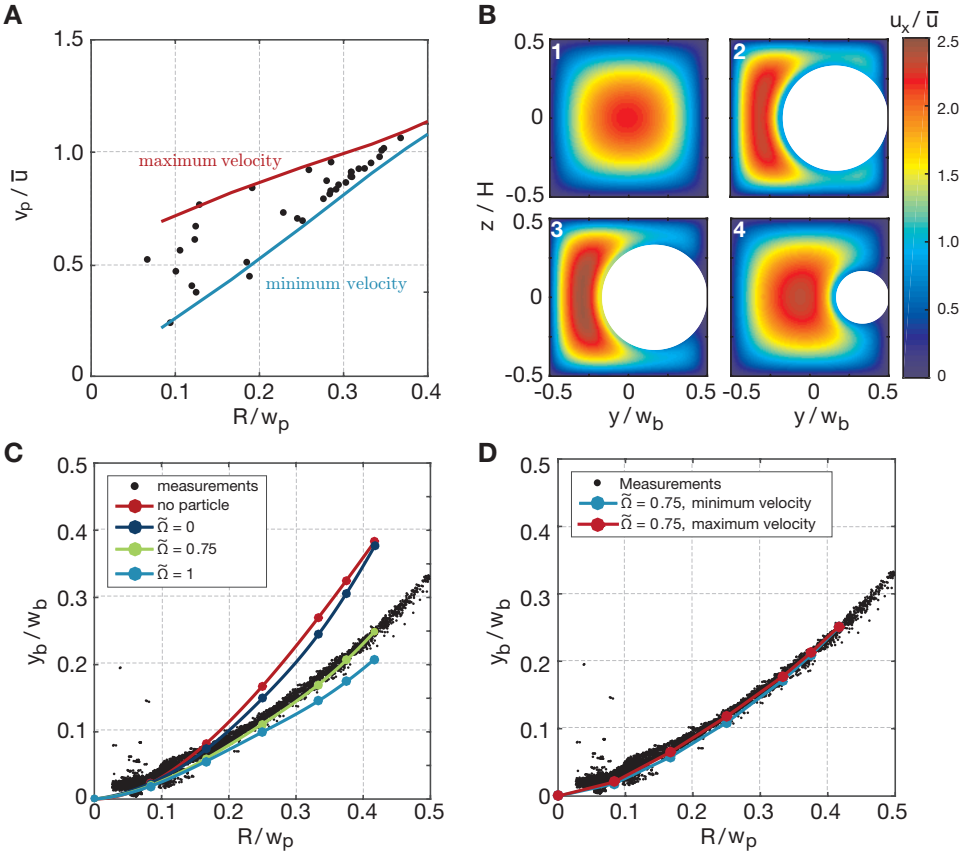

Figure 3.5: A) Measured bubble velocities inside the pinched segment as a function of the radius. The lines indicate the maximum and minimum velocities used in the simulations. B) Flow profiles obtained from 3D simulation using COMSOL Multiphysics, using measured velocities as input. B1) The undisturbed flow field, B2) the flow field with a translating but rotationless particle, B3) and B4) the flow field with a particle translating and rotating ($\widetilde{\Omega} = 0.75$), for two different radii. C) The position in the broadened segment as a function of size and dimensionless rotation rate, obtained by using the velocity profiles as direct input into eq. 3.1. D) Comparison of the numerical results for a value of $\widetilde{\Omega} = 0.75$ for the minimum and maximum velocities to the measured locations.

similar to results obtained previously in a numerical study[126]. Figure 3.5D shows the results of the model for $\widetilde{\Omega} = 0.75$, using the minimum and maximum velocities as indicated in Fig. 3.5A. Thus, the range of velocities does not significantly change the sorting position.

3.4 Discussion

Pinched flow fractionation has many promising advantages as a method for enriching UCAs. The absence of external forcing significantly simplifies device design and the absence of flow rate dependency, as shown here, leads to high repeatability, even when used by general medical practitioners. These characteristics, combined with the simple geometries involved, allow for direct integration with medical syringes, allowing for a point-of-care device capable of producing monodisperse UCA wherever needed, at low cost.
A typical dose of ultrasound contrast agent consists of several billion microbubbles. Injecting an enriched bubble population may decrease the need for such a high volume, a decrease of a factor of 20-40 is expected. However, with only a single sorting channel, as reported in this study, it would still take tens of hours for a single dose, at a sorting rate of about 500 bubbles per second per channel. As mentioned before, sorting devices based on pinched flow fractionation have a simple design, which positions them ideally for parallelization. One thousand parallel channels would already decrease the sorting time to two minutes. This should fit comfortably within a device with a volume of one cubic centimeter, capable of being attached to standard syringes. The low cost of individual units would allow for a single-use device design, which is highly preferable in medical environments due to sterility requirements.
There are several points to be addressed concerning the modelling of the bubble sorting. The dimensionless rotation rate was varied between 0 and 1, corresponding to a state of pure translation and of the particle rolling perfectly along the sidewall. Our experimental results fit closely to $\widetilde{\Omega} = 0.75$, in agreement with earlier numerical results[126]. Due to the homogeneous and spherical nature of our particles and bubbles, we were unable to measure the rotation rate in the current setup. A more rigorous physical insight into the rotation problem will be the subject of further studies.
It is implicitly assumed that the deformability of the bubbles does not play a role in their sorting behavior. To confirm this, the very same sorting device was used to sort solid particles in the same size range. Figure 3.6 shows the sorting position as a function of the particle size, for both microbubbles and solid particles. These curves show nearly identical results for microbubbles

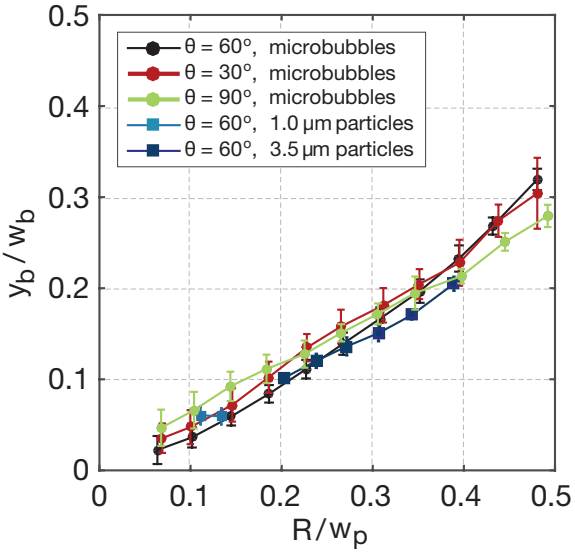

Figure 3.6: Comparison of experimental results for varying broadening angle θ, and type of particle used.

and solid particles, which therefore excludes any deformability and density effects.

As stated in the device design parameters, the broadening angle used was $\theta = 60°$. In their pioneering paper, Yamada *et al.*[84], state that they find an influence of this angle on the sorting behavior. However, to our knowledge, this result has never been reproduced in experiment, and is also absent in modelling. Measurements were performed using devices with broadening angles between 30 and 90°, see Fig. 3.6. Our results do not show a significant difference between the results for these devices.
A possible downside of sorting bubbles by size using pinched flow fractionation with the aim of increasing ultrasound sensitivity, is that the phospholipid packing density in the shell may vary slightly from bubble to bubble. This means that two bubbles of identical size need not necessarily show identical acoustical behavior[109]. This problem is inherent to all sorting methods aimed at sorting by size, and can only be lessened by improving the initial production. To assess the actual gain in sensitivity between unsorted and enriched microbubble populations, we plan to acoustically characterize the enriched population and compare it to the native population.

3.5 Conclusions

We have demonstrated a simple lab-on-a-chip device capable of sorting coated microbubbles on-line, using pinched flow fractionation. We have shown that the present models for pinched flow fractionation can be successfully extended to larger particles, of the same order of size as the pinched segment width, by including particle rotation. Pinched flow fractionation is ideally suited for parallelization, due to its simple geometry and flow parameters. Upscaled devices based on this design are capable of producing multiple particle suspensions with a narrow size distribution from a single suspension with a broad size distribution.

Acknowledgements

We thank Peter Frinking, Nico de Jong, Stephan Gekle and Achim Guckenberger for stimulating discussions. We also want to thank Gert-Wim Bruggert, Martin Bos, and Bas Benschop for their skilful technical assistance. We thank Bracco Research Geneva for the supply of BR-14 ultrasound contrast agents. This work is supported by NanoNextNL, a micro and nanotechnology consortium of the Government of the Netherlands and 130 partners.

4

Uniform scattering and attenuation of acoustically sorted ultrasound contrast agents: modeling and experiments[1]

A polydisperse ultrasound contrast agent was sorted in a lab-on-a-chip acoustic bubble sorting device. A traveling acoustic wave separated resonant from the non-resonant bubbles. The scattering and attenuation coefficients of the sorted bubble suspensions were measured simultaneously over a frequency range of 0.7 to 5.5 MHz at acoustic pressures of 10, 25, and 50 kPa. The attenuation was also measured using a single acoustic characterization pulse for each frequency over the same spectral range for peak negative pressures of 5 to 75 kPa with a step size of 2.5 kPa. Modeled scattering and attenuation coefficients were fitted to the measured data to give the shell parameters for the sorted bubbles. The modeled scattering and attenuation coefficients were obtained by integration of the non-linear response of all bubbles within the acoustic beam of the transmit transducer. Quantitative agreement was found between measured and modeled scattering and attenuation curves for all acoustic characterization pressures using a unique set of shell parameters, both for the overall dynamical response as well as for the absolute magnitude. This confirms that acoustically sorted bubbles have a uniform acoustic response.

[1]To be submitted as: T. Segers, N. de Jong, M. Versluis, *Uniform scattering and attenuation of acoustically sorted ultrasound contrast agents: modeling and experiments* (2015)

4.1 Introduction

Ultrasound contrast agents (UCA) consist of a suspension of coated microbubbles. Microbubbles are highly echogenic due to the compressibility of their gas cores. At resonance they generate harmonics of the driving ultrasound field which produces increased contrast of their echoes from the linear tissue echoes. The contrast enhancement makes it possible to visualize the blood pool and to quantify organ perfusion[1]. The potential to detect even single bubbles *in-vivo* allows for targeted molecular imaging applications using ultrasound[3]. Functionalized microbubbles can also be loaded with drugs, for the use in highly-localized delivery of drugs with a low therapeutic index such as chemotherapeutic drugs[91,92] or genes such as siRNA[7,8] or mRNA[117].

Commercially available contrast agents contain microbubbles with radii ranging from 1 to 10 μm. The acoustic response of a single bubble to a driving ultrasound field strongly depends on its size and the maximum response is reached when the bubble is driven at its resonance frequency[37]. Clinical ultrasound systems typically operate at a single ultrasound frequency that is optimized for the imaging application and the type of ultrasound transducer. Therefore, only a small fraction of the total bubble population will resonate to the driving ultrasound field. Thus, the sensitivity in diagnostic imaging can be improved by the use of bubbles of a single size that are resonant to the driving ultrasound frequency. Moreover, a resonant drug-loaded bubble population will be much more efficient in the local delivery of its payload to target cells. Finally, for the use of targeted molecular imaging with ultrasound the narrow spectral response of monodisperse bubbles would be highly beneficial to discriminate adherent bubbles from freely floating ones through a spectral shift of the adherent bubbles[2]. For all these reasons it is of great interest to inject only the resonant bubbles.

A monodisperse bubble population can be produced directly in a microfluidic flow-focusing device, where a gas thread is focused through a narrow orifice by two liquid co-flows, resulting in a highly controlled pinch-off into monodisperse bubbles[60–62]. However, it was found to be challenging to maintain the monodispersity over time[64,66]. Moreover, only very specific phospholipid mixtures allow for the production of stable monodisperse bubbles in a flow focusing device[65].

Filtering or sorting of a polydisperse bubble suspension offers a high degree of freedom in the choice of lipid shell composition and microbubble payload since the bubble of interest can be made using conventional UCA production techniques, e.g. sonication or mechanical agitation[118]. Mechan-

ical filtration[79], centrifugation[83] and decantation[82] have been reported for the sorting of microbubbles. A well-controlled microfluidic size-sorting technique for contrast bubbles was recently reported and it was based on a pinched flow fractionation technique[88]. On the other hand, it was shown recently that the shell surfactant concentration of phospholipid coated bubbles can be very different from bubble to bubble, even for bubbles of the same size[40,109]. The reason is that the encapsulation of the bubble, typically consisting of a phospholipid monolayer, dramatically changes the resonance behaviour of the bubbles. The non-linear behaviour of the viscoelastic shell increases the resonance frequency due to its stiffness and the viscosity of the shell increases in the damping[41,74].Therefore, bubbles with the same size, but with different phospholipid surface packing densities can have very different resonance behaviour.

Contrast bubbles can also be sorted to their acoustic properties as was shown very recently by Segers *et al*[85]. In an acoustic bubble sorting chip resonant bubbles are sorted on-line from a polydisperse bubble suspension. A traveling ultrasound wave exerts an acoustic radiation force[37] and the forcing is shown to be maximum for the resonant bubbles, hence it pushes the resonant bubbles away from the non-resonant bubbles. Acoustically sorted bubbles have great potential since they offer acoustically uniform behaviour. In order to optimize the acoustic bubble sorting technique for contrast enrichement applications, it is crucial to characterize these sorted bubble suspensions.

The response of a single microbubble to a driving ultrasound wave can be directly measured using optical ultra-high speed imaging[76,77]. Detailed information about the nonlinear bubble dynamics, e.g. especially the pressure-dependent resonance behaviour[80], compression-only behavior[40,127] and surface mode oscillations[128] were obtained. While ultra high-speed imaging of UCA has led to the successful development of advanced Rayleigh-Plesset type bubble dynamics models, it is of interest here to characterize the acoustic response of a complete population of bubbles[129,130] to evaluate the acoustic uniformity of the sorted bubbles.

In this study, we measure the combined scattering and attenuation of acoustically sorted bubbles. The shell properties of the bubbles in the suspensions are obtained from a match of the model, that integrates all individual non-linear bubble responses, to the measured data. The model includes the non-linear pressure and frequency dependent scattering and attenuation properties of the bubbles in the transmit field of the acoustic characterization pulse. In the theoretical section we first describe how measured scattering and attenuation curves can reveal the shell properties of the

bubbles. Then, we describe the experimental methods to characterize the sorted bubble suspension. The results are presented in the form of measured data compared to the modeled scattering and attenuation curves. Finally, the results will be discussed and we end with the conclusions.

4.2 Theoretical

H. Medwin[131] showed already in 1977 that the acoustic response of a bubble population is obtained by integration over all individual bubble responses. Later, De Jong *et al.*[129,132] used this principle to model the scattering and attenuation of coated contrast bubbles. Since then, the understanding of coated bubble dynamics increased substantially over the years. Here, we follow the reasoning of Medwin and De Jong however, we use a recent bubble dynamics model to calculate the non-linear theoretical scattering and attenuation coefficients of a bubble population.

The radial oscillations of phospholipid coated microbubbles can be modeled by including the pressure contributions from the viscoelastic shell in a Rayleigh-Plesset-type equation[41]:

$$\begin{aligned}\rho\left(\ddot{R}R+\frac{3}{2}\dot{R}^2\right)=&\left(P_0+\frac{2\sigma(R_0)}{R_0}\right)\left(\frac{R_0}{R}\right)^{3\kappa}\left(1-\frac{3\kappa\dot{R}}{c}\right)\\&-P_0-P_A(t)-\frac{2\sigma(R)}{R}-\frac{4\mu\dot{R}}{R}-\frac{4\kappa_s\dot{R}}{R^2}\end{aligned}\tag{4.1}$$

where ρ is the liquid density, μ the liquid viscosity, c the speed of sound in the liquid, κ the polytropic exponent of the gas inside the bubble, with P_0 the ambient pressure and P_A the acoustic pressure. R_0 is the initial bubble radius, R the time-dependent radius of the bubble and the overdots denote its time derivatives. κ_s accounts for the dilatational viscosity of the shell. The effective surface tension is captured by $\sigma(R)$ and in an elastic regime, it varies linearly with the surface area of the bubble as $\sigma(R) = \chi(R^2/R_b^2 - 1)$ where χ is the shell elasticity. The shell buckles for radii smaller than the buckling radius R_b, it ruptures for radii larger than R_r, and it is dependent on the initial surface tension of the bubble $\sigma(R_0)$ as $R_b = R_0/\sqrt{\sigma(R_0)/\chi - 1}$. The effective surface tension is limited to zero and to the surface tension of the surrounding liquid for a buckled and a ruptured bubble, respectively.

The solution of Eq. 4.1 results in the instantaneous bubble radius, $R(t)$. The scattered acoustic pressure wave at the bubble wall in an incompressible

medium is given by[36]:

$$P_s(t) = \rho(R\ddot{R} + \frac{3}{2}\dot{R}^2) \tag{4.2}$$

with R being time dependent. The energy loss of an acoustic wave due to scattering of a single bubble can be expressed as the ratio of the scattered energy $|P_s|^2$ to the incident acoustic intensity $|P_T|^2$ at frequency f and it is called the scattering cross-section:

$$\sigma_s = 4\pi R_0^2 \frac{|P_s|^2}{|P_T|^2} \tag{4.3}$$

with the dimensions of area. It is used here in the frequency domain for the interest in the harmonic components. Please note that through P_s the scattering cross-section is a function of the shell parameters and that it depends on the frequency and the pressure amplitude of the acoustic wave. Similarly, the *total* energy loss of the acoustic wave due to the scattering and damping, can be expressed as the ratio of the total energy loss per bubble to the intensity of the acoustic wave, the extinction cross-section σ_e. It is found by multiplication of the scattering cross-section with the ratio of the total damping δ_{tot} to the radiation damping δ_{rad}. The total damping is a summation of the damping that arises from re-radiation of sound and from the bulk and shell viscosities: $\delta_{tot} = \delta_{rad} + \delta_{vis} + \delta_{shell}$. The dimensionless damping coefficients can be obtained by linearizing the Rayleigh-Plesset equation to find[37]:

$$\delta_{rad} = \frac{3P_0\kappa}{\rho\omega c R_0}, \qquad \delta_{vis} = \frac{4\mu}{\rho\omega R_0^2}, \qquad \delta_{shell} = \frac{4\kappa_s}{\rho\omega R_0^3} \tag{4.4}$$

A microbubble also experiences damping due to thermal diffusion. Thermal damping is more difficult to calculate[37,38] and since for UCA bubbles it is of the same order as the viscous damping, typically the viscosity is increased by a factor 2 to account for thermal damping.

The total amount of scattered and absorbed energy of an acoustic wave traveling through a dilute cloud of homogeneously distributed bubbles can be obtained by integration over the pressure dependent scattering and extinction cross-sections of all the individual bubbles present in the acoustic beam[129] by assuming that higher order scattering effects are negligible[82]. The attenuation is found by multiplication of the volume averaged extinction cross-section, having units of length^{-1}, by the path length d of the acoustic wave through the bubble cloud:

$$\alpha_{model} = -\frac{10}{ln(10)} \frac{\int_V n(R)\ \sigma_s\ \delta_{tot}\ \delta_{rad}^{-1}\ dV}{\int_V dV} d. \tag{4.5}$$

where $n(R)$ is the number of bubbles with radius R per unit volume dV and corresponding scattering cross-section σ_s.

The theoretical scattering coefficient (in units of steradians) of a bubble cloud measured under a 90°angle with respect to the direction of wave propagation of the insonifying wave can be obtained in a similar way:

$$\eta_{model} = -\frac{1}{4\pi}\frac{\int_V n(R)\ \sigma_s\ T\ dV}{\int_V T\ dV}, \tag{4.6}$$

where $T = T(x, y, z)$ is a function that describes the volumetric sensitivity of the receiving element. It characterizes the volume over which the scattering is recorded experimentally by a transducer with a limited aperture. T varies between zero and unity and it has to be calibrated separately.

4.3 Experimental

4.3.1 Acoustic bubble sorting

The acoustic sorting method outlined by Segers *et al.*[85] is employed here to sort a perfluorobutane-based ultrasound contrast agent (Bracco BR-14, Bracco Research Geneva) containing bubbles coated with a DSPC and DPPG phospholipid mixture[109]. The sorting chip used here is differerent from that reported by Segers *et al.*[85] in that it comprises two outlet channels to separate the resonant from the non-resonant bubbles. The cross-section of the sorting channel was 14 × 200 μm^2 and the width of the resonant-bubble outlet was 50 μm (Fig. 4.1B). The contrast agent was supplied in a vial containing the UCA in powder form. It was reconstituted in 5 mL of Milli-Q water (Millipore Corporation, Billerica, MA, USA) and put to rest for 10 min to allow the bubbles to stabilize. A volume of 300 μL was extracted from the vial in a 1 mL syringe and it was diluted with Milli-Q water (Millipore Corporation, Billerica, MA, USA) by a factor 1.5. The flow rates were controlled by high-precision syringe pumps (Harvard Apparatus, PHD 2000, Holliston, MA, USA). Acoustic sorting resulted in two bubble suspensions used in two different characterization experiments: suspension 1 was sorted at an UCA flow rate of 0.5 μL/min and a co-flow rate of 25 μL/min and suspension 2 was sorted at an UCA flow rate of 1 μL/min and a co-flow rate of 35 μL/min.

A 2 MHz traveling acoustic wave was generated by a 6 mm diameter piezo element (Pz26, Ferroperm, Denmark) with a thickness of 1 mm positioned at a 4 mm distance from the sorting channel. The piezo was driven in its thickness mode by a waveform generator (Tabor Electronics, WW1072) operated in continuous mode. The amplitude of the sinusoidal driving voltage

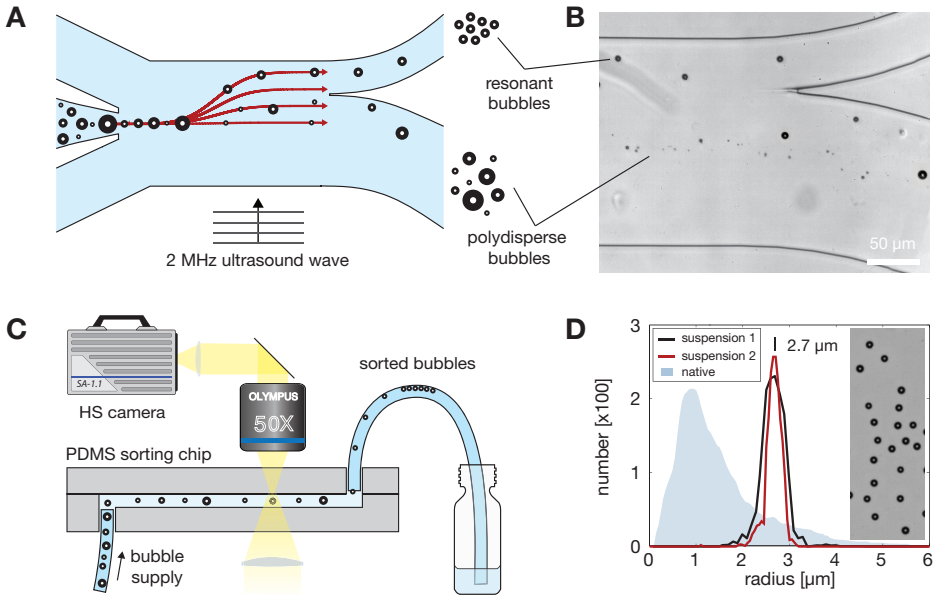

Figure 4.1: (A) Resonant microbubbles are sorted from a polydisperse ultrasound contrast agent suspension in an acoustic bubble sorting chip operated at 2 MHz. B) Photograph of the sorting chip in action. C) Microbubbles enter and leave the sorting chip in their direction of flotation. The sorted bubbles are imaged using a high-speed camera to obtain their sizes. D) Size distribution of the acoustically sorted bubbles. The inset shows a micrograph of the sorted bubbles.

was 1.8 V during the sorting procedure of suspension 1 and 2.3 V during the sorting of suspension 2. The acoustic pressure amplitude field was measured using the method described by Segers *et al.*[85] and it had a maximum pressure amplitude of 20 kPa. The resonant bubbles, passing through the upper outlet, see Fig. 4.1B, were imaged using a microscope (Olympus, BX-FM) equipped with a 50× objective lens connected to a high-speed camera (Photron SA1.1). The resulting spatial resolution was 400 nm/pixel. Suspension 1 was collected by running the sorting procedure for 25 min and suspension 2 was harvested during 15 minutes of bubble sorting. During the sorting procedures, a high-speed recording with a duration of 1 s was captured every 3 minutes at a frame rate of 5,000 fps. The shutter time was set to 8 µs to minimize motion blur. The size distribution of the acoustically sorted bubbles was obtained by processing the high-speed movie frames with an automated image analysis procedure programed in MATLAB. The size of the bubbles was measured from the inflection point of the intensity

profiles of the individual bubbles[85]. The size distributions of both bubble suspensions are shown in figure 4.1D. The maximum bubble number in both suspensions lies at a bubble radius of 2.7 μm. The standard deviation of suspension 1 is 0.24 μm and that of suspension 2 is 0.14 μm. The standard deviation of the size distribution of the native agent was 1.1 μm.

The sorted bubble suspensions were diluted with Milli-Q water (Millipore Corporation, Billerica, MA, USA) to a total volume of 22.5 mL for suspension 1, and to 4.5 mL for suspension 2. From the high-speed movies an estimate could be made on the total amount of sorted bubbles and therefore on the bubble concentration. It was approximately 4×10^3 bubbles per mL for suspension 1 in the diluted sample. The diluted samples were stored on a roller-mixer operating at 1 rpm, thereby gently agitating the bubble suspension to maximize the interbubble spacing and to minimize gas diffusion effects, such as Ostwald ripening that can lead to diffusive bubble growth of the larger bubbles by gas originating from smaller bubbles with a higher Laplace overpressure in the bubble. Four samples containing 4.5 mL of suspension 1 were characterized by acoustic scattering and attenuation measurements at four peak negative pressures in the following order: 50 kPa, 10 kPa, 25 kPa, and 100 kPa. Suspension 2 was only characterized by attenuation measurements.

4.3.2 Acoustic characterization setup

The combined scattering and attenuation measurements were performed with a single transducer over a frequency range of 0.7 MHz to 5.5 MHz in 0.1 MHz steps at acoustic pressures of 10, 25, 50, and 100 kPa in a water tank at room temperature, see Fig. 4.2. The transmit transducer had a center frequency of 2.25 MHz, a focal distance of 1″, and a 19 mm aperture (A305S, Panametrics-NDT). Its frequency dependent response was calibrated using a 0.2 mm needle hydrophone (Precision Acoustics). A second transducer measuring the scattering (Vermon, SR 885C1001, 3 MHz, f=2″, A=1″) was mounted under a 90°angle with respect to the transmit transducer and it was mounted on x-y-z translation stages to aid the alignment process. The acoustic foci were co-aligned using a 0.5 mm diameter steel ball positioned in the transmit beam focus that was found in pulse-echo mode. A third transducer measuring the transmission (C308, Panametrics-NDT, 5 MHz, $f = 1''$, A=19 mm) was also mounted on x-y-z translation stages and it was aligned such that the signal received from the transmit transducer was at maximum. The bubble suspensions were confined by a 1.5×1.5 cm^2 container made of acoustically transparent polystyrene membrane (Opticell®). The cross section of the bubble container enclosed the transducer foci and a

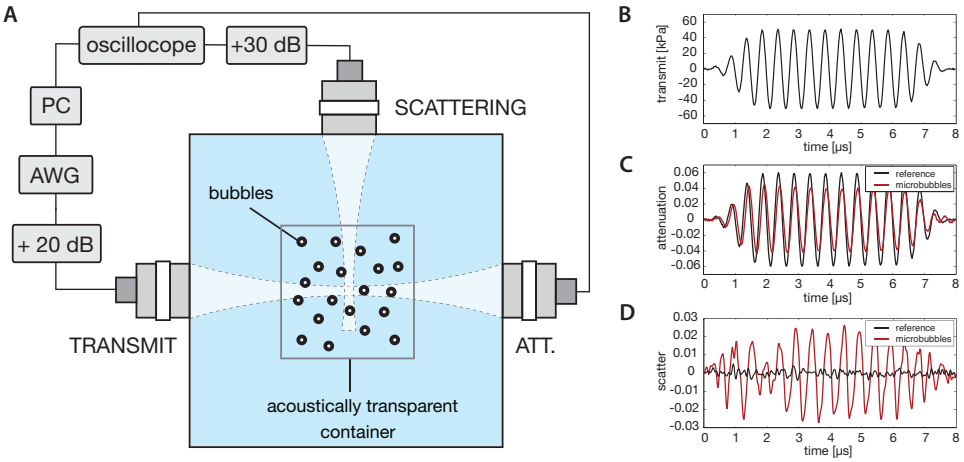

Figure 4.2: (A) Schematic representation of the acoustic characterization setup for simultaneous attenuation and scattering measurements. B) Narrowband 16-cycle acoustic pulses at a constant pressure amplitude are transmitted through the bubble sample and they are received by a transducer at the opposite side of the water tank. C) The ratio of the received signals of a water-filled container to that of a container filled with a bubble suspension gives the frequency-dependent and pressure-dependent attenuation of the bubble cloud. At the same time a transducer placed at a 90 degree angle with respect to the transmit transducer measures the scattered acoustic signal (D). The process is automated and controlled from a PC. The bubble suspension is continuously stirred to ensure a homogeneous bubble concentration throughout the sample holder. The time traces shown in figures (B), (C), and (D) are measured time traces at a transmit frequency of 2 MHz by a hydrophone, the transducer measuring the transmission and the transducer measuring the scattering, respectively.

magnetic stirrer bar placed inside the container ensured a homogeneous bubble suspension. The bubbles were insonified at a constant acoustic pressure by a series of 100 narrowband 16-cycle ultrasound pulses per transmit frequency, to obtain a statistically relevant scattering signal, at a rate of 100 Hz . A Gaussian tapering over 4 cycles on each side of the pulse (Fig. 4.2B) was applied to minimize transient effects. The pulses were generated by a programmable arbitrary waveform generator (8026, Tabor Electronics), attenuated by 30 dB to reduce the noise level and amplified by a 50 dB linear power amplifier (350L, E&I).

The received scattered signals were amplified by 30 dB (5077PR, Panametrics-NDT) and recorded by an oscilloscope (TDS5034B, Tektronix) operating in sequence acquisition mode at a 50 MHz sampling rate. Simultaneously, the

transmission signals were recorded by the oscilloscope. A MATLAB computer program was written to fully automate the measurement series by transferring the 100 time traces to a PC and by uploading a new waveform at a 100 kHz higher frequency, to the AWG. A complete measurement over the full frequency range (0.7 MHz - 5.5 MHz) at a constant acoustic pressure took 6 minutes and in total 4900 pulses were sent.

At every transmit frequency an average power spectrum was obtained from the power spectra of the 100 individual time traces. The attenuation coefficient α at the transmit frequency f_T was determined from the power spectrum obtained from a measurement with bubbles present and from a reference measurement without bubbles present as follows:

$$\alpha = \frac{10}{d} log_{10} \frac{|\langle V_{bub} \rangle|^2}{|\langle V_{ref} \rangle|^2} \tag{4.7}$$

where $|\langle V_{bub} \rangle|^2$ and $|\langle V_{ref} \rangle|^2$ are the total power of the time trace with and without bubbles present, respectively, and d is the acoustic path length over which bubbles are present.

The experimental acoustic scattering coefficient was determined in the frequency domain for every transmit frequency as follows:

$$\eta = \frac{|V_{scat}(f)|^2}{|\langle V_{ref}(f_T) \rangle|^2}, \frac{16z^2}{D^2}. \tag{4.8}$$

where $|V_{scat}(f)|^2$ is the power spectrum of the recorded scattering signal and $|\langle V_{ref}(f_T) \rangle|^2$ is the total transmitted power at the transmit frequency f_T. The total frequency dependent transmitted acoustic power was measured using a stainless steel reflector positioned at a 45°angle with respect to the transmit transducer. Using simple geometrical arguments and by neglecting diffraction, it can be calculated that the area of the acoustic wave reflected from the steel reflector has an area that is 4.5 times larger than the aperture of the scatter receiving transducer. Therefore, the measured power from the steel reflector was corrected by a factor 4.5. Furthermore, the scattering coefficients are compensated for the limited aperture of the receiving transducer where z is the focal distance and D is the transducer diameter[132]. The volume over which the receiving transducer measures the scattering, T in Eq. 4.6, was measured by translating the transducer in parallel with the direction of wave propagation of the transmitted ultrasound waves while a steel sphere (0.5 mm diameter) was positioned in the acoustic focus of the transmit beam. The focal region of a focused transducer is typically much larger in length than it is in width, see Fig. 4.3 and since

the focal region of the transducer receiving the scattered signal is co-aligned with the focus of transmitting transducer under a 90°angle, the sensitivity of the transducer T is not measured in y and z-direction and it was set to unity.

Bubble suspension 2 was characterized by attenuation measurements only which allows for limiting the number of insonations per transmit frequency from 100 to 1, to measure the effect of multiple insonations on the bubble dynamics. Large numbers of acoustic excitations, especially at higher acoustic pressures (>50kPa), may have a deleterious effect on the lifetime and stability of bubbles and change their acoustic response[133]. A single acoustic wave for each frequency is sufficient to measure attenuation since it is measured from the response of many (order 10^3) bubbles in the acoustic path length. The sample holder was decreased in size to a cross-section of 0.5×0.5 cm^2 to confine only the acoustic focus of the transmit transducer in order to obtain attenuation curves representing the bubble response over a narrow range of acoustic pressures. Attenuation curves were measured at peak negative acoustic pressures ranging from 5 kPa to 75 kPa in steps of 2.5 kPa and they were all measured from the same bubble sample. Before the measurement, all the excitation pulses were uploaded at once to the AWG. The pulser receiver (BNC555, Berkeley Nucleonics Corporation) produced the 1323 TTL pulses at a rate of 50 Hz to trigger the waveform generator and the oscilloscope. A complete measurement of 29 attenuation curves was performed within 30 seconds.

4.3.3 Modeling

The acoustic pressure field generated by the transmit transducer in experiment were numerically evaluated. The acoustic transmit field was modeled axi-symmetrically in 2-D (k-Wave toolbox[134]) for all experimentally employed transmit frequencies for a curved transducer with a 19 mm aperture focused at 1 inch. The modeled axial pressure field at 1, 2, and 3 MHz is shown in Fig. 4.3A. The grey areas represent the dimensions of the sample container in the acoustic characterization setup. Figure 4.3B shows the lateral pressure distribution at the acoustic focus located at a lateral position of 2.5 cm.

The radial response equation (Eq. 4.1) was solved numerically using the `ode45` solver in MATLAB to find the scattered pressure (Eq. 4.2) for all the bubble sizes in the optically measured size distribution (Fig. 4.1D, black line) with a 100 nm bin size and initial conditions $R = R_0$ and $\dot{R} = 0$. The driving ultrasound pulse $P(t)$ was the same as the 16-cycle pulse used experimentally and the bubble response was solved for 9 different acoustic

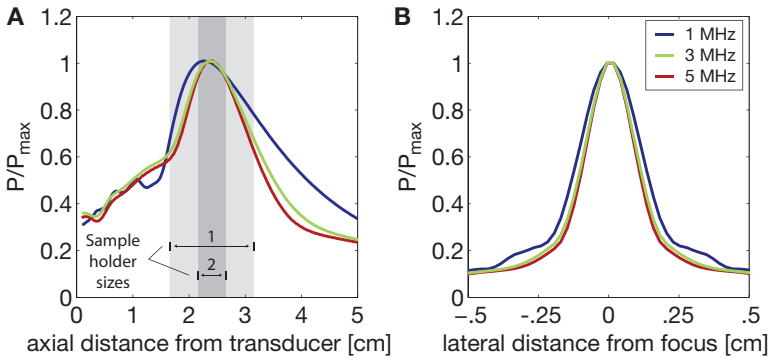

Figure 4.3: A) Modeled acoustic pressure field of a transducer with a focal length of 1″ and an aperture of 19 mm normal to the transducer aperture along the direction of wave propagation at ultrasound frequencies of 1, 3, and 5 MHz. The transducer is located at the origin. B) Pressure amplitudes at the focus normal to the direction of wave propagation. The bubbles in a cloud with finite dimensions (gray area) are exposed to very different acoustic pressure amplitudes.

pressure amplitudes ranging from the maximum pressure in the modeled acoustic pressure field P_A down to $0.2P_A$ over the -14 dB volume of the transmit beam. The scattering and attenuation coefficients were calculated using Eq. 4.6 and Eq. 4.5, respectively, using the modeled acoustic pressure field and the linear damping coefficients (Eq. 4.4). The physical constants used for the liquid are the density, $\rho = 1000$ kg/m^3, the speed of sound c = 1500 m/s, and the surface tension $\sigma = 0.072$ N/m. The viscosity was set to be twice the viscosity of water at, $\mu = 0.002$ Pa $\cdot$ s, to account for thermal damping. The polytropic exponent of the gas was set to $\kappa = 1.07$ for perfluorobutane (C_4F_{10}) and the ambient pressure P_0 to atmospheric pressure.

4.4 Results

Figures 4.4A, B, and C show the measured frequency dependent attenuation coefficients (black dots) of bubble suspension 1 at peak negative acoustic pressures of 10, 25, and 50 kPa, respectively. The scattering coefficients were measured simultaneously and those of the fundamental frequency are presented in figures 4.4D, E, and F at a pressure of 10, 25, and 50 kPa (black dots), respectively. The scattering coefficients at the second harmonic η_{2ndH} of the transmit frequency f_T are presented in figures 4.4G, H, and I with the acoustic pressures amplitudes as before. The non-linear

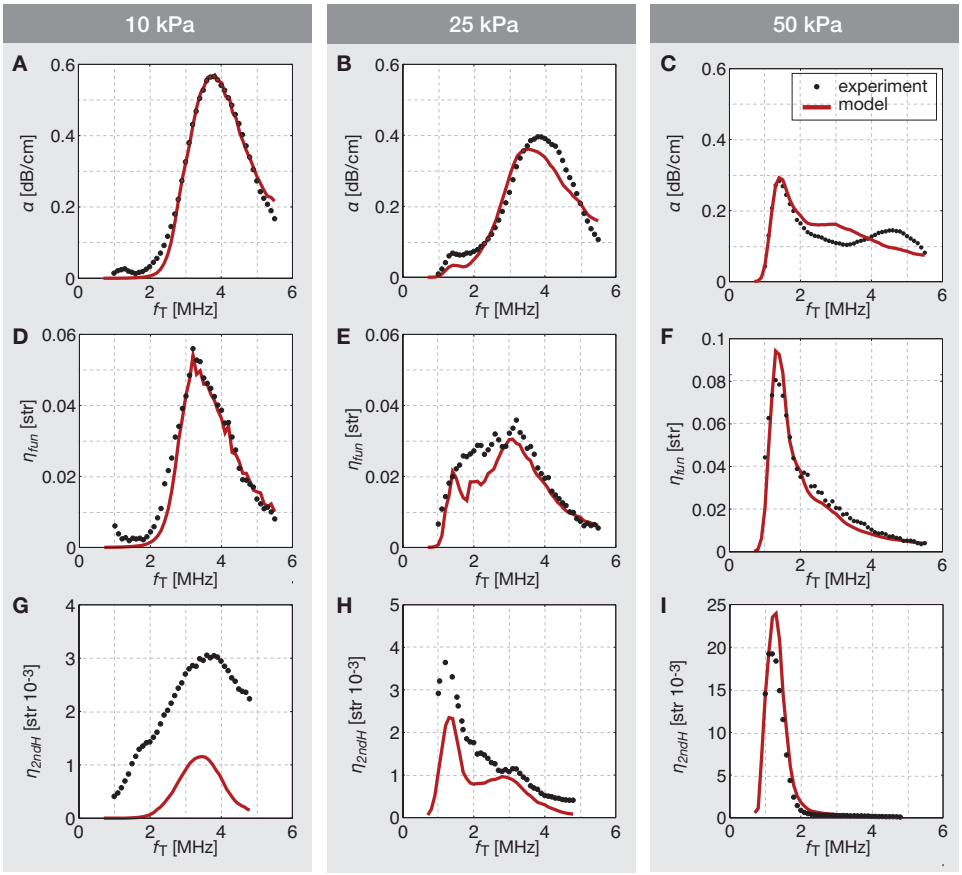

Figure 4.4: Figures A,B, and C show the frequency dependent attenuation coefficient of acoustically sorted contrast agent at 10, 25 and 50 kPa peak negative pressure, respectively. Figures, D, E, and F show the scattering coefficients at the fundamental, or transmit frequency measured at peak negative pressures 10, 25 and 50 kPa, respectively. Figures, G, H, and I present the frequency dependent scattering coefficients at the second harmonic of the transmit frequency. The scattering and attenuation were measured simultaneously. The solid red lines show the modeled scattering and attenuation coefficients and good agreement is found for a unique set of shell parameters, i.e. $\chi = 2.5$ N/m, $\kappa_s = 3{\times}10^{-9}$ Pa·s, and $\sigma(R_0) = 0.02$ N/m.

pressure dependent resonance behaviour is clearly visible from the resonance frequency shift towards lower frequencies for increasing acoustic pressures[75]. Please note that the scattering and attenuation coefficients, while measured simultaneously, can still have a slightly different frequency of maximum response. Scattering is measured from a relatively small focal region of the transmit acoustic field at relatively high acoustic pressures while the attenuation is measured over the total width of the sample holder. Since the acoustic waves are focused, the acoustic pressure increases towards the focal region and decreases thereafter. As a result, the attenuation curves present a summation of bubble responses at a range of acoustic pressures. Due to the pressure-dependent resonance behaviour of the bubbles this results in a spectrally broader attenuation curve as compared to that of the scattering. It is most clearly observed from the scattering and attenuation coefficients at a pressure of 25 kPa where the resonance frequency at the acoustic focus is 1.5 MHz, recognized from the peak in the second harmonic scattering coefficient, Fig. 4.4H, while the attenuation coefficients show that only very few bubbles resonate at a frequency of 1.5 MHz as the maximum response is found at a frequency of 3.8 MHz and originates from the total volume contained by the intersection of the acoustic beam and the sample container.

The solid red lines in the figures represent the modeled scattering and attenuation coefficients. The best agreement was found using a unique set of shell parameters: a shell elasticity of $\chi = 2.5$ N/m ± 0.1 N/m, a shell viscosity of $\kappa_s = 3.0 \times 10^{-9}$ Pa·s $\pm\ 1.5 \times 10^{-9}$ Pa·s and an initial surface tension of $\sigma(R_0) = 0.02$ N/m $\pm$ 0.002 N/m. The shell elasticity was constant throughout all simulations. These shell parameters are in very good agreement with previously obtained BR-14 shell parameters[75] and with the shell parameters used by Segers *et al.*[85] to model the on-chip displacement of BR-14 microbubbles in the sorting channel of the acoustic bubble sorter. The bubble concentration $n(R)$ in the simulation was set to match the maximum attenuation coefficient at 10 kPa (Fig. 4.4A) and it was kept unchanged during all further simulations at 25, and 50 kPa at a concentration of $4.3{\times}10^3$ bubbles per mL. This is in excellent agreement with the bubble concentration obtained from the high-speed movies which was $4{\times}10^3$ bubbles per mL. Moreover, we find a very good agreement between the measured and the modeled scattering and attenuation coefficients using a unique set of shell parameters and bubble concentration, which confirms the acoustic uniformity of acoustically sorted bubbles.

Figure 4.5A shows the measured attenuation coefficient of suspension 2 for different acoustic pressures. In total, 29 attenuation curves were measured

where the first curve was obtained at a peak negative pressure of 5 kPa and the final curve at a pressure of 75 kPa with pressure increments of 2.5 kPa. While the size distribution of suspension 2 is nearly identical to that of suspension 1, the attenuation curves are narrower here due to the smaller sample container. The acoustic excitation pressure field is more uniform, hence decreasing the dispersity in bubble responses. The frequency of maximum response at the lower acoustic pressures lies at a frequency of 5.0 MHz which is 1.0 MHz higher than that of bubble suspension 1. The attenuation curves also show that the bubble response at intermediate acoustic pressures (30 kPa $< P_A <$ 50 kPa) is relatively broadband since the resonance frequency of the bubbles at the acoustic focus is near 1.4 MHz, due to the elevated pressure in the focus, whereas the bubbles away from the focus resonate at a frequency of 3.6 MHz.

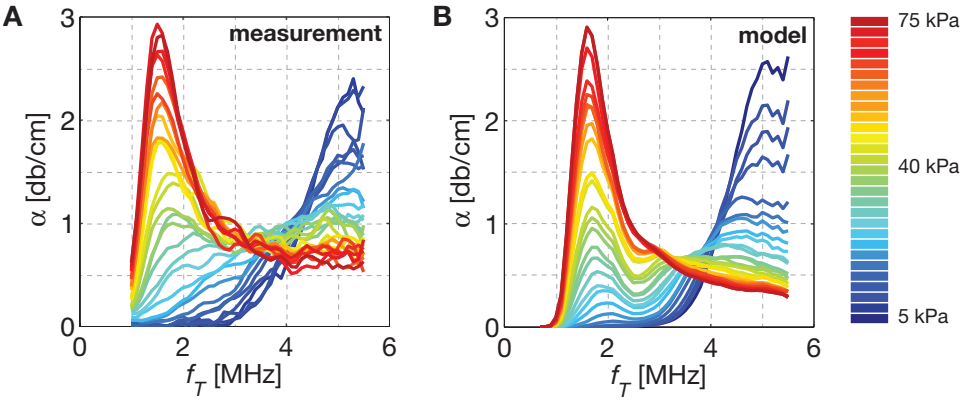

Figure 4.5: A) Attenuation of acoustically sorted bubbles measured at 29 different acoustic peak negative pressures increasing from 5 to 75 kPa. The size distribution of the bubbles is shown in figure 4.1D. B) Modeled attenuation of the sorted bubbles. Input to the model were a shell stiffness of $\chi = 3.5$ N/m, a shell viscosity of $\kappa_s = 3 \times 10^{-9}$ Pa·s and initial surface tenstion $\sigma(R_0) = 0.02$ N/m.

Figure 4.5B shows the modeled attenuation curves for the measured size distribution of suspension 2 (Fig. 4.1D). The modeled curves were obtained as before. To capture the resonance frequency at the lower acoustic pressures the shell stiffness was set to $\chi = 3.5$ N/m $\pm$ 0.1 N/m. The shell viscosity κ_s and the initial surface tension $\sigma(R_0)$ were used as before. The bubble concentration $n(R)$ in the simulation was set to 4.1×10^4 bubbles per mL. The modeled attenuation curves are in excellent agreement with the measured attenuation curves in both, absolute magnitude and resonance be-

haviour over the full pressure range. Bubbles with an on-chip displacement in the range of 70 to 100% of the maximum displacement were collected in the sorted bubble outlet to obtain a sufficiently large amount of bubbles for the characterization experiments. The resulting small variation in the initial surface tension of the sorted bubbles[85] may, to a great certainty, have resulted in the minimal difference between the model and the measurements present at a frequency of 2.5 MHz.

4.5 Discussion

It is of interest to say a few words on the sensitivity of the characterization method to discriminate changes in shell properties. The shell stiffness is directly obtained from the low pressure response; it sets the resonance frequency of the elastic bubble oscillations and it is therefore obtained with high precision. The shell viscosity has a large contribution to the total damping[80] and it is found by matching the width of the modeled scatter and attenuation coefficients to the ones measured experimentally. The total damping of the bubble oscillations determines the ratio of the amplitudes of the scattering and attenuation coefficients at high and low acoustic pressure. For these reasons, the shell viscosity can be determined accurately from our model. The third shell parameter, the initial surface tension $\sigma(R_0)$, has a dramatic influence on the nonlinear bubble dynamics. The lower the initial surface tension, the lower the acoustic pressure at which the bubble starts to buckle and thus, the lower the acoustic pressure at which a resonance frequency starts to shift to lower frequencies. The uncertainty in the obtained initial surface tension is surprisingly low and it is determined with the highest precicion from the intermediate acoustic pressure regime ($P_A \approx 25$ kPa) where the bubbles in the acoustic focus of the transmit field oscillate in the buckled state while other bubbles oscillate in the elastic state at the lower acoustic pressure regions outside the focus. Thus, the inclusion of the position-dependent acoustic pressure distribution in our model is essential for an accurate description of the pressure-dependent nonlinear bubble response within the monodisperse bubble suspension.

Suspension 1 was characterized by a bubble shell stiffness of 2.5 N/m, whereas suspension 2 was characterized by a shell stiffness of 3.5 N/m. The bubbles originated from two different BR-14 vials and one possibility is that the shell properties varied from vial to vial. Another more likely explanation is that the difference in co-flow rates between the two sorting procedures influenced the sorting procedure. The co-flow rate was 25 μL/min for suspension 1 and 35 μL/min for suspension 2 resulting in a pressure drop over

the sorting channel (length 1 cm) of 100 kPa and 140 kPa, respectively. The 40% higher ambient overpressure may have resulted in a change of the resonance frequency and a slightly modified sorting leaded to a set of stiffer bubbles.

The attenuation curve measured at a pressure of 50 kPa shown in Fig. 4.4C shows two maxima. The first maximum is located at a frequency of 1.5 MHz, which is the expected resonance frequency, see also the harmonic response at lower pressures in Fig. 4.4H. The second maximum is located at a much higher frequency of 5.0 MHz which is higher than the frequencies of main maximum response in the measured attenuation curves at pressures of 10 and 25 kPa. As the higher pressure response gives the predicted resonance frequency at 1.5 MHz, it can be concluded that the bubble size did not change substantially during the multiple 50 kPa insonations. The higher frequency of maximum response may be a result of a change in the shell properties during multiple insonations at sufficient acoustic pressure. Such a substantial change in the shell properties is discussed extensively in Chapter 6.

The initial surface tension of the bubbles was characterized at a value of 0.02 N/m. Segers *et al.*[85] showed that bubbles with an initial surface tension close to zero are displaced over the largest distances by the primary radiation force in the acoustic bubble sorting chip[85]. The higher initial surface tension found here may have resulted from the volumetric expansion of the sorted bubbles at the outlet of the sorting chip were the ambient pressure is atmospheric while the bubbles are sorted at an overpressure. The overpressure compresses the bubbles which decreases the surface tension though a higher phospholipid packing density. Moreover, the resonance frequency of bubbles at a higher ambient pressure increases as can be directly observed from the linearized Rayleigh-Plesset equation[80].

Our model does not take into account the decrease in pressure amplitude of the acoustic characterization wave while it propagates through the bubble suspension. The bubble concentration (4×10^3 bubbles/mL) was deliberately kept low during the experiments to allow a quantitative comparison between the measurements and the model. For higher concentrations bubble-wave and bubble-bubble interactions need to be taken into account to fully describe the (*in-vivo*) scattering and attenuation properties. For characterization purposes, however, a low bubble concentration and the simple model presented here is sufficiently accurate.

Scattering and attenuation coefficients at a peak negative pressure of 100 kPa showed a frequency of maximum scattering and attenuation at 1.8 MHz which is higher than the 1.5 MHz measured at a peak negative

pressure of 50 kPa. This indicates that the bubble size distribution has changed and that bubbles had become smaller. Thus, the high number of insonations at 100 kPa had a deleterious effect on the quality of the monodisperse bubble suspension and this data was excluded for characterization purposes.

The geometrical approximation used in obtaining the total transmitted power, to which the scattered power is scaled (Eq. 4.8) allowed us to downscale all scattering coefficients by a factor 1.3 in order to match the amplitude of the modeled 10 kPa scattering coefficient at the fundamental to that of the measured fundamental scattering coefficient at 10 kPa.

4.6 Conclusions

Good agreement was found between measured and modeled scattering and attenuation curves for all acoustic characterization pressures, both in the overall dynamical response, as well as in the absolute magnitude using a unique set of shell parameters and bubble concentration. This confirms the uniformity of the responses of the acoustically sorted bubbles. We have shown that it is crucial to include the pressure-dependent resonance behaviour in the modeling of the scattering and attenuation behaviour of a bubble cloud exposed to a typical focused ultrasound beam. The sensitive pressure-dependent attenuation measurements, presented here using a small amount of acoustic insonations, have great potential in the rapid characterization of contrast agents. It provides valuable insight into an optimized bubble response obtained from contrast enrichment strategies such as sorting in addition to fundamental insight into bubble shell parameters. The displayed accuracy and sensitivity of the characterization of monodisperse bubbles may have the potential to improve the present ad-hoc theoretical viscoelastic shell models. Acoustically uniform bubble suspension are of great interest for targeted molecular imaging using ultrasound, and for drug and gene delivery applications due to their controlled and acoustic well-defined and well described response.

Acknowledgements

We thank Guillaume Lajoinie and Peter Frinking for stimulating discussions. We thank Bracco Research Geneva for the supply of BR-14 ultrasound contrast agents. We also want to thank Gert-Wim Bruggert, Martin Bos, and Bas Benschop for their skilful technical assistance. This work is supported by NanoNextNL, a micro and nanotechnology consortium of the

Government of the Netherlands and 130 partners.

5

Sorted ultrasound contrast agents boost the scattering-to-attenuation ratio

The use of monodisperse bubbles as ultrasound contrast agents (UCA) in imaging and therapy with ultrasound is often proposed to increase the efficiency and the sensitivity. Here, we measure experimentally the efficiency of monodisperse bubble suspensions, compare it to that of a polydisperse agent and find a 10 times increase at the fundamental frequency and a 20 times increase at the second harmonic. The efficiency is expressed by the scattering-to-attenuation ratio and scattering and attenuation were measured simultaneously using a focused ultrasound beam. Narrowband 16-cycle ultrasound pulses with a frequency ranging from 0.7 MHz to 5.5 MHz at peak negative acoustic pressures of 10, 25, 50 and 100 kPa were used. From the pressure and frequency dependent measurements, we show that a focused ultrasound wave can tunnel through a contrast agent suspension, without being attenuated, until it reaches the focus. The measured narrowband nonlinear response of sorted agents can thereby be exploited to minimize shadowing effects in deep tissue imaging with contrast.

[1]To be submitted as: T. Segers, M.P. Kok, G. Lajoinie, D. Fernandez-Rivas, N. de Jong, M. Versluis, *Uniform scattering and attenuation of acoustically sorted ultrasound contrast agents: modeling and experiments* (2015)

5.1 Introduction

Ultrasound contrast agents produced with conventional methods such as sonication and mechanical agitation[67,118] contain microbubbles in a size range from 1 to 10 μm in radius. The microbubbles are stabilized against dissolution and coalescence by a surfactant shell, typically consisting of biocompatible phospholipids. The echogenicity of the contrast agent results from the large compressibility of the microbubble gas cores. The radial oscillations, in response to a driving ultrasound field, are highly non-linear and they increase the scattering cross-section up to three orders of magnitude when a bubble is driven at its resonance frequency[33]. Clinical ultrasound scanners operate at a narrow frequency bandwidth and as the resonance frequency of a bubble is directly related to its size[37], only a small fraction of the UCA population resonates to the driving ultrasound field.

The sensitivity increase that may result from the use of monodisperse UCA was already frequently suggested[4,64,65,118,135–137]. *In-vitro* experiments have shown that the echo response of monodisperse bubbles presents a higher inter-echo correlation than that of a polydisperse population[4]. *In-vivo* experiments have shown a higher video intensity[68] for monodispere bubbles. The use of monodisperse bubbles was reported to be of main interest for molecular imaging[3] and drug delivery[7,8,91,92,117] applications where only small amounts of bubbles are retained at the target site[4]. For blood pool imaging, a large number of bubbles, on the order of one billion, is injected intravenously to increase the sensitivity and monodispersity was thought to be of less importance here[4,136]. However, a large bubble concentration present in the blood pool may result in a strong attenuation of the transmitted ultrasound wave resulting in shadowing of the underlying tissues. Thus, scattering alone is not the only important measure in the quantification of the efficiency of contrast agents. The ideal contrast agent scatters ultrasound efficiently while it absorbs little energy. Thus, the efficiency is characterized by its scattering to attenuation ratio (STAR)[89,132,138–141].

The scattering and attenuation of ultrasound contrast agents is strongly dependent on the driving parameters such as the frequency and the acoustic pressure[87,141,142] due to the nonlinear viscoelastic properties of the bubble shell[40,75,109]. The elasticity of the shell increases the resonance frequency and its viscosity increases the energy dissipation through damping[80]. Moreover, rupture and buckling of the phospholipid shell at substantial radial oscillations was shown to gradually decrease the resonance frequency with increasing driving pressure, through a decrease of the effective shell stiffness[41,75].

Here, we characterize the efficiency of two narrow size distribution bubble populations obtained by sorting of a polydisperse contrast agent and we compare them to that of the native agent. The efficiency is measured by scattering and attenuation measurements using a focused ultrasound beam to be close to clinical contrast enhanced imaging with focused ultrasound field. The efficiency, as obtained from the STAR, is measured as a function of the insonation pressure and frequency as will be shown in the Experimental section. The efficiency results are presented thereafter together with a theoretical pressure dependent analysis of the microbubble scattering as a function of its position in the transmit wave. Finally, we discuss the potential of size sorted bubble populations for perfusion imaging and we finish with the conclusions.

5.2 Experimental

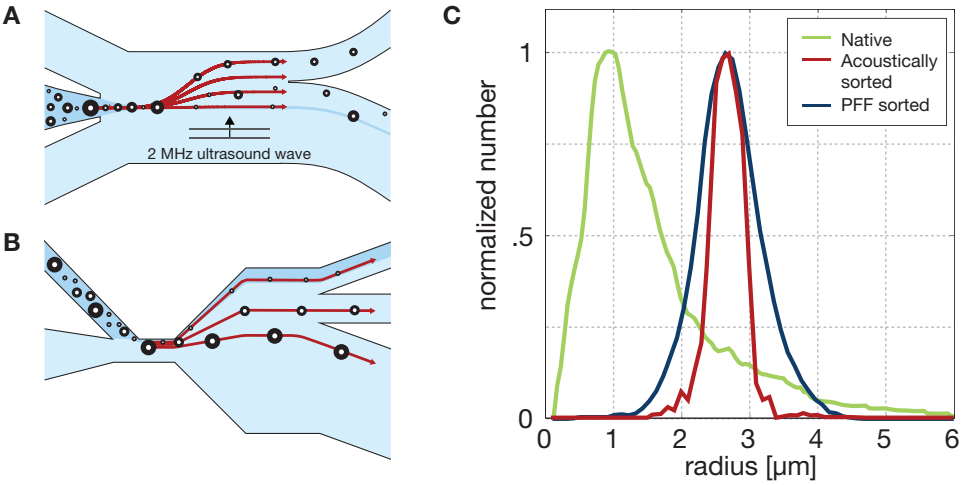

Figure 5.1: A polydisperse contrast agent is sorted using two microfluidic sorting techniques. A) In an acoustic bubble sorting chip, resonant bubbles are separated from non-resonant bubbles by the primary radiation force[85]. B) The contrast agent is sorted to size in a pinched flow fractionation geometry[88]. C) Size distributions of the acoustically sorted bubbles, the size sorted bubbles and the native bubble population.

A polydisperse perfluorobutane-based ultrasound contrast agent (Bracco BR-14, Bracco Research Geneva) containing bubbles coated with DSPC and DPPG lipids[109] is used. The contrast agent was reconstituted by the

addition of 5 mL water (Milli-Q, Millipore Corporation, Billerica, MA, USA) and it was put to rest for at least 10 min to allow the bubbles to stabilize. The optically measured size distribution of the native agent is shown in figure 5.1C.

An acoustically sorted bubble suspension is produced with the acoustic bubble sorting method that is outlined by Segers *et al.*[85] and the sorting chip was operated at a frequency of 2 MHz, see Ch. 2. The acoustic sorting procedure is described in detail in Ch. 4. The size distribution of the acoustically sorted agent is shown in figure 5.1C.

The size-sorted suspension was obtained from sorting the native agent in a pinched flow fractionation (PFF) lab-on-a-chip device. The sorting behaviour of the applied PFF chip was fully characterized by Kok *et al.*[88], see Ch. 3. The PFF chip was operated for 1 hour at an UCA flow-rate of 0.2 μL/min and a co-flow rate of 12 μL/min. The optically measured (400 nm/pixel resolution) size distribution of the PFF sorted bubbles is shown in figure 5.1C.

The sorted bubble suspensions were diluted with water (Milli-Q, Millipore Corporation, Billerica, MA, USA) in a vial to a total volume of 18 mL. The vial was placed on a roller mixer operated at 1 rpm. The gentle continuous agitation maximized the interbubble spacing and it therefore minimized gas diffusion effects, such as Ostwald ripening, that can potentially change the bubble size distribution. The diluted bubble suspension was subdivided in 4 samples of 4.5 mL. The first sample was characterized by scattering and attenuation measurements at a peak negative pressure of 50 kPa. The subsequent 4.5 mL samples were characterized at pressures of 10 kPa, 25 kPa, and 100 kPa.

The scattering and attenuation curves were measured in a water tank at room temperature as described in detail in Ch. 4. In brief, the bubble suspension, confined by a 1.5 $\times$1.5 cm^2 cross-sectional acoustically transparent container, was insonified at a constant acoustic pressure by a series of 100 narrowband 16-cycle ultrasound pulses per transmit frequency with a Gaussian tapering of 4 cycles on each side of the pulse, over a frequency range from 0.7 to 5.5 MHz in 0.1 MHz steps. The transmit beam of the first transducer (A305S, Panametrics-NDT, 2.25 MHz, 19 mm aperture) was focused at 1″ in the center of the sample container. The transmitted ultrasound pulse is received by a second transducer (C308, Panametrics-NDT, 5 MHz, 1″, 19 mm aperture) opposing the transmit transducer and the attenuation is measured from the average of the 100 received time traces

per transmit frequency as follows:

$$\alpha = \frac{10}{d} log_{10} \frac{|\langle V_{bub} \rangle|^2}{|\langle V_{ref} \rangle|^2} \tag{5.1}$$

where $|\langle V_{bub} \rangle|^2$ and $|\langle V_{ref} \rangle|^2$ are the total power of the time traces with and without bubbles present in the sample holder and d is the length of the sample container. The scattering coefficient is measured at the same time by a third transducer (Vermon, SR 885C1001, 3 MHz, 2″, 1″ aperture) positioned at a 90°angle with respect to the transmit beam with its focus co-aligned with that of the transmit beam as follows:

$$\eta = \frac{|V_{scat}(f)|^2}{|\langle V_{ref}(f_T) \rangle|^2} \frac{16 z^2}{D^2}, \tag{5.2}$$

where $|V_{scat}(f)|^2$ is the power spectrum of the scattered time traces averaged over the 100 identical transmit pulses and the total transmitted power $|\langle V_{ref}(f_T) \rangle|^2$ measured from the reflection of the transmit pulse from stainless steel reflector placed at an angle of 45°at the position of the sample container. The scattering coefficient was compensated for the limited aperture of the receiving transducer; z is the focal distance of the receiving transducer and D represents its aperture[132]. The scattering coefficient was expressed in the frequency domain for the interest of the harmonic components. The transmit signals were generated by a arbitrary waveform generator (8026, Tabor Electronics), attenuated by 30 dB to decrease the noise level and amplified by a 50 dB power amplifier (350L, E&I). The measured scattering signals were amplified by 30 dB (5077PR, Panametrics-NDT). The signals were recorded by an oscilloscope (TDS5034B, Tektronix) and a complete measurement scan took 6 minutes and it was fully automated and controlled from a PC.

5.3 Results

The measured scattering and attenuation coefficients are shown in Fig. 5.2. The first column presents the data of the native agent, the second column that of the size-sorted agent, and the third column shows the data of the acoustically sorted agent. The attenuation curves of the three agents are plotted in the first row, Figs. 5.2A-C. The pressure levels were 10 kPa (blue), at 25 kPa (green), at 50 kPa (red), and at 100 kPa (grey). The typical pressure dependent response of the bubble populations was found to be similar: the frequency of maximum response decreases for increasing

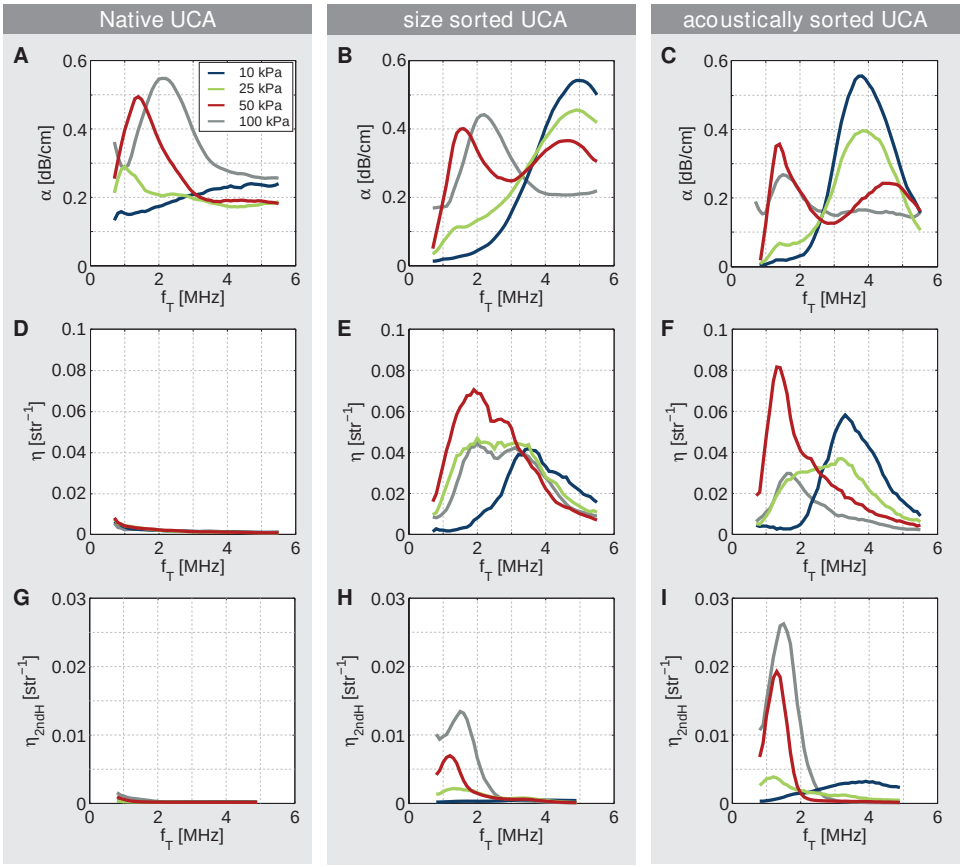

Figure 5.2: Measured frequency dependent attenuation coefficients of (A) the native contrast agent, (B) the size sorted agent, and (C) the acoustically sorted agent. Attenuation curves were measured at peak negative pressures of 10, 25, 50, and 100 kPa. The simultaneously measured scattering coefficients at the fundamental requency are shown in figures D-F and the second harmonic scattering coefficients are shown in figures G-I.

acoustic pressures. A closer look reveals that the sorted agents present almost no attenuation at low frequencies measured at a pressure of 10 kPa where the native agent has an offset of approximately 0.2 dB/cm in its attenuation curves. On top of that, the absolute attenuation of the native agent increases with increasing acoustic pressure while that of the sorted agents decreases with increasing pressures. At a pressure of 10 kPa, the frequency of maximum response of the size sorted agent is higher than that of the acoustically sorted agent, suggesting that the shell stiffness of the size sorted bubbles is larger than that of the acoustically sorted agent[75]. The attenuation curves of the bubble populations at a pressure of 100 kPa have a frequency of maximum response that is higher than that at a pressure of 50 kPa. This indicates that the mean bubble size had become smaller. Thus, the high number of insonations at 100 kPa had a deleterious effect on the monodispersity of the bubble suspensions.

The fundamental scattering coefficients (scattering at the transmit frequency) of the bubble suspensions are shown in the second row, in Figs. 5.2D-E. The scattering property of the native agent is very different from that of the sorted bubble populations, while the absolute magnitude of the attenuation was similar for all bubble suspensions. First, the scattering is at least a factor 10 lower. Please note the different absolute scales in Figs. 5.2. Second, the scattering curves of the sorted agents present a strong pressure and frequency dependency while that of the native agent is nearly independent of the insonation pressure and it increases exponentially with decreasing insonation frequencies. The acoustically sorted agent presents a more narrowband scattering than the size-sorted agent at all insonation pressures.

The scattering coefficients at the second harmonic of the transmit frequency are plotted in the third row, Figs. 5.2G-I. Similar to the fundamental scattering coefficients, the second harmonic scattering coefficients of the sorted agents are at least 10 times larger than that of the native agent. In addition, the second harmonic scattering coefficient of the acoustically sorted agent is approximately 3 times larger than that of the sorted agent and at 100 kPa it is even 180 times larger than the second harmonic STAR of the native agent.

To summarize, the sorted agents scatter at least 10 times the acoustic power as compared to the native agent, while the amount of energy that is absorbed from the acoustic wave is similar to that of the native agent. A comparison between the sorted agents shows that the response of the acoustically sorted agent is much more narrowband than that of the size-sorted agent, as expected. This can be explained from the acoustic uniformity of

the acoustically sorted agent, see Ch. 4. The main difference in the absolute amplitude is found in the scattering coefficient at the second harmonic that is at least two times larger for the acoustically sorted agent.

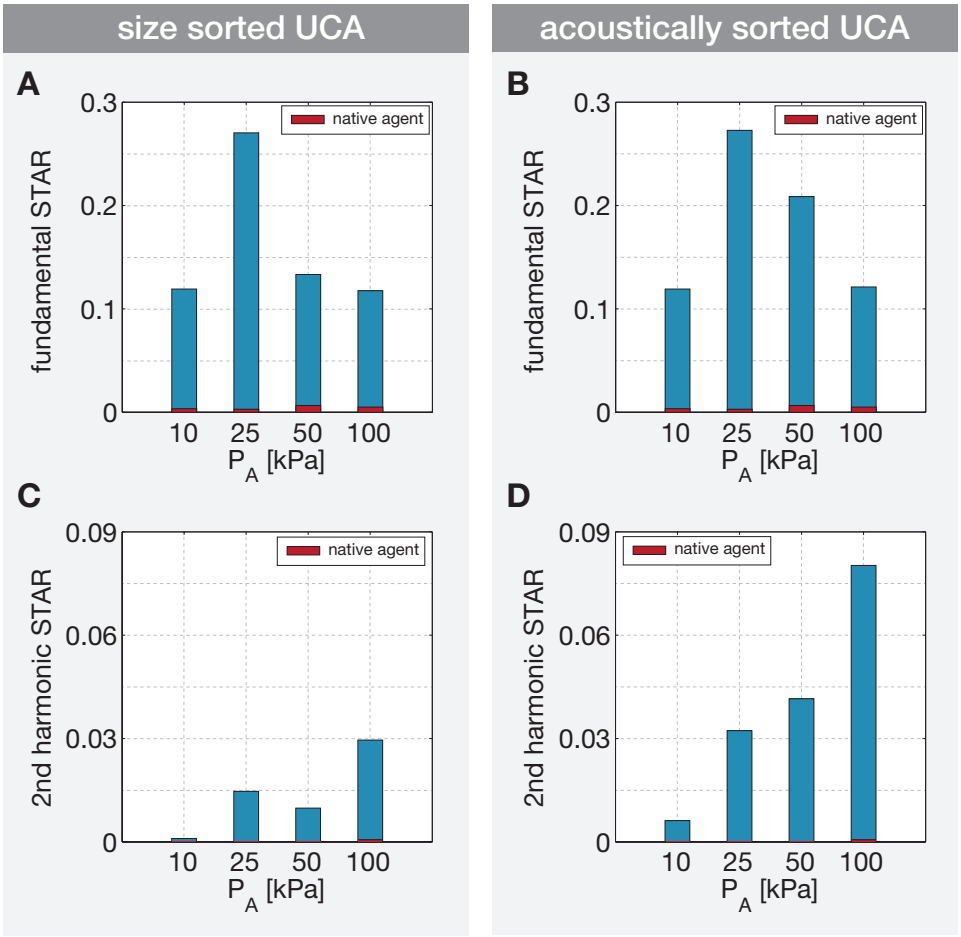

Figure 5.3: Scattering to attenuation ratio (STAR) at the resonance frequency of the contrast agent in the acoustic focus for (A) the size sorted agent and (B) the acoustically sorted agent.

The bubble suspensions were characterized in a focused ultrasound field that was non-uniform over the width of the experimental cell containing the bubbles. A consequence of the highly nonlinear pressure-dependent resonance behaviour of the sorted bubbles, together with the elevated pressure in the acoustic focus, is that the resonance frequency of the bubbles in the acoustic focus is different from that of the bubbles away from the acoustic

focus. This suggests that the imaging frequency and acoustic pressure in the focal region can be chosen such that the bubble population only resonates in the acoustic focus of the transmit field and that it thereby only attenuates the acoustic transmit wave at the focal region. Thus, shadowing effects of underlying tissues can potentially be minimized. To investigate this *tunnelling* effect, we obtain the scattering-to-attenuation ratio at the resonance frequency of the bubbles in the acoustic focus. The frequency at which the bubbles resonate in the focal region is found from the frequency of maximum response of the second harmonic since harmonics are purely generated by radially oscillating bubbles.

Figure 5.3 presents the STAR values with the STAR of the size sorted agent in the left column and the STAR of the acoustically sorted agent in the the right column. Figures 5.3A and B show the fundamental STAR and Figs. 5.3C and D show the STAR at the second harmonic. As a reference, the STAR of the native agent is also shown (red bars). The absolute STAR of the sorted agents is of similar magnitude and it is at least 20 times larger than the STAR of the native agent. The increase in STAR at the intermediate pressures 25-50 kPa is maximal, which can be explained from the narrow bandwidth of the pressure dependent resonance behaviour of the sorted bubbles[75].

At low acoustic pressures the bubbles oscillate linearly at a resonance frequency that is mainly determined from the elasticity of the bubble shell. At high acoustic pressures, the bubbles resonate at a frequency close to the resonance frequency of an uncoated bubble[75] and the frequency is determined mainly by the size of the bubble. Thus, bubbles with a similar shell stiffness and a similar size present a very similar acoustic behavior at low and at high acoustic pressure. Therefore, the STARs at 10 kPa and 100 kPa is of an equal value. However, at the intermediate acoustic pressures, the resonance frequency in the acoustic focus is close to that of an uncoated bubble whereas that away from the focus is that of the elastically oscillating bubble. Therefore, so called tunnelling of acoustic waves through the contrast agent is demonstrated from the increased STAR values at intermediate acoustic pressures.

The difference in the STARs of the size sorted and the acoustically sorted agent can be explained from differences in the initial surface tension of the bubble populations. The initial surface tension determines the onset of the non-linear buckled oscillations. Contrast bubbles of the same size where shown to have different initial surface tension[40,85,109]. However, the acoustically sorted bubble suspension is sorted to its acoustic property and it can therefore be expected to have a different acoustical, and more uniform,

response than the size sorted agent.

In Chapter 4 it was shown that the acoustically sorted agent is characterized by a shell stiffness of 2.5 N/m, a shell viscosity of $\kappa_s = 3 \times 10^{-9}$ Pa·s, and an initial surface tension of 0.2 N/m. To illustrate the tunneling effect theoretically, we model the average scattering cross-section, per bubble, as a function of the lateral on-axis position in the acoustic field generated by the transmit transducer with an axial resolution of 0.23 mm. We use the model described in Ch. 4. The transmit field was numerically evaluated (k-Wave toolbox[134]) at a transmit frequency of 1.4 MHz for acoustic pressure amplitudes P_A of 10 kPa to 50 kPa, see Fig. 5.4A. The average scattering cross-section per bubble as a function of the lateral on-axis position is plotted in Fig. 5.4B. The figure shows that when the focal pressure and imaging frequency are carefully chosen, the scattering by the bubbles is confined to the focal region.

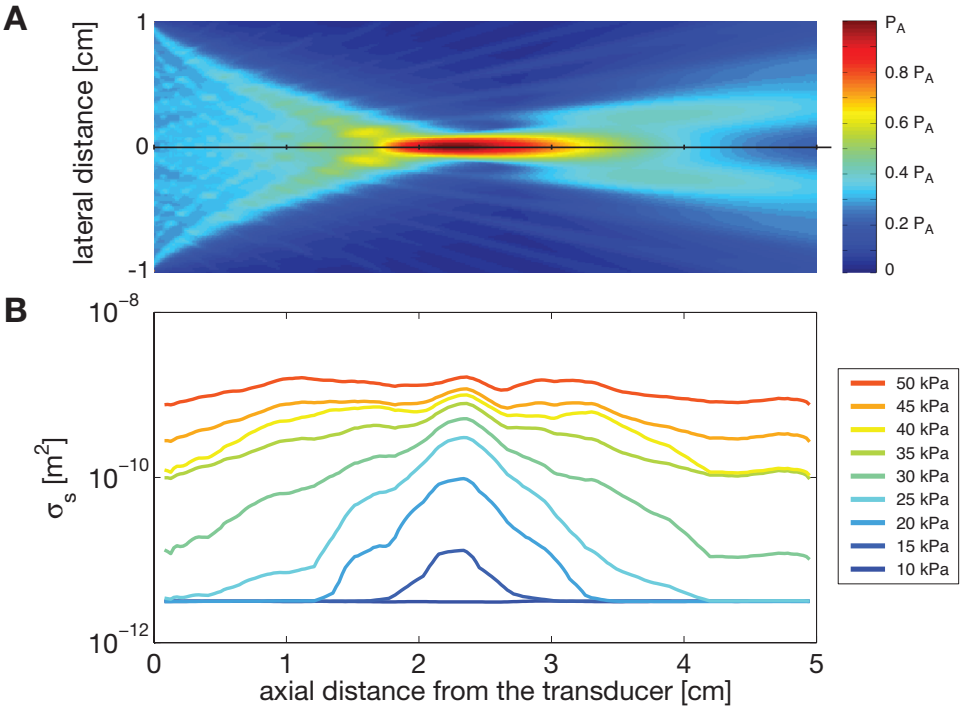

Figure 5.4: A) Acoustic pressure field of a 19 mm aperture single element transducer focused at 1 Inch. B) Modeled average on-axis scattering cross-section, per bubble, as a function of the axial position in the transmit field for a range of peak negative acoustic pressures amplitudes P_A.

Recently, the use of plane wave contrast enhanced ultrasound imaging was introduced[143]. In contrast imaging with plane waves shadowing effects can potentially be minimized by exploiting the non-linear property of sorted bubble populations by transmitting a plane wave at a frequency resonant to elastically oscillating bubbles, e.g. 3.6 MHz for the acoustically sorted agent. By increasing the pressure amplitude of the transmitted plane wave, resonating bubbles will be found at increasing tissue depths due to the attenuation of the acoustic wave by the tissue. Thus, the depth at which bubbles resonate to the driving ultrasound field can be tuned by the pressure amplitude of the transmitted ultrasound wave and thereby shadowing effects can potentially also be minimized in plane wave imaging.

5.4 Conclusions

At the fundamental frequency, a sorted UCA driven at its resonance frequency is at least a 10 times more efficient contrast agent than a conventional polydisperse UCA through a 10 times stronger scattering while the magnitude of attenuation is of the same order. At the second harmonic the efficiency increases by at least a factor 20 for the sorted bubble population as compared to the native UCA. The uniform pressure and frequency dependent resonance behaviour of the sorted bubbles allows for the selection of an imaging frequency and focal pressure such that the scattering and attenuation are confined to the acoustic focus. Thus, the narrowband nonlinear response of sorted agents can be exploited to minimize shadowing effects in deep tissue contrast enhanced ultrasound imaging.

Acknowledgements

We thank Peter Frinking for stimulating discussions. We thank Bracco Research Geneva for the supply of BR-14 ultrasound contrast agents. We also want to thank Gert-Wim Bruggert, Martin Bos, and Bas Benschop for their skilful technical assistance. This work is supported by NanoNextNL, a micro and nanotechnology consortium of the Government of the Netherlands and 130 partners.

6

On the stability of monodisperse phospholipid-coated microbubbles formed by flow-focusing at high production rates

Monodisperse ultrasound contrast agents may dramatically increase the sensitivity and efficiency in contrast enhanced ultrasound imaging and therapy with microbubbles and ultrasound. Monodisperse bubbles can be produced in a flow-focusing device. Up to now, the production of monodisperse phospholipid coated bubbles at high rates was challenging. Here, we demonstrate the successful formation of monodisperse bubbles at rates up to one million bubbles per second. Bubbles with radii in a range of 2 to 10 μ*m are produced and their size stability was characterized over a 2 hour time window. It was found that* all *bubbles dissolve to reach a stable final bubble radius that is 2.55 times smaller than their initial radius and it was found to be independent of the nozzle size and the nozzle shear rate. The acoustic stability of a stable bubble suspension was characterized by attenuation measurements over a frequency range from 0.7 to 5.5 MHz at an acoustic pressure ranging from 5 to 70 kPa in pressure steps of 2.5 kPa. The acoustic characterization revealed that the shell stiffness of the monodisperse bubbles gradually increased from 0.8 N/m to 2.5 N/m with increasing number of insonations through the loss of lipid emulsifier molecules. The experimental data is supported by modeled attenuation curves in which the full non-linear bubble response was included.*

[1]To be submitted as: T. Segers, L. de Rond, M. Borden, N. de Jong, M. Versluis, *On the stability of monodisperse phospholipid-coated microbubbles formed by flow-focusing at high production rates* (2015)

6.1 Introduction

Ultrasound contrast agents (UCA) are used clinically in contrast-enhanced ultrasound imaging for more than 20 years. They consist of a suspension of stabilized microbubbles that scatter ultrasound efficiently owing to the large compressibility of the microbubble gas core. When injected intravenously they can be used as a blood pool agent to quantify the perfusion of organs[1]. Microbubbles generate also harmonics of the driving ultrasound field[33] and these nonlinear bubble echoes further boost the ultrasound contrast over the linear tissue echoes. Moreover, recently the use of targeted microbubbles has gained interest for use in molecular imaging[3] and drug[91,92] and gene[7,8] delivery with ultrasound.

The microbubbles resonate to the driving ultrasound field and the bubble echo amplitude is governed by a strong coupling between the microbubble size and the frequency of the ultrasound field through the eigenfrequency of the bubble[39]. Commercially available contrast agents contain microbubble suspensions with a relatively wide size distribution with bubble radii ranging from 1 to 10 μm. Medical ultrasound transducers operate at a single frequency that is dictated by the design of the ultrasound transducer. As a consequence, only a small fraction of the contrast agent resonates to the driving ultrasound field. The sensitivity can be improved using monodisperse bubbles of a size that is resonant to the ultrasound driving frequency. Moreover, by using a monodisperse bubble population a high degree of control can be assured in therapeutic applications with microbubbles. Including local drug delivery and sonoporation[144], i.e. the controlled formation of pores in cells with microbubbles and ultrasound. Both are highly sensitive to the amplitude at which the bubbles oscillate. Large amplitudes will irreversibly damage the cell membrane. Low amplitude oscillations will be unable to porate the cell. Monodispersity is also essential in optimizing the local delivery efficiency of therapeutic drugs incorporated or loaded on the microbubble shell[133]. Finally, advanced imaging techniques that exploit the non-linear response of the microbubbles would benefit greatly from a narrow-size bubble population for its stronger harmonic response.

Monodisperse bubble populations can be obtained by filtering and sorting of a polydisperse agent[61,83,85,88]. Another approach is to readily produce monodisperse bubbles in a flow-focusing device, a proven versatile tool for the highly controlled production of monodisperse bubbles[60,61]. In a flow focusing device a gas thread is focused by two perpendicular flows through a narrow orifice where the gas thread pinches off to release monodisperse bubbles[62,63]. Surfactants are added to the co-flows to stabilize the formed

bubbles against coalescence and dissolution. Using simple short chain surfactants, with low molecular interaction forces, and therefore a relatively high critical micelle concentration (CMC) and high aqueous solubility, flow focusing methods were shown to be able to produce bubbles up to a rate of 1 million bubbles per second[145]. However, the coating process of the gas interface is shown to be less efficient for the use of biocompatible phospholipids[65]. Due to the large hydrophilic tails, the CMC of phospholipids is relatively low, thus in an aqueous solution they self-assemble into micelles and liposomes. The large intermolecular forces present between lipid molecules in aggregates hinder their adsorption to the bubble gas-liquid interface. Standard UCA preparation techniques, i.e. sonication and mechanical agitation, operate at high shear forces to disrupt the micelles and liposomes and promote their adsorption to the gas-liquid interface[57,146]. With the only region of substantial shear in a flow-focusing device being the nozzle, it is suggested[147] that the adsorption of the phospholipids is confined to the nozzle region and that higher shear rates may promote the adsorption of lipids through the more efficient disruption of lipid aggregates.

Once a bubble is formed, gas diffuses out of the bubble due to the Laplace overpressure within the bubble resulting from a finite surface tension of the gas-liquid interface[64,66,146]. Dissolution of the bubble leads to a compression of the lipid monolayer until it reaches a high packing density with a surface pressure close to the surface tension of water. This then cancels the overpressure within the bubble and removes the mechanism behind pressure driven gas diffusion. The solid-like shell around the bubble has viscoelastic properties, i.e. a shell elasticity and a shell viscosity that dramatically change the resonance behaviour of the bubble. The resonance frequency increases due to the increased stiffness of the shell and the damping increases due to the shell viscous dissipation. High-speed imaging performed on single bubbles can be employed as a function of frequency and pressure to obtain the shell parameters of single bubbles[76,80]. The effective viscoelastic shell parameters of bubbles in a suspension can be obtained by attenuation measurements[74,129,130]. Typically, the overlap of the resonance curves of bubbles of a different size results in a broadband frequency response of such a bubble cloud, see also Chapter 5. Therefore, the characterization of viscoelastic shell parameters can only be obtained from a narrow bubble size distribution.

The medical application of monodisperse bubbles produced in a flow-focusing device puts some stringent demands on the flow-focusing technology. First, high production rates are necessary, in the order of 10^5 - 10^6 bubbles per second, to produce bubble suspensions with clinically relevant

bubble number, within a time frame of minutes. At these high production rates, the dynamics of the coating process has to be fast enough, in the order of tens of nanoseconds, to stabilize the bubbles against coalescence. Second, the bubbles must keep their monodispersity over a time frame in the order of one hour to cover the full production time and subsequent administration of a single injection dose. Moreover, during administration, the bubbles have to withstand the injection-overpressure[148]. Third, after injection the bubbles need to be stable upon acoustic excitation to produce contrast during multiple insonations.

Here, we characterize the production rate and the long term stability of microbubbles produced in a flow-focusing device. The effect of the shear rate on the coating characteristics is studied through the size-stability of the produced bubbles. The nonlinear acoustic response of the bubbles and the stability of the nonlinear response after multiple insonations is obtained from frequency dependent attenuation measurements over a range of acoustic pressures. The experiments are supported by modeled attenuation curves obtained by integration over the modeled nonlinear acoustic response of all bubbles in the transmit beam of the acoustic characterization setup. We finish with a discussion and with the conclusions.

6.2 Materials and methods

6.2.1 Phospholipid formulation

A Definity-like lipid mixture was used containing DPPC, DPPA and DSPE-mPEG5000 in a 80:10:10 molar weight ratio. Lipids dissolved in chloroform (Avanti Polar Lipids, Alabaster, Al, USA) were mixed, and dried on the wall of a glass vial under a stream of nitrogen gas and further dried overnight at a low ambient pressure. The lipid film was rehydrated in a 60°C mixture of water (Milli-Q, Millipore Corporation, Billerica, MA, USA), propylene glycol, and glycerol mixed in a 80:10:10 volume ratio to a total lipid concentration of 10 mg/mL. Subsequently, the lipid solution was sonicated in a water bath at 60°C for 30 minutes and stored at 4°C. Prior to all experiments the lipid solution was sonicated by a tip sonicator for 1 minute, degassed, and saturated with perfluorobutane gas.

6.2.2 Chip fabrication

The molds for the polydimethylsiloxane (PDMS) chips were fabricated using standard soft lithography techniques[106]. PDMS was mixed in the standard 1 : 10 ratio, degassed, poured over the mold and cured at 65°C for one hour,

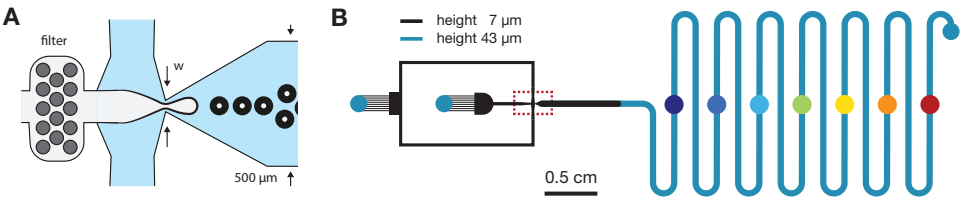

Figure 6.1: A) Flow focusing geometry with an expanding 7 µm nozzle. The width of the outlet channel is 500 µm. B) The flow focusing geometry feeds a serpentine channel to characterize the bubble stability over the first minute after their formation.

then cut to size. Fluidic ports were punched through the PDMS before the channels were sealed by bonding them to a microscope slide using a plasma cleaner (Harrick Plasma, Model PDC-002, Ithaca, NY, USA). Teflon tubing (PEEK, Upchurch) was connected to the inlet channels through which gas and liquid were supplied. The channels were filled with water (Milli-Q, Millipore Corporation, Billerica, MA, USA) immediately after bonding to maintain their hydrophilicity.

6.2.3 Imaging setup

The imaging system used in the presented experiments consisted of an inverted microscope (Nikon Instruments, Eclipse TE2000-U) equipped with a two objectives (20× and 60× magnification, Nikon Instruments, Plan Fluor ELWD) and an additional 1.5× magnification lens. Two cameras were connected to the microscope: a CCD camera (Lumenera, LM165M) with a pixelsize of 6.45 µm and a high-speed camera (Photron SA1.1) with 20.0 µm pixel size. The recordings were processed with an automated image analysis algorithm programmed in MATLAB to obtain the sizes of the bubbles from the inflection points of their intensity profiles[85].

6.2.4 Bubble production

Microbubbles were produced in a flow-focusing device with an expanding nozzle geometry[149] (Fig. 6.1A). The outlet channel was 500 µm in width. The width of the nozzle was 7 µm and, to prevent it from clogging, on-chip filters were incorporated into the design (Fig. 6.1A). A serpentine channel with a total length of 15 cm was added downstream of the flow-focusing device to monitor the bubble stability during the first minute after production, see Fig. 6.1B. The channel height of the flow focusing device was 13.6 µm

and the channel height of the serpentine channel was 43 μm to decrease the pressure drop over the outlet channel and to increase the retention time of the bubbles in the channel.

Bubbles were produced with pressurized perfluorobutane gas (F2 Chemicals Ltd.). The gas pressure was 1.08 bar and it was controled by a pressure regulator (Omega, PRG101-25) connected to a pressure sensor (Omega, DPG1000B-30G). The flow rate of the phospholipid solution was controlled using a high-precision syringe pump (Harvard Apparatus, PHD 2000, Holliston, MA, USA) and it was 15 μL/min. The bubble size distribution in the serpentine channel was measured optically at seven locations marked by the colored dots in Fig. 6.1B. At each position 100 frames were captured with a spatial resolution of 0.22 μm/pixel.

The size stability of the bubbles after the first minute after formation is measured by transferring a drop of the bubble suspension from the chip outlet to a flow cell (IBIDI μ-slide). The bubble suspension was diluted in the flow cell by flushing water (Milli-Q, Millipore Corporation, Billerica, MA, USA) through the channel until the bubble concentration was such that individual bubbles were visible. Dissolution curves were obtained from images taken at a 60 s time interval over a period of 1.5 hours.

6.2.5 Nozzle design and flow rates

The relation between nozzle shear rate and the size stability of the bubbles was measured using a range of flow rates at a constant gas pressure to produce bubbles of different sizes. Flow focusing devices with nozzle sizes of 3, 5, and 7 μm were used to produce bubbles in the same size range at different co-flow rates, or shear rates. Flow rates ranging from 3 μL/min up to 34 μL/min were used with perfluorobutane gas pressures of 1.08 bar and 1.2 bar. The role of the filling gas was measured by the production of air bubbles from a 5 μm orifice at a gas pressure of 1.08 bar. No serpentine channel was incorporated here, the outlet channel was a straight channel, 500 μm in width, with a total length of 1.5 cm. The channel height was constant throughout the device: 13.6 μm.

After setting the flow rate, the bubble production was left to stabilize for at least 5 minutes. Then, the size of the bubbles produced, as well as the production rate, was measured by means of optical recordings at a frame rate of 225 kfps and a spatial resolution of 0.67 μm/pixel.

The bubble suspension produced at the outlet port of the chip was pipetted, diluted in a 80:10:10 v% water, propylene glycol, and glycerol mixture (GPW), and transferred to a flow cell (IBIDI μ-slide, Martinsried, Germany) to measure the size distribution of the bubbles over time. During a

2 hour time period the size distribution was measured every 15 minutes by acquiring images with a CCD camera (Lumenera, LM165M) at 100 different locations in the flow cell resulting in a total bubble count of at least 1500 per size distribution. The spatial resolution was 215 nm/pixel or 108 nm/pixel, and it was chosen such that the minimum area per bubble consisted of at least 60 pixels.

6.2.6 Acoustic characterization setup

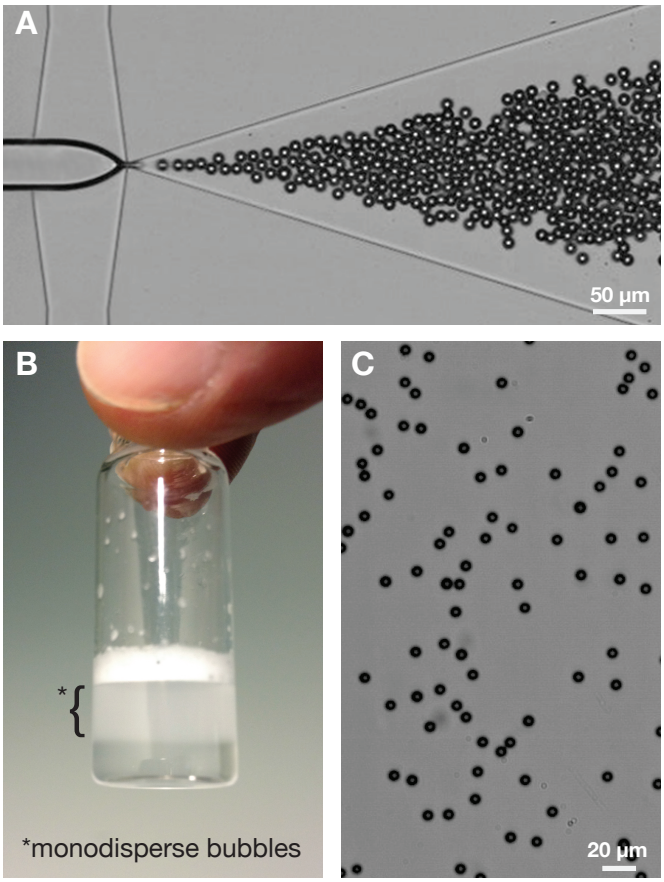

Figure 6.2: (A) Acoustically characterized bubbles are produced in a flow focusing geometry with a 5 µm nozzle. The produced bubble suspension is diluted in 2 mL GPW solution and set to rest for stabilization. B) After 1.5 hours the vial is gently mixed and set to rest for another 10 minutes. An opaque layer of stabilized monodisperse bubbles appears below the foam layer (C).

Bubbles with an initial radius of 6.9 μm were produced in a flow-focusing device with a 5 μm nozzle and a straight 1.5 cm long and 500 μm wide outlet channel (Fig. 6.2A). The height of the microfluidic channel was 13.6 μm throughout. The gas pressure was 1.08 bar and the liquid flow rate was 13 μL/min. After 5 minutes, a droplet of the bubble suspension formed at the outlet was pipetted and transferred to a 4 mL vial containing 2 mL of the standard GPW mixture. The bubble suspension was gently mixed and set to rest. After 1.5 hours the bubble suspension was again mixed gently and set to rest for another 10 minutes. From the opaque layer below the foam on top (Fig. 6.2B) 50 μL was pipetted of which approximately 10 μL was transferred to the sample holder of the acoustic characterization setup containing air saturated water (Milli-Q, Millipore Corporation, Billerica, MA, USA). The remaining solution was injected into a flow cell (IBIDI μ-slide, Martinsried, Germany) for optical sizing (Fig. 6.2C).

Attenuation curves were measured as described in detail in Ch. 4. In short, we use two co-aligned transducers over a frequency range from 0.7 MHz to 5.5 MHz with 0.1 MHz steps at acoustic pressures ranging from 5 kPa to 70 kPa in steps of 2.5 kPa in a water tank at room temperature. The transmission transducer had a center frequency of 2.25 MHz, a focal distance of 1″ and an aperture of 19 mm (A305S, Panametrics-NDT). The receiving transducer with a 5 MHz center frequency, 19 mm aperture and 1″ focal distance (C308, Panametrics-NDT) was mounted on x-y-z translation stage to aid the alignment. The bubble suspension was confined by a 1.5 × 1.5 cm^2 container made of acoustically transparent polystyrene membrane (Opticell). The cross section of the bubble container enclosed the acoustic focus of the transmit transducer and a magnetic stirrer bar to ensure a homogeneous bubble suspension. The bubbles were insonified by a 16-cycle narrowband ultrasound pulse with a Gaussian taperering over 4 cycles at each side of the pulse. The attenuation was calculated from a single pulse for each frequency and for each acoustic pressure. The total amount of 1323 acoustic pulses was uploaded to a programmable arbitrary waveform generator (8026, Tabor Electronics) before the measurement. A pulser receiver (BNC555, Berkeley Nucleonics Corporation) was used to produce 1323 TTL pulses at a rate of 50 Hz to trigger the waveform generator and the oscilloscope. The transducer driving pulse was attenuated by 30 dB and its amplitude was amplified by a 50 dB linear power amplifier (350L, E&I). The time traces were recorded by a digital storage oscilloscope (TDS5034B, Tektronix) operated in sequence mode. A complete scan was performed within 30 seconds. The frequency-dependent pressure amplitude of the transmitting transducer was measured using a calibrated 0.2 mm

tip hydrophone (Precision Acoustics) and the driving voltage was compensated for the frequency dependent transducer response to ensure a constant acoustic pressure during the frequency scan.

6.3 Results

6.3.1 Size stability

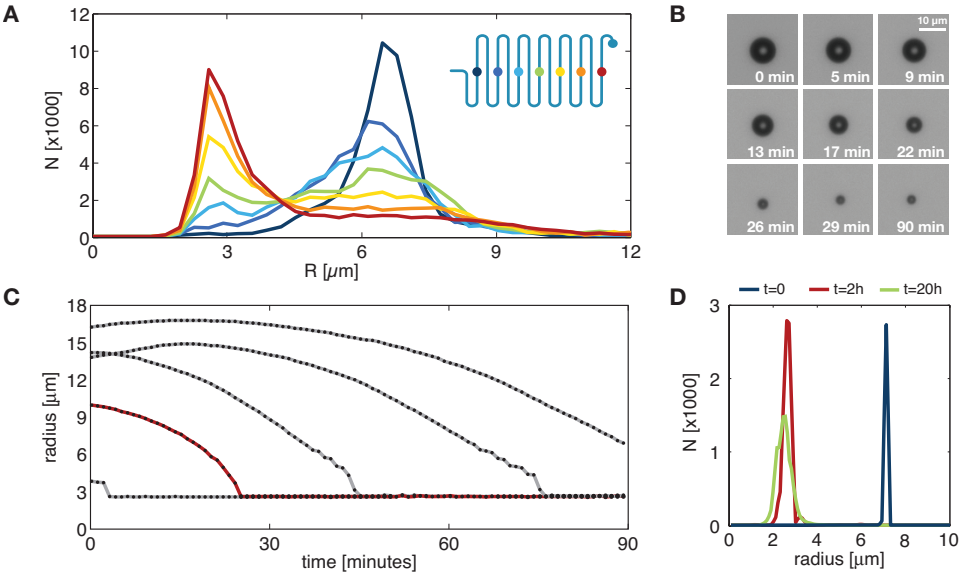

Figure 6.3: A) Optically measured size distributions in the serpentine channel. The color of the plots corresponds to the color of the circle mark on the serpentine channel in Fig. 6.1B. B) Dissolution of a bubble with a radius of 10.5 μm that was initially produced at a radius of 7.1 μm and increased in size during the first minute after its formation. C) Dissolution curves of bubbles initially produced at a radius of 7.1 μm, the bubbles increased in size during the first minute after production but dissolved all to their stable radius of 2.8 μm. D) The size distribution of the bubble population at its formation (blue), after two hours (red) and after 20 hours (red).

Figure 6.3A shows the size distributions at seven different locations in the serpentine channel. The color of the size distribution plot corresponds to the color of the circle mark on the serpentine channel (inset in Fig. 6.3A) and it defines the location where the size distribution was measured optically. The total travel time of the bubbles through the serpentine channel was approximately 1 minute. The bubbles are produced at a radius of 7.1 μm

$\pm$ 0.2 µm and at a rate of 10^5 bubbles per second; both were measured directly in the orifice, see $t = 0$ in Fig. 6.3D. The size distributions show that the produced bubble suspension already becomes polydisperse at the second measurement point, i.e. after 10 seconds. Then, by reaching the end of the serpentine channel the majority of the bubbles has dissolved to a 2.8 µm radius.

The size stability of the bubble suspension at the exit of the serpentine channel was further characterized over time in a flow cell. Figure 6.3B shows the dissolution of a 10.5 µm bubble that was initially formed at a radius of 7.1 µm. The bubble dissolves also to a final radius of 2.8 µm, where it remains stable for the rest of the characterization time window of 1.5 hrs. (Fig. 6.3C red curve). Figure 6.3C shows that bubbles can grow to a size as much as two times the initial bubble size and that they also dissolve to the stable final bubble radius of 2.8 µm. Figure 6.3D shows the size distribution of the bubbles directly after their production in the flow-focusing device, after 1.5 hours and after 20 hours. Please note that after 2 hours of ageing all bubbles have dissolved to a radius that is 2.5 times smaller than their initial radius. Thus, the total amount of phospholipid molecules on the bubble surface does not change after the formation of the bubble as adsorption or shedding of the shell material during the growth or shrinkage of a bubble would have resulted in a polydisperse bubble suspension.

In the pioneering work by Hettiarachchi *et al.*[65], and more recently by Shih and coworkers[64], it was shown that the polydispersity of bubbles produced in a flow focusing device increases within minutes. It was also shown that the monodispersity of the produced bubbles could be maintained[66] by increasing the interbubble spacing to decrease gas exchange effects between neighbouring bubbles through Ostwald ripening. This, however, goes at the expense of the production rate. Upon dissolution, largely spaced bubbles lose their gas to the surrounding liquid instead of to each other and therefore, their monodispersity remains high. However, here we now show for our lipid formulation that the short term exchange of gas in a high concentration bubble suspension, first indeed results in a polydisperse bubble size distribution, but that the long term stability is governed by the total amount of lipids on the surface of the bubbles upon formation. The observed long term stability effect that in the end leads to a highly monodisperse size distribution may have been left unnoticed in previous work as the time scale is on the order of one hour.

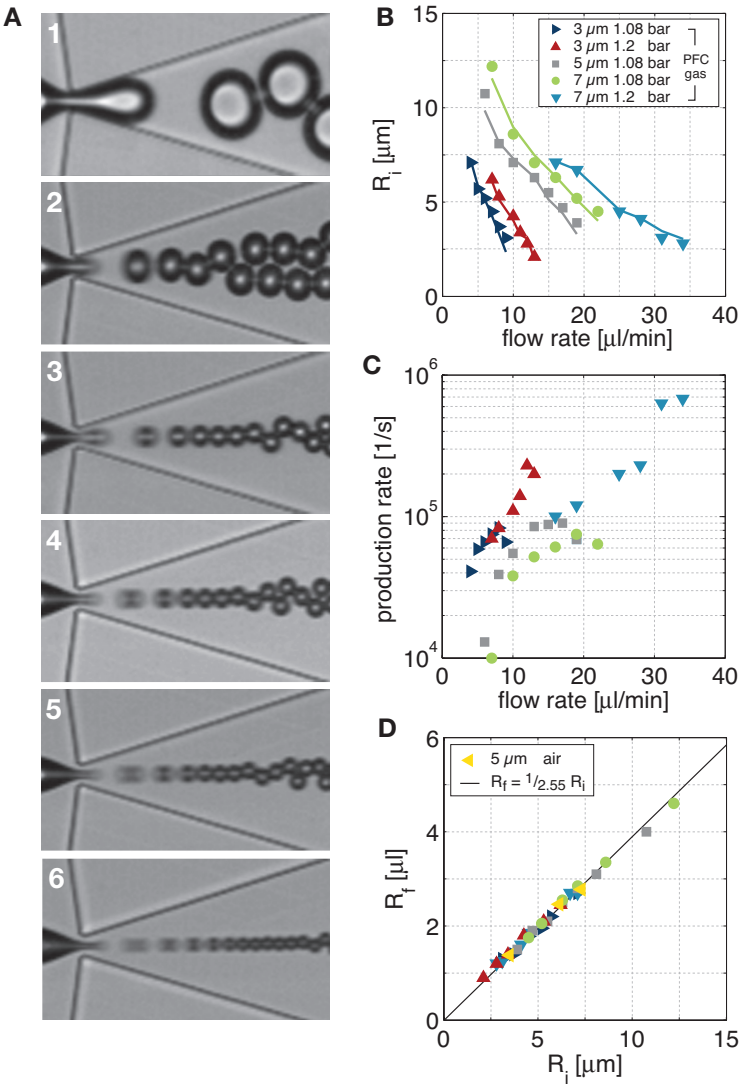

Figure 6.4: A1-A6) Monodisperse bubble formation from a 7 μm nozzle at co-flow rates of 7, 19, 25, 28, 31, and 34 μL/min for figures A-1 to A-6 at a constant gas pressure. Bubbles are formed in the dripping and in the jetting regime. B) Formed initial bubble radius R_i as a function of the co-flow rate for different nozzle sizes and gas pressures. C) The bubble production rates as a function of the co-flow rate. D) The final bubble radius R_f as a function of the initial bubble radius R_i for bubbles filled with perfluorobutane and for bubbles filled with air. All bubbles dissolve to a final radius 2.55 times smaller than their initial radius.

6.3.2 Shear rate dependency

Figures 6.4A-1 to A-6 show high-speed recordings of a 7 μm nozzle flow focusing device operated at flow rates of 7, 19, 25, 28, 31, and 34 μL/min. The gas pressure in Fig. 6.4A-1 was 1.08 bar and in Figs. 6.4A-2 to 6.4A-6 it was 1.20 bar. Bubbles are produced both in the dripping regime and in the jetting regime[145]. At the lower liquid flow rates, the gas thread drips from the orifice by blocking the liquid flow within the nozzle. At the higher flow rates the gas thread forms a jet that breaks up into bubbles downstream from the orifice. The initial bubble radius R_i is plotted in Fig. 6.4B as a function of the co-flow rate for different nozzle sizes and gas pressure combinations. The spherical radius of bubbles with diameters larger than the channel height were calculated from the equivalent volume of a disk and a circle that fit in the cross-section of a compressed bubble as viewed from the side.

The bubble production rate as a function of the flow rate for the different nozzle sizes and gas pressures is presented in Fig. 6.4C. Bubbles are produced at a rate ranging from 10^4 to almost 10^6 bubbles per second and no coalescence was observed in the outlet channel and directly at the nozzle, as can be readily seen from Figs. 6.4A1-A-6.

The scaling law for bubble formation in a planar flow-focusing device at high Reynolds numbers is given by[60]: $d_b/w \propto (Q_{gas}/Q_{liquid})^{2/5}$ for $Q_{gas} < Q_{liquid}$. d_b is the apparent diameter of the bubble (diameter in top-view), w is the nozzle width, and Q_{gas} and Q_{liquid} are the gas and liquid flow-rates, respectively. In our experiment the gas pressure was kept constant and therefore the gas flow rate changes with a changing liquid flow-rate. The gas flow rates were calculated directly from the measured bubble size and the measured production rate. The solid lines in Fig. 6.4B show that the formation of the bubbles follows the scaling law.

The produced bubbles were left to stabilize in a flow cell. The amount of gas exchange for bubbles to stabilize scales with the volume of the bubble and with the pressure gradient across the surface or Laplace pressure which decreases with $1/R$[37]. As a result, the stability window for the smallest bubbles was on the order of minutes while the larger bubbles reached their final size only after 2 hours. The optically measured final bubble radius is plotted in Fig. 6.4D as a function of the initial bubble radius. A unique shear rate independent relation is found between the initial bubble R_i size and the final bubble size R_f where the final bubble size is *always* 2.55 times smaller than the initial bubble size. Thus, the surface area of a freshly produced bubble decreases by a factor 6.6 before the bubble reaches its final size. It was reported that perfluorocarbon gasses increase the rate of

lipid adsorption on the gas-liquid interface with respect to air as a filling gas[150,151]. Here, we do not see such an effect of the filling gas, air bubbles follow exactly the same trend, see Fig. 6.4D.

Overpressures between 4 and 140 kPa are applied to drive the flow through the microfluidic channel. Consequently, bubbles expand in volume from 1 % to 34 % when they translate downstream from the nozzle to the atmospheric pressure conditions at the chip outlet. Bubbles produced at the same size, at different flow rates and at different overpressures, all dissolve to the same stable bubble size which is one more additional proof that the bubbles do not adsorb, or shed lipids after their formation.

In the dripping regime, at low flow rates, the gas thread is in contact with the top and bottom wall of the channel and as a result also the formed bubbles (Fig. 6.4A-1). In the jetting regime, the gas thread is fully surrounded by a flow of high shear and it breaks up at a position downstream from the nozzle (Fig. 6.4A-6). Since a shear rate and production mechanism independent dissolution ratio is found, it is expected that the complete gas thread, or at least the tip of the gas thread that is subject to high shear flow, is covered with a saturated surface concentration of the phospholipids. Thus, it is hypothesized that the lipid adsorption process has reached its saturation surface concentration *before* the bubble pinches off and before the gas thread even reaches the nozzle. Interestingly, this saturation concentration is already reached at the lowest flow rates used here. It was shown by Lozano and Longo[152] that surface pressure-area isotherms of a mixture of a primary lipid and an emulsifier lipid show very different behavior for different mixing ratios. Therefore, it would be interesting to obtain the dissolution ratio for different primary lipid to emulsifier ratios to investigate the role of the saturation concentration. This will be the subject of a future study.

For a bubble to keep its size over an hour time scale, the surface tension needs to be zero or very close to zero to cancel the Laplace overpressure in the bubble. The hydrophobic heads of the lipid molecules attract each other and the hydrophobic tails repel due to chain oscillations[153]. Moreover, once lipids are adsorbed micelles and liposomes are repelled by steric repulsion. It is therefore unlikely that the phospholipid molecules can be adsorbed such that they form a readily compressed monolayer with a surface pressure high enough to cancel the Laplace pressure. The compression of DPPC monolayers was subject of extensive study since DPPC is one of the most important pulmonary surfactants, see e.g. Yu *et al.*[154]. Langmuir trough surface pressure-area isotherms show that the surface pressure of a DPPC monolayer reaches the surface tension of water when the monolayer is compressed

to the condensed phase[153,155]. To the best of the authors' knowledge, no pressure-area isotherms are available for the exact phospholipid/emulsifier mixture used here. However, it is known that the molecules in lipid aggregates are in the liquid state[156] and Lozano and Longo[152] showed that the surface area per molecule of lipids right at the start of the phase were there is a coexistence of lipids in the liquid-expanded phase and in the liquid-condensed phase in a monolayer comprised of a 9:1 molar weight ratio mixture of a DPPC and DSPE-PEG_{2000} is 1.2-1.6 nm^2. Interestingly, when the monolayer is compressed to reach an area per molecule that is 6-8 times smaller, the Langmuir trough surface pressure-area isoterm shows that the lipid monolayer has just reached the surface tension of water. Thus, lipid molecules are adsorbed to the gas-liquid interface of a bubble in the liquid state. Subsequently, they form a disordered monolayer that can cancel the Laplace overpressure in the bubble only when its area is decreased by a factor 6-8, which is in very good agreement with the value of 6.6 that we found in our experimental observations.

6.3.3 Acoustic characterization and acoustic stability

A sample with a microbubble suspension with the size distribution shown in the inset of Fig. 6.5A is characterized acoustically by attenuation measurements. Figure 6.5A shows the first series of measurements where 27 attenuation curves are measured for increasing peak negative pressures ranging from 5 to 70 kPa in steps of 2.5 kPa. The frequency scan ranges from 0.7 MHz to 5.5 MHz with a 100 kHz step size. The measurement series was repeated 10 times on the very same bubble sample to measure the influence of repeated insonations on the response of the bubbles, and as such, its acoustic stability. The time between successive measurements was approximately 2 minutes. Figure 6.5B shows the second series and Fig. 6.5C shows the eighth series. Please note that the frequency of maximum response at the lowest acoustic pressures increases with the number of repetitions. The frequency of maximum response at a driving pressure of 5 kPa is plotted as a function of the series number in Fig. 6.5D (blue dots) where it is seen to increase from a frequency of 1.8 MHz to 3.6 MHz. Figure 6.5D also shows that the frequency of maximum response at 70 kPa remains constant for the whole series at a frequency of 1.4 MHz. This indicates that the mean bubble size is unchanged during the multiple insonations since the resonance frequency of a bubble insonified at these relatively high acoustic pressures approaches that of a free, uncoated bubble[2]. Note the absolute scale in Figs. 6.5A-C; the attenuation at the frequency of maximum response at 70 kPa decreases from 5.3 dB/cm to 2.0 dB/cm over the 10 repeated mea-

surements, see the discussion in the final paragraph of the Results.

The increase in resonance frequency at low acoustic driving pressures may be explained both from an increase in shell elasticity or from an increase in the initial surface tension[41,75]. To quantify the change in the shell parameters with the number of insonations we model the pressure-dependent attenuation with the model described in Chapter 4 for the size distribution shown in Fig. 6.5A. The properties of the water were set to $\sigma = 0.072$ N/m for the surface tension and $\rho_l = 1000$ kg/m^3 for the density. The polytropic gas constant was set to unity, $\kappa = 1$. Figure 6.5D shows the modeled attenuation curves for the 27 driving pressures employed during the measurements. The shell stiffness χ was 2.5 N/m for all bubbles in the size distribution and the initial surface tension $\sigma(R_0)$ was fixed at 0.001 N/m. The shell viscosity κ_s was set to $6 \cdot 10^{-9}$ kg/s. To investigate the effect of an increasing initial surface tension we plot the modeled frequency of maximum response f_{MR} with increasing $\sigma(R_0)$ over a typical range of $\sigma(R_0)$ from 0.001 to 0.03 N/m at a driving pressure of 5 kPa, see Fig. 6.5H. A rather abrupt change of the frequency of maximum response is observed in our model, which is not in agreement with the monotonous increase of the frequency of maximum response, as observed in the measurements of Fig. 6.5D.

Figure 6.5F presents the modeled attenuation curves for bubbles with a shell stiffness of 0.8 N/m and an initial surface tension of 0.020 N/m, and Fig. 6.5G presents that for bubbles with a shell stiffness of 2.5 N/m. From the quantitative agreement of the modeled attenuation curves with the second and eighth measurement series, it can be seen that the increasing frequency of maximum response at low driving pressures is mainly originating from an increasing shell stiffness. The increase in shell stiffness at low driving pressures can be calculated from the linearized Rayleigh-Plesset equation[41] and it is found to increase from 0.8 N/m to 2.5 N/m during the repeated attenuation measurements in a similar trend as observed in Fig. 6.5D.

Lipid shedding[133,157], has very often been suggested to occur during multiple insonations. Typically, it also leads to a decrease in bubble size which is not observed here. The lipid shell consists of different types of phospholipid molecules with different aqueous solubilities expressed by their CMCs. It can be calculated that the ratio of the residence times of two different phospholipid molecules in an aggregate, as found on the bubble interface, is simply the ratio of their CMSs[156]. From the CMC ratio of DPPC to DSPE-PEG$_{5000}$ it follows that the residence time of a DPPC molecule in a lipid aggregate is 30,000 times longer than that of a DSPE-PEG$_{5000}$ molecule[158,159]. The attractive van der Waals forces between lipid molecules in the solid-like

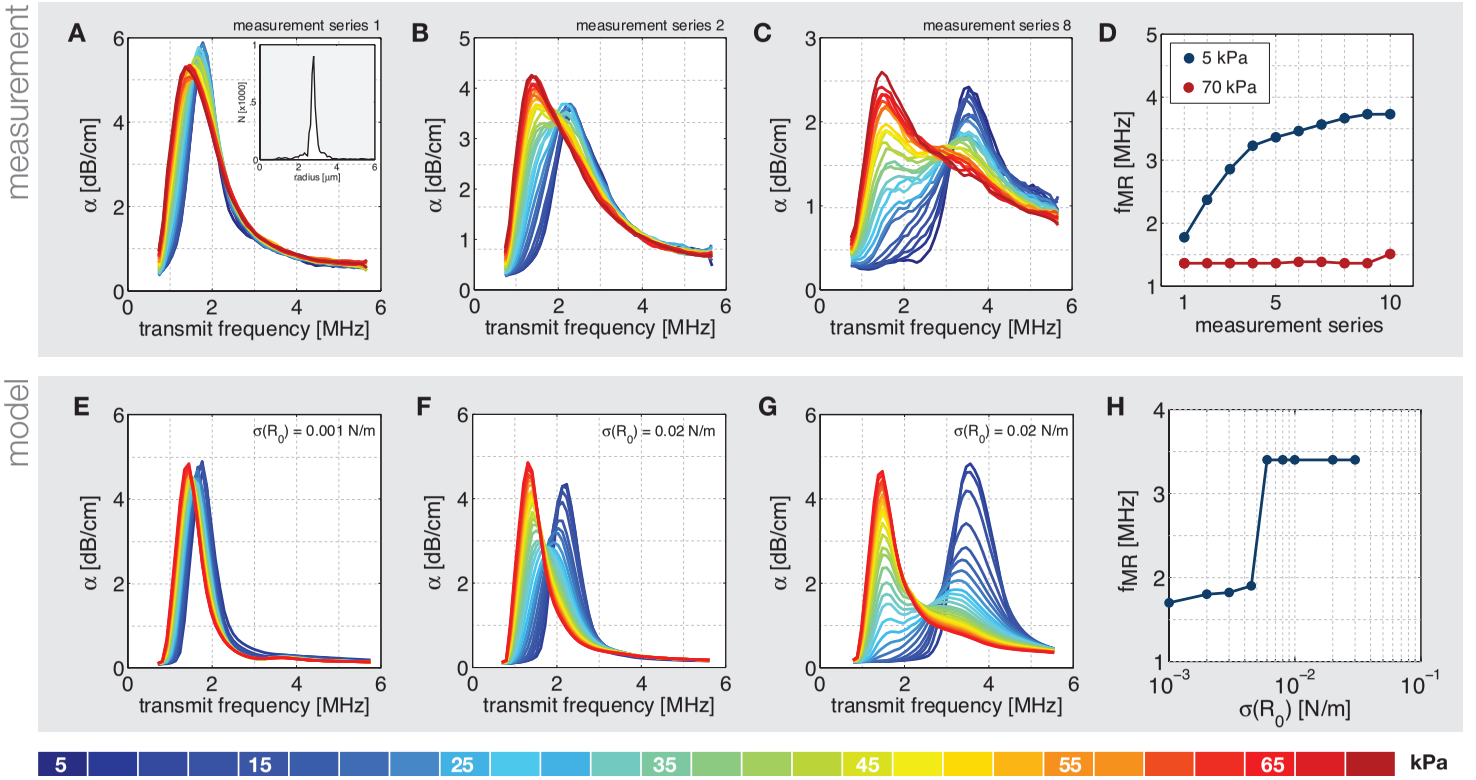

Figure 6.5: A) Measured attenuation curves as a function of the insonation frequency at peak negative acoustic pressures of 5 to 70 kPa. The measurement series was repeated 10 times on the very same bubble sample. B) Shows the second measurement series and (C) shows the 8th measurement series. D) Measured frequency of maximum response f_{max} at a driving pressure of 5 kPa and 70 kPa over the measurement series. E) Modeled attenuation curves for bubbles with an initial surface tension of 0.001 N/m and a shell elasticity of 2.5 N/m. F) Modeled attenuation curves for bubbles with an initial surface tension of 0.02 N/m and a shell elasticity of 0.8 N/m. G) Modeled attenuation curves for bubbles with an initial surface tension of 0.02 N/m and a shell elasticity of 2.5 N/m. I) Modeled frequency of maximum response at a driving pressure of 5 kPa as a function of the initial surface tension $\sigma(R_0)$.

shell of a stable microbubble are large due to the high packing fraction of the lipids within the shell. Consequently, at rest the emulsifier molecules are retained in the shell and this explains the long shelf life of microbubbles in solution while the shell composition is unchanged. When the bubble oscillates at sufficiently high radial amplitude the shell can rupture[41], increasing the free energy per molecule. This results in a higher probability of the lipid molecules to be expelled from the monolayer and, as a result, the bubbles lose emulsifier molecules while the primary lipid molecules are retained in the shell. Since only 1 in 70 lipid molecules is an emulsifier molecule, the loss of DSPE-PEG_{5000} molecules from the bubble shell is not expected to change the bubble size. However, it may have a direct effect on the acoustic property of the bubble. Lozano and Longo[152] showed that the derivative of the surface pressure-area isotherm, i.e. the monolayer elasticity, of a DPPC-DSPE-PEG_{2000} monolayer increases with decreasing DSPE-PEG_{2000} fraction. Thus, the loss of emulsifier molecules results in a gradually increasing shell stiffness. The size of the hydrophilic brush of the DSPE-PEG_{5000} molecules used in this study is about two times larger than that of the DSPE-PEG_{2000} molecules. It is therefore expected to have and even larger effect on the change of the monolayer elasticity.

The increase in shell stiffness upon multiple insonations has some important consequences. First of all, the attenuation curves become more broadband. This is a direct result of the nonlinear bubble behavior and the non-uniformity of the transmit beam. The resonance frequency of the bubbles at the acoustic focus is near 1.4 MHz, due to the elevated pressure in the focus, whereas bubbles away from the focus resonate at higher frequencies, due to the lower pressures. Secondly, the decreased uniformity in the acoustic response of the bubbles in the sample cell over which the attenuation is measured decreases the absolute attenuation. And finally, another consequence of the non-uniform transmit field is that there arises a dispersity in shell elasticities in the bubble population since not all bubbles in the suspension are exposed to the same driving pressures. Bubbles driven at larger amplitudes of oscillation will lose emulsifier molecules more easily. Nevertheless, the measured response is in quantitative agreement with the modeled attenuation curves and it reveals clearly the average change in the effective shell parameters of the bubble cloud due to multiple insonations.

The final size distribution of the stable bubbles after 2 hours, Fig. 6.3D, has a mean bubble radius of 2.8 μm and its standard deviation is 0.2 μm. The size distribution of the corresponding freshly produced bubbles, also shown in Fig. 6.3D, had a mean bubble radius of 7.1 μm and a standard deviation of 0.1 μm. The larger standard deviation of the final stable bubbles

may have resulted from a dispersity in the lipid surface concentration on the freshly produced bubbles during the formation. Two bubbles produced at the very same size, having even a tiny difference in the phospholipid packing density, will dissolve to a slightly different final bubble size. Future experiments, e.g. using a recently reported microfluidic bubble force spectroscopy method[85] or by using fluorescent lifetime imaging[160], can confirm and quantify the measured difference in surface surfactant concentration from bubble to bubble right after the formation of the bubbles.

6.4 Conclusions

Phospholipid coated bubbles produced in a flow focusing device with a DPPC-DPPA-DSPE-PEG$_{5000}$ lipid formulation are stable once they have dissolved to a radius that is 2.55 times smaller than their initial radius. The amount of phospholipids on the bubble surface does not change after bubble formation, not when the bubble dissolves, nor when it expands volumetrically. The size stability is independent of the flow-focusing nozzle shear rate and production rate. It was shown that monodisperse bubbles can be produced with a rate up to 1 million bubbles per second from a single nozzle. Attenuation measurements together with modeled attenuation curves in which the full non-linear bubble response was included revealed that the shell stiffness of the bubbles increased from 0.8 N/m to 2.5 N/m with increasing number of insonations due to the loss of emulsifier molecules.

Acknowledgements

We thank Elena Castro-Hernandez for the constructive discussions about microfluidics. We also warmly thank Heleen Dewitte, Tom van Rooij, and Klazina Kooijman for the stimulating discussions about phospholipid formulations and the preparation thereof. Furthermore, we acknowledge Gert-Wim Bruggert, Martin Bos, and Bas Benschop for their skilful technical assistance. This work is supported by NanoNextNL, a micro and nanotechnology consortium of the Government of the Netherlands and 130 partners.

7

Resonant vaporization of perfluorocarbon phase change agents with surface acoustic waves

Phase change agents consist of low boiling point perfluorocarbon droplets that can be triggered by ultrasound to phase-change from the metastable liquid state to the thermodynamically stable gas state, a process termed acoustic droplet vaporization (ADV). The potential of ADV for imaging and therapy is promising, however the acoustic pressures required to trigger the vaporization process are near or even beyond the FDA approved limit for diagnostic ultrasound. Here, we report ADV with high-frequency ultrasound, generated by leaky surface acoustic waves (SAW) generated using interdigitized transducers (IDTs) operating at a frequency of 19.6 MHz and 45.4 MHz. A theoretical model was developed describing the acoustic coupling between the aqueous medium and the phase-change droplet and it revealed the existence of a resonant coupling between the drop size and the ultrasound frequency. Ultra high-speed imaging was employed to visualize the vaporization events and the measurements confirmed the theoretical droplet size-dependent resonance behaviour with very good agreement. The presented results show that it is essential to drive phase change droplets at their resonance frequency for efficient ADV. Furthermore, during a second ultrasound exposure the vaporization of almost all droplets with sizes down to 100 nm is triggered by the presence of precursor bubbles. The resonant droplet vaporization and the phase-change dynamics during multiple ultrasound exposures may have great potential for the future clinical use of phase-change agents.

[1]To be submitted as: T. Segers, G. Lajoinie, M. Versluis, *Resonant vaporization of perfluorocarbon phase change agents with surface acoustic waves* (2015)

7.1 Introduction

Phase change agents are droplets made from a low boiling point liquid, typically a perfluorocarbon (PFC) dispersed in an aqueous phase. The droplets are stabilized by surfactants such as fluorosurfactants[161,162] or by phospholipids[163,164]. While the boiling point of the perfluorcarbon is low (e.g. perfluoropentane, $T_b = 29°C$), the droplets do not spontaneously vaporize *in-vivo* at a temperature of 37°due to the confinement of the PFC to a micron sized sphere[165] that does not present nucleation sites. Moreover, the overpressure within the droplet resulting from the interfacial surface tension increases the boiling point of the PFC for an increased droplet stability. Perfluorocarbons are inert, non-toxic in small quantities and are already clinically used. The shelf life of a PFC droplet emulsion is on the order of months since PFCs are immiscible in water, they have a high molecular weight and a low surface tension[166]. The droplets can also be loaded with drugs, e.g. by using nanoemulsions[167] within the droplet, that are otherwise difficult to bring to the target site. Additionally, droplets injected *in-vivo* are stable for days[168] which makes them highly suitable for biomedical applications.

Exposure of superheated droplets to ultrasound can trigger the phase-change of the droplet from the metastable liquid state to the thermodynamically stable gas state through a volumetric expansion process. This phase transition phenomenon is known as acoustic droplet vaporization (ADV). Upon vaporization, the payload within a droplet is released and the droplet itself is converted into a highly echogenic bubble of similar size as conventional ultrasound contrast agents. Thus, they can be visualized using clinical ultrasound scanners which has a great interest for monitored drug delivery. Recently, it was shown that nanometer sized droplets (≈ 200 nm) may extravasate blood vessels through leaky tumor vasculature[169,170] (EPR effect) and as a result, passively accumulate in tumorous tissue where the controlled release of chemotherapeutic drugs is of greatest interest. Once vaporized, these phase change agents become echogenic and allow for tumor imaging with ultrasound, without the strict limitation of the classic ultrasound agents to the vascular network.

The acoustic pressures required to vaporize the droplets are reported to be in the MPa range[171] with mechanical indices[172] as high as four, well above the FDA-approved limit of MI = 1.9 for diagnostic ultrasound. At low acoustic pressures, the probability of vaporizing a droplet is negligible up to a certain threshold after which the probability increases linearly with the applied acoustic pressure[161,171]. Several groups have reported

the decrease in the acoustic pressure threshold for increasing driving frequencies[161,171,173,174]. Recently, Shpak *et al.*[175] have revealed that droplet vaporization is initiated by focusing of the nonlinear acoustic wave by the spherical droplet due to a mismatch in acoustic impedance between the PFC droplet and the surrounding water. The multiple superharmonics generated during the non-linear propagation of the acoustic wave reach wavelengths on the order of the size of the droplet allowing for a superharmonic focusing effect to occur. The peak negative pressure of the incident wave is typically amplified by a factor 6 for a 10 μm radius droplet and a by factor 2.2 for a 4 μm droplet. Thus, the amplification decreases with a decreasing droplet size.

Human tissue has a nonlinearity parameter B/A up to two times that of water, however, its attenuation coefficient ranges from 100 to 300 times that of water, for blood and tissues, respectively. It therefore becomes much more difficult to generate the harmonics of the driving ultrasound frequency required for the focusing effect to occur *in-vivo* as the attenuation increases exponentially with the frequency. Furthermore, the generation of significant superharmonics intrinsically requires the use of high insonation pressures in order to obtain non-linear propagation, which is one of the main limiting factors of the clinical application of the superharmonic focussing effect. These difficulties regarding the applicability of the focusing mechanism emphasize the need to go from a gentle passive focussing of the ultrasound wave in the droplet, to a resonant mechanism that does not require non-linear propagation but does drive the pressure in the drop below its vaporization threshold in order to vaporize it.

Here, we investigate the vaporization of micrometer-sized droplets by high frequency ultrasound. An interdigitized transducer (IDTs) was employed to generate surface acoustic waves (SAW) on a piezoelectric lithium niobate ($LiNbO_3$) substrate that generates bulk acoustic waves once in contact with a water sample on top of the substrate containing the PFP droplets. IDTs have proven to be a versatile and an efficient tool for the acoustic forcing of microfluidics by ultrasound frequencies ranging from 10 to 500 MHz[176–178]. The use of SAW to investigate acoustic droplet vaporization at high ultrasound frequencies has the advantage over conventional transducers that the droplets are spatially confined within micrometer distance from the position where the bulk ultrasound waves are generated. Therefore, the ultrasound wave will consist purely of a sinusoidal wave at the frequency of the SAW as there is no propagation distance allowing for the wave to become non-linear. The use of SAW is therefore an excellent way to investigate the vaporization of phase change agents at high ultrasound frequencies. In the

present study, we experimentally investigate ADV using IDTs generating high frequency ultrasound, at a frequency of 19.6 MHz and 45.4 MHz. The vaporization events are recorded using ultra-high speed imaging to access the instantaneous size-dependent droplet vaporization. First, a theoretical model is developed describing the acoustic coupling the acoustic wave and the droplet in the aqueous medium. Second, the experimental setup is described. In the Results section the measured size-dependent droplet vaporization is compared to the modeled pressure amplification within the droplet as a function of size. We also investigate droplet vaporization at multiple ultrasound exposures and its efficiency. Finally, the results are discussed to end with our conclusions.

7.2 Theory

Full details of the theoretical analysis describing the resonant coupling between an ultrasound wave and a droplet of a given size are given in a forthcoming paper[179]. Here, we briefly explain the principle idea of the theoretical analysis and present the most important results. The studied physical system is comprised of two liquid media separated by an interface. Medium 1 consists of perfluoropentane (PFP) that forms the droplet with radius R. It has a density ρ_{PFP} and speed of sound c_{PFP}. The surrounding water forms medium 0 and in first approximation it is considered to be of infinite size. Its density is ρ_w and it has a speed of sound c_w.

The dynamical behavior of the PFP droplet can be derived in an analogous way as the derivation of the bubble dynamics equation, a.k.a the Rayleigh-Plesset equation. The main difference here is that, while the gas pressure can be assumed constant in the bubble case, the pressure distribution in the droplet needs to be calculated explicitly. The interest here lies in the fundamental volumetric oscillation mode of the droplets, since it is expected to be of larger amplitude and dominant over the higher-order modes. We therefore consider a purely spherical geometry. Due to the difference in the speed of sound of the PFP ($c_{PFP} = 457.3$ m/s at 20°C) and that of water ($c_w = 1490$ m/s at 20°C), the acoustic wavelength is more than three times shorter in the PFP droplet than it is in the surrounding medium. In the following we therefore also assume the droplet to be small compared to the acoustic wavelength in the water. This assumption is later validated by showing that the resonant droplet size is close to 1/4-th of the wavelength in the PFP. Thus, it is approximately 1/15-th of the acoustic wavelength in water.

With the above assumptions the droplet dynamics can be described us-

ing a set of three equations: the momentum equation, the mass conservation equation and the compressibility equation, all linearized and written in spherical coordinates:

$$\beta \frac{\partial P}{\partial t} = -\frac{2v}{r} - \frac{\partial v}{\partial r}, \tag{7.1}$$

$$\frac{\partial v}{\partial t} = -\frac{1}{\rho_{PFP}} \frac{\partial P}{\partial r}, \tag{7.2}$$

$$\beta \rho_{PFP} P = \rho. \tag{7.3}$$

Combining Eqs. 7.1–7.3 results in the following wave equation:

$$x^2 \frac{\partial^2 v}{\partial x^2} + 2x \frac{\partial v}{\partial x} + v\left(x^2 - 2\right) = 0, \tag{7.4}$$

where the variable $x = k \cdot r$, with $k = \omega/c$ the wavenumber and $\omega = 2\pi f$ the angular frequency with driving frequency f. Equation 7.4 is a spherical Bessel differential equation with index $n = 1$. The two linearly independent solutions to the spherical Bessel differential equation are the spherical Bessel functions j_n and the spherical Neumann functions y_n. Divergence of y_n at $r = 0$ excludes any combination of this solution. Thus, for our simplified case with $n = 1$, we obtain an expression for the velocity field directly from $j_1(x)$:

$$v(r,t) = \alpha(t) \left(\frac{sin(x)}{x^2} - \frac{cos(x)}{x} \right), \tag{7.5}$$

with $\alpha(t)$ the time-dependent solution. The form of $\alpha(t)$ follows directly from the velocity boundary condition at the droplet interface $v(R,t) = \dot{R}$, with R the time-dependent radius of the droplet. The velocity field in the droplet then becomes:

$$v(r,t) = \frac{\dot{R}R^2}{r^2} \frac{sin\,(x) - x cos\,(x)}{sin\,(X) - X cos\,(X)} = \frac{\dot{R}R^2}{r^2} \frac{T\,(x)}{T\,(X)}, \tag{7.6}$$

with $X = k \cdot R$.

Equations 7.1–7.3 relate the velocity field $v(r,t)$ with the pressure field $P(r,t)$. By integration over space and subsequently over time we find:

$$P\,(R_-,t) - P\,(r,t) = -\rho_{PFP} \left(\frac{sin\,(x)}{x} - \frac{sin\,(X)}{X} \right) \frac{\omega}{c} \left(\frac{\ddot{R}R^2 + 2\dot{R}^2 R}{T\,(X)} + \dot{R}^2 R^3 \frac{\omega^2}{c^2} \frac{sin\,(X)}{T\,(X)^2} \right), \tag{7.7}$$

and

$$P(r,t) - \left(P_{at} + \frac{2\sigma}{R_i}\right) = -\rho_{PFP}\omega c \frac{sin(x)}{x} \frac{R - R_i}{\frac{sin(X_i)}{{X_i}^2} - \frac{cos(X_i)}{X_i}}. \tag{7.8}$$

Here, and in the following, $X_i = k \cdot R_i$ with R_i the initial droplet radius. The motion of the fluid in the external medium can be described by potential flow because of the low Mach numbers involved here[180]. A final boundary condition for the pressure field balances the normal stress tensor on each side of the interface, which also brings viscosity into the problem. Combining these equations with the previous by adding all the pressure terms and also accounting for the energy reradiated by the droplet[181,182], we find a differential equation at the droplet interface:

$$\begin{aligned} \rho_w \left(R\ddot{R} + \frac{3}{2}\dot{R}^2\right) = &-4(\mu_w - \mu_{PFP})\frac{\dot{R}}{R} - 2\sigma\left(\frac{1}{R} - \frac{1}{R_i}\right) \\ &-\rho_{PFP}\omega c \frac{sin(X)}{X} \frac{R - R_i}{\frac{sin(X_i)}{{X_i}^2} - \frac{cos(X_i)}{X_i}} - P_{ac} \\ &-\frac{\rho_{PFP}{c_{PFP}}^2}{c_w} sin(X) \frac{\dot{R}}{\frac{sin(X_i)}{{X_i}^2} - \frac{cos(X_i)}{X_i}}, \end{aligned} \tag{7.9}$$

and adding the interaction with the rigid substrate[2], as in our case, changes the left-hand side of Eq. 7.9 to $\rho_w\left(\frac{3}{2}R\ddot{R} + 2\dot{R}^2\right)$. This equation can be solved numerically and the corresponding pressure field and pressure at the center of the droplet can be calculated from the velocity of the interface using Eq. 7.8. The theoretical resonance frequency of such droplets can be extracted by linearization from Eq. 7.9:

$$\omega_0^2 = K_{RS} \frac{\frac{\rho_{PFP}\omega_0 c_{PFP}}{\frac{c_{PFP}}{R_i\omega} - cot\left(\frac{R_i\omega_0}{c_{PFP}}\right)} + \frac{2\sigma}{{R_i}^2}}{\rho_w R_i}, \tag{7.10}$$

with $K_{RS} = 1$ if the droplet is in the free field and $K_{RS} = \frac{2}{3}$ if the droplet is near a rigid boundary.

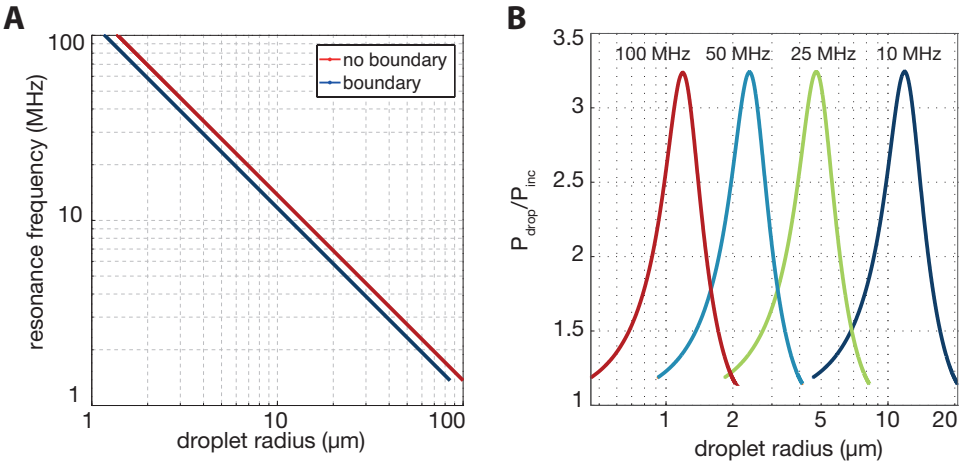

Figure 7.1: A) Theoretical resonance frequency as a function of size for a droplet in an infinite medium (red) and near a rigid boundary (blue). B) Theoretical resonance curves in pressure amplification within the droplet for 10, 25, 50 and 100MHz.

7.3 Numerical simulations

The numerical simulation was performed using a non-stiff ODE 113 solver in Matlab and the theoretical resonance frequency as a function of the droplet size following Eq. 7.10 is plotted in Fig. 7.1A. The resonance frequency of a microdroplet is much higher than that of a bubble of a comparable size. The resonance behavior of the droplets is depicted in Fig. 7.1B. Here the resonance curves of droplets insonified at 10MHz, 25MHz, 50MHz and 100MHz are plotted. Figure 7.1B shows the simulated amplitude of the pressure at the center of the droplet relatively to the incident pressure. The amplification factor shows very little variation which is a crucial property for the size reduction of the agents.

The pressure amplification at resonance predicted from our theory is plotted in Fig. 7.2A and B as a function of the incident acoustic pressure and the droplet radius, the latter directly related to the ultrasound frequency. The figure also shows the pressure amplification in a droplet resulting from superharmonic focusing of an acoustic wave propagating in water with a frequency of 3.5 MHz and peak negative pressures of 1.5, 3, and 5 MPa[175]. A direct comparison of the efficiency of the resonant vaporization of droplets and that due to superharmonic focusing is difficult since the generation of superharmonics is an interplay between the transducer geometry, acoustic

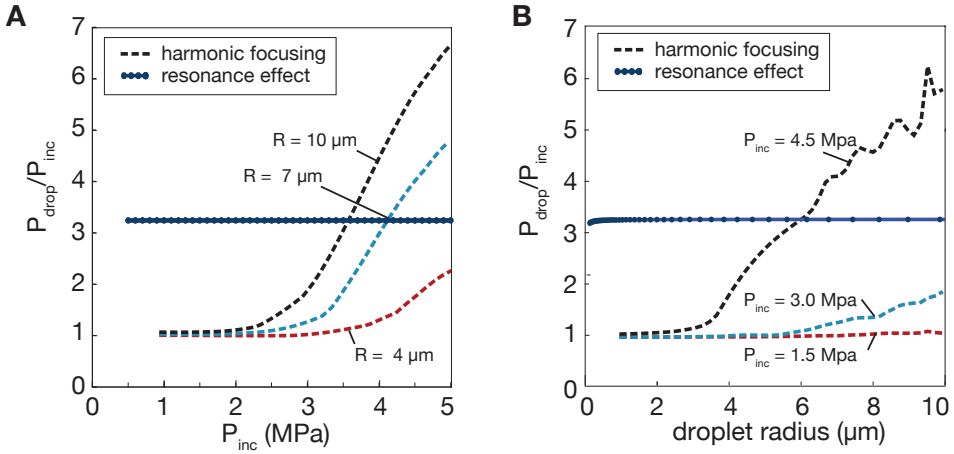

Figure 7.2: A) Comparison the the efficiency of the harmonic focusing phenomenon and resonance phenomenon for an increasing incident pressure. B) Comparison the the efficiency of the harmonic focusing phenomenon and resonance phenomenon for diverse droplets radii.

pressure, the nonlinear propagation distance, the frequency, and the droplet size. However, Fig. 7.2 shows that high insonation pressures and relatively large droplet sizes are required for sufficient superharmonic focussing to occur. On the other hand, the pressure amplification factor due to the mechanical resonance effect shows no dependence on the acoustic driving pressure, nor does it show a dependence on the droplet size. As said before, this property can be crucial for *in-vivo* applications were the generation of the required harmonics for superharmonic focusing will be difficult due to tissue attenuation.

7.4 Experimental methods

Straight electrode IDTs with a single electrode pair per wavelength were used in this study, see Fig. 7.3. When a sinusoidal driving signal is applied at a the resonance frequency of the IDT a SAW is generated traveling with the same amplitude away from the IDT in both directions. The width of the generated SAW is typically equal to the aperture width and it remains at this size for long distances with respect to the wavelength[176]. The energy efficiency can be increased by using a more complex design, including reflectors and unidirectional IDTs (SPUDT)[176] and the acoustic intensity can be increased by designing curved electrodes to focus the acoustic waves.

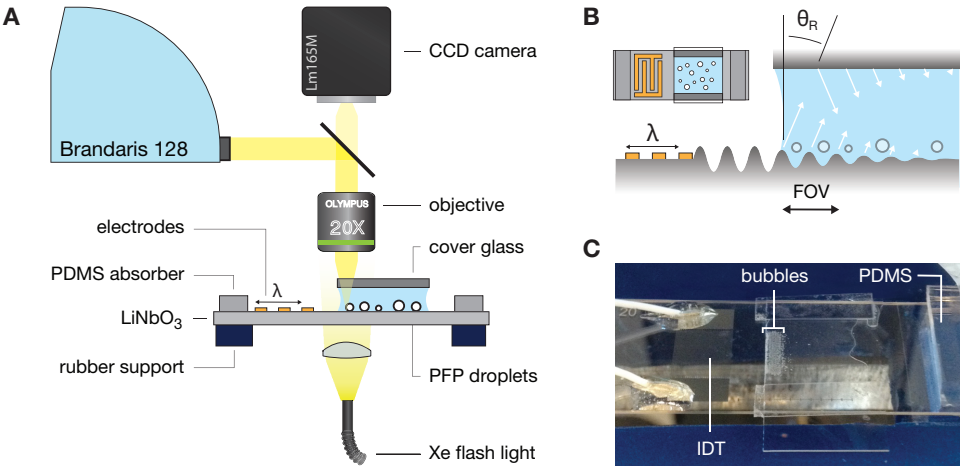

Figure 7.3: A) Schematic representation of the experimental setup. The vaporization of PFP droplets is imaged using the Brandaris128 ultra-high speed camera operated 10 million frames per second. B) A leaky SAW generates a longitudinal pressure wave in the fluid chamber at the Rayleigh angle θ_R. C) The fluid chamber is fabricated using double sided tape and a microscope cover glass. The image shows bubbles nucleated from PFP droplets through their efficient SAW induced vaporization.

Straight IDTs were used here to ease the reproducibility of the experiments without the need for a precise alignment of the IDT focus with both the imaging system and the sample.

Two IDTs with different operating frequencies were designed having 202 μm and 88 μm wide electrodes spaced by the electrode width. Each of the 1 cm aperture transducers had 60 aluminium electrode pairs fabricated on a 128° rotated Y-cut X-propagating lithium niobate ($LiNbO_3$, Roditi, United Kingdom) single crystal wafer using standard soft lithography techniques. The substrate was sputtercoated with aluminium to an approximate thickness of 750 nm. The electrodes were carefully aligned normal to the X-axis to generate a Rayleigh wave propagating along the X-axis upon RF actuation. The wafer was diced to size and wires were connected using conduction silver paint reinforced by epoxy glue (Fig. 7.3C). Impedance measurements were performed to find the exact resonance frequency of the IDTs and they were 19.6 MHz and 45.4 MHz, respectively.

A microfluidic chamber 100 µm in height was fabricated using double sided tape (3M Scotch 665 Permanent) placed directly on top of piezoelectric substrate aside of the IDT aperture. A microscope cover glass (thickness

100 μm) was placed 6 mm from the IDT aperture on top of the tape to seal the chamber resulting in a channel that was open in the direction of SAW wave propagation, see Fig. 7.3 B and C. The open channel allowed for the direct coupling between the SAW and the fluid. The PFP droplet emulsion was diluted in ultrapure water (Mili-Q, Millipore) and dispersed in the chamber by capillary suction.

The IDTs were driven with a 50-cycle sinusoidal ultrasound pulse generated by a waveform generator (8026, Tabor Electronics) connected to a 50 dB linear power amplifier (350L, E&I). Due to the difference in speed of sound in the piezoelectric substrate and in the fluid, a SAW will be radiated into the fluid at the Rayleigh angle (θ_R), which can be calculated from the ratio of the speed of sound in the piezoelectric substrate and in the fluid, $\theta_R = sin^{-1}(c_w/c_s)$. The speed of sound in water c_w and in lithium niobate substrate in the absence of fluid loading c_s is 1450 m/s and 3990 m/s, respectively at room temperature giving $\theta_R \approx 23°$. Due to the leakage of acoustic energy into the fluid, a longitudinal pressure wave is generated that will trigger the vaporization of the PFP droplets. The amplitude of the driving voltage was varied to investigate its influence on the vaporization dynamics. The acoustic energy reaching the boundaries of the piezoelectric substrate is absorbed by rubber (PDMS, Dow Corning,) and the substrate holder is also made of sound absorbing rubber. The SAW is built up on the substrate by superposition of the waves of a single wavelengths produces by the individual electrode pairs. Therefore the IDT has a transient on the order of the number of electrode pairs. While a sinusoidal driving pulse is applied to the IDT, the pressure increases linearly during such a transient and conversely, when the driving signal is switched of the amplitude of the acoustic wave decreases linearly.

Perfluoropentane (PFP) droplet emulsions were prepared by mixing ultrapure water (Milli-Q, Millipore) with 5% v/v of PFP (Sigma Aldrich) and 0.1% v/v of negatively charged fluorosurfactant Zonyl PFP (Sigma Aldrich). The mixture was mechanically agitated for 30 s using a CapMix™ (3M, Saint Paul, Minesota) to produce a polydisperse droplet emulsion. The size distribution of the emulsion was measured using a Coulter Counter, see Fig 7.4.

Droplet vaporization was imaged using an inverted microscope (Olympus BX-FM) equipped with a 20× magnification objective (Olympus SLMPlan N, NA 0.25) coupled to the Brandaris 128 ultra high-speed camera[76,77] operated at 15 million frames per second, see Fig 7.3. The field of view (FOV) was 138 μm × 98 μm and the resolution was 0.29 μm per pixel. Sufficient illumination intensity were achieved using a Xenon flash light (MVS 7010

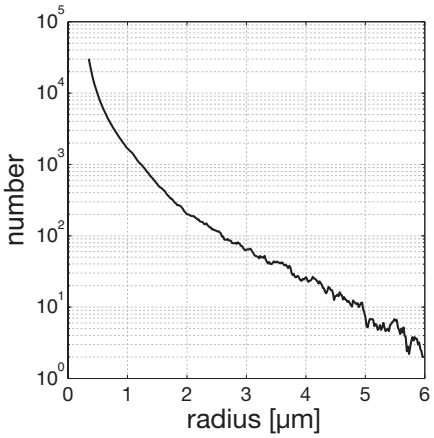

Figure 7.4: Size distribution of the droplet suspension used for the vaporization study.

XE, Perkin Elmer, Waltham, MA). Six successive high speed recordings of 128 frames each were recorded with an interval of approximately 100 ms. Only during the first recording the IDT was not actuated for reference. A CCD camera (Lumenera, LW165M) was used to monitor the optical focusing. Measurements to relate relative pressure amplitudes to the amount of nucleated droplets were imaged using a high-speed camera (Photron SA-X2) operated at 50.000 frames per second. The exposure time was set to 1.25 μs to minimize motion blur. All measurements were performed at a 20°C room temperature. The droplets were therefore not in a superheated state.

The optical recordings were processed with specialized image processing software programmed in MATLAB to obtain the initial radius of the droplets that vaporized. The radius of the droplets was measured from the inflection point on the averaged intensity profile of the droplet[85].

7.5 Results

Figure 7.5A shows an image sequence of the vaporization of PFP droplets by a 19.6 MHz ultrasound wave. Nucleated droplets are marked by the red-dotted circles. It is observed that the nucleation bubble grows rapidly under acoustic forcing[183]. When the ultrasound is turned of, the bubble rapidly decreases in size. However, from the last frame at t=100 ms, it can be observed that every nucleation site produces a stable bubble.

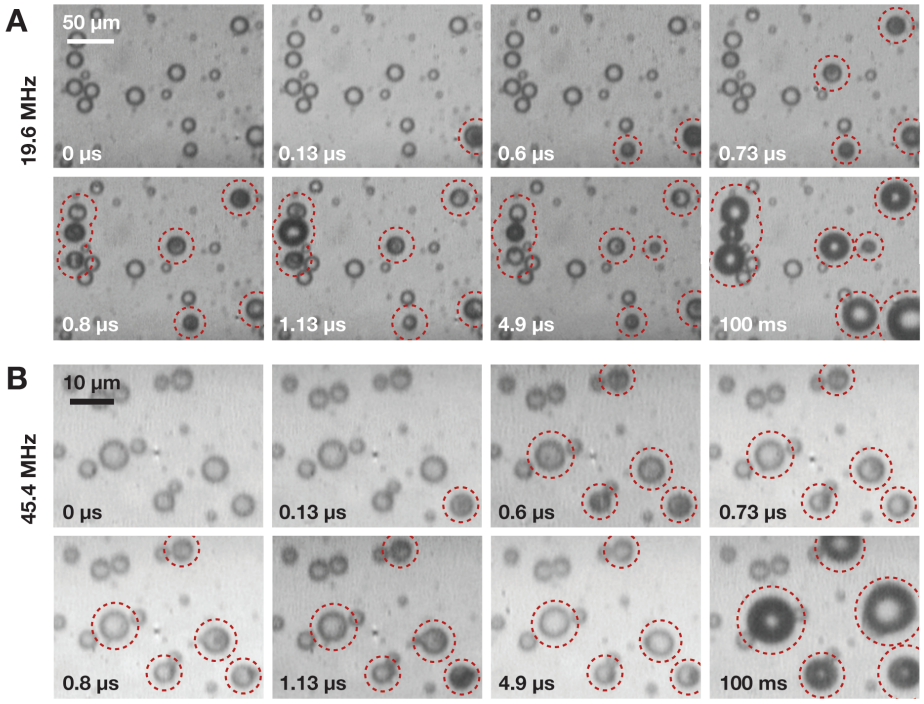

Figure 7.5: A) Image sequence captured at 15 million frames per second of the vaporization of PFP droplets at a frequency of 19.6 MHz. The nucleated droplets are marked by the red dotted circles. Nucleation bubbles generated during the first insonation grow in the first microsecond and in the successive microseconds their size decreases largely. The last frame, 100 ms later than the first frame, shows that a stable bubble is formed from all nucleated droplets. B) Vaporization of PFP droplets by an acoustic wave with a frequency of 45.4 MHz. Clearly, the nucleation process is less violent than at the previous 19.6 MHz case. Small nucleation bubbles appear that grow all to stable bubbles over times as can be seen from the last frame captured 100 ms later than the first frame.

The observed vaporization process for the very same PFP droplets in a 45.4 MHz ultrasound wave is less violent as can be observed from the images in Fig 7.5B where nucleated droplets are also marked by red-dotted circles. The nucleation bubbles that appear within the droplet are much smaller than those observed at a frequency of 19.6 MHz. It was also observed that the bubbles expand at much lower growth rates. However, as can be observed from the last image, t=100 ms after ultrasound exposure, all nucleated droplets produce a stable bubble.

From both image sequences in Fig. 7.5 it can be observed that the nucleation process initiated by the ultrasound exposure is not instantaneous in time, as was also shown before[183]. Fig. 7.6 shows for both ultrasound frequencies the time dependent number of droplets that nucleated over a 0.2 μs window (red solid lines) for 217 nucleation and 120 nucleation events at a frequency of 19.6 MHz and 45.4 MHz, respectively. From high speed movies captured at the second ultrasound exposure the arrival time of the acoustic wave can be observed from the movement of the nucleation bubbles through secondary radiation forces[17], marked by the green areas. The green areas also show the temporal length of the 50 cycle ultrasound pulse. From Fig. 7.6A it can be observed that at a driving frequency of 19.6 MHz the droplets generally start to nucleate at the end of the 50-cycle ultrasound exposure. This is expected as the pressure generated by the IDTs has a transient increase over time. At a SAW driving frequency of 45 MHz the nucleation events start closer to the start of the ultrasound exposure. A smaller number of droplets nucleates when the ultrasound wave has passed, probably due to a reflection of the insonation wave. Fig. 7.6A and B show the size of the nucleated droplets from which no obvious relation between the size of the nucleated droplet and the time at which the event occurs. The time variable is thus only increasing the probability of occurrence of the an ADV event, without influencing the underlying mechanism.

The size distribution of the droplets that nucleated is presented in figures 7.7A and 7.7B. Figure 7.7A shows the size distribution of 217 droplets that nucleated during the first ultrasound exposure at a frequency of 19.6 MHz. A maximum in the response is observed at a droplet radius of 4.6 μm ± 0.29 μm. Figure 7.7B shows the response of droplets that nucleated during the first ultrasound exposure at a frequency of 45.4 MHz. A clear size-dependent droplet vaporization is observed where smaller bubbles are resonant to higher ultrasound frequencies, and shorter wavelengths. The modeled pressure amplification within the droplet is plotted in Fig. 7.7C and D as a function of the size of the droplet for a SAW frequency of 19.6 MHz and 45.4 MHz, respectively. A clear resonance is observed here that is in

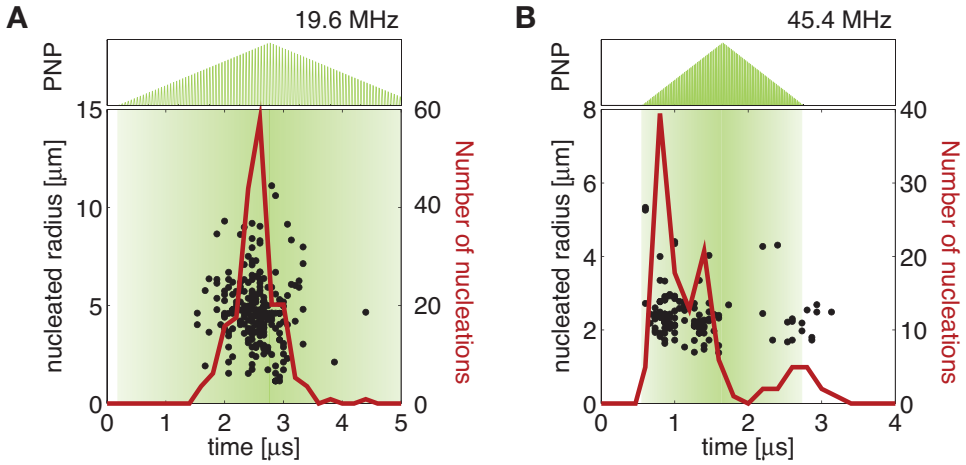

Figure 7.6: The number of nucleation events over time and the radius of the droplet corresponding to the nucleation event at a frequency of (A) 19.6 MHz and (B) 45.4 MHz acoustic forcing.

good agreement with the measured droplet behavior as depicted in Fig. 7.7A and 7.7B. The modeled size-dependent pressure within the droplet is a mechanical resonance very similar to that of a microbubble under ultrasound exposure. Due to the bulk modulus of the liquid core however, these resonance frequencies are more than 2 orders higher. Please note that the pressure amplification in Fig. 7.7C and D shows that the coupling efficiency for droplets driven at off-resonance frequency quickly drops to unity. Moreover, it crosses unity which shows that at off-resonance frequencies the peak negative pressure of the driving ultrasound wave is not transferred to the droplet. This can partly explain the experimental difficulty of triggering ADV with low ultrasound frequencies.

Figures 7.8A and B show the theoretical velocity profiles (orange) and the pressure profiles (red) for a resonant droplet driven at a SAW frequency of 19.6 MHz and 45.4 MHz, respectively. The velocity profile in the drop follows a spherical Bessel function of the first kind with index 1 and decreases with $1/r^2$ outside the droplet due to continuity of the potential flow. The spherical symmetry condition results in a zero velocity at $r = 0$. Please note that the size of the drop is on the order of a quarter of the wavelength in the PFP. The velocity has to be continuous across the droplet interface, this boundary condition results in a resonance frequency: the frequency at which the coupling is most efficient, see Fig. 7.8. The pressure profile

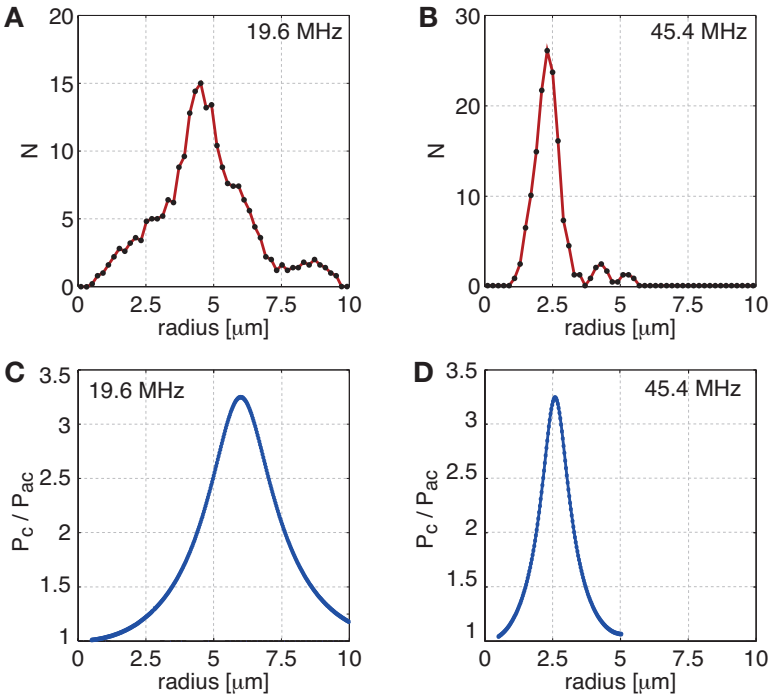

Figure 7.7: A) Resonant vaporization for 19.6 MHz ultrasound and B) for 45.4 MHz ultrasound. A clear resonance behavior is observed. The modeled (C and D) size-dependent pressure amplification within the droplet is in good agreement with the measured resonance behavior.

inside the droplet is a *sinc* function, i.e. the spherical Bessel function of first kind with index 0. Due to the properties of the *sinc* function, any specific point on the pressure profile (zeros in the function or optimum other than in $r = 0$) is located far outside the drop. The pressure profile therefore undergoes a rather smooth variation within the drop and does not play a direct role in the resonance mechanism. Thus the resonance originates from the coupling of the velocity inside and outside the drop. From the pressure profile of the resonant droplet it can also be observed that the amplitude of the pressure at the droplet center exceeds the incident pressure by a factor 2.2. The higher pressure amplification in the center of the droplet results in the largest probability of finding nucleation sites in the center of the droplet, in contrast to the previously developed superharmonic focusing theory [175].

The statistical increase in the number of vaporization events as a function of the acoustic forcing was investigated by varying the amplitude of the 50-

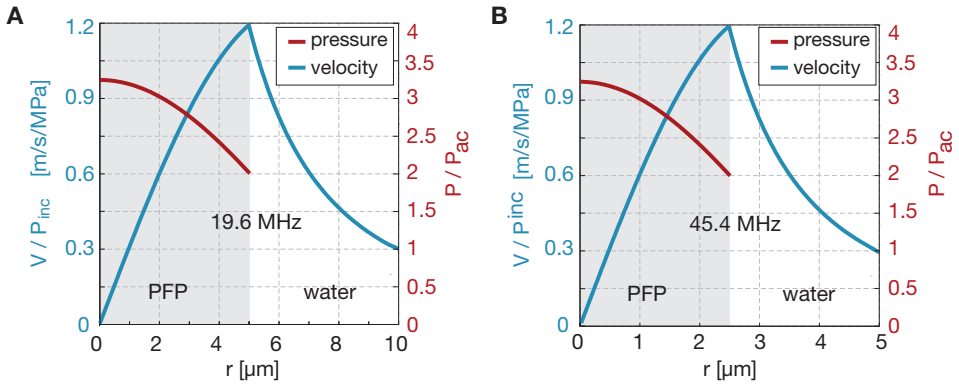

Figure 7.8: Pressure profiles in the drop and velocity profiles in the system for a resonant droplet for a A) 19.6 MHz insonation frequency and B) a 45.4 MHz insonation frequency. The pressure undergoes a smooth variation within the drop corresponding to the center part of a sinc function whereas the velocity varies strongly and couples to the potential flow outside the drop to create the resonance effect.

cycle ultrasound pulses. The percentage of droplets that nucleated in the field of view of 20 high-speed movies captured at 50 kfps is presented in Fig 7.9A and B as a function of the amplitude of the driving signal (before amplification) for a SAW frequency of 19.6 MHz and 45.4 MHz, respectively. Since the absolute pressure amplitude within the microfluidic chamber could not be measured directly, and since the voltage over the IDT electrodes was unknown due to the non-negligible impedance mismatch between the amplifier and the IDT, including the electrical wiring, we plotted the voltage amplitude of the driving US pulse. A linear relationship between the driving voltage and the percentage of droplets that vaporized during the first insonation is observed.

For the second insonation, pre-nucleated bubbles are already present in the sample that originate from the resonant vaporization of droplets during the first exposure to ultrasound. Figure 7.10A-F show two sequences of 3 images extracted from high-speed movies captured at 15 million frames per second for a SAW driving frequency of 19.6 MHz and 45.4 MHz. During the second insonation at 19.6 MHz, a high number of nucleation events is observed where most droplets, including those of the smallest sizes, are vaporized, see Fig. 7.10C. For similar droplet concentrations, the amount of nucleation events in the field of view of 9 high speed movies was counted during the first and during the second ultrasound insonation. Figure 7.10G

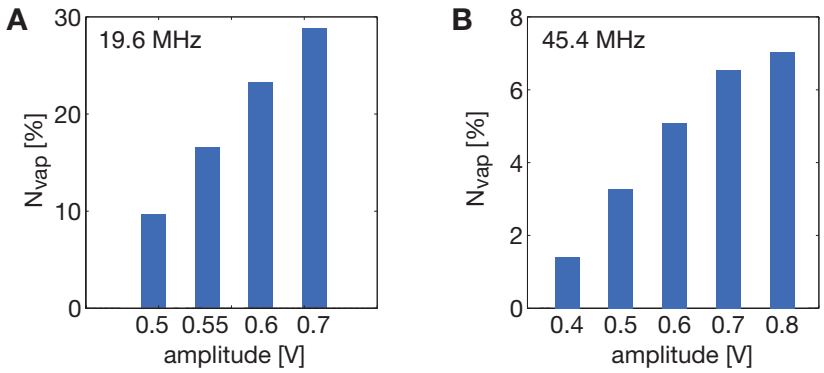

Figure 7.9: The amount of bubbles with respect to the total amount of bubbles in the FOV that nucleates during for increasing amplitudes at (A) 19.6 MHz and (B) 45.4 MHz. A linear amplitude dependency is found where at the same amplitudes droplets are vaporized more difficult at the higher frequency.

shows that during the first ultrasound exposure at 19.6 MHz on average 7 droplets are vaporized, whereas during the second insonation as much as 100 droplets nucleate. A difference in the vaporization dynamics at the second insonation for a SAW frequency of 45.4 MHz is observed. Figure 7.10D-E show an image sequence of the second insonation at a SAW frequency of 45.4 MHz with pre-nucleated bubbles present. The observed nucleation sites are indicated by the 3 arrows. During the first ultrasound exposure 5 droplets nucleated, as can be seen from the bubbles present in Fig. 7.10D. Thus the amount of nucleation events during the second SAW exposure is similar to the amount of nucleation events observed during the first insonation, see Fig. 7.10H. The effect of a lower vaporization threshold observed when bubbles are present seems therefore highly frequency dependent and is much more effective at the lowest of the two frequencies used here, namely at a IDT driving frequency of 19.5 MHz.

7.6 Discussion

In human tissues, and in fluids in general, attenuation increases exponentially with the ultrasound frequency. Therefore, the vaporization of submicron droplets, requiring frequencies above 100 MHz, implies the use of catheter-based transducers to allow for the exposure of the droplets to ultrasound of sufficiently high pressures and frequencies. Non-invasive interventions would therefore be limited to superficial treatments, e.g. skin cancers.

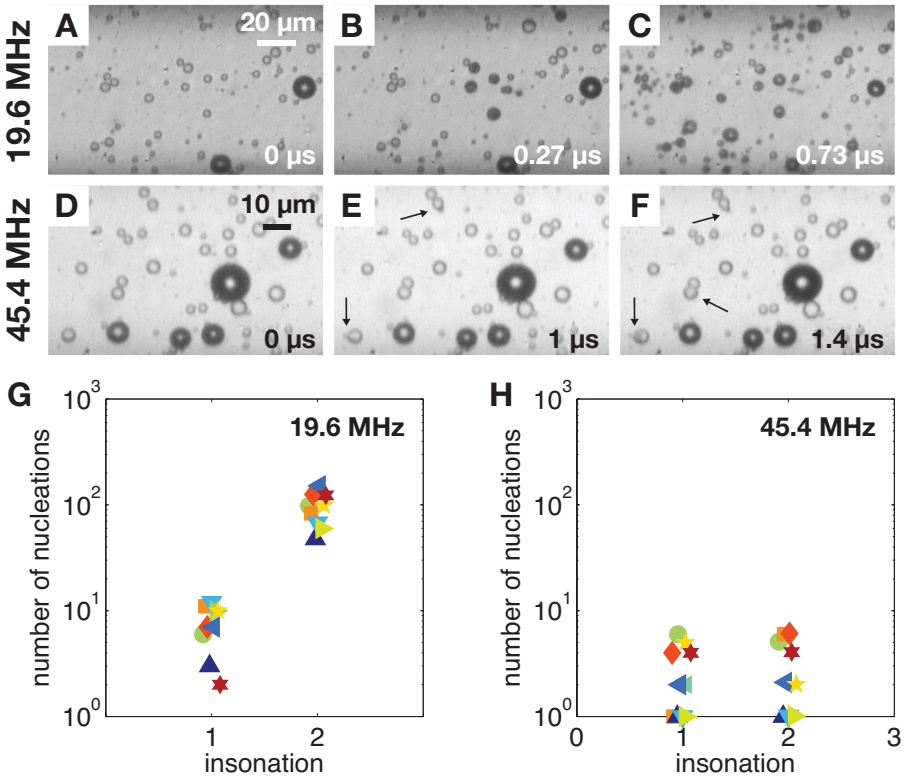

Figure 7.10: Observed vaporization dynamics during the second ultrasound exposure with nucleation bubbles present from the previous ultrasound exposure at a frequency of (A-C) 19.6 MHz and at (D-F) 45.4 MHz. The number of observed nucleation events for 9 different insonation events during the first and during the second ultrasound exposure is plotted in figure G and H at 19.6 MHz and 45.4 MHz, respectively. At a frequency of 45.4 MHz a similar vaporization behaviour is observed during the second ultrasound exposure as compared to the first ultrasound exposure. At 19.6 MHz only few resonant droplets are nucleated during the first exposure, during the second ultrasound exposure the vaporization of almost all droplets with sizes down to 100 nm is triggered by the bubbles already present.

The resonance frequencies of phase-change droplets can be lowered by using liquids with an even lower speed of sound than PFP, which will however will be difficult to find.

The imaging window in the setup was chosen such to be as close as possible to the meniscus of the water sample containing the PFP droplets to prevent acoustic reflections from the top glass wall of the microfluidic channel that could interfere with the primary acoustic wave. Nonetheless, since the Rayleigh angle is 23°, the first reflected wave from the cover glass will return to the substrate at a position 85 μm away from the meniscus. The field of view in our setup was 98 μm wide and it is therefore expected that the droplets are vaporized by traveling acoustic waves alone. However, at the end of the 50-cycle ultrasound exposure, the buildup of a standing wave can no longer be excluded, resulting in a perturbation of the vaporization efficiency results. However, no difference is expected in the size-dependent resonant vaporization as the frequency is unchanged.

The effect of a highly increased number of vaporization events during the second ultrasound exposure can not be explained at this moment. However, it is of great interest for clinical applications with phase-change agents. The efficiency of therapy, local drug delivery and imaging with phase-change agents will increase tremendously by employing optimized ultrasound pulse schemes to first vaporize the resonant droplets, that to trigger the complete vaporization of a polydisperse droplet population.

The proposed model is a simple model based on spherical symmetry. The approximations and conclusions are only valid for the description of the fundamental radial response of the drop. We chose not to incorporate the harmonic behavior since in a physical resonant system, the harmonic is significantly less efficient as compared to the fundamental resonance frequency. Our model is only valid for droplet radii $R \leq \lambda/2$ with λ the acoustic wavelength in the liquid constituting the droplet. An independent model describing the harmonic droplet dynamics can be developed with the very same equations and reasoning as the ones used here to describe the fundamental response. The proposed model still shows some discrepancy in term of the absolute resonance frequency. We chose a simple treatment of the interaction between the droplet and the rigid surface that is known to have a limited precision also for vibrating microbubbles[114,184]. Therefore we expect that a more rigorous derivation of the influence of the rigid surface could account for this minor discrepancy.

Experiments were performed at room temperature for the ease and reproducibility of the experiments. It can be expected that the vaporization efficiency increases for higher temperatures, however, we do not expect this

effect to be of significance for the size-dependant nucleation process. The critical point of PFP is at a temperature of 148°C. The temperature difference between room temperature and 37°C is approximately 10% of the critical temperature. Following the spinodal decomposition theory[185], the difference in pressures required to vaporize the PFP at both temperatures should be of the same order. This was also confirmed by previous experiments were the difference in the required pressure was minimal. On the other hand, the temperature at which the experiments are performed will have a critical influence on the stability of the bubbles formed after the ADV process[186].This is however outside the scope of the present study.

7.7 Conclusions

It was shown that an efficient vaporization can be performed by driving phase-change PFP droplets at their fundamental resonance frequency. Good agreement was found between the modeled size-dependent pressure amplification within the droplet and the measured size dependent vaporization probability. Thus, it is crucial for efficient droplet vaporization to use acoustic frequencies matching the resonant droplet size proposed in this paper. Moreover, very efficient vaporization is obtained by driving the droplets with multiple acoustic exposures since the presence of pre-nucleated bubbles increases dramatically the vaporization efficiency. This work shows that, in order to make efficient phase-change agents, the monodispersity of the agent is crucial. The resonant droplet vaporization and the phase-change dynamics during multiple ultrasound exposures may have great potential for the future clinical use of these types of phase-change agents.

Acknowledgments

We thank James Friend for the stimulating discussions about IDTs and SAWs. This work was funded by NanoNextNL, a micro and nanotechnology consortium of the Government of the Netherlands and 130 partners. The authors want to thank Gert-Wim Bruggert, Martin Bos and Bas Benschop for their skilful support.

8

Droplet formation of monodisperse perfluorocarbon droplets for highly controlled acoustic droplet vaporization

Acoustic droplet vaporization has great potential in nanomedicine for the local delivery of drugs, for embolotherapy, and for tumor imaging with ultrasound. The dynamics of the droplet vaporization, as well as the nucleation efficiency, strongly depend on the size of the droplet with respect to the employed driving frequency. Here, we give an overview of microfluidic production techniques that can be used for the highly controlled formation of monodisperse droplets. The vaporization of the monodisperse microdroplets down to a size of 200 nm was studied by means of ultra high-speed imaging. It was shown that the vaporization of monodisperse droplets has a high degree of symmetry and that the variation in the nucleation threshold is as small as 2% of the driving pressure.

[1]To be submitted as: T. Segers, G. Lajoinie, O. Shpak, L. Shui, J. Eijkel, M. Versluis, *Droplet formation of monodisperse perfluorocarbon droplets for highly controlled acoustic droplet vaporization* (2015)

8.1 Introduction

The process of the acoustically triggered vaporization of superheated droplets, termed acoustic droplet vaporization (ADV), has great potential in nanomedicine. The severe side effects of the systemic injection of chemotherapeutic drugs on healthy tissue can potentially be lowered by encapsulation of the drug in phase-change droplets[187–189]. The droplets typically consist of a low boiling point perfluorocarbon oil, such as perfluoropentane (T_b = 29°C), and they do not spontaneously vaporize when injected *in-vivo* until the droplets are exposed to a high pressure ultrasound pulse[165,171]. Recent studies have shown that nanodroplets (diameter $\sim$ 200 nm) may extravasate out of leaky vasculature present in tumorous tissue. The nanodroplets then passively accumulate in a tumor where the controlled release of a chemotherapeutic drug is of greatest interest[169,170]. In addition, vaporized droplets form highly echogenic vapor bubbles resonant to standard diagnostic ultrasound frequencies which allows for monitored drug delivery and tumor imaging. Moreover, the vaporization of microdroplets is of interest for embolotherapy applications[171,190].

Recently, Shpak *et al.*[175] showed that the vaporization of droplets with ultrasound frequencies in the MHz range is induced by the focusing of superharmonic waves, generated by nonlinear propagation of the ultrasound, with wavelengths of the order of the droplet size. The peak negative pressure in the focal region is droplet size and frequency dependent, in other words the vaporization efficiency is governed by a strong coupling between droplet size and the pressure and frequency of the ultrasound wave. In Chapter 7, it was shown that phase-change droplets can also be vaporized by driving them at their radial resonance frequency that is on the order of 10 MHz for a droplet with a radius of 10 μm and near 100 MHz for that with a radius of 1 μm. Conventional phase-change agent production methods including sonication and mechanical agitation result in a relatively broad size distribution with droplet radii between 1 and 10 μm[164]. Thus, the vaporization efficiency and control can be dramatically increased by narrowing down the size distribution to a droplet size that is resonant to the applied ultrasound field.

Microfluidic methods have proven to be versatile tools for the highly controlled mass-generation of monodisperse bubbles and droplets. In a flow-focusing geometry a liquid or gas is focused by two co-flows through a constriction where the jet pinches off regularly to form monodisperse droplets or bubbles [60–62]. The size of the produced droplets or bubbles is limited to the size of the nozzle. With standard soft lithography techniques[106]

the diameter is limited to 2-3 μm. Smaller monodisperse droplets can be produced at a nano-microchannel interface where the dispersed phase is forced through the nanochannel and when it reaches the microchannel, it destabilizes due to capillary instability and breaks up into monodisperse droplets[191,192]. It was shown that the droplet size scales linearly with the height of the nanochannel[191,193] and it was also shown that it is feasible to produce monodisperse droplets with sizes down to 400 nm[194]. The production rates for a single nano-microchannel interface were shown to be limited to approximately 10^3 droplets per second[193].

The low boiling point of the PFCs allows for an alternative approach where monodisperse droplets are formed after the recondensation of vapor bubbles produced in a flow-focusing device[195,196]. Due to the density difference of a factor 5 between the PFC liquid and the PFC vapor, a recondensed droplet is approximately 5 times smaller in size than the vapor bubble. Thus, nanodroplets can be produced from a flow-focusing device by the recondensation of micron-sized bubbles from a micron-sized nozzle. Moreover, the production rates of a flow-focusing device were shown to reach almost a million bubbles per second from a single nozzle, see Ch. 6, allowing for the rapid production of ADV droplet samples[145].

Here, we discuss three production techniques for monodisperse PFC droplets, namely: flow-focusing device, nano-microchannel interface chip, and recondensation of vapor bubbles produced in a flow-focusing device. With the produced monodisperse droplets the vaporization threshold of droplets of a single size is investigated. Furthermore, the vaporization dynamics of two identical droplets with an inter-droplet spacing on the order of the droplet size is studied for various droplet sizes. Finally, the visualization of a cluster of monodisperse droplets is presented. We finish with our conclusions.

8.2 Monodisperse production methods

All droplets and bubbles produced in this study were formed in an aqueous mixture of a 1% V-V mixture of negatively charged fluorosurfact Zonyl FSP (Sigma Aldrich). The flow-rate of the water-surfactant mixture and the flow-rate of the PFP were controlled by high-precision syringe pumps (PHD 22/2000, Harvard Apparatus) for the first two production methods, namely the direct production of droplets in a flow focusing device and for the droplet production in a nano-micochannel interface device. For the recondensation method, the water was pressure-driven for an increased flow stability using a pressurized container and a pressure regulator (Omega, PRG101-25). The gas pressure was set by the temperature of the system.

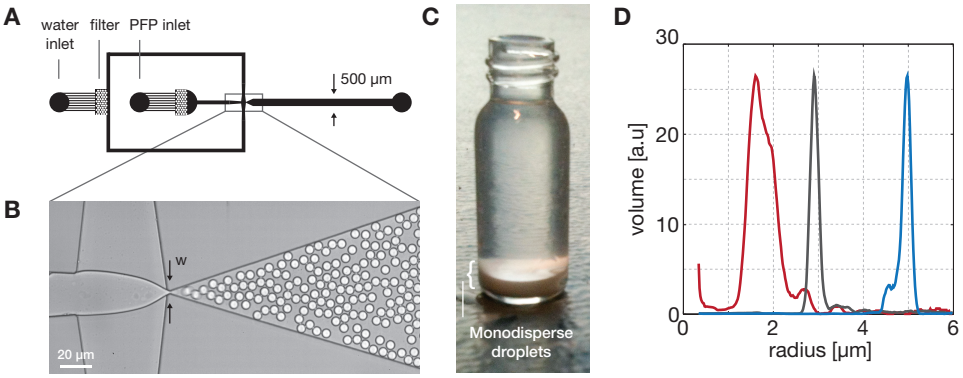

Figure 8.1: A) Design of the microfluidic flow-focusing geometry. B) Image of the formation of monodisperse droplets with a radius of 5.4 µm in the flow-focusing device with a nozzle width w of 3 µm. C) The droplets are collected in a vial where they settle at the bottom. D) Size distributions of PFP droplets produced with the flow-focusing device measured with a Coulter-counter.

8.2.1 Flow-focusing technology

A flow-focusing device with a 3 µm expanding nozzle was designed, see Fig. 8.1A. The channels were 13.6 µm in height throughout the device and filters consisting of closely spaced cylindrical pillars were incorporated in the design of the fluid and gas supply channels to prevent the nozzle from clogging by dust particles and to ensure a stable droplet formation for hours.

The mold for the polydimethylsiloxane (PDMS) devices was fabricated using standard soft lithography techniques with SU-8[106,197]. PDMS was poured over the mold in the standard 1:10 ratio, cured for 1 hour at 65 °C and cut to size. Fluidic ports were punched through the PDMS prior to the plasma-bonding (Harrick Plasma, Model PDC-002, Ithaca, NY, USA) of the PDMS to a glass microscope slide. To maintain the channel hydrophilicity, the channels were filled with water immediately after bonding. The fluidic ports were connected to teflon tubing (PEEK, Upchurch) for the supply of PFP and the water-surfactant mixture.

The PFP flow-rate was 4 µL/min and the co-flow rate was varied to adjust the size of the produced droplets. The flow rates were 20, 25, and 30 µL/min. The droplet formation was imaged using a high-speed camera (Photron SA1.1) and an inverted microscope (Nicon Instruments, Eclipse TE2000-U). The spatial resolution was 0.67 µm/pixel. Fig 8.1B shows the flow-focusing chip in operation, producing droplets with a radius of 5.4 µm. When the flow-rate was changed, the droplet formation was first left to

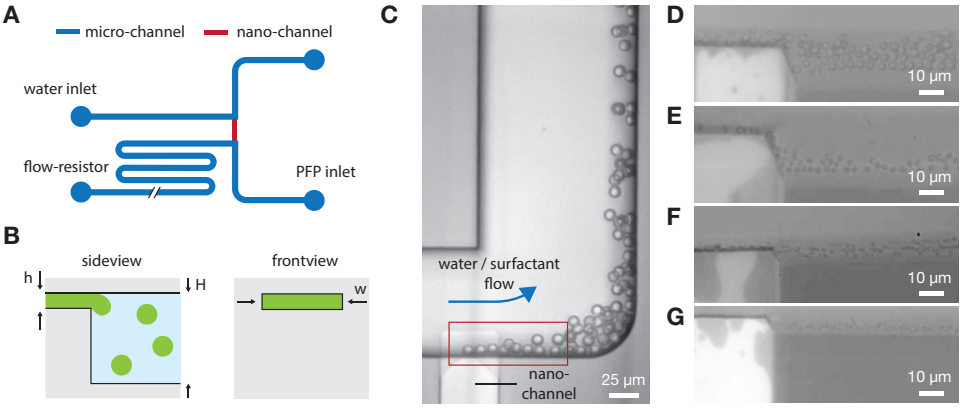

Figure 8.2: A) Schematic representation of the nano-microchannel device. The nanoliter flow-rate through the nanochannel is regulated with high-precision by the hydrodynamic resistance of the nanochannel and the flow-resistor in a 1:100 flow-rate ratio. B) The PFP breaks up regularly to form monodisperse droplets at the nano-microchannel inteface. C) The formation of monodisperse droplets with a radius of 3.8 µm. D-G) Images of the formation of nanodroplets from nanochannel heights of 390, 290, 180, and 80 nm, respectively. The images shows a zoom of the region marked by the red rectangular in Fig. C.

stabilize for at least 10 min. Subsequently, the droplet sample was harvested for 15 min in a 2 mL vial that was connected to the outlet port of the flow-focusing device by teflon tubing. The size distribution of the produced droplet samples was characterized using a Coulter counter (Multisizer 4, Beckman). Before the Coulter measurements, the samples were washed by centrifugation to minimize interference from surfactant aggregates in the medium.

The measured size distributions are shown in Fig. 8.1C. The size distributions of the 3 µm and 5 µm radius droplets have a FWHM of 0.2 µm (PDI = 0.05 and 0.03, respectively). In comparison, the size distribution of the 1.6 µm radius droplets is broader with a FWHM of 0.7 µm (PDI = 0.3). The formation of droplets with sizes on the order of the width of the nozzle requires high flow-rates leading to droplet coalescence and unstable droplet formation. Clearly, the system is pushed to its limit, thereby decreasing the monodispersity.

8.2.2 Nano-microchannel interface device

The microfluidic nano-microchannel design reported by Shui *et al.*[194] was adapted here, see Fig. 8.2A. The employed nanochannel heights h were 80, 180, 290, 390, and 1150 nm, the width w of the nanochannel was 50 μm for all devices, see Fig. 8.2B. The microchannel was 10 μm in height and approximately 100 µm in width. The PFP liquid is introduced in the nanochannel (red) via a T-junction connected to a microchannel with an inlet and a pressure regulating outlet channel. The PFP flow splits at the T-junction with a ratio of 1:100 to allows for a precise control of the low nanochannel flow-rates (10-100 nL/min) with a conventional high-precision syringe pump.

The devices were fabricated in 500 µm thick Borofloat glass wafers (Schott Technical Glasses, Germany) using standard photolithography techniques. In the first wafer, the micro and nanochannels were isotropically etched. In the second wafer, the inlet and outlet ports were formed by powder blasting. The wafers were aligned and thermally bonded before individual chips (size of 10 × 20 mm) were produced by dicing the bonded wafers. A tailor-made chip holder ensured a leak-tight connection between the chip and the fused silica tubing through Nanoport connectors (Upchurch Scientific).

Fig. 8.2C shows the production of droplets with a radius of 3.8 µm from the nanochannel with a height of 1150 nm. The optically measured size distribution had a FWHM of 0.65 µm (PDI = 0.12). Fig. 8.2D-G show the formation of droplets at the position marked by the red rectangular in Fig. 8.2 from nanochannels with a height of 390, 290, 180, and 80 nm, respectively. The optical resolution did not allow for accurate optical sizing of the smaller droplets. Following the scaling arguments given by Shui *et al.*[194] for $Q_o = Q_w \approx 1nl/min$, the droplet radii can be estimated to be two times the height of the nano channel. Thus, the produced droplet sizes are in the range of 160 to 800 nm in radius.

8.2.3 Recondensating flow-focusing device

Fig. 8.3A shows a schematic representation of the setup for the production of monodisperse PFP droplets by the recondensation of monodisperse PFP vapor bubbles. A perspex box containing a hot plate is temperature controlled to set the PFP vapor pressure. A temperature of 100°C results in a vapor overpressure of 6.7 bar and it decreases to ambient pressure at room temperature. Here, the temperature was controlled at 70°C resulting in a PFP overpressure of approximately 2.7 bars that is used to drive a flow-focusing device. The flow-focusing device with a nozzle size of 3 µm

presented in Fig. 8.1 was also used here. The co-flow of the flow focusing device was also pressure driven and it was controlled at pressures ranging from 1 to 3 bar to change the bubble sizes formed.

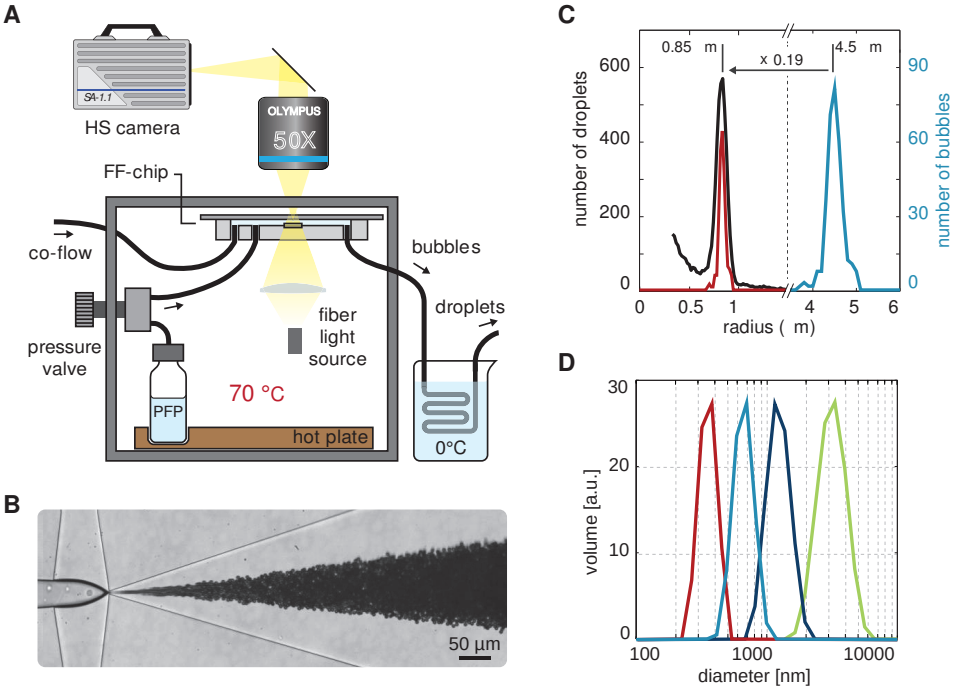

Figure 8.3: A) Schematic representation of the setup for the production of monodisperse droplets via the recondensation of monodisperse vapor bubbles in a temperature controlled environment. (B) The vapor pressure of the superheated PFP is employed to drive a vapor flow through a microfluidic flow-focusing device. The formed vapor bubbles are recondensed in an ice bath and the size of the droplets is characterized using a Zeta-sizer. C) size distribution of the the microbubbles produced by flow focusing sized optically (blue curve) and resulting droplets (black curve) sized by coulter counter. The droplet size distribution predicted from the bubble size distribution is represented by the green curve. D) Size distributions of the collected droplets.

The vapor bubble formation was imaged using a microscope (Olympus BX-FM) equipped with a 20× magnification objective connected to a high-speed camera (Photron SA1.1). The spatial resolution of the imaging system was 0.72 µm/pixel. Sufficient illumination was provided by a cold LED light source (Schott KL 2500 LED) in combination with a collimation lens. Fig. 8.3B shows a typical recording of the vapor bubble formation at a rate

of approximately 300,000 bubbles per second. High-speed microscopy was used to size the formed vapor bubbles and to relate the bubble size to the size of the recondensed droplets. A frame-rate of 5000 fps and an exposure time of 2 μs were used to image the bubble formation. The recondensation of the droplets took place outside the heated box in a cooling loop positioned in an ice bath. The droplets were harvested in a 2 mL vial. Only the larger vapor bubbles could be sized optically due to the optical diffraction limit. The size distribution of bubbles formed at a size of 4.5 μm is represented in Fig. 8.3C (blue). The bubbles were recondensed and the size distribution of the resulting droplets was measured using a Coulter counter (Multisizer4, Beckman) and is also shown in Fig. 8.3C (black). The size of the recondensed droplets is 5.3 times smaller than their precursor bubbles.

The ratio of formed bubbles to the size of the recondensed droplets can be calculated from a simple mass conservation argument involving the densities of the gaseous and the liquid PFP. The liquid is assumed to be incompressible and therefore its density is independent of the experimental parameters. On the other hand, the density of the gas varies with both the surrounding pressure and the temperature. Due to the high density of bubbles in the outlet channel of the flow-focusing device, the pressure drop across the outlet channel is considered to be negligible, hence the pressure surrounding the bubbles is assumed to be atmospheric. The pressure inside and outside the bubble is assumed to be equal since the bubbles are coated with surfactants that cancel the Laplace overpressure in the bubble through a decrease in the surface tension. Thus, the density of the gas is only dependent on the temperature in the system and therefore the ratio of the droplet radius R_d to the radius of its precursor bubble R_b is:

$$\frac{R_d}{R_b} = \left(\frac{\rho_g(T)}{\rho_l}\right)^{\frac{1}{3}}. \tag{8.1}$$

The density of the gas can now be calculated. Due to the limited accuracy of the ideal gas law for the high molecular weight PFP, we use the higher order Redlich-Kwong equation of state[198]:

$$P_0 = \frac{R_g T}{\frac{M_{mol}}{\rho_g} - b} - \frac{a}{\sqrt{T}\frac{M_{mol}}{\rho_g}\left(\frac{M_{mol}}{\rho_g} + b\right)}, \tag{8.2}$$

where a and b are expressed as:

$$a = \frac{0.42748 R_g^2 T_c^{2.5}}{P_c}, \qquad b = \frac{0.08662 R_g T_c}{P_c}. \tag{8.3}$$

$R_g = 8.314$ is the perfect gas constant, $T_c = 422$K is the critical temperature of PFP and $P_c = 2.036$ MPa is the critical pressure of PFP [199–201]. The molar mass of the PFP $M_{mol} = 288 \times 10^{-3}$ kg/mol [200]. Since for PFP, $\frac{M_{mol}}{\rho_g} \ll b$ Eq. 8.2 can be rewritten to obtain a simple expression for ρ_g as a function of the ambient pressure P_0 and the temperature T as follows:

$$\rho_g = \frac{M_{mol}\sqrt{T}}{2a}\left(R_g T - \sqrt{R_g^2 T^2 - \frac{4P_0 a}{\sqrt{T}}}\right) \tag{8.4}$$

By substitution of Eq. 8.4 in Eq. 8.1 we obtain:

$$\frac{R_d}{R_b} = \left(\frac{\frac{M_{mol}\sqrt{T}}{2a}\left(R_g T - \sqrt{R_g^2 T^2 - \frac{4P_0 a}{\sqrt{T}}}\right)}{\rho_l}\right)^{\frac{1}{3}} \tag{8.5}$$

With the properties of PFP, as given before, and with the experimental conditions during bubble formation ($P_0 = 100$ kPa and $T = 343$K) Eq. 8.5 results in a factor 0.186. Thus, theoretically, the recondensed droplets are 5.38 times smaller than their precursor bubbles. The ratio is sensitive to the PFP temperature and it varies from 5.13 at 29°C to 5.55 at 100°C. In Fig. 8.3C we plot the theoretical droplet size distribution calculated from Eq. 8.5 and from the experimentally obtained bubble size distribution (red). We find perfect agreement with the experimentally measured droplet size plotted in the same figure (black).

The droplet sizes formed from smaller PFP gas bubbles were characterized using a Zeta-sizer (Malvern Instruments Ltd). The size distribution of four samples is shown in Fig. 8.3D. The smallest droplet size produced using this recondensation technique has a mean diameter of 300 nm. Thus, it is possible to produce monodisperse nanometer-sized droplets using micrometer sized channels at production rates close to one million bubbles per second.

8.3 Vaporization dynamics of monodipserse droplets

The vaporization of monodisperse droplets with a radius of 1.3 μm formed in a nano-microchannel interface device and with a radius of 3.6, and 12 μm formed by flow-focusing was imaged using a microscope (Olympus BX-FM) connected to the Brandaris 128 ultra-high speed imaging system [76]. The

frame rate was set to 15 million frames per second and a spatial resolution of 163 nm per pixel was obtained. The droplets were confined by an Opticell container placed in a water tank that was temperature controlled at 33°C. The microscope objective was co-aligned with the focus of the 3.5 MHz transmit transducer (A308S, Olympus). The transducer output was calibrated using a 0.2 mm needle hydrophone (Precision Acoustics, Dorchester, UK). The 10-cycle transducer driving pulses were generated by an arbitrary waveform generator (8026, Tabor, Tel Hanan, Israel) and amplified by 50 dB using a high power RF amplifier (ENI 2000L, Rochester, NY, USA).

First, the nucleation threshold of the monodisperse droplets was studied by insonifying single droplets at increasing acoustic pressures. Each droplet size was insonified 5 times at a fixed acoustic pressure after which it was increased with a 0.1 MPa step size. At each insonation a high-speed recording was recovered to observe whether the droplet had vaporized. The vaporization thresholds for droplets with radii of 1.3, 3.8 and 12 μm were found to be 5.3 ± 0.2, 3.8 ± 0.3 and 3.1 ± 0.1 MPa, respectively.

Second, the vaporization of two droplets of the same size at an interdroplet spacing of approximately 10 μm was visualized. The droplets with radii of 1.3, 3.6, and 12 μm were vaporized at peak negative acoustic pressures of 5.3, 3.8 and 3.1 MPa, respectively, exactly at their nucleation threshold. Fig. 8.4A, B, and C show the vaporization events of two identical PFP droplets at a nanosecond time scale. Please note the remarkable degree of symmetry in the three vaporization events. The nucleated droplets present identical behavior, even at the very first moment of the nucleation. The spacing between the vaporized droplets decreases over time due to the strong attractive secondary radiation force[17] present once the vapor nuclei is formed and while US is on. Whether droplets merge or not depends both on their size and initial separation distance. The vapor bubbles originating from the smaller vaporized droplets have a size close to the resonant size at a frequency of 3.5 MHz, resulting in a strong attractive force. On top of that, the relatively small droplets encounter less viscous drag from the surrounding fluid than the bigger droplets. Therefore, the bigger droplets (Fig. 8.4C) do not translate as much as the smaller droplets of Figs. 8.4A and B. At prologue time scales, in the order of microseconds, vaporizing droplets can merge and fragment[202]. Both the merging and the fragmentation of vaporizing monodisperse droplets have a remarkable degree of symmetry. It was also repeatedly observed that if one vaporizing monodisperse droplet fragments into multiple vapor bubbles, the neighboring droplet has identical behavior.

Third, the vaporization dynamics of a hexagonal, densely packed, clus-

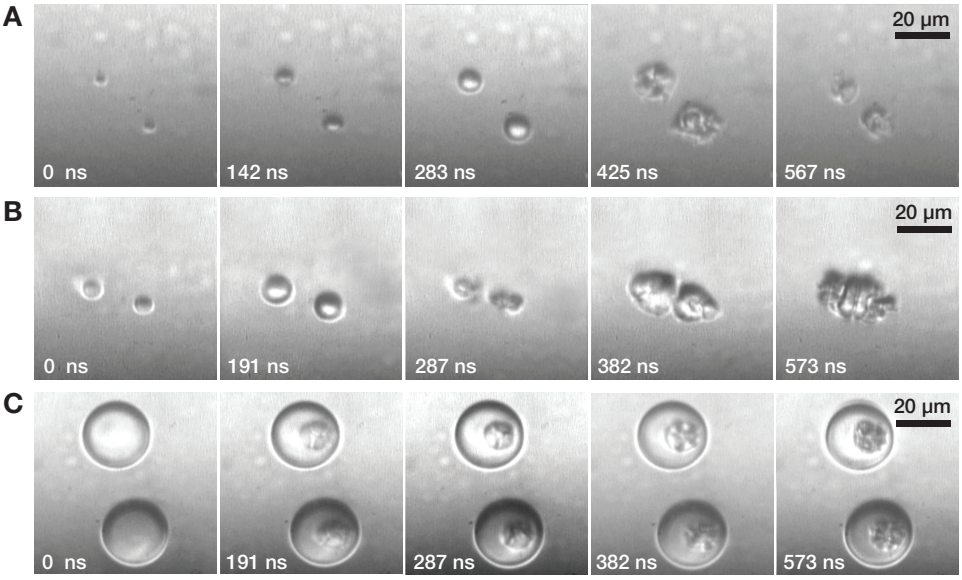

Figure 8.4: Acoustically triggered vaporization of two droplets with a radius of (A) 1.3 µm, (B) 3.6 µm, and (C) 12 µm. There is a remarkable degree of symmetry in the vaporization dynamics between two droplets of an identical size.

ter of monodisperse droplets with a radius of 12 µm radius was visualized. It was observed that clusters of droplets are much easier to vaporize than single droplets. The strong scattering of the incident acoustic wave may constructively interfere in a way similar to Bragg diffraction in solid-state physics to lower the nucleation threshold. Figure 8.5 shows the nucleation of such a hexagonal densely packed droplet cluster. The image at t = 0.4 µs shows that the droplet at the geometric center of the droplet cluster nucleates first. At t = 0.9 µs the primary nucleus has expanded and secondary nucleation sites appear in three nearby droplets. Please appreciate that the lines through both secondary nuclei in each droplet pass through the center of the droplet that nucleated first. The subsequent conversion of PFP liquid into vapor is shown by the image taken at t = 1.2 µs. It is remarkable that only the 3 closest neighbours above the first nucleating droplet undergo a secondary nucleation, but not the three lower ones. This can be attributed to the fact that the upper droplets have more neighbouring droplets. The ultrasound reflected from monodisperse droplets arranged into symmetric order can positively interfere and it may thereby decrease the nucleation threshold. Please note that the droplet on the left vaporizes more violently

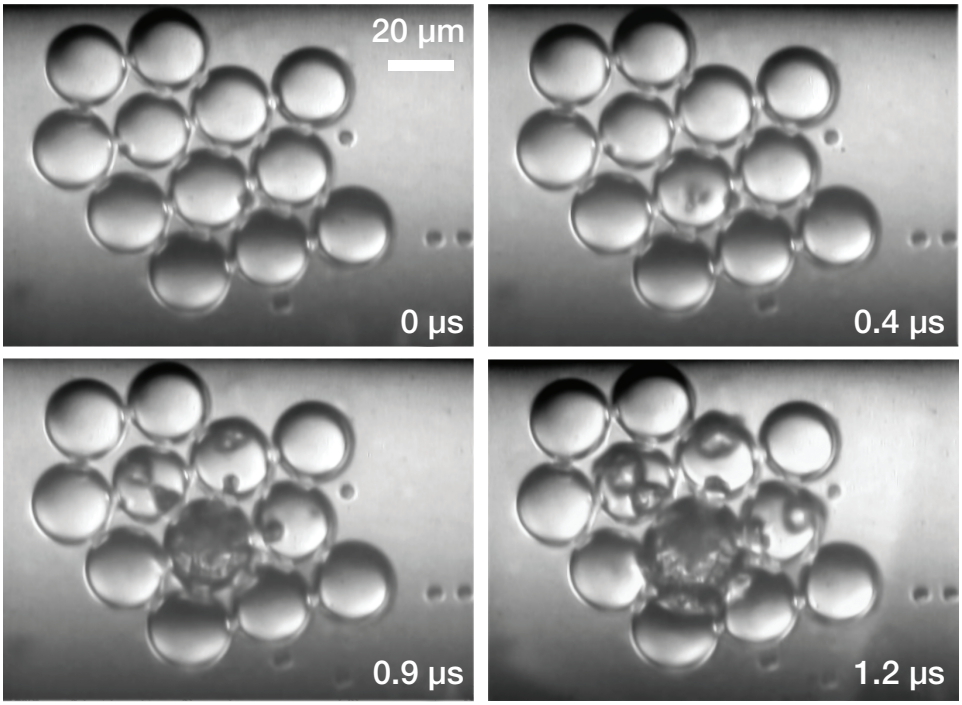

Figure 8.5: Vaporization of a hexagonally aranged cluster of monodisperse droplets with a radii of 12 µm. The vaporization is triggered by a 10-cycle, 3.5 MHz ultrasound wave at a peak negative pressure of 3.1 MPa.

than the droplet on the right and here the explanation is the same, namely that the droplet on the left has more neighbouring droplets that can scatter the acoustic. The scattered waves increase the local acoustic pressure through positive interference.

8.4 Conclusions

Flow-focusing devices produced with standard soft-lithography techniques can be efficiently used to produce monodisperse droplets down to a radius of 2 μm with a size distribution with a FWHM of the order of 5%. A second technique makes use of the simple and relatively cheap PDMS flow-focusing device with a nozzle of micrometer size to produce monodisperse droplets with radii down to 300 nm at high production rates through the condensation of micrometer sized vapor bubbles. Droplets can be at even smaller size, down to approximately 150 nm in radius, with great control, but at

lower production rates, in a device that comprises a nano-microchannel interface etched in glass. Together, these three techniques cover the range of droplets sizes potentially interesting for medical applications. The experiments show that the vaporization dynamics of monodisperse droplets shows an exceptional degree of repeatability. It was found that the uncertainty in the thresholds for vaporization of monodisperse droplets falls below 5% of the driving pressure. Altogether, the nucleation dynamics of monodisperse droplets was found to be symmetric, well-controlled and reproducible. A narrow step-response of ADV is highly desirable for clinical applications with phase-change agents such as tumor imaging and drug-delivery with ultrasound.

Acknowledgments

This project was funded by NanonextNL. The authors warmly thank Elena De Castro for constructive discussions on microfluidic devices. The authors are also grateful to the staff of Nanomi (Oldenzaal, The Netherlands) for their assistance in the sizing experiments of the nanodroplets.

9

Acoustic bubble counting and sizing for cardiopulmonary bypass systems: an in-vitro characterization

The sizing and counting performance of two clinically available acoustic bubble counters was measured in an in-vitro *setup with full control over bubble size, bubble position, bubble velocity, and bubble concentration. Monodisperse bubbles with a radius of 43.0* μm *produced in a flow focusing lab-on-a-chip device were first optically recorded using high speed imaging and subsequently guided through the bubble counter system at 11 different lateral positions. Despite the monodispersity of the introduced bubbles the counters show a large variation in the measured bubble sizes. Moreover, the measured sizes are strongly dependent on the position of the bubbles within the probes. The BCC200 system counts bubbles accurately, however it overestimates the total gas volume by a factor 20 due to an overprediction of the bubble size. The EDAC system largely overestimates the number of injected bubbles, but inaccurate bubble sizing at bubble diameters much smaller than the actual bubble size leads to a total measured gas volume that is overpredicted only by a factor two. More accurate bubble counter systems need to be developed to enable studies on detailed gaseous microemboli characterization in cardiopulmonary bypass systems and to quantify their potential deleterious effects on the cardiac patient.*

[1]Submitted as: T. Segers, M. C. Stehouwer, F. de Somer, M. Versluis, *Acoustic bubble counting and sizing for cardiopulmonary bypass systems: an* in-vitro *characterization*, J. of artificial organs, (2015)

9.1 Introduction

During cardiac surgery with cardiopulmonary bypass (CPB) microbubbles, or gaseous microemboli (GME), are always detectable in the arterial line and these microbubbles may reach the arterial circulation of the patient. The microbubbles originate mainly from interventions by the perfusionist, e.g. through air entrainment in a venous reservoir with a low volume level or through the administration of (drug-containing) liquids where the larger bubbles are fractionated into smaller GME by the different components of the CPB circuit[203]. GME are considered to contribute to the adverse outcome of cardiac surgery and they are associated with brain injury[204] as was statistically shown in several studies where transcranial Doppler ultrasound (TCD) imaging was used to measure GME loads *in-vivo*[205–207]. However, with TCD only the presence of scatterers can be detected and no quantitative correlation between the size and the number of bubbles with the severity of the damage can be obtained. It is hypothesized that the total number of introduced microbubbles may correlate with the amount of mechanical damage to the endothelium and that the size of the microbubbles correlates to the duration of ischemia of the microcirculation[204]. However, it is very difficult to measure the microbubble sizes, their number and concentration accurately in an optically opaque liquid.

Ultrasound techniques are explored already for decades for bubble counting and sizing in liquids[131,208]. Two commercially bubble counters for medical use are available since the early 2000s: the BCC200 (Gampt GmbH) and the EDAC (Luna Innovations Inc). Numerous studies have been conducted evaluating the air removal properties of CPB circuits and their components using these bubble counters[209–214]. However, validation of the bubble counters is difficult since there is a 3 orders length scale difference between the microbubble size and the tubing diameter which complicates optical sizing of the bubbles, even in a transparent blood substitute. De Somer *et al.*[215] performed optical and acoustical bubble sizing experiments with the BCC200 and the EDAC system. Measurements with large amounts of bubbles were performed where the bubble concentration was measured using light scattering. It was concluded that both bubble detectors had major limitations in the detection of high bubble concentrations. This is however inherent to acoustic pulsed-Doppler sizing techniques. The achievable resolution is limited by the acoustic wavelength, the time of flight of the echoes and the amount of acoustic pulses per pulsed-Doppler time window. De Somer *et al.*[215] also criticized the sizing capabilities of both systems. On the other hand, a polydisperse bubble size distribution was used which only allows for

a statistical correlation between the injected and the acoustically measured bubble sizes.

Here, we present acoustic bubble sizing measurements with full control over the bubble size, bubble position, bubble velocity, and bubble concentration. Monodisperse bubbles are generated and directed one-by-one past the ultrasonic detectors of the acoustic bubble counters. The position of the monodisperse bubbles in the detection volume was varied to gain insight in the sizing accuracy as a function of the bubble position. Optical microscopy combined with high-speed imaging was employed to image every single bubble. This allowed for the position-dependent and time-dependent relation of the detected bubbles to the actual amount of bubbles. First, acoustic bubble sizing theory is briefly discussed. Then the experimental setup is described. In the Results section we present the acoustically measured bubbles sizes and compare those with the optically measured bubble sizes. Furthermore, the ratio of the actual amount of injected bubbles to the detected amount of bubbles as a function of the position of the bubble within the detectors is presented. Finally, we discuss the measured data and finish with the conclusions.

9.2 Bubble sizing theory

Bubbles are highly efficient scatterers of ultrasound due to the acoustic impedance mismatch between their gas core and the surrounding liquid. This property is exploited in clinical ultrasonography where contrast enhancement can be achieved through the injection of microbubbles as ultrasound contrast agents[129]. The microbubbles are resonant to the ultrasound pressure field and the resulting radial oscillations produce a strong scatter echo. Acoustic bubble counters employ an ultrasound frequency that is much higher than the resonance frequencies of the bubbles they aim to measure. In this so-called geometrical scattering regime the scattering cross-section, i.e. the ratio of the amount of scattered power by a bubble with radius R to the intensity of the incident acoustic wave, is linearly dependent on the cross-sectional area of the bubble[131]. From energy conservation in a lossless medium it can be derived that the scattered pressure amplitude P_s at a distance r away from the bubble is:

$$P_s(r) = \frac{R}{r} P_A(R) \tag{9.1}$$

for a plane wave with acoustic pressure amplitude $P_A(R)$ at the bubble wall[216]. Eq. 9.1 shows that there is a linear dependency between the bubble

size and the amplitude of the scattered pressure wave. Thus, the bubble size R can be determined directly from the scattered pressure amplitude P_s when the distance between the bubble and the receiving element r is known and when the transmit pressure field is well calibrated in order for the pressure amplitude at the bubble wall $P_A(R)$ to be known.

Both, the BCC200 and the EDAC use this geometrical scattering principle to measure bubble sizes with a technique called pulsed-Doppler. A pulser-receiver circuit transmits short ultrasound pulses under a fixed angle θ with respect to the blood flow direction using a single element transducer, see Fig. 9.1A. Between each transmitted pulse the piezo transducer is used as a receiver to record the bubble echo, see Fig. 9.1B. A time window is used in which several pulses are transmitted and recorded. When a single bubble passes through the ultrasound field within this time window, the amplitude of the resulting echo signal first increases and then decreases (Fig. 9.1B). Echoes from non-moving objects do not have this echo response and it is therefore used to discriminate moving from non-moving scatterers based on the Doppler principle. The bubble size is determined from the amplitude maximum in the echo envelope of a single time window. The BCC200 system sizes only the largest bubble echo in the echo envelope within a time window, A_1 in Fig. 9.1B. It has a time window of 5 ms and therefore the maximum amount of single bubbles that can be detected is 200 bubbles per second. The EDAC system uses a tracking algorithm to track all moving echoes within the time window and it calculates a bubble size from all local envelope maxima within the time window[217,218], A_1 and A_2 in Fig. 9.1B.

The distance of the bubble to the transducer and the acoustic pressure at the position of the bubble needs to be known, see Eq. 9.1. The BCC200 system uses a reference echo from a reflector behind the measurement volume as a measure for the acoustic pressure P_A in the measurement volume[219]. The distance from the bubble to the transducer can be calculated from the time of flight of the echoes. However, the BCC200 system does not account for the exact position of the bubble[220] and it is therefore a potential source of error in the size determination. It is unknown if the EDAC system accounts for the exact position of the bubble as we have no direct access to the sizing algorithms in the software. In addition, the acoustic pressure field generated by a single element transducer is not uniform[221]. As a result, the acoustic pressure at the bubble position is unknown if the position of the bubble in the acoustic field is unknown. Finally, the sensitivity of the piezo transducer to acoustic waves from point sources located away from the natural focus of the transducer, i.e. echoes originating from bubbles close to the boundaries of the measurement volume, decreases with increas-

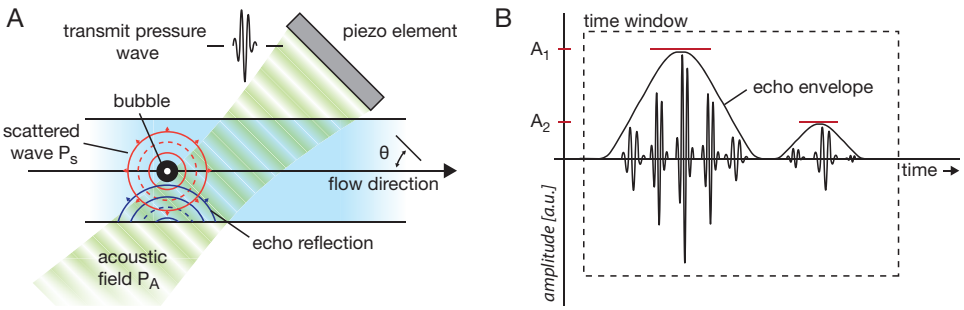

Figure 9.1: A) Schematic representation of the pulsed-Doppler technique. A piezo element transmits ultrasound pulses under a fixed angle θ with respect to the blood flow direction. In between the transmit pulses, the scattered pressure waves originating from a bubble passing through the acoustic field are recorded by the same piezo element. B) The amplitudes of the recorded scattered waves are first increasing, then decreasing when a bubble passes through the acoustic field. The bubble echo with amplitude A_1 is reflected from the wall of the CPB tube and it can results in a secondary echo with amplitude A_2.

ing lateral distances with respect to the natural focus. Thus, the detected size of a bubble located at different positions in the measurement probe of the bubble counter systems can be different from location to location depending on: 1) whether the sizing algorithm calculates the distance between the bubble and the receiving element, 2) the uniformity of the transmitted pressure field, 3) the uniformity in the position-dependent sensitivity of the piezo in receive mode. For all these reasons, we now investigate experimentally the bubble sizing capabilities of the BCC200 and the EDAC systems at different bubble locations in their measurement volume.

9.3 Experimental setup

Monodisperse bubbles were produced in a microfluidic chip made in polydimethylsiloxane (PDMS) using standard soft lithography techniques[106]. The chip is comprised of a planar flow-focusing device[149] in which a gas thread is focused between two liquid co-flows through an orifice to release monodisperse bubbles (Fig. 9.2A). A fused silica capillary with an inner diameter of 150 μm positioned in the outlet channel of the flow-focusing geometry downstream of the orifice and in-line with the microfluidic channel guides the bubbles one-by-one to the measurement volume (Fig. 9.2B). The bubbles were produced at a rate of approximately 10 bubbles per second, the orifice size was 100 μm and the average radius of the produced bubbles

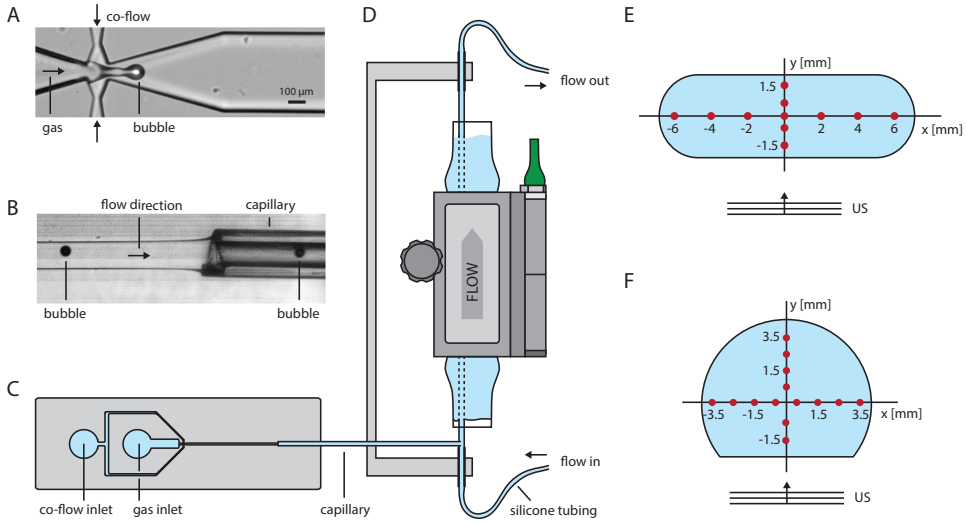

Figure 9.2: A) Monodisperse bubbles are produced in a flow focusing device microfluidic chip. B) The bubbles produced on-chip are transported through a fused silica capillary and injected into an acoustically transparent silicone tube (C). The silicone tube guides the bubbles at different positions through the detectors. E) Cross-section of a 0.95-cm diameter CPB tube mounted in the BCC200 probe holder. F) Cross-section of the CPB tube mounted in the EDAC probe holder. Measurements were performed at the locations marked by the red dots.

was 43 µm with a polydispersity index[222] of less than 3%.

The capillary guiding the microbubbles to the probes of the bubble counter was imaged using an inverted microscope system (Nikon Instruments, Eclipse TE2000-U) equipped with a 6× magnification objective lens connected to a high-speed camera (Photron SA1.1) operating at 125 fps to image every bubble that was directed to the BC200 and EDAC probes. The optical resolution was 3 µm/pixel and it therefore allowed for accurate optical sizing of the produced bubbles.

The monodisperse bubbles were injected into a 500 µm inner diameter acoustically transparent silicone tube that was guiding the bubbles through the bubble counter probes at a fixed position. To compensate for the larger cross-section of the silicone tube, as well as to be able to control the translational velocity of the bubbles, a flow rate-controlled syringe pump was driving an extra flow through the silicone tube. The total flow rate of the system was 6.6 mL/min resulting in a translational bubble velocity of 1.1 m/s assuming that the bubbles are centered in the silicone tubing. This velocity matches the average flow velocity at a flow-rate of 4.8L/min in

standard clinical 0.95 cm diameter CPB tubing.

The BCC200 probe was clamped centered around the CPB tube extending 1 cm upstream and 1 cm downstream from the probe (Fig. 9.2D). The space between the 500 μm silicone tube and the CPB tube was sealed at the bottom of the CPB tube with a thin rubber membrane allowing for the positioning of the 500 μm tube within the CPB tube while the CPB tube was filled with water for acoustic coupling. The probe was held by a tailor-made clamp and positioned on the microscope stage next to the flow-focusing chip. The acoustically transparent silicone tube was stretched, as per instruction, through the probe's measurement volume, parallel to the walls of the CPB tube, in a U-shaped holder mounted on an x-y translation stage to vary the tube position in the probe volume (Fig. 9.2D). Measurements were performed at 11 different locations marked by the red dots in Fig. 9.2E. The EDAC probe was mounted in the a similar way except that the EDAC probe has to be mounted on a disposable plastic probe holder that is positioned in-line with the CPB tubing. The probe holder has a different cross-section from the one of the BCC200, as shown in Fig. 9.2F. The red dots in Fig. 9.2F represent the 14 locations at which measurements were performed with the EDAC system. A measurement series was conducted by simultaneously starting a high-speed recording and a bubble counter measurement. Subsequently, the gas flow to the flow-focusing device was opened to start the monodisperse bubble production. A total measurement window of 2.5 minutes was used. The high-speed recordings contained 18,750 frames per measurement location and they were processed frame by frame with an automated image processing algorithm programmed in Matlab. The sizing method resulted in a sub-pixel accuracy in the determined bubble radii[85].

9.4 Results

A typical measurement with the BCC200 and EDAC systems is presented in Fig. 9.3. Bubbles with a mean size of 43.0 μm and a standard deviation of 0.9 μm are introduced in the measurement section. Figure 9.3A shows the optically measured size distribution (black) and the acoustically measured size distribution (blue) of the BCC200 system at position [0,0] in Fig. 9.2E. Indeed, a relatively narrow acoustically measured size distribution is observed, however the absolute bubble size is overestimated by a factor 2 (R = 90 μm ± 22 μm). The bubble counts over time are shown in figure 9.3B. The rate at which bubbles are produced fluctuates due to transient pressure and flow variations in the microfluidic bubble production chip (black dots). The total acoustic number count is 1.2 times larger than the total optical

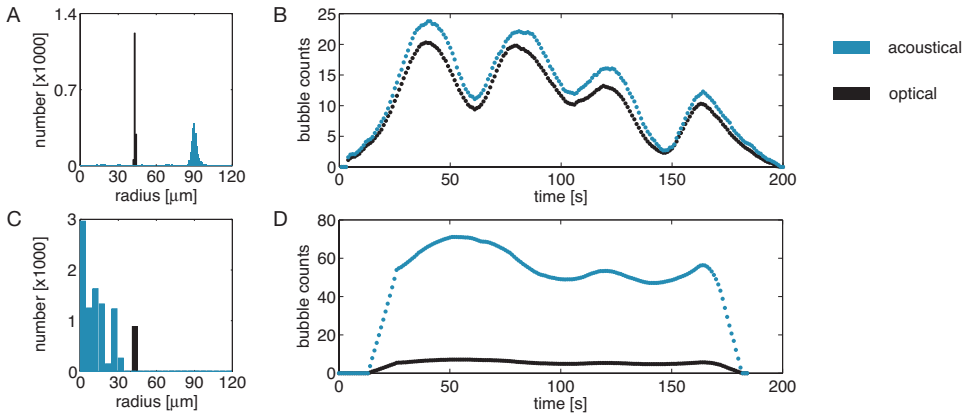

Figure 9.3: A) Optically and acoustically measured bubble size distributions with the BCC200 system at position [0,0] in Fig. 9.2E. B) Bubble counts as a function of time measured with the BCC200 system. C) Optically and acoustically measured size distributions with the EDAC system at position [0,0.5] in Fig. 9.2F. D) Bubble counts as a function of time measured with the EDAC system.

number count.

A typical measurement performed with the EDAC system at position [0,0.5] in Fig. 9.2F is shown in Fig. 9.3C and D. The acoustically measured size distribution shows a high number of counts at bubble sizes down to the smallest detectable bubble size by the EDAC system (2.5 µm in radius). Thus, the EDAC system largely overestimates the amount of bubbles passing its probe and this is confirmed by the number count in figure 9.3D. A closer look at the optically measured number count per second shows similar time dependent number count fluctuations as the acoustically measured time dependent number counts. However, the EDAC system overestimated the bubble passing-rate on average by 9-10 times at this measurement location for the 43 µm bubbles.

The measurements were repeated at all positions marked in Fig. 9.2D with the BCC200 system. The mode of the acoustic bubble counts (bubble radius with largest count number) at all measurement positions is represented by the blue horizontal lines in Figs. 9.4A and B. At two measurement positions ([-4,0] and [4,0]) the system measures a bimodal size distribution with two local maxima, represented by the two blue lines at these measurement locations. Since the size distributions are not symmetrically distributed around the mode, the standard deviation of the data on both sides of the mode is shown (black markers). Figures 9.4C and 9.4D show the normalized

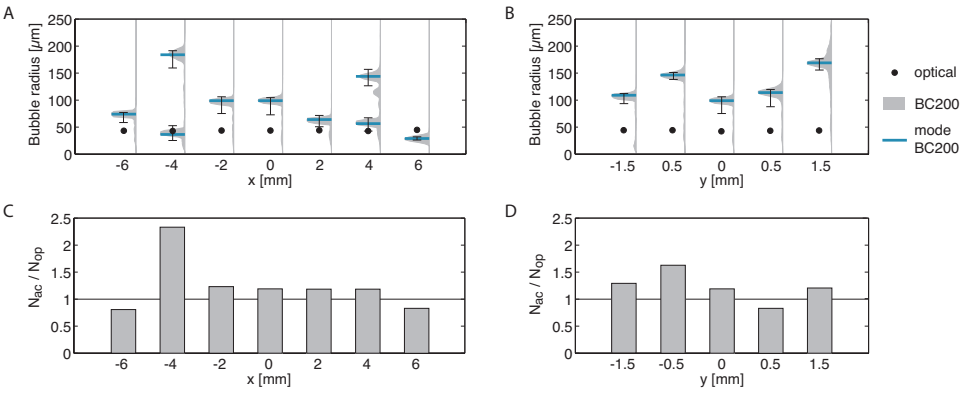

Figure 9.4: Acoustically measured size distribution (gray areas) as a function of the horizontal (A) and vertical (B) bubble position in the BCC200 system. The blue dashes represent the mean of the size distribution of which the standard deviation on both sides is shown by the vertical black dashes. The optically measured bubble radius is represented by the black dots. Figures C and D show the acoustic to optical bubble count ratio for horizontal and vertical bubble positions, respectively.

acoustic bubble counts at each measurement location. A ratio close to one was found for the total acoustic bubble count to the total optical number count. From the size distributions and the bubble counts the total injected gas volume and acoustically measured gas volume are determined and they were 8.3 μL and 198 μL, respectively. While the BCC200 system accurately counts bubbles, it overestimated the total injected gas volume by a factor 25 due to the overprediction of the bubble sizes by a factor 2 to 3.

The size distributions measured with the EDAC system at the measurement locations shown in Fig. 9.2F are shown in Figs. 9.5A and B. Please note the local maximum close to the optical measured bubble size (black dots). As with the previous size distribution all acoustically measured size distributions show large number counts at bubble radii down to the smallest detectable bubble size. No standard deviations were calculated because of the non-Gaussian nature of the acoustically measured size distributions. The ratio of the total acoustic bubble count and the total optical bubble count at every measurement position is shown in Figs. 9.5C and D. On average, the number of bubbles passing the probe is overestimated by a factor 9 by the EDAC system for the injected bubble radius of 43 μm. At bubble positions close to the center of the channel and close to the wall opposing the transducer the mismatch between the acoustic bubble count and the optical bubble count is the largest. The total injected gas volume and the

total measured gas volume were 7.2 µL and 13.8 µL, respectively, thus, with an overprediction approximately by a factor 2.

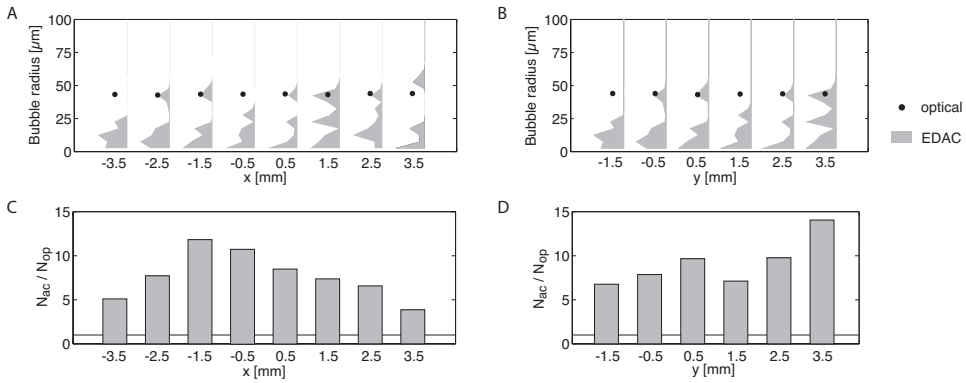

Figure 9.5: Acoustically measured size distribution (gray areas) as a function of the horizontal (A) and vertical (B) bubble position in the BCC200 system. The blue dashes represent the mean of the size distribution of which the standard deviation on both sides is shown by the vertical black dashes. The optically measured bubble radius is represented by the black dots. Figures C and D show the acoustic to optical bubble count ratio for horizontal and vertical bubble positions, respectively.

9.5 Discussion

While monodisperse bubbles were injected, the BCC200 and the EDAC systems were shown to measure a large dispersion in bubble sizes depending on the position of the bubbles in their measurement volume. Equation 9.1 shows that when the exact distance between the bubble and the receiving element is not taken into account that this can lead to position-dependent sizing errors. Regarding the BCC200 system, the maximum distance between two bubbles in the plane normal to the surface of the piezo element is approximately 4 mm (Fig. 9.2). By assuming that the piezo element is positioned 1.5 cm away from the CPB tube a 20% difference in detected bubble size can be calculated for two bubbles of the same size, with the bubble far away from the piezo element being effectively detected smaller. For the EDAC system the difference is 30%. However, no clear decrease in acoustically measured bubble sizes is observed in Figs. 9.4B and 9.5B for increasing bubble-to-transducer distances, i.e. for increasing y-values. What is expected to be of larger influence here, is a non-uniform acoustic pressure amplitude distribution P_A in the measurement volume, an artifact that is

not accounted for in the sizing software. Single-element piezo transducers produce acoustic fields with a spatial pressure distribution which depends on the geometry of the piezo element. The BCC200 probe contains a rectangular piezo element with a cross-section of 1×2 cm^2 and it is known to produce an acoustic field with two pressure maxima equally spaced over the transducer length at the half width of the transducer[220,221]. The positions of the pressure field maxima correlate with the two maxima in the measured bubble sizes at the locations [-4,0] and [4,0] in Fig. 9.4A, and are symmetrically distributed around the center of the measurement volume. At the maxima, bimodal size distributions are measured possibly originating from secondary bubble echoes upon reflection of the primary echo at the CPB tube wall. Since the BCC200 system only measures the size of the largest echo in its Doppler time window this can only occur when the primary and secondary echoes are recorded in two different time windows. The secondary echo will itself be reflected at the CPB tube wall or in case of the EDAC system, at the plastic walls of the probe holder. In this way, an amplitude cascade of bubble echoes will originate from a single bubble insonified by a single acoustic pulse. Since the EDAC processes all measured echoes[218], the EDAC size distributions have large number counts at bubble radii smaller than the injected bubble radius. The probe of the EDAC contains a 1 cm diameter circular piezo transducer generating an axisymmetric acoustic pressure field with a maximum at the center[217,221]. This correlates to the maximum in the acoustic to optical number count ratios at the center of the measurement volume (Fig. 9.5C). We hypothesize as follows: higher pressures result in larger secondary echoes with an amplitude above the detection threshold. The EDAC probe needs to be clamped on a disposable probe holders mounted in-line with the CPB tubing. The holders are made out of plastic which reflects nearly all acoustic energy resulting in secondary bubble echoes with relatively high amplitudes. Thus, probe walls fabricated out of acoustic energy absorbing materials will be more suited for precise acoustic bubble measurements. Moreover, a high degree of control over the acoustic field is necessary when designing accurate bubble sizers. Inspired by medical ultrasound imaging, the use of multi-element array transducers could be explored in future designs as excellent acoustic field shape and amplitude control using multi-element transducers allows for accurate echolocation.

A few words on the invasive measurement procedure with the 500 μm inner diameter silicone tube inside the probes are in order. For both bubble counters, it was verified that the silicone tube does not have an influence on the number of acoustically measured bubbles. Control measurements were

performed in a closed circuit where water was pumped from a reservoir at a flow rate of 2 L/min through the CPB tubing. Bubbles were injected directly in the flow through the fused silica capillary as described before. A clinical 5 μm filter (Maquet, Rastatt, Germany) and a clinical bubble trap (Quart, Maquet, Rastatt, Germany) were incorporated in the circuit to remove the injected residual bubbles that were not removed through buoyancy in the big reservoir. The BCC200 system measured a total number count that was 1.16 times higher than the total number of injected bubbles, which is in very close agreement with the silicone tube measurements. For the EDAC system, the total number count was 8.8 times higher than the optical number count which is also in good agreement with the silicone tube measurements. The effect of the silicone tube on the bubble sizing could not be measured since it was not possible to control the position of the bubbles without the silicone tube in place. However, it is expected that the silicone tube attenuates the insonifying sound wave and resulting bubble echo. Thus, a slightly smaller acoustically measured bubble size is expected when the bubbles are positioned within the silicone tubing.

Water was used during the measurements instead of whole blood. The attenuation of ultrasound in blood is 0.2 dB/cm/MHz[223], which is approximately 100 times higher than the attenuation coefficient of water[223]. The amplitude of an ultrasound wave of 2 MHz (BCC200) and 4 MHz (EDAC) traveling through blood will have a 3% and 6% lower amplitude, respectively, for every 1 cm of propagation distance as compared to the same wave that travels through water. Because of the linear relationship between the acoustically measured bubble size and the pressure amplitude, the effect of water over blood is considered to be negligible in comparison to the observed sizing errors.

Monodisperse bubbles of a single size of 43 μm were used here and the sizing and counting performances were not examined for other bubble radii. However, the measurements clearly reveal the flaws of both bubble counters regarding their sizing and counting capabilities. For the EDAC system it is expected that bubble radii larger than examined here will result in an overestimation of the bubble concentration to an even higher degree because the larger bubbles will produce larger primary echoes, and as a result the more secondary echoes will be detected above the noise level. Conversely, smaller bubbles are predicted to produce a smaller amount of secondary echoes.

The bubble concentration used in this study was deliberately kept low, to obtain the best case sizing and counting properties of the systems. The distance between two bubbles passing the ultrasound probes was approximately

4 cm as can be calculated from the flow rate and the bubble production rate. In a clinical setting, during CPB the amount of detected microbubbles per unit time highly fluctuates and depends strongly on the interventions of the perfusionist, as can be seen from Fig. 9.6. The BCC200 system was employed to measure microbubble activity in the arterial line during two clinical CPB procedures. Figure 9.6 shows that the maximum bubble count was 120 bubbles per second. This is well below the maximum detection rate of the BCC200. Therefore, the measured number of bubbles can be assumed to be in good agreement with the actual amount of bubbles that passes the arterial line. Thus, the single bubble measurements performed in this paper are a good indication of the actual sizing and counting characteristics of the bubble counter systems during *in-vivo* CPB procedures. On the other hand, during CPB interventions, clusters of closely spaced bubbles may be passing the detectors of the bubble counters. It can result in an underestimation of the total amount of bubbles measured with the BCC200 since it only sizes and counts the largest echo in a time window. This would interfere less with the measurements performed with the EDAC system as it counts all detected bubble echoes. Furthermore, we observed that the detected size distribution becomes broader with increasing bubble concentration (measured up to a rate of 100 bubbles per second), which is likely caused by secondary bubble echoes measured in the next time window.

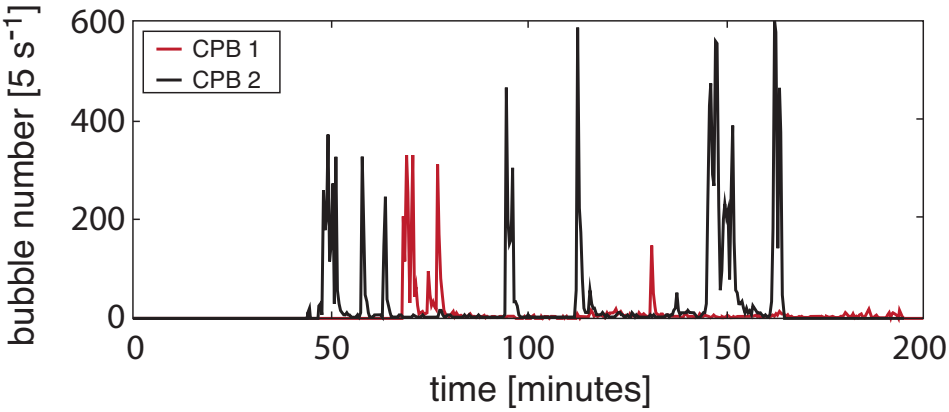

Figure 9.6: Measured bubble count during two clinical CPB procedures. The measurements were performed with the BCC200 system.

9.6 Conclusions

The BCC200 and the EDAC systems are shown to inaccurately size microbubbles despite the low bubble concentrations used in the present study. The measured bubble size is strongly dependent on the position of the bubble within the measurement volume of the device. The BCC200 system is shown to accurately count the number of bubbles because it only sizes and counts the largest bubble passing its probe. The EDAC system processes all detected echoes and since a single bubble produces multiple secondary echoes through reflections at the tubing wall, the number of bubbles counted is largely overpredicted. However, the total gas volume is only overpredicted by a factor two as a result of the decaying nature of the secondary bubble echoes. The BCC200 system overestimates the total gas volume by 20 times due to the largely overpredicted bubble sizes, this however can be solved by recalibration of the device. The different sizing and counting characteristics of both devices make a comparison of mutual experiments of little value. However, both devices can be used to study air removal characteristics of CPB components as, well as for monitoring GME production during CPB interventions. Whether bubble size, bubble count or total gas volume causes potential deleterious effects on the cardiac patient is unknown until today. Therefore new more accurate devices are needed to enable studies on detailed GME characterization in CPB systems and, more importantly, to assess their potential deleterious effects on the cardiac patient.

Acknowledgements

We thank Gampt GmbH for kindly responding to all our questions. We also want to thank Gert-Wim Bruggert, Martin Bos, and Bas Benschop for their skilful technical assistance. This work is supported by NanoNextNL, a micro and nanotechnology consortium of the Government of the Netherlands and 130 partners.

10

Conclusion, outlook, and technology assessment[1]

Ultrasound contrast agents are used worldwide in a clinical setting to perform contrast enhanced ultrasound imaging. They consist of microbubbles that are highly echogenic owing to the large compressibility of the microbubble gas core. The echogenicity allows for their use as a blood pool agent when injected intravenously. Resonating microbubbles generate harmonics of the driving ultrasound field that further boost the ultrasound contrast over the linear tissue echoes. The bubbles are coated with a biocompatible phospholipid shell that changes dramatically the response of the bubbles to the driving ultrasound field. Moreover, there has been experimental evidence that the packing density of the phospholipid monolayer is the key factor in the generation of its nonlinear response[75]. The packing density can vary from bubble to bubble, therefore even bubbles of the same size can have a different acoustic response[40,109]. The use of contrast agents has more applications than just plain ultrasound imaging: microbubbles covered with targeting ligands can be used for molecular imaging with ultrasound and drug delivery with bubbles and ultrasound. The commercially available contrast agents contain bubbles that have radii ranging from 1 to 10 μm and therefore, their contrast is limited to the blood pool. Superheated nanodroplets can extravasate leaky tumor vasculature to passively aggregate in a tumor where their ultrasound-triggered vaporization results in microbubbles with a size on the order of those of ultrasound contrast agents. Thus, phase change agents have a high potential for tumor imaging, localized drug delivery and the monitoring thereof with ultrasound. Conventional production methods result in polydisperse bubbles and droplets and the efficiency of their application can be increased dramatically by decreasing their polydispersity. In this thesis, we show that biocompatible monodisperse microbubble, microdroplet, and nanodroplet suspensions can

[1]Technology assessment is an obligation for NanoNextNL PhD students to bridge the gap between scientifically innovative research and societal impact.

be efficiently produced using microfluidic techniques.

We have demonstrated that contrast bubbles can be sorted to their acoustic property by a novel microfluidic sorting technology termed 'acoustic bubble sorting' (Ch. 2). The coated microbubbles are sorted on-line in a simple lab-on-a-chip device using a traveling acoustic wave. The resonant bubbles are separated from the non-resonant bubbles by the primary radiation force. We show that the scattering and attenuation of a suspension of acoustically sorted bubbles is higly uniform, in frequency and in their pressure dependent response. In addition, we show that its scattering and attenuation can be modeled by integration over the full nonlinear response of all the bubbles in the ultrasound field using a unique set of shell parameters (Ch. 4). The acoustically uniform response of bubbles sorted to their acoustic property has a high potential for targeted molecular imaging, drug and gene delivery applications using ultrasound.

Contrast agent microbubbles can also be efficiently sorted with a high degree of control, and without the need for an external sorting force purely by the expanding geometry of a microfluidic flow field in a pinched flow fractionation device (Ch. 3). The sorting of bubbles, pinned to a wall of a narrow channel with a size on the order of the bubble size, is achieved through the expansion of the narrow channel in a 30 times broader channel. We showed that it is essential to include the rotation of the bubble when it translates through the narrow channel as the rotating bubble changes the local flow field. Pinched flow fractionation is simple, it is highly controlled, its sorting is independent of the flow rates, and it is ideally suited for parallelization. Therefore, it has a great potential to be clinically used for improved (molecular) imaging and drug delivery with ultrasound and bubbles.

We have shown that the acoustic energy scattered by a sorted bubble population is at least ten times higher that the energy scattered from a native contrast agent with equal amount of energy absorption at the first harmonic of the driving frequency (Ch. 5). At the second harmonic, at least 20 times more energy is scattered by a sorted bubble population. Therefore, the efficiency of the sorted bubble suspensions was shown to be 10 to 20 times higher than that of the native agent. In addition, we showed that the uniform pressure and frequency dependent resonance behaviour of the sorted bubbles allows for the selection of an imaging frequency and driving pressure such that the scattering and energy absorption are confined to the acoustic focus of the transmit field. The narrowband pressure dependent response of sorted agents can thereby be exploited to minimize shadowing effects in deep tissue contrast enhanced ultrasound imaging. Thus, monodispersity

not only increases the sensitivity of contrast enhanced ultrasound imaging, it also increases its efficiency.

A second approach to obtain a monodisperse phospholipid coated bubble suspension is the direct formation of bubbles in a flow focusing device. We have shown that bubbles can be produced at rates up to 1 million bubbles per second from a single nozzle and, independent of the flow-focusing nozzle shear rate, the nozzle dimension, or the production rate, the formed bubbles *always* dissolve to reach a final stable bubble size that is 2.55 times smaller than their initial size (Ch. 6). In addition, the amount of lipid shell material on the bubble surface does not change after formation, not when the bubble dissolves, nor when it expands in volume. The formed bubbles are stable in size for at least two hours and attenuation measurements together with modeled attenuation curves in which the full non-linear bubble response was included revealed that the shell stiffness of the bubbles increased from 0.8 N/m to 2.5 N/m with increasing number of insonations due to the loss of emulsifier molecules.

We also showed that the flow-focusing technique is efficient in the highly controlled formation of monodisperse phase change droplets at high production rates down to a size of 2 μm in radius (Ch. 8). Nanodroplets were produced by recondensation of micron-sized PFC gas bubbles formed by flow-focusing. We showed that by using the recondensation technique it is possible to produce a narrow size distribution droplet suspension with a mean diameter down to 300 nm. These small droplet sizes can also be produced, with great control, but lower production rate, in a device that comprises a nano-microchannel interface etched in glass. Together, these three technics cover the range of droplet sizes that are of interest for medical applications such as the extravasation through leaky tumor vasculature (EPR effect). Vaporization of the produced monodisperse droplets, recorded using ultra high-speed imaging, showed that the vaporization dynamics of monodisperse droplets presents an exceptional degree of repeatability. It was found that the uncertainty in the thresholds for vaporization of monodisperse droplets falls below 5% of the required pressure. Altogether, the nucleation dynamics of monodisperse droplets was found to be symmetric, well-controlled and reproducible. A narrow step-response of ADV is highly desirable for clinical applications with phase-change agents such as drug-delivery with ultrasound.

It was shown that an efficient vaporization can be performed by driving phase-change PFP droplets at their fundamental resonance frequency (Ch. 7). This is an entirely different mechanism from the recently proposed focusing effect[175]. Good agreement was found between the modeled size-

dependent pressure amplification within the droplet and the measured size dependent vaporization probability. It is crucial for efficient droplet vaporization to use acoustic frequencies matching the resonance frequency of the droplet. Thus, droplet monodispersity is crucial in order to make efficient phase-change agents. We also showed that efficient vaporization is obtained by driving the droplets with multiple acoustic pulses. The presence of preexisting bubbles was shown to increase the vaporization efficiency by two orders of magnitude.

Uncoated bubbles with sizes larger than 10 μm present in the blood stream are potentially dangerous for several reasons. They can block the blood flow resulting in ischemia and they can mechanically damage the endothelium. During cardiac surgery bubbles are always present in the arterial line of the cardiopulmonary bypass system (CPB) and whether bubble size, bubble count or total gas volume causes potential deleterious effects on the cardiac patient is unknown until today. Using monodisperse bubbles, we have shown in an *in-vitro* setup that the counting and sizing capabilities of the two commercially available bubble counters for medical use are highly inaccurate (Ch. 9). More accurate devices are needed to enable studies on detailed gaseous microemboli characterization in CPB systems and, more importantly, to assess their potential deleterious effects on the cardiac patient.

The sensitive pressure-dependent scattering measurements and the attenuation measurements using a small amount of acoustic insonations presented in this thesis, are of great interest for the rapid characterization of contrast agents. It provides valuable insight into bubble shell parameters and it has the potential to improve the existing theoretical bubble dynamics models such as the popular Marmottant model[41]. The shell elasticity in the Marmottant model is constant for the range over which the bubble oscillates elastically and is zero for buckled and ruptured bubbles. From the scattering measurements presented in Ch. 4 it was observed that the scattering at the second harmonic frequency deviates from the modeled second harmonic scattering. Harmonics produced at low driving pressures mainly originate from the nonlinear properties of the viscoelastic bubble shell and the underestimation at a pressure of 10 kPa indicates that the shell is more nonlinear than described by the model. Moreover, it was shown that the dilatational viscosity may decrease with increasing dilatational rate[75,80]. With the sensitive pressure dependent attenuation measurements presented in this thesis, the decrease in the dilatational viscosity with the dilatation rate can be determined from the absolute magnitude of attenuation for small step changes in the driving pressure. Future studies may include the implementation of

more realistic nonlinear shell properties in the bubble dynamics models that can be experimentally verified by the characterization techniques presented in this thesis.

We have shown that the bubble surface is coated with phospholipids already when it passes through the flow-focusing nozzle and that the amount of lipids does not change after bubble formation, not when the bubble expands in volume, nor when it dissolves. However, it remains unknown where and by which mechanism the gas jet in the flow-focusing geometry is coated and at which time scales the coating process takes place. It would be of great interest to image the bubble formation at high speeds using fluorescent lifetime imaging (FLIM)[160]. An intense laser pulse excites fluorescent molecules that lose their fluorescence depending on their confinement. Thus, molecules confined in the lipid shell may be discriminated from freely floating ones by their fluorescence lifetime. Understanding the exact coating mechanism and adsorption dynamics is of high importance as it can potentially improve future microfluidic flow-focusing designs to increase the lipid adsorption rate and packing density. Moreover, it is has the potential to improve the fundamental understanding of the adsorption kinematics and the role of the different phospholipid components thereon.

In this thesis, it was shown that the response of monodisperse bubbles is very narrowband and highly sensitive to the driving ultrasound pressure and this feature can now be exploited by pulse-echo techniques to increase the contrast-to-tissue ratio. For instance, power modulation schemes would benefit tremendously from the narrowband pressure dependent response of monodisperse bubbles. The imaging frequency can be selected such that only at sufficiently high enough acoustic pressures a bubble response is generated. We have also shown that monodisperse bubbles can be of great interest for perfusion imaging with focused imaging transducers. Monodisperse bubbles can be employed in contrast-enhanced imaging to dramatically minimize shadowing effects in deep-tissue imaging, where imaging frequency and pressure can be selected such that bubbles resonate only in the acoustic focus where the pressure is at maximum. Altogether, we now have the excellent opportunity to increase the sensitivity en efficiency in contrast-enhanced ultrasound imaging and to boost emerging applications such as molecular imaging and drug delivery using ultrasound.

The methods presented in this thesis allow for the excellent control over the acoustic response of an UCA and the technology has the potential to improve healthcare. We now asses the presented technology and provide some possible directions that can be followed to make the technology marketable. Phase change agents did not reach the preclinical stage yet and the

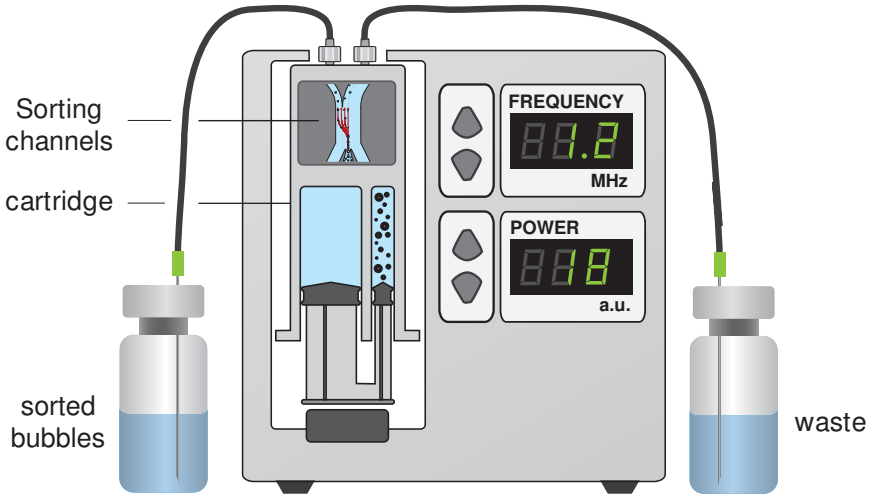

Figure 10.1: Bubble sorting concept.

scientific community first has to prove their value. Therefore, here we focus on microbubble technology alone.

In this thesis, three methods were presented by which a monodisperse bubble suspension can be obtained: 1) acoustic bubble sortig, 2) pinched flow fractionation, and 3) flow-focusing. The methods can be subdivided in two categories: sorting techniques for the enrichment of commercially available UCA and the direct formation of biocompatible phospholipid-coated bubbles by flow-focusing. The advantage of the sorting methods have over flow-focusing technique is that it will cost less effort to get approval of the agency for Food and Drug Administration (FDA) or the European equivalent, European Medicines Agency (EMA) for the clinical use of the produced bubble suspension. This results from the fact that sorting methods involve FDA and EMA approved UCA. The sorted bubbles are not substantially modified during the sorting procedure and the worst case scenario is the dissolution or fragmentation of bubbles due to the relatively large overpressures. However, this is not potentially dangerous after intravenous injection. On the other hand, we have shown in Ch. 6 that bubbles formed by flow-focusing need time to stabilize. It would be challenging to fabricate a bed-side device that produces stable highly reproducible monodisperse bubble suspensions that have properties that are independent of the manipulations of the enduser. The most important requirement is that the dissolution needs to be fully controlled. Another advantage of sorting techniques over flow-focusing is that any commercially available bubble suspension, and more importantly

any suspension that will be commercialised in the future, being purely for imaging, or loaded with targeting ligands or drugs, can be sorted. Until now it was shown that the formation of stable bubbles by flow-focusing is limited to very specific lipid formulations[65]. For all these reasons, the author's opinion is that monodisperse bubbles produced by flow-focusing should be produced in a factory, freeze dried, and sold in a vial similar to the current UCA. This approach is most feasible with a large established pharmaceutical company already active in the world of contrast agents.

Sorting techniques have the potential to be implemented as a tabletop medical device that can be developed and produced by an independent startup company. The acoustic bubble sorting method is scalable and it can easily be parallelized. A revenue model can be based on the marketing of disposable single use cartridges that contain many parallelized sorting channels that is packed under sterile conditions. Figure 10.1 shows an illustration of how such a cartridge may look like. It contains two compartments of a different size, the smaller one to fill with the native UCA and a bigger one to fill with saline to supply the co-flow. The cartridge is placed in a tabletop device that drives the flow through the disposable sterile sorting channels using disposable syringe-like plungers. The frequency and the pressure amplitude is set before the sorting and matched to the ultrasound imaging frequency to be used in the application. A disadvantage of the method may be that acoustic sorting is very sensitive to the acoustic pressure. Since UCA coated by different lipid formulation respond differently to ultrasound, it will be challenging to fully control the system with simple user friendly manipulations.

An easier approach may be found in a similar cartridge with many pinched flow fractionation (PFF) sorting channels. PFF does not require any external sorting force, i.e. it is passive, its sorting behaviour was shown to be flow-rate independent[84] and thus, it is very suitable for parallelization. At least 500 pinched flow fractionation channels with the dimensions of 1 mm in length, 500 μm in width and 20 μm in height fit easily in a 2.5 cm^3 block. The 500 sorting channels allow for the sorting of a typical vial containing 5 mL of UCA within 10 minutes. Thus, from the author's point of view the PFF sorting method is best marketed for relatively short term earnings. Once the PFF sorting is on the market, the startup company may start implementing the acoustic sorting technology in their existing tabletop bubble sorter. An idea for a better health care.

Bibliography

[1] J. R. Lindner, "Microbubbles in medical imaging: current applications and future directions", Nat. Rev. Drug Disc. **3**, 527–533 (2004).

[2] M. Overvelde, "Ultrasound contrast agents, dynamics of coated microbubbles", Ph.D. thesis, University of Twente (2010).

[3] A. L. Klibanov, "Microbubble Contrast Agents: Targeted ultrasound imaging and ultrasound-assisted drug-delivery applications.", Invest. Radiol. **41**, 354–362 (2006).

[4] E. Talu, K. Hettiarachchi, S. Zhao, R. L. Powell, A. P. Lee, M. L. Longo, and P. A. Dayton, "Tailoring the size distribution of ultrasound contrast agents: Possible method for improving sensitivity in molecular imaging", Mol. Imaging **6**, 384–392 (2007).

[5] M. Overvelde, V. Garbin, B. Dollet, N. de Jong, D. Lohse, and M. Versluis, "Dynamics of coated microbubbles adherent to a wall", Ultrasound Med. Biol. **37**, 1500–1508 (2011).

[6] B. Naaijkens, S. J. P. Bogaards, P. A. J. Krijnen, O. Kamp, R. J. P. Musters, T. J. A. Kokhuis, N. de Jong, N. W. M. Niessen, A. Van Dijk, and L. J. M. Juffermans, "Directing stem cells to the infarcted heart using targeted microbubbles: development of a new molecular therapeutic technique", European Heart Journal **34** (2013).

[7] L. E. Deelman, A. E. Declèves, J. J. Rychak, and K. Sharma, "Targeted renal therapies through microbubbles and ultrasound", Adv. Drug Deliv. Rev. **62**, 1369–1377 (2010).

[8] A. R. Carson, C. F. McTiernan, L. Lavery, M. Grata, X. Leng, J. Wang, X. Chen, and F. S. Villanueva, "Ultrasound-targeted microbubble destruction to deliver siRNA cancer therapy", Cancer Res. **72**, 6191–6199 (2012).

[9] R. E. Vandenbroucke, I. Lentacker, J. Demeester, S. C. De Smedt, and N. N. Sanders, "Ultrasound assisted siRNA delivery using PEG-siPlex loaded microbubbles", J. Contr. Rel. **126**, 265–273 (2008).

[10] E. Unger, T. McCreery, R. Sweitzer, V. Caldwell, and Y. Wu, "Acoustically active lipspheres containing paclitaxel: a new therapeutic ultrasound contrast agent", Investigative Radiology **33**, 886–892 (1998).

[11] S. Tinkov, C. Coester, S. Serba, N. A. Geis, H. A. Katus, G. Winter, and R. Bekeredjian, "New doxorubicin-loaded phospholipid microbubbles for targeted tumor therapy: In-vivo characterization", J. Contr. Rel. **148**, 368–372 (2010).

[12] J. Kang, X. Wu, Z. Wang, H. Ran, C. Xu, J. Wu, Z. Wang, and Y. Zhang, "Antitumor Effect of Docetaxel-Loaded Lipid Microbubbles Combined With Ultrasound-Targeted Microbubble Activation on VX2 Rabbit Liver Tumors", Ultrasound Med. Biol. **29**, 61–70 (2010).

[13] B. Geers, I. Lentacker, N. N. Sanders, J. Demeester, S. Meairs, and S. C. De Smedt, "Self-assembled liposome-loaded microbubbles: The missing link for safe and efficient ultrasound triggered drug-delivery", J. Contr. Rel. **152**, 249–256 (2011).

[14] Y. Luan, T. Faez, E. C. Gelderblom, I. Skachkov, B. Geers, I. Lentacker, A. F. W. van der Steen, M. Versluis, and N. de Jong, "Acoustical properties of individual liposome-loaded microbubbles", Ultrasound Med. Biol. **38**, 2174–2185 (2012).

[15] K. Kooiman, M. R. Bohmer, M. Emmer, H. J. Vos, C. Chlon, W. T. Shi, C. S. Hall, S. H. de Winter, K. Schroen, M. Versluis, N. de Jong, and A. van Wamel, "Oil-filled polymer microcapsules for ultrasound-mediated delivery of lipophilic drugs", J. Contr. Rel. **133**, 109–188 (2009).

[16] V. F. K. Bjerknes, "Fields of Force", Columbio University Press, New York 1–136 (1906).

[17] L. A. Crum, "Bjerknes forces on bubbles in a stationary sound field", J. Acoust. Soc. Am. **57**, 1363–1370 (1957).

[18] P. Marmottant, M. Versluis, N. de Jong, S. Hilgenfeldt, and D. Lohse, "High-speed imaging of an ultrasound-driven bubble in contact with a wall: " narcissus" effect and resolved acoustic streaming", Experiments in fluids **41**, 249–256 (2006).

[19] L. Rayleigh, "On the pressure developed in a liquid during the collapse of a spherical cavity", Pilosophical Magazine **34**, 94 – 98 (1917).

[20] O. Lindau and W. Lauterborn, "Cinematographic observation of the collapse and rebound of a laser-produced cavitation bubble near a wall", J. Fluid Mech. **479**, 327 (2003).

[21] T. J. Matula, "Inertial cavitation and single bubble sonoluminescence", Philosophical Transactions of the Royal Society of London. Series A: Mathematical, Physical and Engineering Sciences **357**, 225–249 (1999).

[22] C. D. Ohl, M. Arora, R. Dijkink, V. Janve, and D. Lohse, "Surface cleaning from laser-induced cavitation bubbles", Appl. Phys. Lett. 074102 (2006).

[23] E. Klaseboer, K. C. Hung, C. Wang, C. W. Wang, B. C. Khoo, P. Boyce, S. Debono, and H. Charlier, "Experimental and numerical investigation of the dynamics of an underwater explosion bubble near a resilient/rigid structure", J. Fluid Mech. **537**, 387–413 (2005).

[24] F. Marquet, T. Teichert, S. Wu, Y. C. Tung, M. Downs, S. Wang, C. Chen, V. Ferrera, and E. E. Konofagou, "Real-time, transcranial monitoring of safe blood-brain barrier opening in non-human primates", Plos one **9**, 1–11 (2014).

[25] N. J. Abbott, L. Ronnback, and E. Hansson, "Astrocyte endothelial interactions at the blood brain barrier", Nature Reviews Neuroscience **7**, 41–53 (2006).

[26] R. Paolinelli, M. Corada, F. Orsenigo, and E. Dejana, "The molecular basis of the blood brain barrier differentiation and maintenance. is it still a mystery?", Pharmacological Research **63**, 165–171 (2011).

[27] T. D. Khokhlova, M. S. Canney, V. A. Khokhlova, O. A. Sapozhikov, L. A. Crum, and M. R. Bailey, "Controlled tissue emulsification produced by high intensity focused ultrasound shock waves and millisecond boiling", J. Acoust. Soc. Am. **130**, 3498–3510 (2011).

[28] C. C. Coussios, C. H. Farny, G. Ter Haar, and R. A. Roy, "Role of acoustic cavitation in the delivery and monitoring of cancer treatment by high-intensity focused ultrasound (HIFU)", Int. J. Hyperthermia **23**, 105–120 (2007).

[29] Z. Xu, T. H. Hall, J. B. Fowlkes, and C. A. Cain, "Effects of acoustic parameters on bubble cloud dynamics in ultrasound tissue erosion (histotripsy)", J. Acoust. Soc. Am. **122**, 229–236 (2007).

[30] O. A. Sapozhnikov, V. A. Khokhlova, M. R. Bailey, J. C. Williams, J. A. McAteer, R. O. Cleveland, and L. A. Crum, "Effect of over-

pressure and pulse repetition frequency on cavitation in shock wave lithotripsy", J. Acoust. Soc. Am. **112**, 11831195 (2002).

[31] W. Eisenmenger, "The mechanisms of stone fragmentation in ESWL", Ultrasound Med. Biol. **27**, 683–693 (2001).

[32] B. Petit, E. Gaud, D. Colevret, M. Arditi, F. Yan, F. Tranquart, and E. Allemann, "In vitro sonothrombolysis of human flood clots with br38 microbubbles", Ultrasound Med. Biol. **38**, 1222–1233 (2012).

[33] N. de Jong, F. ten Cate, C. Lancée, J. Roelandt, and N. Bom, "Principles and recent developments in ultrasound contrast agents", Ultrasonics **29**, 324–330 (1991).

[34] J. Sijl, H. J. Vos, T. Rozendal, N. De Jong, D. Lohse, and M. Versluis, "Combined optical and acoustical detection of single microbubble dynamics.", J. Acoust. Soc. Am. **130**, 3271 (2011).

[35] M. S. Plesset, "The dynamics of cavitation bubbles", The Journal of Applied Mechanics **16**, 2777–282 (1949).

[36] K. Vokurka, "On Rayleigh's model of a freely oscillating bubble. 1. Basic relations", Czechoslovak Journal of Physics **35**, 28–40 (1985).

[37] T. G. Leighton, *The Acoustic Bubble* (Academic Press) (1994).

[38] A. Prosperetti, "Thermal effects and damping mechanisms in the forced radial oscillations of gas bubbles in liquids", J. Acoust. Soc. Am. **61**, 17–27 (1976).

[39] M. Minnaert, "On musical air-bubbles and the sound of running water", Philosophical Magazine **16**, 235–248 (1933).

[40] J. Sijl, M. Overvelde, B. Dollet, V. Garbin, N. de Jong, D. Lohse, and M. Versluis, ""Compression-only" behavior: A second-order nonlinear response of ultrasound contrast agent microbubbles", J. Acoust. Soc. Am. **129**, 1729–1739 (2011).

[41] P. Marmottant, S. Van Der Meer, M. Emmer, M. Versluis, N. De Jong, S. Hilgenfeldt, and D. Lohse, "A model for large amplitude oscillations of coated bubbles accounting for buckling and rupture", J. Acoust. Soc. Am. **118**, 3499 – 3505 (2005).

[42] A. Bouakaz, S. Frigstad, F. J. ten Cate, and N. de Jong, "Super harmonic imaging: a new imaging technique for improved contrast detection", Ultrasound Med. Biol. **28**, 59–68 (2002).

[43] D. Hope Simpson, C. T. Chin, and P. N. Burns, "Pulse inversion doppler: a new method for detecting nonlinear echoes from microbubble contrast agents", IEEE Trans. Ultrason. Ferroelec. Freq. Contr. **46**, 372–382 (1999).

[44] G. A. Brock-Fisher, M. D. Poland, and P. G. Rafter, "Means for increasing sensitivity in non-linear ultrasound imaging systems", US patent no. 5577505 (1996).

[45] P. M. Shankar, P. D. Krishna, and V. L. Newhouse, "Advantages of subharmonic over second harmonic backscatter for contrast-to-tissue echo enhancement", Ultrasound Med. Biol. **24**, 395–399 (1998).

[46] P. S. Epstein and M. S. Plesset, "On the stability of gas bubbles in liquid-ga solutions", Journal of Chemical Physics **18**, 1505–1509 (1950).

[47] M. Postema, A. Bouakaz, M. Versluis, and N. de Jong, "Ultrasound-induced gas release from contrast agent microbubbles", IEEE Trans. Ultrason. Ferroelec. Freq. Contr. **52**, 1035–1041 (2005).

[48] "GE Healtcare", URL `http://www3.gehealthcare.com`.

[49] S. B. Feinstein, F. J. Ten Cate, W. Zwehl, K. Ong, G. Maurer, C. Tei, P. M. Shah, S. Meerbaum, and E. Corday, "Two-dimensional contrast echocardiography. I: in vitro development and quantitative analysis of echo contrast agents", J. Am. Coll. Cardiol. **3**, 14–20 (1984).

[50] A. Bouakaz, M. Versluis, and N. de Jong, "High-speed optical observations of contrast agent destruction", UMB **31**, 391–399 (2005).

[51] M. R. Bohmer, R. Schroeders, J. A. M. Steenbakkers, S. H. P. M. de Winter, P. A. Duineveld, J. Lub, W. P. M. Nijssen, J. A. Pikkemaat, and H. R. Stapert, "Preparation of monodisperse polymer particles and capsules by ink-jet printing", Colloid. Surface. A **289**, 96–104 (2006).

[52] E. C. Gelderblom, "Ultra-high-speed fluorescence imaging", Ph.D. thesis, University of Twente, The Netherlands (2012).

[53] "Bracco Suisse S.A.", URL http://www.braccoimaging.com.

[54] "Lantheus Medical Imaging", URL http://www.lantheus.com/.

[55] H. Vos, F. Guidi, E. Boni, and P. Tortoli, "Method for microbubble characterization using primary radiation force", IEEE Trans. Ultrason. Ferroelectr. Freq. Control **54**, 1333–1345 (2007).

[56] "Acusphere", URL http://www.acusphere.com/.

[57] E. Stride and M. Edirisinghe, "Novel microbubble preparation technologies", Soft Matter **4**, 2350–2359 (2008).

[58] D. Lensen, E. C. Gelderblom, D. M. Vriezema, P. Marmottant, N. Verdonschot, M. Versluis, N. de Jong, and C. M. van Hest, "Biodegradable polymeric microcapsules for selective ultrasound-triggered drug release", Soft Matter **7**, 5417–5422 (2011).

[59] "Nanomi monosphere technology, the netherlands", URL http://www.nanomi.com/nanomi/index.html.

[60] A. M. Gañán-Calvo and J. M. Gordillo, "Perfectly monodisperse microbubbling by capillary flow focusing", Phys. Rev. Lett. **87**, 274501 (2001).

[61] S. L. Anna, N. Bontoux, and H. A. Stone, "Formation of dispersions using "flow focusing" in microchannels", Appl. Phys. Lett. **82**, 364–366 (2003).

[62] P. Garstecki, H. A. Stone, and G. M. Whitesides, "Mechanism for Flow-Rate Controlled Breakup in Confined Geometries: A Route to Monodisperse Emulsions", Phys. Rev. Lett. **94**, 164501 (2005).

[63] B. Dollet, W. van Hoeve, J. P. Raven, P. Marmottant, and M. Versluis, "Role of the Channel Geometry on the Bubble Pinch-Off in Flow-Focusing Devices", Phys. Rev. Lett. **100**, 034504 (2008).

[64] R. Shih, D. Bardin, D. T. Martz, P. S. Sheeran, P. A. Dayton, and A. P. Lee, "Flow-focusing regimes for accelerated production of monodisperse drug-loadable microbubbles toward clinical-scale applications", Lab. Chip **13**, 4816–4826 (2013).

[65] K. Hettiarachchi, E. Talu, M. L. Longo, P. A. Dayton, and A. P. Lee, "On-chip generation of microbubbles as a practical technology for manufacturing contrast agents for ultrasonic imaging", Lab. Chip **7**, 463–468 (2007).

[66] E. Talu, K. Hettiarachchi, R. J. Powell, A. P. Lee, P. A. Dayton, and M. L. Longo, "Maintaining monodispersity in a microbubble population formed by flow-focusing", Langmuir **24**, 1745–1749 (2008).

[67] J. J. Kwan and M. A. Borden, "Lipid monolayer mechanics during microbubble gas exchange", Soft Matter **8**, 4756–4766 (2012).

[68] J. E. Streeter, R. Gessner, I. Miles, and P. A. Dayton, "Improving sensitivity in ultrasound molecular imaging by tailoring contrast agent size distribution: in vivo studies", Mol. Imaging **9**, 87–95 (2010).

[69] Y. C. Tan, V. Cristini, and A. P. Lee, "Monodispersed microfluidic droplet generation by shear focusing microfluidic device", Sensors and Actuators B **114**, 350–356 (2006).

[70] "Tide Microfluidics, The Netherlands", URL `http://www.tidemicrofluidics.nl`.

[71] N. de Jong, R. Cornet, and C. Lancée, "Higher harmonics of vibration gas-filled microspheres. part one: simulations", Ultrasonics **32**, 447 (1994).

[72] C. C. Church, "The effect of an elastic solid surface layer on the radial pulsation of gas bubbles", J. Acoust. Soc. Am. **97**, 1510 – 1521 (1995).

[73] L. Hoff, P. Sontum, and J. Hovem, "Oscillations of polymeric microbubbles: Effect of the encapsulating shell", J. Acoust. Soc. Am. **107**, 2272–2280 (2000).

[74] K. Sarkar, W. T. Shi, D. Chatterjee, and F. Forsberg, "Characterization of ultrasound contrast microbubbles using in vitro experiments and viscous and viscoelastic interface models for encapsulation", J. Acoust. Soc. Am. **118**, 539 – 550 (2005).

[75] M. Overvelde, V. Garbin, J. Sijl, B. Dollet, N. de Jong, D. Lohse, and M. Versluis, "Nonlinear shell behavior of phospholipid-coated microbubbles.", Ultrasound Med. Biol. **36**, 2080–2092 (2010).

[76] C. T. Chin, C. Lancee, J. Borsboom, F. Mastik, M. E. Frijlink, N. de Jong, M. Versluis, and D. Lohse, "Brandaris 128: A digital 25 million frames per second camera with 128 highly sensitive frames", Review of Scientific Instruments **74**, 5026–5034 (2003).

[77] E. C. Gelderblom, H. J. Vos, F. Mastik, T. Faez, Y. Luan, T. J. A. Kokhuis, A. F. W. van der Steen, D. Lohse, N. de Jong, and M. Versluis, "Brandaris 128 ultra-high-speed imaging facility: 10 years of operation, updates, and enhanced features", Rev. Sci. Instr. **83**, 103706 (2012).

[78] X. Chen, J. Wang, M. Versluis, N. de Jong, and F. S. Villanueva, "Ultra-fast bright field and fluorescence imaging of the dynamics of micron-sized objects", Review of Scientific Instruments **84**, 063701 (2013).

[79] M. Emmer, A. van Wamel, D. E. Goertz, and N. de Jong, "The onset of microbubble vibration", Ultrasound Med. Biol. **33**, 941–949 (2007).

[80] S. Van Der Meer, B. Dollet, M. Voormolen, C. T. Chin, A. Bouakaz, N. De Jong, M. Versluis, and D. Lohse, "Microbubble spectroscopy of ultrasound contrast agents", J. Acoust. Soc. Am. **121**, 648–656 (2007).

[81] Z. Fan, H. Liu, M. Mayer, and C. X. Deng, "Spatiotemporally controlled single cell sonoporation", Proceedings of the National Academy of Sciences **109**, 16486–16491 (2012).

[82] D. E. Goertz, N. de Jong, and A. F. W. van der Steen, "Attenuation and size distribution measurements of definity and manipulated definity populations", Ultrasound Med. Biol. **33**, 1376–1388 (2007).

[83] J. A. Feshitan, C. C. Chen, J. J. Kwan, and M. A. Borden, "Microbubble size isolation by differential centrifugation.", J. Coll. Interf. Sci **329**, 316–324 (2009).

[84] M. Yamada, M. Nakashima, and M. Seki, "Pinched Flow Fractionation: Continuous Size Separation of Particles Utilizing a Laminar Flow Profile in a Pinched Microchannel", Anal. Chem. **76**, 5465–5471 (2004).

[85] T. Segers and M. Versluis, "Acoustic bubble sorting for ultrasound contrast agent enrichment", Lab. Chip **14**, 1705–1714 (2014).

[86] "Aquamarijn, The Netherlands", URL `http://www.aquamarijn.nl`.

[87] M. Emmer, H. J. Vos, D. E. Goertz, A. van Wamel, M. Versluis, and N. de Jong, "Pressure-dependent attenuation and scattering of phospholipid-coated microbubbles at low acoustic pressures", Ultrasound Med. Biol. **35**, 102–111 (2009).

[88] M. P. Kok, T. Segers, and M. Versluis, "Pinched flow fractionation of microbubbles for ultrasound contrast agent enrichment", Lab. Chip, submitted (2015).

[89] P. J. A. Frinking and N. de Jong, "Acoustic modeling of shell-encapsulated gas bubbles", Ultrasound Med. Biol. **24**, 523–533 (1998).

[90] F. Kiessling, S. Fokong, P. Koezera, W. Lederle, and T. Lammers, "Ultrasound microbubbles for molecular diagnosis, therapy, and theranostics", Molecular and Theranostic Sonography **53**, 345–348 (2012).

[91] J. M. Tsutsui, F. Xie, and R. T. Porter, "The use of microbubbles to target drug delivery", Cardiovasc. Ultrasound **2**, 23 (2004).

[92] S. Hernot and A. L. Klibanov, "Microbubbles in ultrasound-triggered drug and gene delivery ", Adv. Drug Deliv. Rev. **60**, 1153–1166 (2008).

[93] H. A. Nieuwstadt, R. Seda, D. S. Li, J. B. Fowlkes, and J. L. Bull, "Microfluidic particle sorting utilizing inertial lift force", Biomedical Microdevices **13**, 97–105 (2010).

[94] M. Hill and N. R. Harris, "Ultrasonic particle manipulation", in *Microfluidic Technologies for Miniaturized Analysis Systems*, 357–383 (Springer-Verlag, New York) (2007).

[95] T. Laurell, F. Petersson, and A. Nilsson, "Chip integrated strategies for acoustic separation and manipulation of cells and particles", Chemical Society Reviews **36**, 492–506 (2007).

[96] I. González, L. Fernández, T. Enrique Gómez, J. Berganzo, J. L. Soto, and A. Carrato, "A polymeric chip for micromanipulation and particle sorting by ultrasounds based on a multilayer configuration", Sensors and Actuators B: Chemical **144**, 310–317 (2010).

[97] P. Thevoz, J. D. Adams, H. Shea, H. Bruus, and H. T. Soh, "Acoustophoretic synchronization of mammalian cells in microchannels", Anal. Chem. **82**, 3094–3098 (2010).

[98] P. Marmottant, M. Versluis, N. de Jong, S. Hilgenfeldt, and D. Lohse, "High-speed imaging of an ultrasound-driven bubble in contact with a wall: Narcissus effect and resolved acoustic streaming", Exp. Fluids **41**, 147–153 (2006).

[99] T. Watanabe and Y. Kukita, "Translational and radial motions of a bubble in an acoustic standing wave field", Phys. Fluids **5**, 2682–2688 (1993).

[100] S. Zhao, M. Borden, S. H. Bloch, D. Kruse, K. W. Ferrara, and P. A. Dayton, "Radiation-force assisted targeting facilitates ultrasonic molecular imaging", Phys. Fluids **3**, 135–148 (2004).

[101] V. Garbin, B. Dollet, M. Overvelde, D. Cojoc, E. di Fabrizio, L. van Wijngaarden, A. Prosperetti, N. de Jong, D. Lohse, and M. Versluis, "History force on coated microbubbles propelled by ultrasound", Phys. Fluids **21**, 092003 (2009).

[102] L. Landau and E. M. Lifschitz, *Fluid Mechanics*, 2nd edition (Pergamon, New York) (1987).

[103] J. Magnaudet and I. Eames, "The motion of high-Reynolds-number bubbles in inhomogeneous flows", Ann. Rev. Fluid Mech. **32**, 659–708 (2000).

[104] H. Bruus, *Theoretical Microfluidics* (Oxford University Press) (2008).

[105] K. Zell, J. I. Sperl, M. W. Vogel, R. Niessner, and C. Haisch, "Acoustical properties of selected tissue phantom materials for ultrasound imaging", Phys. Med. Biol. **52**, 475–484 (2007).

[106] D. C. Duffy, J. C. McDonald, O. J. A. Schueller, and G. M. Whitesides, "Rapid prototyping of microfluidic systems in poly(dimethylsiloxane)", Anal. Chem. **70**, 211–217 (1998).

[107] R. Barnkob, P. Augustsson, T. Laurell, and H. Bruus, "Measuring the local pressure amplitude in microchannel acoustophoresis", Lab. Chip **10**, 563–570 (2010).

[108] R. T. Held, V. Zderic, T. N. Nguyen, and S. Vaezy, "Annular phased-array high-intensity focused ultrasound device for image-guided therapy of uterine fibroids", Trans. Ultrason. Ferroelect. Freq. Control **53**, 335–348 (2006).

[109] J. Sijl, B. Dollet, M. Overvelde, V. Garbin, T. Rozendal, N. de Jong, D. Lohse, and M. Versluis, "Subharmonic behavior of phospholipid-coated ultrasound contrast agent microbubbles", J. Acoust. Soc. Am. **128**, 3239–3252 (2010).

[110] M. Hashimoto, S. S. Shevkoplyas, B. Zasońska, T. Szymborski, P. Garstecki, and G. Whitesides, "Formation of bubbles and droplets in parallel, coupled flow-focusing geometries", Small **4**, 1795–1805 (2008).

[111] C. Devin, "Survey of Thermal, Radiation, and ViscousDamping of Pulsating Air Bubbles in Water", J. Acoust. Soc. Am. **31**, 1654–1667 (1959).

[112] B. C. Eatock, R. Y. Nishi, and G. W. Johnston, "Numerical studies of the spectrum of low-intensity ultrasound scattered by bubbles", J. Acoust. Soc. Am. **77**, 1692–1701 (1985).

[113] A. A. Doinikov, L. Aired, and A. Bouakaz, "Dynamics of a contrast agent microbubble attached to an elastic wall.", IEEE Trans. Med. Imaging **31**, 654–662 (2012).

[114] T. A. Hay, Y. A. Ilinskii, E. A. Zabolotskaya, and M. F. Hamilton, "Model for bubble pulsation in liquid between parallel viscoelastic layers", J. Acoust. Soc. Am. **132**, 124–137 (2012).

[115] B. L. Helfield and D. E. Goertz, "Nonlinear resonance behavior and linear shell estimates for Definity and MicroMarker assessed with acoustic microbubble spectroscopy", J. Acoust. Soc. Am. **133**, 1158–1168 (2013).

[116] V. Garbin, D. Cojoc, E. Ferrari, E. Di Fabrizio, M. L. J. Overvelde, S. M. Van Der Meer, N. De Jong, D. Lohse, and M. Versluis, "Changes in microbubble dynamics near a boundary revealed by combined optical micromanipulation and high-speed imaging", Appl. Phys. Lett. **90**, 114103–3 (2007).

[117] H. Dewitte, K. Vanderperren, H. Haers, E. Stock, L. Duchateau, M. Hesta, J. H. Saunders, S. C. De Smedt, and I. Lentacker, "Theranostic mRNA-loaded Microbubbles in the Lymphatics of Dogs: Implications for Drug Delivery", Theranostics **5**, 97–109 (2015).

[118] E. Stride and M. Edirisinghe, "Novel preparation techniques for controlling microbubble uniformity: a comparison", Med. Biol. Eng. Comput. **47**, 883–892 (2009).

[119] R. F. Marchington, M. Mazilu, S. Kuriakose, V. Garcés-Chávez, P. J. Reece, T. F. Krauss, M. Gu, and K. Dholakia, "Optical deflection and

sorting of microparticles in a near-field optical geometry", J. Opt. Soc. of Am. **316**, 3712–3726 (2008).

[120] D. F. Chen, W. H. Li, H. Du, and M. Li, "Continuous sorting of microparticles using dielectrophoresis", J. of Nanosc. and Nanotech. **12**, 3035–3039 (2011).

[121] H. Maenaka, M. Yamada, M. Yasuda, and M. Seki, "Continuous and size-dependent sorting of emulsion droplets using hydrodynamics in pinched microchannels", Langmuir **24**, 4405–4410 (2008).

[122] M. Matsuda, M. Yamada, and M. Seki, "Blood cell classification utilizing hydrodynamic filtration", Electronics and Communications in Japan **94**, 1–6 (2011).

[123] K. B. Andersen, S. Levinsen, W. E. Svendsen, and F. Okkels, "A generalized theoretical model for continuous particle separation in a microchannel having asymmetrically arranged multiple branches", Lab on a Chip **9**, 1638–1639 (2009).

[124] A. L. Vig and A. Kristensen, "Separation enhancement in pinched flow fractionation", Applied Physics Letters **93**, 203507 (2004).

[125] "COMSOL Multiphysics", `http://www.comsol.com/`, accessed: March 20, 2015.

[126] O. Shardt, S. K. Mitra, and J. J. Derksen, "Lattice Boltzmann Simulation of Pinched Flow Fractionation", Chemical Engineering Science **75**, 106–119 (2012).

[127] N. de Jong, M. Emmer, C. T. Chin, A. Bouakaz, F. Mastik, D. Lohse, and M. Versluis, ""Compression-Only" behavior of phospholipid-coated contrast bubbles", Ultrasound Med. Biol. **33** (2007).

[128] N. de Jong, M. Emmer, A. van Wamel, and M. Versluis, "Ultrasonic characterization of ultrasound contrast agents", Med. Biol. Eng. Comput. **47**, 861–873 (2009).

[129] N. de Jong, L. Hoff, T. Skotland, and N. Bom, "Absorption and scatter of encapsulated gas filled microspheres: Theoretical considerations and some measurements", Ultrasonics **30**, 95–103 (1992).

[130] L. Hoff, "Acoustic characterization of contrast agents for medical ultrasound imaging", Ph.D. thesis, Norwegian University of Science and Technology (2000).

[131] H. Medwin, "Counting bubbles acoustically: a review", Ultrasonics **15**, 7–13 (1977).

[132] N. de Jong and L. Hoff, "Ultrasound scattering properties of albunex microspheres", Ultrasonics **31** (1993).

[133] Y. Luan, G. Lajoinie, E. Gelderblom, I. Skachkov, A. F. W. van der Steen, H. J. Vos, M. Versluis, and N. de Jong, "Lipid shedding from single oscillating microbubbles", Ultrasound Med. Biol. **40**, 1834–1846 (2014).

[134] B. E. Treeby and B. T. Cox, "Modeling power law absorption and dispersion for acoustic propagation using the fractional laplacian", J. Acoust. Soc. Am. **127**, 2741–2748 (2010).

[135] M. A. Parrales, J. M. Fernandez, M. Perez-Saborid, J. A. Kopechek, and T. M. Porter, "Acoustic characterization of monodisperse lipid-coated microbubbles: Relationship between size and shell viscoelastic properties", J. Acoust. Soc. Am. **136**, 1077–1084 (2014).

[136] M. Kaya, S. Feingold, K. Hettiarachchi, A. P. Lee, and P. A. Dayton, "Acoustic responses of monodisperse lipid-encapsulated microbubble contrast agents produced by flow focusing", Bubble. Sci. Eng. Technol. **2**, 33–40 (2010).

[137] Y. Gong, M. Cabodi, and T. M. Porter, "Acoustic characterization of monodisperse lipid-coated microbubbles: Relationship between size and shell viscoelastic properties", Appl. Phys. Lett. **104**, 074103 (2014).

[138] A. Bouakaz, N. de Jong, and C. Cachard, "Standard properties of ultrasound contrast agents", Ultrasound Med. Biol. **24**, 469–472 (1998).

[139] J. A. Kopecheck and *et al.*, "Acoustic characterization of echogenic liposomes: Frequency-dependent attenuation and backscatter", J. Acoust. Soc. Am. **130**, 3472–3481 (2010).

[140] J. N. Marsh, M. S. Hughes, G. H. Brandenburger, and J. Miller, "Broadband measurement of the scattering-to-attenuation ratio for albunex at 37°C ", Ultrasound Med. Biol. **25**, 1321–1324 (1999).

[141] M. X. Tang, R. J. Eckersley, and J. A. Noble, "Pressure-dependent attenuation with microbubbles at low mechanical index", Ultrasound Med. Biol. **31**, 377–384 (2005).

[142] Q. Chen, J. Zagzebski, T. Wilson, and T. Stiles, "Pressure-dependent attenuation in ultrasound contrast agents", Ultrasound Med. Biol. **28**, 1041–1051 (2002).

[143] O. Couture, M. Fink, and M. Tanter, "Ultrasound contrast plane wave imaging", Ultrasonics, Ferroelectrics, and Frequency Control, IEEE Transactions on **59**, 2676–83 (2012).

[144] A. van Wamel, K. Kooiman, M. Harteveld, M. Emmer, F. J. ten Cate, M. Versluis, and N. de Jong, "Vibrating microbubbles poking individual cells: Drug transfer into cells via sonoporation", J. Contr. Rel. **112**, 149–155 (2006).

[145] A. S. Utada, A. Fernandez-Nieves, H. A. Stone, and D. A. Weitz, "Dripping to jetting transitions in coflowing liquid streams", Phys. Rev. Lett. **99**, 094502–1 (2007).

[146] J. J. Kwan and M. A. Borden, "Lipid monolayer collapse and microbubble stability", Adv. Colloid Interface Sci. **183**, 82–99 (2012).

[147] K. Wang, Y. C. Lu, J. H. Xu, and G. S. Luo, "Determination of Dynamic Interfacial Tension and Its Effect on Droplet Formation in the T-Shaped Microdispersion Process", Langmuir **25**, 2153–2158 (2009).

[148] E. Talu, R. L. Powell, M. L. Longo, and P. A. Dayton, "Needle size and injection rate impact on microbubble contrast agent population", Ultrasound Med. Biol. **34**, 1182–1185 (2008).

[149] Y. C. Tan, V. Cristini, and A. P. Lee, "Monodispersed microfluidic droplet generation by shear focusing microfluidic device", Sensors and Actuators B: Chemical **114**, 350–356 (2005).

[150] C. Szijjarto, S. Rossi, G. Waton, and M. P. Krafft, "Effects of perfluorocarbon gases on the size and stability characteristics of phospholipid-coated microbubbles: Osmotic effect versus interfacial film stabilization", Langmuir **28**, 1182–1189 (2012).

[151] P. N. Nguyen, T. Trinh Dang, G. Waton, T. Vandamme, and M. Krafft, "A nonpolar, nonamphiphilic molecule can accelerate adsorption of phospholipids and lower their surface tension at the air/water interface", Chem. Phys. Chem **12**, 2646–2652 (2011).

[152] M. M. Lozano and M. L. Longo, "Complex formation and other phase transformations mapped in saturated phosphatidylcholine/DSPE-PEG2000 monolayers", Soft Matter **5**, 1822–1834 (2009).

[153] G. Ma and H. C. Allen, "DPPC Langmuir Monolayer at the Air-Water Interface: Probing the Tail and Head Groups by Vibrational Sum Frequency Generation Spectroscopy", Langmuir **22**, 5341–5349 (2006).

[154] S. H. Yu and F. Possmayer, "Adsorption, compression and stability of surface films from natural, lipid extract and reconstituted pulmonary surfactants", Biochimica et Biophysica Acta **1167**, 264–271 (1993).

[155] M. R. Rodriguez Nino, A. Lucero, and J. M. Rodriguez Patino, "Relaxation phenomena in phospholipid monolayers at the air/water interface", Colloids and Surfaces A **320**, 260–270 (2008).

[156] J. N. Israelachvili, *Intermolecular and Surface Forces*, volume 2 (Academic Press) (1992).

[157] M. A. Borden, D. E. Kruse, C. F. Caskey, S. K. Zhao, P. A. Dayton, and K. W. Ferrara, "Influence of lipid shell physicochemical properties on ultrasoundinduced microbubble destruction", IEEE Trans. Ultrason. Ferroelectr. Freq. Control **52**, 1992–2002 (2005).

[158] D. Marsh, *Handbook of Lipid Bilayers* (CRC Press, Inc.) (1990).

[159] V. P. Torchilin, "Micellar nanocarriers: Pharmaceutical perspectives", Pharmaceutical Research **24**, 1–16 (2007).

[160] N. A. Hosny, G. Mohamedi, P. Rademeyer, J. Owen, Y. Wu, M. X. Tang, R. J. Eckersley, E. Stride, and M. K. Kuimova, "Mapping microbubble viscosity using fluorescence lifetime imaging of molecular rotors", Proc. Natl. Acad. Sci. **110**, 9225–9235 (2013).

[161] R. Williams, C. Wright, E. Cherin, N. Reznik, M. Lee, I. Gorelikov, F. S. Foster, N. Matsuura, and P. N. Burns, "Characterization of submicron phase-change perfluorocarbon droplets for extravascular ultrasound imaging of cancer", Ultrasound Med. Biol. **39**, 475–489 (2013).

[162] O. Couture, P. D. Bevan, E. Cherin, K. Cheung, P. N. Burns, and F. S. Foster, "Investigating perfluorohexane particles with high-frequency ultrasound", Ultrasound Med. Biol. **32**, 73–82 (2006).

[163] P. Sheeran, S. Luois, L. Mullin, T. Matsunaga, and P. A. Dayton, "Design of ultrasonically-activatable nanoparticles using low boiling point perfluorocarbons", Biomaterials **33**, 3262–3269 (2012).

[164] N. Reznik, M. Seo, R. Williams, E. Bolewska-Pedyczak, M. Lee, N. Matsuura, J. Gariepy, F. S. Foster, and P. N. Burns, "Optical studies of vaporization and stability of fluorescently labelled perfluorocarbon droplets", Phys. Med. Biol. **57**, 7205–7217 (2012).

[165] D. R. Evans, D. F. Parsons, and V. S. J. Craig, "Physical properties of phase-change emulsions", Langmuir **22**, 9538–9545 (2006).

[166] M. P. Krafft, "Fluorocarbons and fluorinated amphiphiles in drug delivery and biomedical research", Adv. Drug Deliv. Rev. **47**, 209–28 (2001).

[167] O. Couture, A. Urban, A. Bretagne, L. Martinez, M. Tanter, and P. Tabeling, "*In vivo* targeted delivery of large payloads with an ultrasound clinical scanner", Med. Phys. **39**, 5229–5237 (2012).

[168] R. F. Mattrey, "Perfluorooctylbromide: A new contrast agent for ct, sonography, and mr imaging", AJR Am. J. Roentgenol. **152**, 247–52 (1989).

[169] N. Y. Rapoport, Z. Gao, and A. Kennedy, "Multifunctional nanoparticles for combining ultrasonic tumor imaging and targeted chemotherapy", J. Natl. Cancer Inst. **99**, 1095–1106 (2007).

[170] P. Mohan and N. Rapoport, "Doxorubicin as a molecular nanotheranostic agent: Effect of doxorubicin encapsulation in micelles or nanoemulsions on the ultrasound-mediated intracellular delivery and nuclear trafficking", Mol. Pharm. **7**, 1959–1973 (2010).

[171] O. D. Kripfgans, J. B. Fowlkes, D. L. Miller, O. P. Eldevik, and P. L. Carson, "Acoustic droplet vaporization for therapeutic and diagnostic applications", Ultrasound Med. Biol. **26**, 1177–1189 (2000).

[172] R. E. Apfel and C. K. Holland, "Gauging the likelihood of cavitation from short-pulse, low-duty cycle diagnostic ultrasound", Phys. Med. Biol. **17**, 179–185 (1991).

[173] T. Giesecke and K. Hynynen, "Ultrasound-mediated cavitation thresholds of liquid perfluorocarbon droplets in vitro", Ultrasound Med. Biol. **29**, 1359–1365 (2003).

[174] K. C. Schad and K. Hynynen, "In vitro characterization of perfluorocarbon droplets for focused ultrasound therapy", Phys. Med. Biol. **55**, 4933–4947 (2010).

[175] O. Shpak, M. Verweij, H. J. Vos, N. de Jong, D. Lohse, and M. Versluis, "Acoustic droplet vaporization is initiated by superharmonic focusing", Proc. Natl. Acad. Sci. U.S.A. **111**, 1697–1702 (2014).

[176] R. Shilton, M. K. Tan, L. Y. Yeo, and J. R. Friend, "Particle concentration and mixing in microdrops driven by focused surface acoustic waves", Journal of Applied Physics **104**, 014910 (2008).

[177] Z. Wang and J. Zhe, "Recent advances in particle and droplet manipulation for lab-on-a-chip devices based on surface acoustic waves.", Lab. Chip **11**, 1280–5 (2011).

[178] Y. Y. Yeo and J. R. Friend, "Surface Acoustic Wave Microfluidics", Annu. Rev. Fluid Mech. **46**, 379–406 (2014).

[179] T. Segers, G. Lajoinie, and M. Versluis, "Resonant vaporization of phase change agents with surface acoustic waves", to be submitted (2015).

[180] P. K. Kundu, I. M. Cohen, and D. R. Dowling, *Fluid Mechanics*, volume 6 (Academic Press) (1994).

[181] J. B. Keller and I. I. Kolodner, "Damping of underwater explosion bubble oscillations", J. Applied Phys. **27**, 1152–1161 (1956).

[182] A. Prosperetti and A. Lezzi, "Bubble dynamics in a compressible liquid", J. Fluid Mech. **168**, 457–478 (1986).

[183] O. Shpak, T. Kokhuis, Y. Luan, D. Lohse, N. de Jong, J. B. Fowlkes, M. L. Fabiilli, and M. Versluis, "Ultrafast dynamics of the acoustic vaporization of phase-change microdroplets", J. Acoust. Soc. Am. **134**, 1610–1621 (2013).

[184] A. Doinikov, L. Aired, and A. Bouakaz, "Acoustic response from a bubble pulsating near a fluid layer of finite density and thickness.", J. Acoust. Soc. Am. **129**, 616–621 (2011).

[185] F. Caupin and E. Herbert, "Cavitation in water: a review", C. R. Physique **7**, 1000–1017 (2006).

[186] O. Shpak, L. Stricker, M. Versluis, and D. Lohse, "The role of gas in ultrasonically driven vapor bubble growth", Phys. Med. Biol. **58**, 2523–2535 (2013).

[187] C. Wang and *et al.*, "Aptamer-conjugated and drug-loaded acoustic droplets for ultrasound theranosis", Biomaterials **33**, 1939–1947 (2012).

[188] M. Fabiilli and *et al.* , "Delivery of chlorambucil using an acoustically-triggered perfluoropentane emulsion", Ultrasound Med. Biol. **36**, 1364–1375. (2010).

[189] J. Fang, C. Hung, S. Hua, and T. Hwang, "Acoustically active perfluorocarbon nano-emulsions as drug delivery carriers for camptothecin: Drug release and cytoxicity against cancer cells", Ultrasonics **49**, 39–46 (2009).

[190] M. Zhang, M. Fabiilli, K. Haworth, J. B. Fowlkes, O. Kripfgans, W. Roberts, K. Ives, and P. Carson, "Initial investigation of acoustic droplet vaporization for occlusion in canine kidney", Ultrasound Med. Biol. **36**, 1691–1703 (2010).

[191] S. Sugiura, M. Nakajima, and M. Seki, "Prediction of droplet diameter for microchannel emulsification", Langmuir **18**, 3854–3859 (2002).

[192] K. C. van Dijke, K. Schroen, and R. M. Boom, "Microchannel emulsification: From computational fluid dynamics to predictive analytical model", Langmuir **24**, 10107–10115 (2008).

[193] F. Malloggi, N. Pannacci, R. Attia, F. Monti, P. Mary, H. Willaime, and P. Tabeling, "Monodisperse colloids synthesized with nanofluidic technology", Langmuir **26**, 2369–2373 (2010).

[194] L. Shui, A. van den Berg, and J. C. T. Eijkel, "Scalable attoliter monodisperse droplet formation using multiphase nano-microfluidics", Microfluid. Nanofluid. **11**, 87–92 (2011).

[195] M. Seo and N. Matsuura, "Mondisperse, submicrometer droplets via condensation of microfluidc-generated gas bubbles", Small **8**, 2704–2714 (2012).

[196] K. Wang, L. Xie, Y. Lu, and G. Luo, "Generation of monodispersed microdroplets by temperature controlled bubble condensation processes", Lab. Chip **13**, 73–76 (2013).

[197] J. C. McDonald, D. C. Duffy, J. R. Anderson, D. T. Chiu, H. Wu, O. J. A. Schueller, and G. M. Whitesides, "Fabrication of microfluidic systems in poly (dimethylsiloxane)", Electrophoresis **21**, 27–40 (2000).

[198] O. Redlich and J. N. S. Kwong, "On the thermodynamics of solutions V", Chem. Rev. **44**, 233–244 (1949).

[199] H. V. Ermakov and V. P. Skripov, "Saturation line critical parameters and reachable overheat of perfluoroparaffins", Zh. Fiz. Khim **41**, 77–81 (1967).

[200] E. W. Lemmon, M. O. McLinden, and D. G. Friend, *NIST Chemistry WebBook, NIST Standard Reference Database*, 69 (National Institute of Standards and Technology) (1994).

[201] J. Aftienjew and A. Zawisza, "High-pressure liquid-vapour equilibria, critical state, and p(V,T,x) up to 503.15 K and 4.560 MPa for n-pentane + n-perfuorpentane", J. Chem. Thermodynamics **9**, 153–165 (1977).

[202] N. Reznik, O. Shpak, E. C. Gelderblom, R. Williams, N. de Jong, M. Versluis, and P. N. Burns, "The efficiency and stability of bubble formation by acoustic vaporization of submicron perfluorocarbon droplets", Ultrasonics **53**, 1368–1376 (2013).

[203] R. A. Rodriguez, K. A. Williams, A. Babaev, F. Rubens, and H. J. Nathan, "Effect of perfusionist technique on cerebral embolization during cardiopulmonary bypass", Perfusion **20**, 3–10 (2005).

[204] M. Barak and Y. Katz, "Microbubbles: pathophysiology and clinical implications", Chest **128**, 2918–2932 (2005).

[205] D. Barbut, Y. W. Lo, J. P. Gold, R. R. Trifiletti, F. S. F. Yao, D. N. Hager, R. B. Hinton, and O. W. Isom, "Impact of embolization during coronary artery bypass grafting on outcome and length of stay", Ann. Thorac. Surgery. **63**, 998–1002 (1997).

[206] R. E. Clark, J. Brillman, D. A. Davis, M. R. Lovell, T. R. P. Price, and G. L. Macgovern, "Microemboli during coronary artery bypass grafting", J. Thorac. Cardiovasc. Surg. **109**, 249–258 (1995).

[207] P. D. Raymond and N. A. Marsh, "Alteration to haemostasis following cardiopulmonary bypass and the relation- ship of these changes to neurocognitive morbidity", Blood. Coag. and Fig. **12**, 601–618 (2001).

[208] R. Y. Nishi, "Ultrasonic detection of bubbles with doppler flow transducers", Ultrasonics **10**, 173–9 (1972).

[209] F. De Somer, "Impact of oxygenator characteristics on its capability to remove gaseous microemboli", J. Extra. Corpor. Technol. **39**, 271–273 (2007).

[210] M. C. Stehouwer, C. Boers, R. de Vroege, C. Kelder, A. Yilmaz, and P. Bruins, "Clinical evaluation of the air removal characteristics of an oxygenator with integrated arterial filter in a minimized extracorporeal circuit", J. Artif. Organs. **34**, 374–382 (2011).

[211] S. Liu, R. F. Newland, P. J. Tully, S. C. Tuble, and R. A. Baker, "In vitro evaluation of gaseous microemboli handling of cardiopulmonary bypass circuits with and without integrated arterial line filters", J. Extra. Corpor. Technol. **43**, 107–114 (2011).

[212] K. C. Potger, D. McMillan, and M. Ambrose, "Microbubble transmission during cardiotomy infusion of a hardshell venous reservoir with integrated cardiotomy versus a softshell venous reservoir with separated cardiotomy: an in vitro comparison", J. Extra. Corpor. Technol. **45**, 77–85 (2013).

[213] D. Johagen, M. Appelblad, and S. Svenmarker, "Can the oxygenator screen filter reduce gaseous microemboli?", J. Extra Corpor. Technol. **46**, 60–66 (2014).

[214] R. W. Melchior, T. Rosenthal, and A. C. Glatz, "An in vitro comparison of the ability of three commonly used pediatric cardiopulmonary bypass circuits to filter gaseous microemboli", Perfusion **25**, 255–263 (2010).

[215] F. M. De Somer, M. R. Vetrano, J. P. Van Beeck, and G. J. van Nooten, "Extracorporeal bubbles: a word of caution", Interact. Cardiovasc. Thorac. Surg. **10**, 995–1002 (2010).

[216] D. Maresca, M. Emmer, P. L. M. J. van Neer, H. J. Vos, M. Versluis, M. Muller, N. de Jong, and A. F. W. van der Steen, "Acoustic sizing of an ultrasound contrast agent", Ultrasound Med. Biol. **36**, 1713–1721 (2010).

[217] J. E. Lynch, A. Pouch, R. Sanders, M. Hinders, K. Rudd, and J. Sevick, "Gaseous microemboli sizing in extracorporeal circuits using ultrasound backscatter", Ultrasound Med. Biol. **33**, 1661–1675 (2007).

[218] J. B. Lynch, J. E. Riley, "Microemboli detection on extracorporeal bypass circuits", Perfusion **23**, 23–32 (2008).

[219] S. Brand, R. Klaua, G. Dietrich, and M. Schultz, "Ultrasonic detection and quantitative analysis of microscopic bubbles and particles in solution: enhanced by attenuation compensation", in *Proceedings of the IEEE Ultrasonics Symposium*, volume 1, 1840–1843 (2006).

[220] K. V. Jenderka, M. Schultz, G. Dietrich, and P. Fornara, "Detection and sizing of micro bubbles in streaming fluids with ultrasound", in *Sensors, 2002. Proceedings of IEEE*, volume 1, 528–531 vol.1 (2002).

[221] T. Szabo, *Diagnostic Ultrasound Imaging: Inside Out* (Academic Press) (2004).

[222] P. Garstecki, I. Gitlin, W. DiLuzio, and G. M. Whitesides, "Formation of monodisperse bubbles in a microfluidic flow-focusing device", Appl. Phys. Lett. **85**, 2649–2651 (2004).

[223] M. O. Culjat, D. Goldenberg, P. Tewari, and R. Singh, "A review of tissue substitutes for ultrasound imaging", Ultrasound Med. Biol. **36**, 861–873 (2010).

Samenvatting

Echografie wordt wereldwijd gebruikt als diagnostisch instrument in onder meer cardiologie, urologie en gynaecologie. De geluidsgolven die reflecteren op grensvlakken tussen zachte en harde structuren maken het mogelijk om bijvoorbeeld organen of een foetus in beeld te brengen. Om het bloed zichtbaar te maken kan een contrastvloeistof ingespoten worden. Zo'n contrastvloeistof bevat biljoenen microbellen die een sterkte echo produceren doordat ze trillen in het aandrijvende ultrageluidsveld. De bellen zijn klein genoeg, tussen de 1 en 10 micrometer, om probleemloos door de kleinste haarvaten te stromen zonder deze te verstoppen. Bovendien zijn ze gecoat met een schil van fosfolipiden om te voorkomen dat ze oplossen. De schil heeft viscoelastische eigenschappen; de stijfheid van de schil leidt tot een hogere resonantiefrequentie en de viscositeit van de schil resulteert in een hogere demping. Eerder is aangetoond dat de oppervlakteconcentratie van de lipiden kan verschillen van bel tot bel waardoor bellen van dezelfde grootte een heel ander akoestisch gedrag kunnen hebben[75]. De schil van de bel vormt bovendien een geschikte aanhechtingsplaats voor medicijnen en antilichamen. De aanhechting kan zo gekozen worden dat deze aangrijpt op zieke cellen of bijvoorbeeld op tumoren. Wanneer de bellen vervolgens in trilling worden gebracht, schudden ze de medicijnen van zich af. Microbellen kunnen dus gebruikt worden voor de gecontroleerde lokale afgifte van medicijnen. Echter, de medicijnafgifte beperkt zich tot het vasculaire bed omdat contrastbellen te groot zijn om bloedvaten te kunnen verlaten. In tegenstelling tot microbellen kunnen medicijnhoudende druppels met een diameter van rond de 200 nm uit het bloedvat treden waardoor ze ophopen in tumoren. Deze nanodruppels hebben een kookpunt lager dan de lichaamstemperatuur en hun verdamping kan geïnitieerd worden met ultrageluid. Na verdamping vormen de druppels microbellen die het mogelijk maken de locatie van de medicijnafgifte in beeld te brengen met diagnostisch ultrageluid. Druppel- en belsuspensies geproduceerd op conventionele wijze hebben een brede grootteverdeling. De amplitude van de bel-echo en de efficiëntie van de verdamping zijn echter sterk afhankelijk van de bel- en druppelgrootte. Een grote winst in efficiëntie kan dus behaald worden door alle druppels en microbellen even groot te maken. In dit proefschrift wordt aangetoond dat monodisperse microbellen, microdruppels, en nanodruppels efficiënt geproduceerd kunnen worden met microfluïdische technieken.

In hoofdstuk 2 laten we laten zien dat microbellen gesorteerd kunnen worden op hun akoestische gedrag. In een microkanaal worden resonante bellen

weggeduwd uit een polydisperse belsuspensie door middel van akoestische stralingsdruk, die het grootst is op resonantie. Het akoestische gedrag van gesorteerde bellen is gemeten aan de hand van de verstrooiing en verzwakking van een akoestische golf lopend door de belsuspensie. We laten zien dat de echo's van de gesorteerde microbellen heel uniform zijn en dat de echoamplitude sterk afhankelijk is van de frequentie en van de druk waarmee de bellen aangestraald worden. Bovendien is de respons van gesorteerde bellen goed te modelleren door alle niet-lineaire echo's van de bellen die zich in de belsuspensie bevinden op te tellen en door gebruik te maken van één unieke set van viscoelastische schileigenschappen (H4). De zeer uniforme en goed gedefinieerde druk- en frequentie afhankelijke respons van de gesorteerde bellen geeft nieuwe mogelijkheden in het verbeteren van ultrasone beeldvorming en in de gecontroleerde lokale medicijnafgifte met microbellen.

Microbellen kunnen ook efficiënt worden gesorteerd op grootte zonder dat er externe krachten op worden uitgeoefend met de zogenaamde 'pinched flow fractionation' methode. In een smal kanaaltje worden microbellen tegen de wand geduwd door een meegevoerde stroming. Daardoor komen bellen van verschillende grootte op verschillende stroomlijnen te liggen. Door het smalle kanaal vervolgens 30 keer te verbreden, trek je de stroomlijnen verder uit elkaar waardoor je selectief op positie, en dus op grootte, kan sorteren. We hebben laten zien dat het essentieel is, voor een correcte modelmatige beschrijving van het sorteergedrag, om de rotatie van de bellen in het smalle kanaal mee te nemen in het model omdat roterende bellen het stromingsveld sterk beïnvloeden. Een van de voordelen van de pinched flow fractionation methode is dat het sorteergedrag onafhankelijk is van de stroomsnelheid. Bovendien maakt de eenvoud van deze sorteertechniek haar goed geschikt voor parallellisatie, waardoor de techniek in principe veel potentie heeft, bijvoorbeeld geïmplementeerd in steriele wegwerp-sorteermodules.

De efficiëntie van de akoestisch, en op grootte, gesorteerde contrastmiddelen zijn vergeleken met de efficiëntie van het niet gesorteerde, originele polydisperse contrastmiddel aan de hand van de gemeten verstrooide en geabsorbeerde akoestische energie van een ultrageluidsgolf voortbewegend door het contrastmiddel. De terugontvangen echo van de gesorteerde belsuspensies was tenminste tien keer hoger dan die van het originele contrastmiddel, terwijl de hoeveelheid geabsorbeerde energie gelijk was. Op de harmonische van de aanstraalfrequentie was de hoeveelheid verstrooide energie aan de gesorteerde belsuspensies zelfs 20 keer hoger. De hoeveelheid verstrooide energie is bovendien sterk afhankelijk van de frequentie en van de druk van het ultrageluid. Deze unieke eigenschap maakt het mogelijk om tijdens klinische echografie de frequentie en de druk zodanig te kiezen dat alleen de

bellen die zich in het akoestische focus bevinden energie verstrooien en energie absorberen. De ultrageluidsgolf wordt dus niet verzwakt door bellen die zich tussen de probe en het akoestische focus bevinden met het ontbreken van storende schaduweffecten, die onderliggend weefsel onzichtbaar maken, tot gevolg. Monodisperse bellen verhogen dus niet alleen de amplitude van de echorespons, ze verhogen ook de efficiëntie van contrast echografie.

Monodisperse bellen kunnen ook direct gevormd worden in een microfluïdische chip door een gas stroom met een vloeistofstroming door een kleine gaatje, een nozzle, te persen, de zgn. 'flow-focusing' techniek. Als het gas de nozzle verlaat breekt het op in microbellen allemaal precies even groot. We hebben laten zien dat het mogelijk is om 1 miljoen monodisperse fosfolipidegecoate bellen per seconde te produceren met een enkele micrometer-grote nozzle. De gevormde bellen lossen op totdat ze precies 2.55 maal kleiner zijn in grootte. De stabiliteit van de gevormde microbellen is onafhankelijk van de afschuifspanning in de nozzle (H6). Bovendien hebben we aangetoond dat de hoeveelheid fosfolipiden op het beloppervlak niet meer verandert nadat de bel de nozzle heeft verlaten, niet als de bel groeit en ook niet als de bel oplost. De gekrompen bellen zijn stabiel in grootte voor een periode van tenminste 2 uur. Met akoestische verzwakkingsmetingen hebben we aangetoond dat de belschil geleidelijk stijver wordt naarmate de bel langer trilt. Dit komt omdat de bel een lipide component verliest uit de schil, te weten een emulgator met de hoogste oplosbaarheid in water.

We hebben laten zien dat de flow-focusing techniek ook gebruikt kan worden om op zeer gecontroleerde en efficiënte wijze monodisperse microdruppels te produceren, met een minimum diameter van 4 μm (H8). Kleinere monodisperse nanodruppels kunnen ook geproduceerd worden, bijv. door micrometer grote dampbellen te vormen met de flow-focusing techniek en deze vervolgens te re-condenseren. De op deze manier gevormde druppels zijn bij benadering 5 keer kleiner dan de dampbellen van waaruit ze gevormd zijn. In een microfluïdische chip met een nanometer diep kanaal dat uitmond in een micrometer diep kanaal kunnen ook monodisperse nanodruppels geproduceerd worden. Echter, gebeurt dit bij een veel lagere productiesnelheid. Met de drie besproken productiemethoden is het mogelijk om monodisperse druppels te maken met groottes die geschikt zijn voor medisch gebruik. De verdamping van de gevormde monodisperse druppels gefilmd met een hogesnelheidscamera heeft laten zien dat het verdampingsproces van druppels van dezelfde grootte zeer reproduceerbaar is. De akoestische drukken die nodig waren om de verdamping te initiëren lagen, voor meerdere experimenten, binnen een marge van 5% van ultrageluidsdruk. De verdamping van druppels die zich in clusters bevonden was symmetrisch

en de druk nodig voor de verdamping was lager dan voor enkele druppels. De gemeten stap-respons van de verdamping als functie van de akoestische druk is van groot belang voor bijvoorbeeld de gecontroleerde afgifte van medicijnen met druppels en ultrageluid.

We hebben laten zien dat druppels efficiënt verdampt kunnen worden door ze aan te stralen op hun radiële resonantiefrequentie (H7). Het resonante verdampingsmechanisme is nieuw en verschilt van het eerder gevonden verdampingsmechanisme waarbij geluidsgolven focusseren in de druppel[175]. We vonden een goede overeenkomst tussen de gemodelleerde en de gemeten druppelgrootte-afhankelijke verdampingsefficiëntie. Voor een efficiënte toepassing van nanodruppels in de medische technologie is het dus van cruciaal belang dat de druppelverdamping wordt geïnitieerd met ultrageluid van een frequentie gelijk aan de resonantiefrequentie van de gebruikte druppels. De verdampingefficiëntie neemt exponentieel toe tijdens herhaald aanstralen van de druppelsuspensie. De al aanwezige dampbellen, die gevormd zijn tijdens de eerste ultrageluidspuls, initiëren de verdamping van de meest kleine druppels tijdens de tweede ultrageluidspuls.

Bellen in de bloedbaan zijn niet altijd nuttig. Gas bellen groter dan 10 µm in diameter kunnen haarvaten verstoppen en kunnen daarom gevaarlijk zijn. Tijdens een open hartoperatie kunnen luchtbellen in het bloed terechtkomen en het is nog niet bekend of deze bellen, en welke grootte van bellen precies, gevaarlijk zijn en of ze een negatief effect hebben op het herstel van de patiënt na de operatie. Daarom worden wel eens bellentellers gebuikt om de bellen in een hart-longmachine te volgen. We hebben monodisperse bellen gebruikt om de twee beschikbare klinische bellentellers te testen op hun nauwkeurigheid in het tellen en het meten van de grootte van bellen. Onze metingen laten zien dat de beschikbare bellentellers erg onnauwkeurig zijn in het bepalen van de belgrootte en in het meten van de hoeveelheid bellen. De potentiele negatieve effecten van luchtbellen op het herstel van de patiënt na een openhartoperatie kunnen dus alleen goed gevolgd worden als er nieuwe bellentellers ontwikkeld worden met een hogere meetnauwkeurigheid.

Dankwoord

Mijn proefschrift is af, nou ja, bijna dan. De waarschijnlijk meest gelezen zinnen van 'het boekje' moeten nog geschreven worden: het dankwoord. Tijd om eens terug te kijken. Al terugkijkend merk ik dat het iets is wat ik niet vaak en met weinig genoegen doe. 'Meer dan het verleden interesseert mij de toekomst, want daarin ben ik van plan te leven', zei meneer Einstein ooit. Maar goed, nu moet het.

Alweer 5 jaar geleden begon ik aan mijn afstudeeropdracht. 'Ik heb wel een creatieve fröbelopdracht voor je', zei Michel. Bij de woorden creatief en fröbelen werd, en word ik nog steeds enthousiast. Ik mocht een manier verzinnen om belletjes te sorteren, een opdracht omschrijving waar vrienden nog steeds om moeten lachen. Het heeft de basis gelegd voor dit proefschrift, namelijk hoofdstuk 2. Blijkbaar vond ik die belletjes leuk genoeg om er nog eens 4 jaar aan te besteden: het promotieonderzoek. Leuk was het zeker, vaak dan, in ieder geval. Ik wil dan ook Michel en Detlef bedanken voor de mogelijkheid die ze mij gegeven hebben om een promotieonderzoek binnen hun vakgroep uit te voeren. Vier mooie jaren waarin ik erg veel geleerd heb. Bijvoorbeeld wat ik leuk vind en waar ik goed in ben maar natuurlijk heb ik ook veel geleerd op het gebied van het doen van wetenschappelijk onderzoek. De persoon die daar het grootste aandeel in heeft gehad is Michel. Een ontzettend prettige mentor die mij geleerd heeft hoe je verhalen vertelt, bijvoorbeeld tijdens een presentatie, in een artikel of tijdens een televisie uitzending (NOS Studio sport en De Kennis Van Nu). Waarschijnlijk even belangrijk: hij leerde me kritische vragen te stellen en de antwoorden op deze vragen te vinden; de inhoud van het verhaal. De inhoud van de verhalen tijdens het avondprogramma van de vele (buitenlandse) conferenties was minder serieus, gelukkig. 'Het was zo gezellig hè' zei je lachend toen er een collega bij ons groepje kwam zitten die over werk begon te praten. 'Zo, nu eerst een groot glas koud bier', nog zo'n mooie uitspraak van je die ik graag hoorde. Michel, onwijs bedankt voor de leuke tijd!

Nico, tijdens onze meetings wou ik vaak je mening horen over een specifiek stukje van mijn onderzoek. Een stukje waarvan ik het gevoel had dat het beter kon maar voordat ik toe kwam aan het stellen van mijn eigenlijke vraag was de meeting vaak alweer voorbij. Niet omdat deze zo kort duurde maar omdat jij datgene waarvan ik vrij zeker was toch nog wist te doen laten rammelen. Mede daardoor waren de discussies van grote waarde, bedankt!

I would like to thank Bracco en Peter Frinking for supplying me with phospholipid coated microbubbles. Peter, bedankt voor de prettige samen-

werking en voor het zitting nemen in de promotiecommissie. Ik heb genoten van de discussies waarin je tussen de zinnen door je antwoord verstopte op mijn vragen over fosfolipiden en hun invloed op het gedrag van bellen.

The work presented in this thesis and the work that dind't make it to the thesis was performed in collaboration with many people: Maarten, Leonie, Guillaume, Elena, Marco, Filip, Mark, Alex, Tom 1, Tom 2, Klazina, Heleen, Ine, Ying, Jason, David, Jan, Lingling, Detlef, Nico, and Michel. Thank you for all the help and the inspiring scientific discussions. Een aantal mensen wil ik in het bijzonder bedanken. Marco, bedankt voor de prettige samenwerking en voor de indrukwekkende ochtend die ik naast jou doorbracht in een operatie kamer tijdens een openhartoperatie. Maarten en Leonie, jullie afstudeerwerk heeft een mooie plek in dit proefschrift gekregen, bedankt! Elena, thanks a lot for your kind help in the preparation of aqueous lipid solutions. Mark, many thanks for the help and insight you gave us on interfacial chemistry. Mijn dank ben ik ook zeker verschuldigd aan Michel, Guillaume en Maarten voor de grote hoeveelheid tijd die zij, in de laatste weken voordat mijn boekje naar de commissie moest, gestoken hebben in het meedenken en in het corrigeren van de hoofdstukken. Bedankt!

Gert-Wim, Martin en Bas. De drie technici waar de vakgroep op draait. Bedankt voor de technische ondersteuning zowel binnen de vakgroep als daarbuiten. De praatjes over onder meer motoren, uitlaatdempers en elektronische circuits heb ik altijd erg leuk gevonden. Joanita, op iedere organisatorische vraag wist jij een antwoord of vond jij een antwoord, dankjewel.

Ex-kantoorgenoten van 'the chearfull office', Aaldert, Erik, en Arjan bedankt voor het inwijden van ondergetekende in het promotietraject. The chearfull office werd later 'the cool office' met drie warmbloedigen die het meest productief zijn in een kantoor met een open raam en een frisse omgevingstemperatuur: Guillaume, Pascal en ik. Pascal bedankt voor het verruimen van mijn woordenschat met de bijvoeglijke naamwoorden: 'koningen' en 'episch', voor je organisatorische adviezen maar bovenal voor de gezelligheid en de lol om je bulderlach. Guillaume, op wetenschappelijk gebied hebben we behoorlijk wat samen gedaan, bedankt voor de leuke samenwerking. Van de conferenties waar ik geweest ben heb ik er bovendien veel samen met jou meegemaakt. Ik wil je bedanken voor de vele leuke momenten in bijvoorbeeld Hong Kong (waar we als excuus voor onze jetlag tot diep in de nacht de kroegen verkenden), in Rotterdam, in Leiden en tijdens de toffe road trips die we maakten in de VS en in Canada. Mark-Jan, eigenlijk was jij ook een soort van kantoorgenoot voor ons. Koffie, extrastrong extra-long alsjeblieft. De niet werk gerelateerde activiteiten vond ik

ook leuk; het regelen van de PoF borrel bijvoorbeeld en de las-cursus die we gevolgd hebben.

Talking about fun; I would like to thank Tom 1, Tom 2, Maarten, Heleen, kleine Ine, grote Ine, Verya, Ilya, Libertario, Ying, en Alex for the nice time we had during conferences and meetings in Leeds and Rotterdam.

An essential part of the good time at PoF was the atmosphere and the great colleagues. Thanks go to all current and past PoF members. I enjoyed the drinks, group outings, summer schools, Christmas dinners and afternoon walks.

De laatste woorden zijn voor de leuksten, mensen van wie hun support zo vanzelfsprekend lijkt te zijn dat een bedankje vaak vergeten wordt. Rob, Melvin, Djuri thanks voor de leukste tijden. Pa en ma bedankt voor het nog altijd warme nest met Lex, Marijn en Wibo, en Betsie. Marijn en Lex, heel leuk dat jullie mijn paranimfen willen zijn :-)